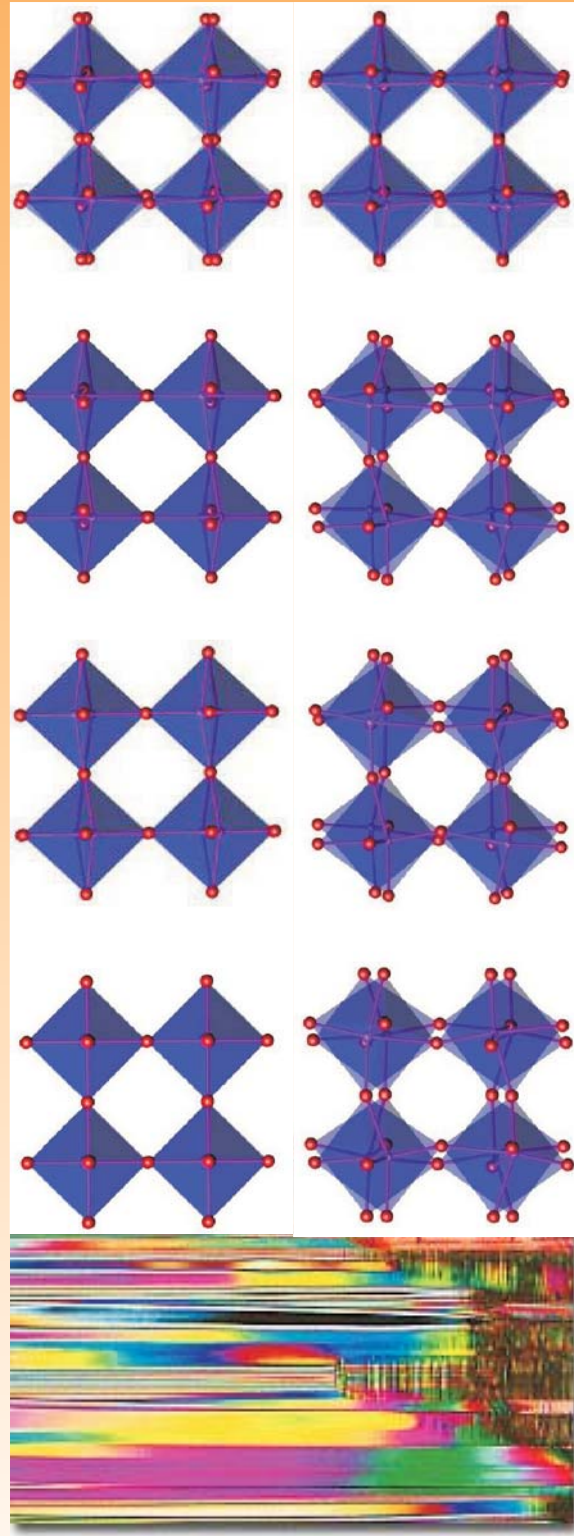
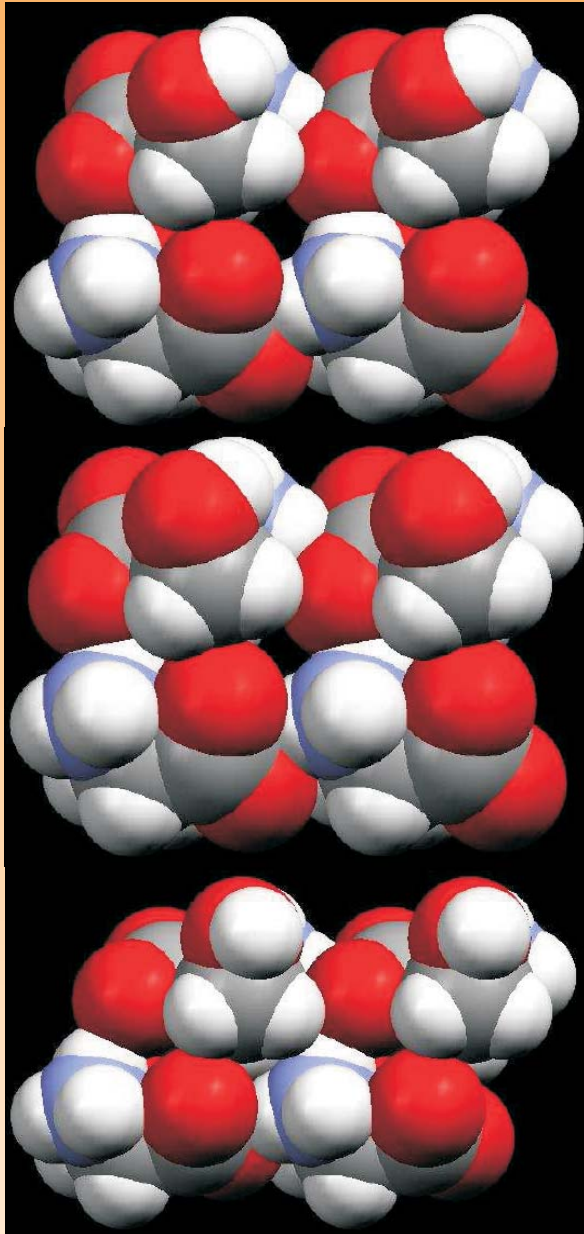


PHASE TRANSITIONS



TRANSACTIONS OF THE SYMPOSIUM HELD AT THE 2009 AMERICAN CRYSTALLOGRAPHIC
ASSOCIATION ANNUAL MEETING, TORONTO, JULY 25TH - 30TH 2009

PHASE TRANSITIONS

TRANSACTIONS OF THE SYMPOSIUM HELD AT THE 2009 AMERICAN CRYSTALLOGRAPHIC ASSOCIATION ANNUAL MEETING, TORONTO, JULY 25TH – 30TH 2009

CONTENTS

Introduction

Acknowledgements

Part 1: Energetics and Structure

High-pressure phase transitions in molecular crystals.

S. Parsons, University of Edinburgh.

Phase transitions in microporous materials.

D. Gatta, University of Milan.

Structural Chemistry across phase boundaries

I. D. Brown, McMaster University.

Part 2: Structural Phase Transitions

Nature's basis for parameterizing structural phase transitions.

B. Campbell, Brigham Young University

Symmetry aspects of structural phase transitions: Ferroics and Multiferroics.

M. Perez-Mato, University of the Basque Country.

Local structure and crystallographic phase transitions.

T. Proffen, Los Alamos National Laboratory.

Part 3: Crystallographic Methods for Studying Phase Transitions.

Advances in automated twin data processing in CrysAlis^{Pro}.

M. Meyer, Oxford Diffraction, Wroclaw

Data Collection and Processing of Incommensurately Modulated Structures at Varying Temperatures.

M. Ruf, Bruker AXS, Madison.

Modulated phases and their analysis with Jana2006.

M. Dusek, Institute of Physics, Prague

INTRODUCTION

R.J. Angel
Virginia Tech Crystallography Laboratory,
Virginia Tech, Blacksburg, VA 24060 USA

Phase transitions, in which a structure changes from one atomic arrangement to another without a change in composition, provide the most rigorous arena for testing ideas about the forces and balances of forces that stabilize particular atomic configurations in crystal structures. The study of phase transitions has direct applications in pharmacology and drug design where the issue of stable polymorphs is critical, and most modern materials used in devices (gmr materials, piezo- and ferro-electrics and multi-ferroics) derive their technological properties as a result of structural phase transitions. While the study of phase transitions has previously been a major focus of solid state physics and mineralogy, the advent of fast and accurate area detector technologies together with reliable and automated temperature control systems, means that the study of phase transitions in molecular systems can become routine, provided the methods of analysis are known. In the Transactions Symposium of the 2009 ACA meeting in Toronto a broad selection of the concepts and characterization techniques for studying phase transitions that have been developed in many sub-disciplines of crystallography were presented.

In the first contribution, Simon Parsons (Edinburgh), uses the example of his work on the high-pressure polymorphism of salicylaldoxime and of serine to demonstrate that while phase transitions sometimes appear to be driven by bonding forces, such as H-bonds being forced to become short, the dominant factor in determining polymorph stability at high pressures is the packing efficiency. The pressures involved, of several GPa, mean that the PV term becomes the dominant component of the free energy of a molecular crystal. The same conclusion is drawn by the wide-ranging review of the behaviour of zeolites at high pressures by Diego Gatta (Milan); their general response to increasing pressure is one of continuous rotations of the tetrahedral units comprising the framework, and the relatively rare transitions occur through the same rotations in a discontinuous way, so as to greatly decrease the volume. The essential message is summarized by I. David Brown (Hamilton, ON) who, in the context of an exploration of bonding forces through the concept of bond valence once again emphasizes that chemistry does not change between phases or across phase boundaries, but that phase transitions are driven by changes in the intensive external thermodynamic variables such as temperature or pressure.

Structural phase transitions are a special class of transitions in which the symmetries of the two phases have a group-subgroup relationship, and the lower-symmetry structure can be regarded as distorted version of the high-symmetry form. The power of analyzing structural phase transitions, and the resulting structures, from a group-theoretical point is emphasized in two contributions. Branton Campbell (Provo, UT) shows that the apparently complex structural evolution of the distorted low-symmetry phase below a transition can often be more simply and naturally explained in terms of “symmetry-

adapted distortion modes” which he points out are “Nature’s basis for parameterizing structural phase transitions”. The essence of a distortion can often be captured by a relatively small number of the available modes, while the other modes have amplitudes that cluster near zero. As a consequence, the symmetry-adapted description reduces the effective complexity, leading to a clearer understanding and more stable refinement of crystal structures to diffraction data. Close to high-temperature phase transitions such modes can represent the dynamic fluctuations of the structure. Thomas Proeffen (Los Alamos) shows that, by analyzing the total scattering in terms of a probability density function, many displacive transitions in oxides involve no change in local structure but merely a change in the long-range correlations. Manuel Perez-Mato (Bilbao) extends the symmetry-mode approach to the analysis of phase transitions giving rise to multi-ferroic materials, and introduced the audience to the power of Landau theory and the concept of symmetry-adapted order parameters, equivalent to the mode amplitudes, to couple macroscopic thermodynamics of the low-symmetry phase directly to the microscopic distortions of its atomic structure.

One session of the symposium was devoted to presentations of software tools that help in the processing and refinement of the more complex diffraction data that arises from crystals that have undergone phase transitions. Mathias Meyer (Oxford Diffraction) demonstrates that indexing and integrating diffraction patterns from crystals that have become twinned as a result of a phase transition is straightforward with the tools now available and Michel Ruf (Bruker-AXS) shows the same is true for the integration of diffraction patterns from incommensurately modulated crystals. Michel Dusek (Prague) demonstrates the power of the Jana software for determining and refining both twinned and modulated structures.

The program was completed by a large number of contributed papers which covered a range of types of transitions and materials so broad that they cannot be described in detail here.

Ross J. Angel
Virginia Tech

ACKNOWLEDGEMENTS

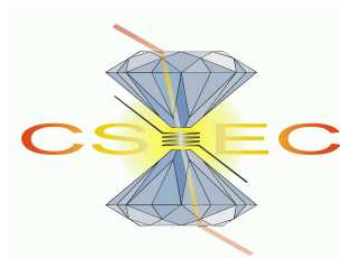
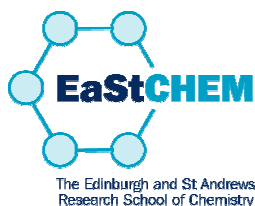
Financial support for the symposium was generously provided by:

- American Crystallographic Association
- International Union of Crystallography
- National Sciences and Engineering Research Council of Canada
- Oxford Diffraction
- Petroleum Research Fund of the American Chemical Society



And the symposium was sponsored by the following *Special Interest Groups* of the American Crystallographic Association:

- *Powder diffraction*
- *Materials Science*
- *Service Crystallography*
- *Small Molecules*
- *Small Angle Scattering*
- *General Interest*



HIGH PRESSURE PHASE TRANSITIONS IN MOLECULAR CRYSTALS

Simon Parsons

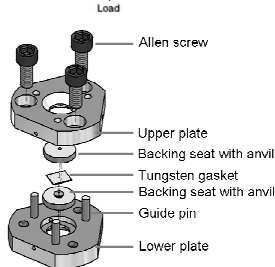
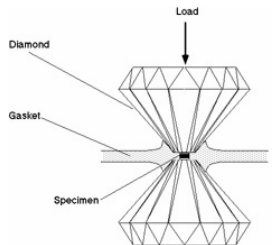
We are interested in the behaviour of molecular crystal structures in the pressure regime up to 10 GPa. 1000 atm = 1 kbar ~ 0.1 GPa; so 10 GPa is 100 000 atm. The pressure at the bottom of deep sea trenches can reach 0.1 GPa or 1000 atm.

A number of different classes of material have been studied at pressure, and many undergo phase transitions. For example in the amino acids, which were one of the first series of molecular compounds to be systematically investigated, crystallographic confirmation of high-pressure polymorphism has been obtained for glycine, L-cysteine, L-serine and L-leucine.

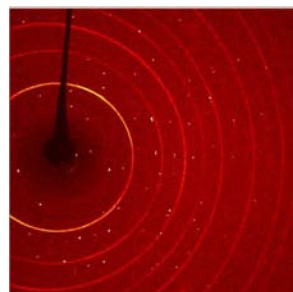
The issue I want to address here is why high pressure transitions occur. We'll look at two case studies: serine and salicylaldoxime.



The Edinburgh and St Andrews Research School of Chemistry



Diamond Anvil Cell



Merrill, Bassett (1974). *Rev. Sci. Instrum.*, **45**, 290-294.
Moggach, Allan, Parsons, Warren (2008). *J Appl. Cryst.* **41**, 249-251

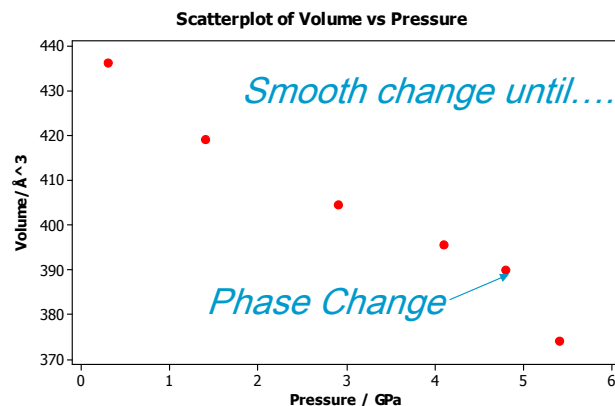
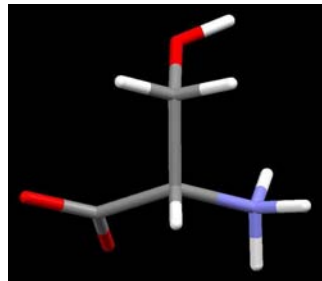
This slide summarises equipment that we use for high pressure crystallography in the range from 0.1 GPa to 10 GPa.

The Merrill-Bassett diamond anvil cell is small enough to fit on a standard goniometer head, and it can be used on a normal diffractometer with only few modifications needed. A short collimator should be used so that the cell can rotate; it may also be necessary to modify the beam-stop to accommodate the cell.

Procedures for data collections using a CCD diffractometer are described in Dawson, A., Allan, D. R., Parsons, S. & Ruf, M. (2004). *Journal Applied Crystallography* **37**, 410-416.

Images are contaminated by components of the cell, in the case of the one shown on this slide by powder rings from the tungsten gasket. Diamonds also diffract strongly and show up as very bright spots on images. Merrill and Bassett's original design of cell used Be backing disks, and powder rings from these can cause serious contamination of the images. A new design recently described by Moggach et al (2008) removes the need for Be, using instead a conically-ground WC backing disk. This results in much cleaner images.

Super-Short H-bonds?



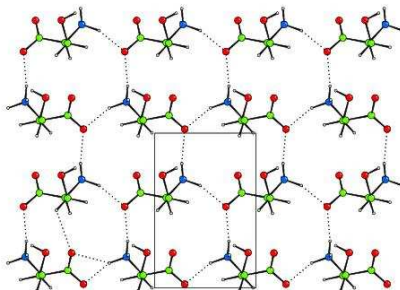
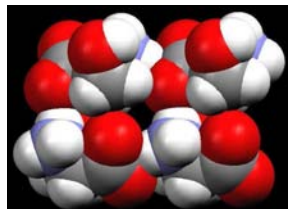
Moggach, Allan, Morrison, Parsons, and Sawyer, *Acta Crystallogr., Sect. B* 61, 58-68 (2005).
Moggach, Marshall, and Parsons, *Acta Crystallogr., Sect. B* B62, 815-825 (2006).

Prior to systematic studies of H-bonded solids at high pressure it was thought possible that pressure could be used to engineer unusually short intermolecular interactions.

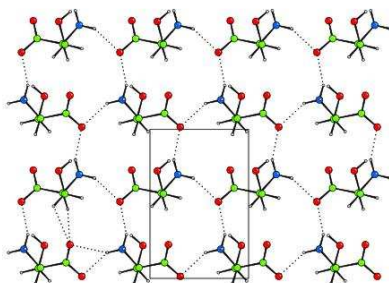
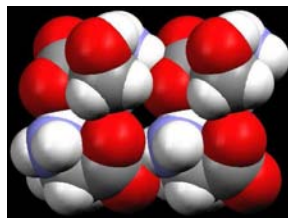
In the following slides this idea is tested using the amino acid serine and the important metal-extraction ligand salicylaldoxime.

Serine undergoes a phase transition at ca 5 GPa to a new high pressure phase.

0 GPa



4.8 GPa



Up to 4.8 GPa serine stays in a compressed form of its ambient pressure phase.

The structure consists of layers of molecules connected together by NH...O hydrogen bonds.

The images on this slide are on the same scale and the compression of intermolecular interactions can be seen in the lower diagrams.

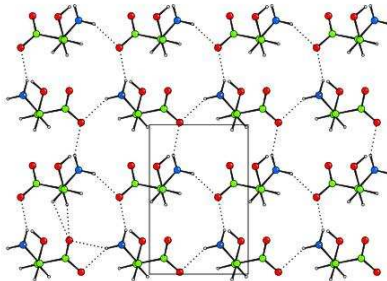
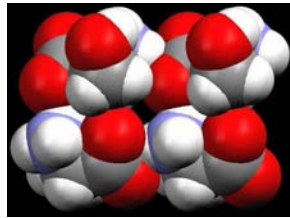
Up to 4.8 GPa one of the NH...O H-bonds compresses from N...O = 2.89 to 2.69 Å.

In spite of the compression in H-bonds interstitial voids are still present in the structure even at 4.8 GPa.

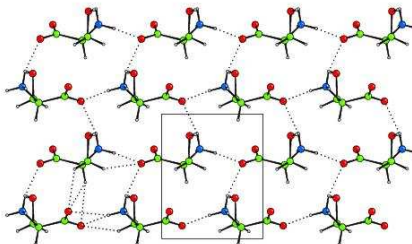
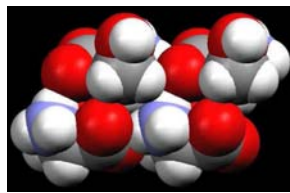


The Edinburgh and St Andrews Research School of Chemistry

4.8 GPa



5.4 GPa



New Phase.

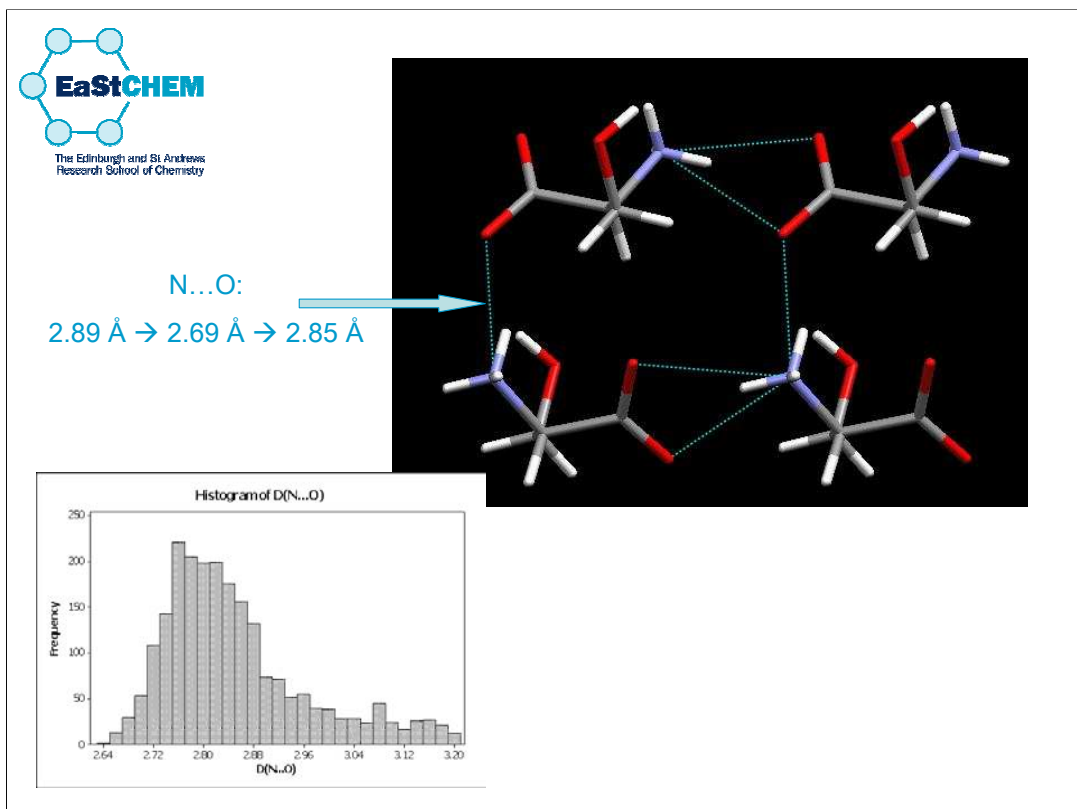
$2.69 \rightarrow 2.85 \text{ \AA}$

On increasing the pressure on serine from 4.8 to 5.2 GPa the structure transforms to a new high-pressure phase, serine-II.

Over the course of this transition the NH...O H-bond which has reached 2.69 Å *lengthens* to 2.85 Å.

The serine layers slide in opposite directions which allows them to compress further in the vertical direction, closing up the interstitial voids noted on the previous slide.

As before, both diagrams are on the same scale, and the more efficient packing in phase-II is clear.



A search of the CSD for $\text{NH} \dots \text{O}$ H-bond distances in amino acids shows that 2.69 \AA is near the lower limit for this type of interaction.

Could it be that the intermolecular interactions are being pushed into a repulsive region of their potentials?

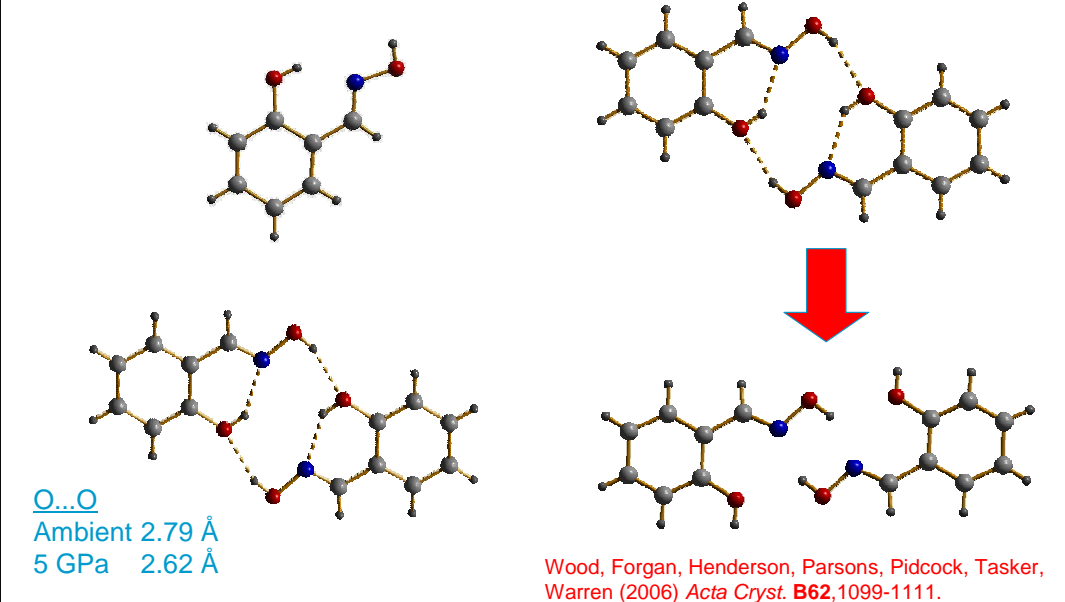
This would explain why the phase transition occurs – it relieves strain built up in compressed H-bonds.

It turns out that the original idea that super-short H-bonds can be formed at high pressure is not right: in no case, even in structures at 10 GPa, have we seen any H-bond which is shorter than the CSD minimum.

The next slide shows another example.



Salicylaldoxime



Salicylaldoximes are used in hydrometallurgical extraction of copper. About 30% of the World's Cu is extracted in this way.

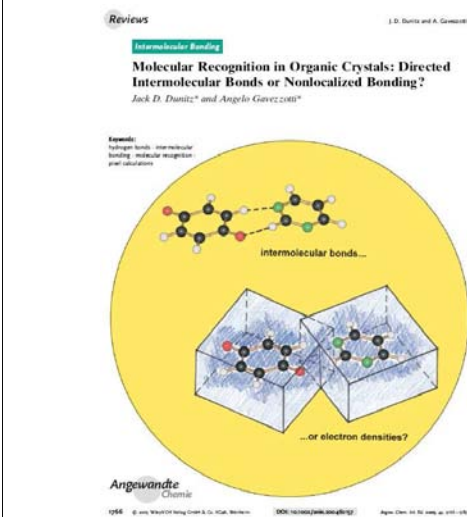
The compound is such an effective ligand for Cu because it forms pseudomacrocyclic dimers through oxime to hydroxyl H-bonds. Cu²⁺ ions are of the right size to sit in the cavity formed by removal of two protons.

We have studied salicylaldoxime (and a number of its derivatives) at high pressure. In the parent compound, the dimer-forming H-bond reaches O...O = 2.62 Å at 5 GPa. This figure is close to the CSD minimum distance for this class of interaction, and on increasing the pressure further the crystal transforms to a new phase where the H-bonding in the strained region is relieved.

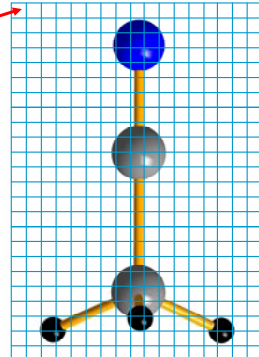
This fits our theory of why phase transitions occur, as outlined on the previous slide.



Gavezzotti's PIXEL Method



Charge known at each pixel.



A. Gavezzotti, Z. Krist., 2005, 220, 499-510.

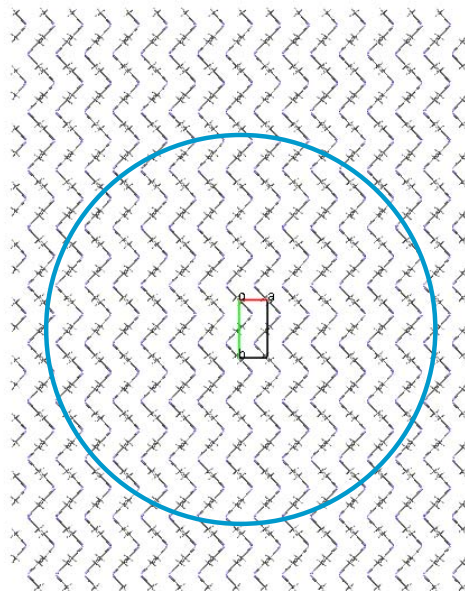
At about the time we were doing the work on serine and salicylaldoxime, this paper by Dunitz and Gavezzotti was published in Angew. Chem.

It described a method which had been developed by Gavezzotti for the evaluation of crystal packing energies. Rather than decompose molecule-molecule energies into individual parameterised atom-atom interactions energy terms are calculated from the whole-molecule electron densities.

The method is described in detail in Gavezzotti's Z. Krist paper, cited at the bottom of the slide.

The first stage of the procedure is to calculate the electron density of the molecules using Gaussian. This produces an array of pixels in a cube distributed about the molecule.

Gavezzotti's PIXEL Method



This array of pixels is then placed back into the crystal structure, and space group symmetry used to generate symmetry-related arrays of pixels out to a defined radius (typically 20 Å).

Gavezzotti's PIXEL Method

Reference Molecule

| | | | |
|-----|-----|-----|-----|
| Q1 | Q2 | Q3 | Q4 |
| Q5 | Q6 | Q7 | Q8 |
| Q9 | Q10 | Q11 | Q12 |
| Q13 | Q14 | Q15 | Q16 |
| Q17 | Q18 | Q19 | Q20 |
| Q21 | Q22 | Q23 | Q24 |



Symmetry Equivalent

| | | | |
|-----|-----|-----|-----|
| Q24 | Q23 | Q22 | Q21 |
| Q20 | Q19 | Q18 | Q17 |
| Q16 | Q15 | Q14 | Q13 |
| Q12 | Q11 | Q10 | Q9 |
| Q8 | Q7 | Q6 | Q5 |
| Q4 | Q3 | Q2 | Q1 |

$$E_{\text{coul}} = \frac{Q_1 Q_4}{4\pi\epsilon_0 r}$$

$$E_{\text{latt}} = E_{\text{coul}} + E_{\text{Disp}} + E_{\text{Pol}} + E_{\text{Rep}}$$

Energies between the reference molecule and all the other molecules in the cluster are then evaluated.

Molecule-molecule energies are broken down into electrostatic, polarisation, dispersion and repulsion terms. Each term is calculated by summing pair-wise contributions from the pixels in each molecule. The procedure for the electrostatic energy is illustrated, similar equations are available for the other energy terms.

The sum of all the energy terms gives the lattice energy.

Principal interactions are also identified.

Each energy is broken down into chemically meaningful electrostatic, polarisation, dispersion and repulsion terms, which can then be interpreted



Gavezzotti's PIXEL Method

836 *J. Chem. Theory Comput.*, Vol. 1, No. 5, 2005

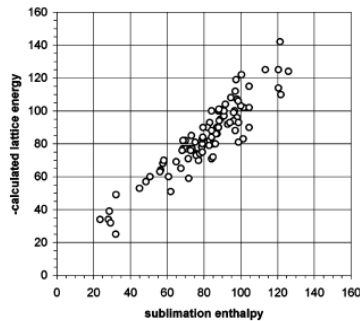
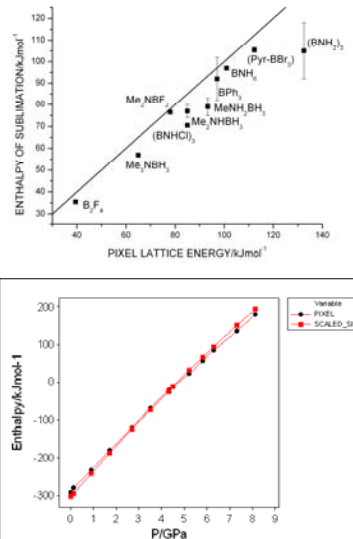


Figure 1. Negative of Pixel-calculated lattice energies versus experimental heats of sublimation for 91 organic crystals (kJ mol⁻¹). The least-squares line is $y = 1.03x$; $R^2 = 0.84$.



Wood, Francis, Marshall, Moggach, Parsons, Pidcock and Rohl, *CrystEngComm*, 2008, 10, 1154 - 1166.
Aldridge, Downs, Tang, Parsons, Clarke, Johnstone, Robertson, Rankin, Wann. *JACS*. In press.

This slide illustrates results of pixel calculations compared to experimental sublimation enthalpies for organic compounds and boron-containing compounds.

Also shown is a comparison of PIXEL and plane-wave DFT energies for serine at high-pressure.

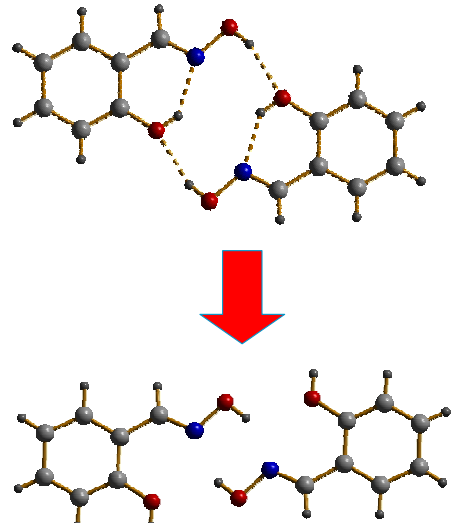
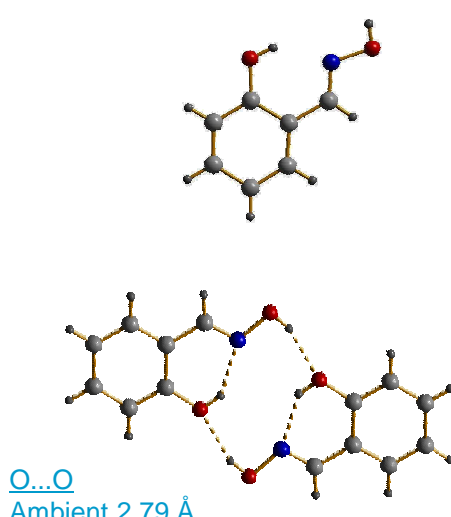
While there are some absolute deviations in some cases it is clear that PIXEL faithfully reproduces trends in packing energies.

We now go on to apply the PIXEL method to high-pressure structures with the aim of testing the idea that phase transitions are caused by molecules being pushed into repulsive regions of their interaction potentials.



The Edinburgh and St Andrews
Research School of Chemistry

Salicylaldoxime

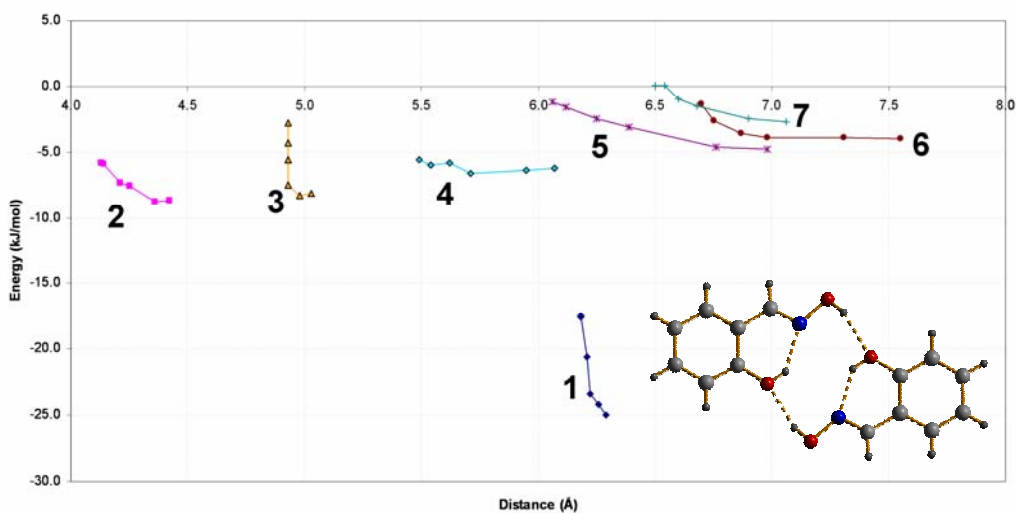


A reminder of the salicylaldoxime results shown earlier...



Salicylaldoxime

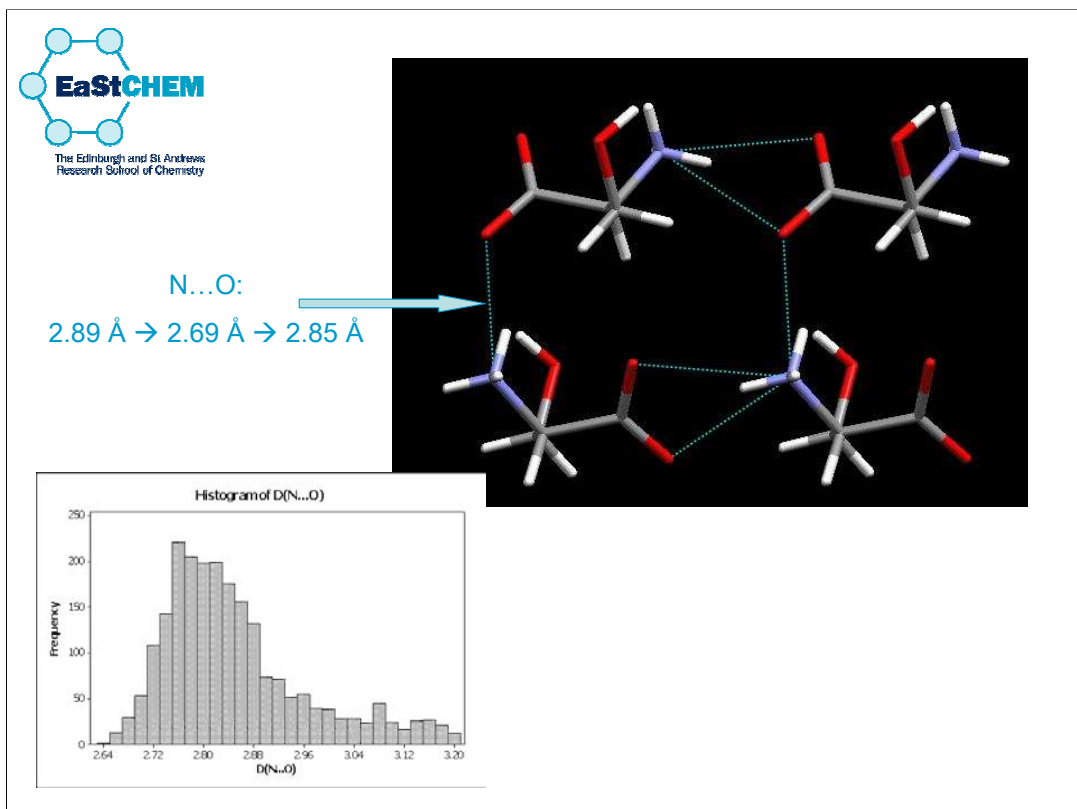
Graph of Interaction Energy against Molecular Centroid Separation



Interaction 1 is the H-bonded dimer where the O...O distance approaches the CSD minimum. The curve shows that as pressure increases the interaction is pushed into the repulsive region of the potential.

The same happens to a pi-stacking contact.

This slide shows that our picture of the driving force for the phase transition is valid. The transition relieves strained interactions.

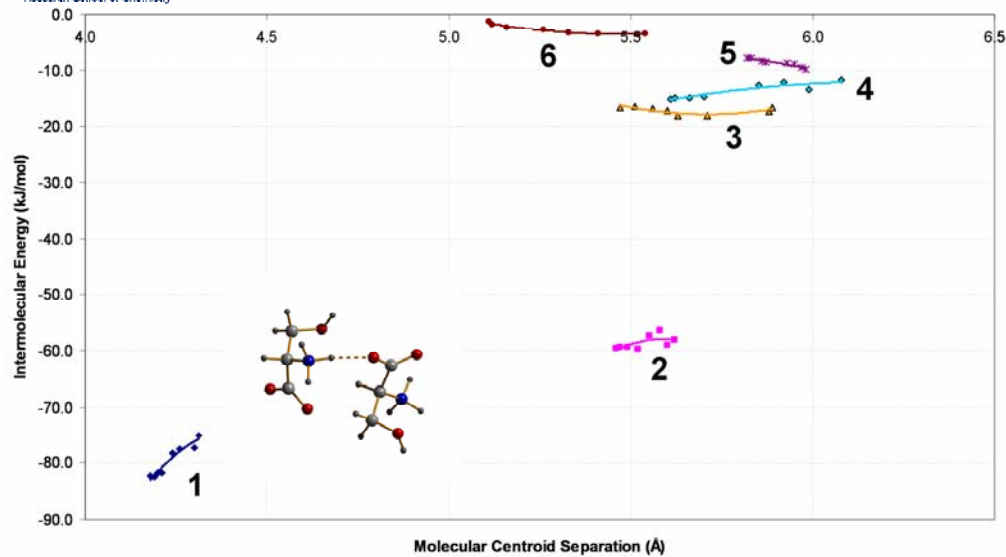


A reminder of the serine results....



The Edinburgh and St Andrews
Research School of Chemistry

Serine



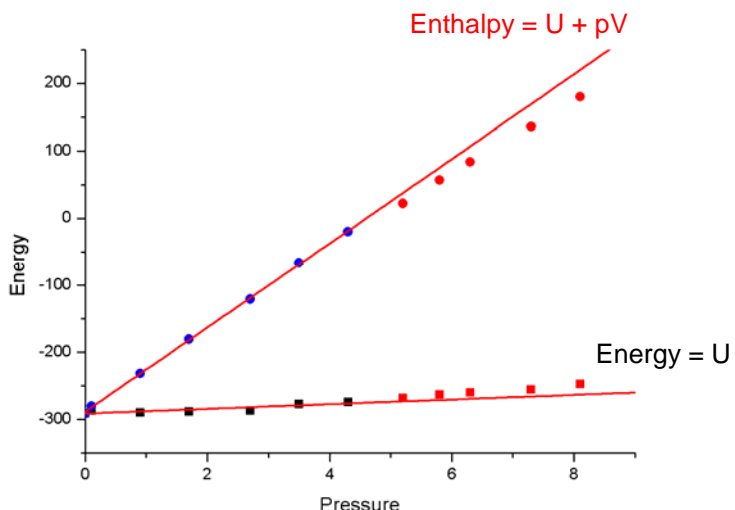
Wood, Francis, Marshall, Moggach, Parsons, Pidcock and Rohl, *CrystEngComm*, 2008, 10, 1154 - 1166.

Note that none of the interactions becomes repulsive here.

Interactions 1 is the H-bond which was pushed to the far left of the histogram showing NH...O distances in the CSD (previous slide). Pressure actually *stabilises* this interaction. We can hardly describe it as being strained.

This shows that our simple picture for why phase transitions happen at pressure, though it is right for salicylaldoxime, is wrong from serine.

Effect on Energy



Why doesn't our simple model work?

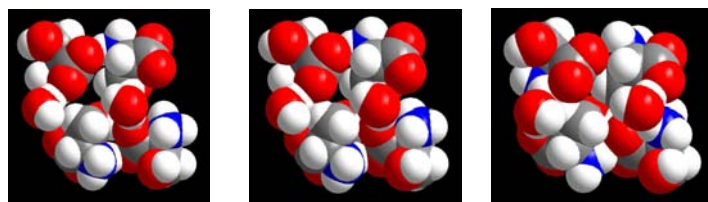
In considering the lattice energy we are only considering one thermodynamic term contributing to free energy.

We can calculate the change in lattice enthalpy by including a pV term (recall $H = U + pV$).

When the pV term is included the reason for the stability of phase-II above 5 GPa become clear: it is more efficiently packed. This efficient packing makes up for the fact that the intermolecular interactions are less energetic in phase II than in phase-I.



What Drives Phase Transitions?



$$G = U + pV - TS$$

In salicylaldoxime the phase transition was driven by the U-term in this famous equation. The volume change in the phase-I-to-II transition is small, and there is not much contribution (estimated 1 kJ/mol) from the pV-term.

In serine it is the pV term that is important.

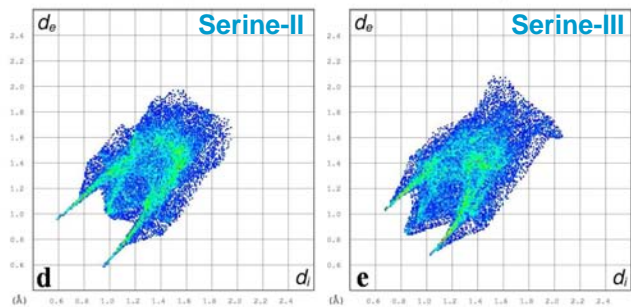
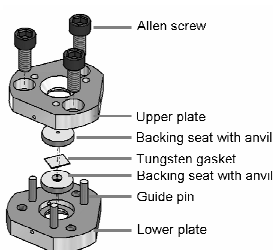


The Edinburgh and St Andrews
Research School of Chemistry

Use of the Allen Key in Crystal Engineering



- The pV term becomes ever more important as P increases.
- Serine-II \rightarrow Serine-III



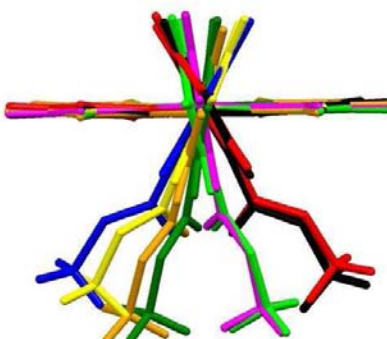
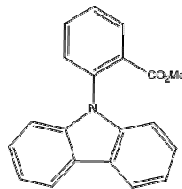
The pV term become progressively more important as pressure increases, and this can lead to some counter-intuitive effects.

In serine there is another phase transition at 8 GPa to another high-pressure phase, serine-III. The Hirshfeld fingerprint plot shows that the H-bond distances increase during the transition, but H...H interactions become more important. The prominent H...H feature is something that is associated with packing in hydrocarbons: pressure is making serine behave less like and H-bonded solid and more like an alkane!

This implies that high pressure can be used as a tool to tune the importance of intermolecular interactions in crystal engineering.

Oddities: High Z' Structures

- Only 0.1% of structures have $Z' > 4$.
- Why do they form?
- Structural frustration
 - E.g. chiral acids
- Isoenergetic conformers
 - CARZIF, $Z' = 8$



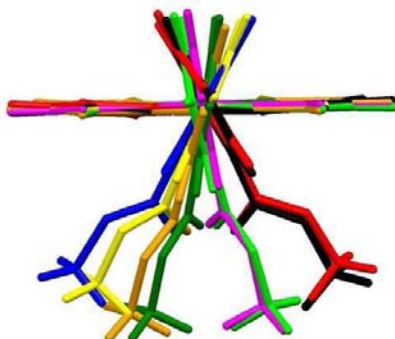
We can illustrate this idea by looking at some structural oddities.

High Z' structures are unusual. There are no universally applicable theories (yet) about why they form, but there are some classes of material that are susceptible. 60% of chirally pure carboxylic acids have $Z' > 1$. The tendency for acid groups to form centrosymmetric dimers conflicts with the fact that inversion centres are forbidden in chirally-pure crystal structures. This is referred to as structural frustration and it often results in high Z' structures (see K. M. Anderson, A. E. Goeta and J. W. Steed *Cryst. Growth Des.*, 2008, **8**, 2517).

Another factor what can lead to high Z' structures is when a molule is conformationally flexible. This is the case with the compound 'CARZIF', which has $Z' = 8$.

CARZIF

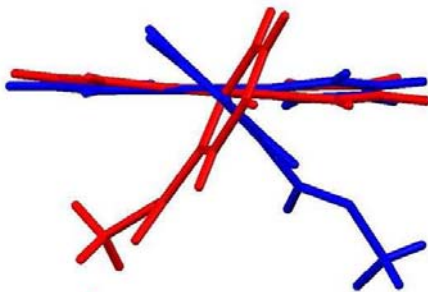
- The need to pack efficiently means that a structure should ‘select’ low volume or ‘well-packing’ conformers.



Can the need to pack efficiently be used to select well-packing conformer to force a high Z' structure into a low Z' phase?

CARZIF

- The need to pack efficiently means that a structure should ‘select’ low volume or ‘well-packing’ conformers.

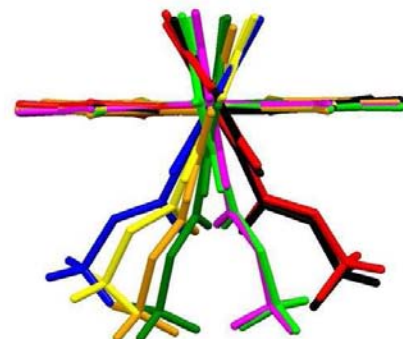


At 5.3 GPa CARZIF transforms to a $Z'=2$ phase with only two conformations present.

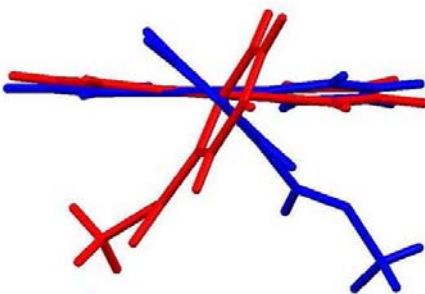


The Edinburgh and St Andrews Research School of Chemistry

CARZIF



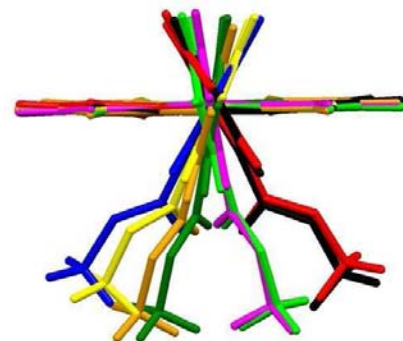
Phase I: Volume/molecule = 307 \AA^3



Phase II: Volume/molecule = 300 \AA^3

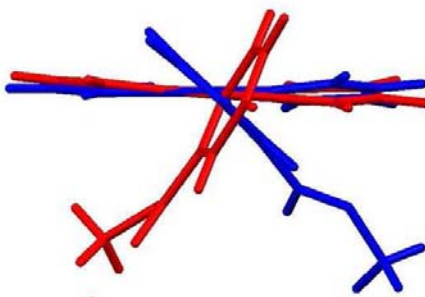
Note that in the high-pressure conformation the molecules are ‘thinner’ than at low pressure: they will take up less volume in this form. The idea of using an Allen key for crystal engineering has worked!

They also pack more efficiently, as can be seen from the volume/molecule in each structure. The value for the $Z'=8$ form is extrapolated to the same pressure (5.3 GPa) as the $Z'=2$ form.



Phase I: Volume/molecule = 307 \AA^3

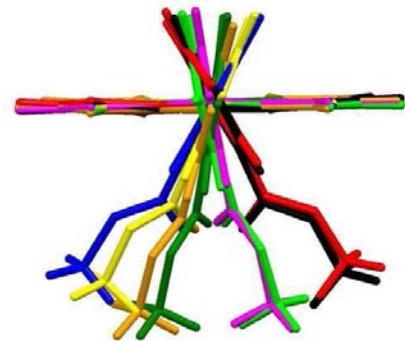
$\Delta E \sim 6 \text{ kJmol}^{-1}$



Phase II: Volume/molecule = 300 \AA^3

$\Delta E < 1 \text{ kJmol}^{-1}$

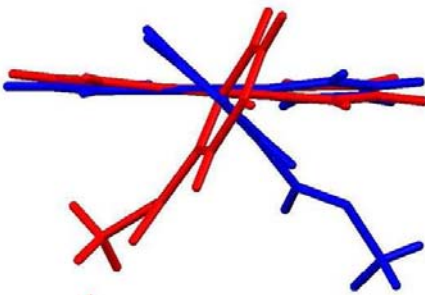
Usually in polymorphs and high Z' structures molecular conformational energies differ by at most around 5 kJmol^{-1} . This is the case for conformers within phases-I or II.



Phase I: Volume/molecule = 307 \AA^3

$\Delta E \sim 6 \text{ kJmol}^{-1}$

BUT ΔE between phases is $+23 \text{ kJmol}^{-1}$



Phase II: Volume/molecule = 300 \AA^3

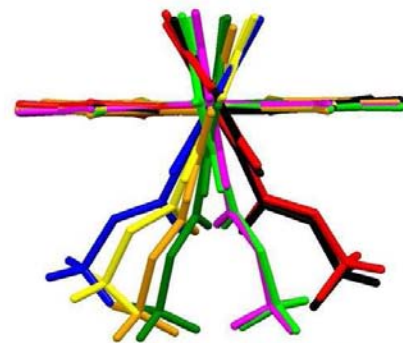
$\Delta E < 1 \text{ kJmol}^{-1}$

But the average difference in energy between the phases is 23 kJmol^{-1} . This is an enormous difference, arising from the puckering in the carbazole ring, the change in conformation about the C-N bond, the change in conformation about the phenyl-ester bond and the eclipsed conformation of the methyl group.

How can such a large energy difference be sustained?



CARZIF

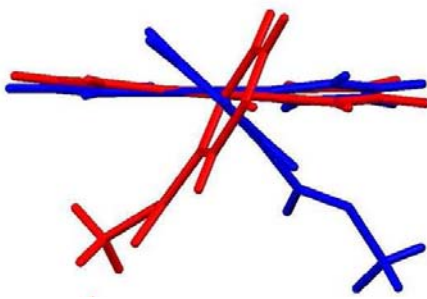


Phase I: Volume/molecule = 307 \AA^3

$\Delta E \sim 6 \text{ kJmol}^{-1}$

BUT ΔE between phases is $+23 \text{ kJmol}^{-1}$

pV term = $5.3 \times -7 \times 0.6 = -22.3 \text{ kJmol}^{-1}$



Phase II: Volume/molecule = 300 \AA^3

$\Delta E < 1 \text{ kJmol}^{-1}$

Johnstone et al. In preparation.

The answer is the pV term: this (almost) cancels out the conformational energy difference between the two phases.



Summary & Conclusions

- Polymorphism in organic compounds
 - Supershort contacts not formed up to 10 GPa
 - Avoid repulsive interactions
 - Volume reduction
 - Makes high pressure a way of stabilising unusual conformations: using an Allen key for crystal engineering.

Moggach, Parsons & Wood *Cryst. Rev.* (2008) **14** 143-184

Moggach & Parsons *RSC Specialist Periodical Reports* (2009) In Press.



The Edinburgh and St Andrews
Research School of Chemistry

Edinburgh
Steve Moggach
Russell Johnstone

Alice Dawson
Peter Tasker
Ross Forgan
Hamish McNab
Maria Ieva

CCDC
Elna Pidcock
Peter Wood

STFC
Dave Allan
Bill Marshall
John Warren

Milan
Angelo Gavezzotti

Acknowledgements



G. Diego Gatta

Department of Earth Sciences, University of Milan, Italy

E-mail: diego.gatta@unimi.it

PHASE-TRANSITIONS IN MICROPOROUS MATERIALS

2009 ACA Meeting, July 25 - 30



UNIVERSITÀ
DEGLI STUDI
DI MILANO

What is a microporous material?

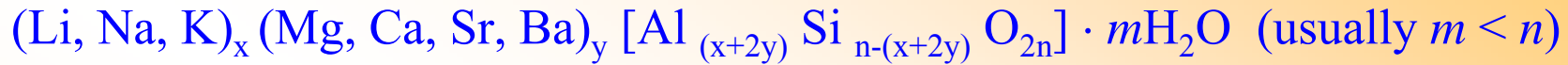
Zeolites: a class of microporous materials

"Recommended nomenclature for zeolite minerals: report of the Subcommittee on Zeolites of International Mineralogical Association, Commission on new minerals and minerals names" (Coombs et al., 1997):

"A zeolite mineral is a crystalline substance with a structure characterized by a framework of linked tetrahedra, each consisting of four O atoms surrounding a cation. This framework contains open cavities in the form of channels and cages. These are usually occupied by H₂O molecules and extra-framework cations that are commonly exchangeable. The channels are large enough to allow the passage of guest species. In the hydrated phases, dehydration occurs at temperature mostly below about 400°C and is largely reversible. The framework may be interrupted by (OH, F) groups; these occupy a tetrahedron apex that is not shared with adjacent tetrahedra".



General chemical formula for zeolites:



Framework density (FD):

The framework density is defined as the number of T-atoms per 1000 Å³. For non-zeolitic framework structures, values of at least 20 to 21 T/1000 Å³ are generally obtained, while for zeolites the observed values range from about 12.1 for structures with the largest pore volume to around 20.6.

Quartz FD=26.4 T/1000 Å³

Albite FD=24 T/1000 Å³

Scapolite FD=21.6 T/1000 Å³

Paracelsian FD = 21.3 T/1000 Å³



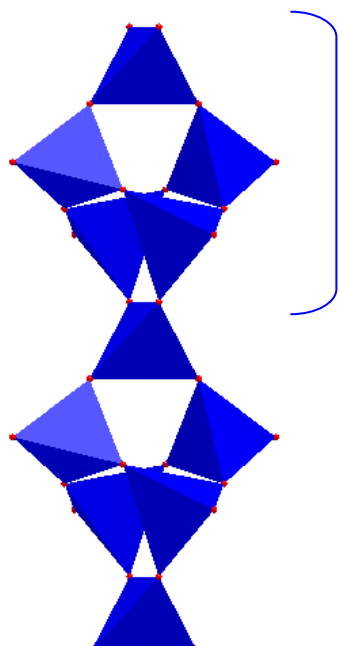
Number of crystal structures reported in ICSD for selected mineral groups

| | |
|---------------------------|-----|
| Cation-exchanged zeolites | 409 |
| Zeolites | 273 |
| Feldspars | 136 |
| Amphiboles | 99 |
| SiO_2 polymorphs | 76 |
| Micas | 75 |
| Pyroxenes | 51 |

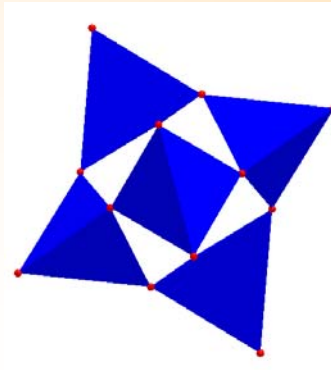
(in Armbruster and Gunter 2001, *Rev Mineral Geochem*, 45)

Classification of (natural) zeolites

1) Fibrous zeolites – zeolites with T_5O_{10} units



T_5O_{10} units

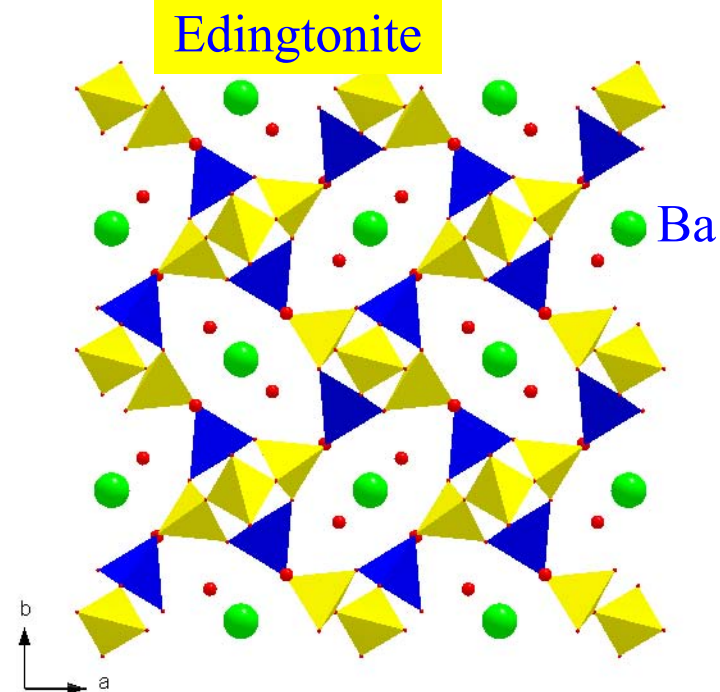


natrolite ($Na_{16}Al_{16}Si_{24}O_{80} \cdot 16H_2O$), scolecite ($Ca_8Al_{16}Si_{24}O_{80} \cdot 24H_2O$),
edingtonite ($Ba_2Al_4Si_6O_{20} \cdot 8H_2O$), thomsonite ($Na_4Ca_8Al_{20}Si_{20}O_{80} \cdot 24 H_2O$)

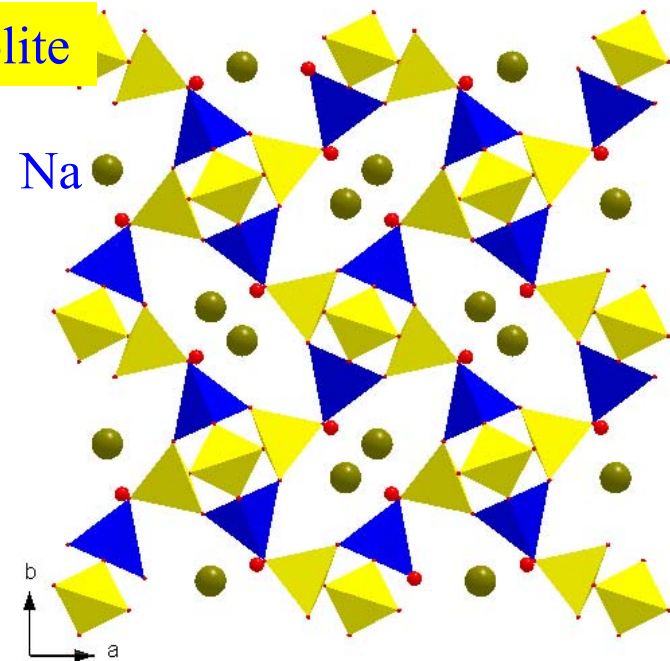


UNIVERSITÀ
DEGLI STUDI
DI MILANO

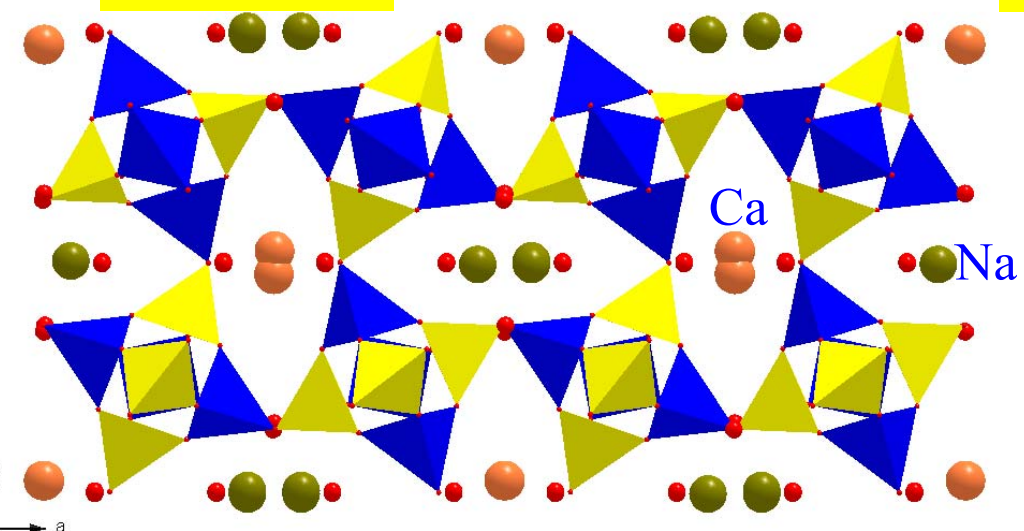
Edingtonite



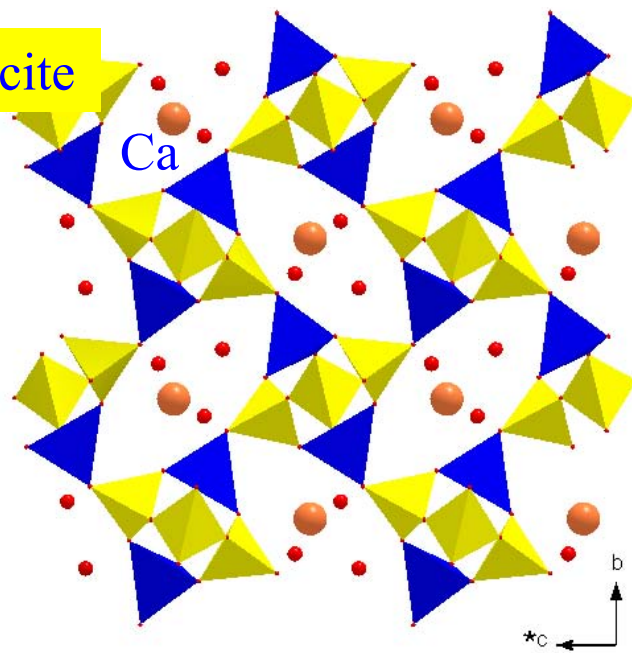
Natrolite



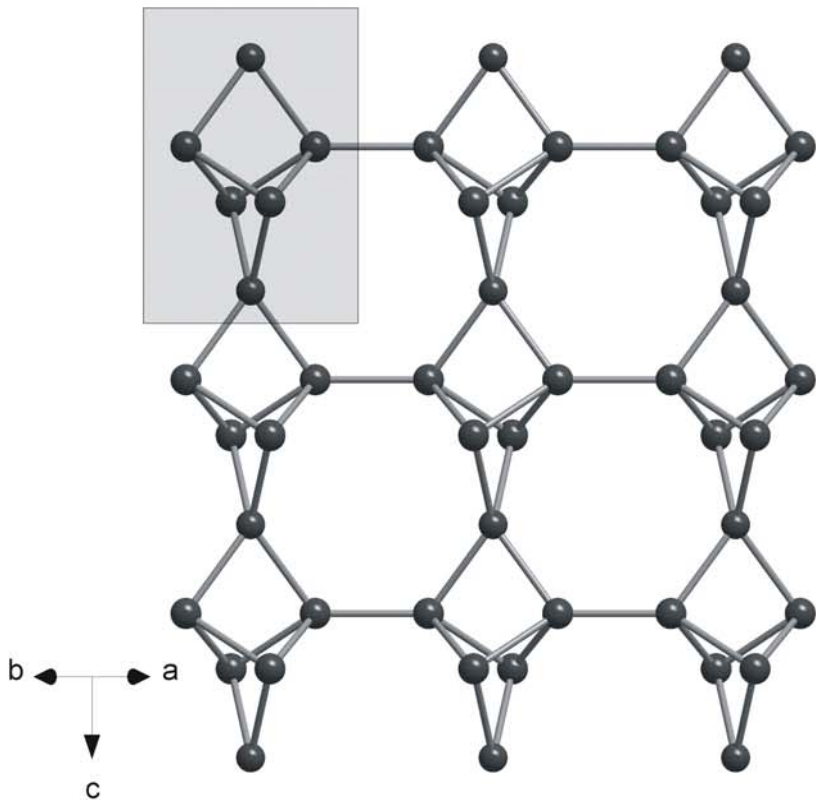
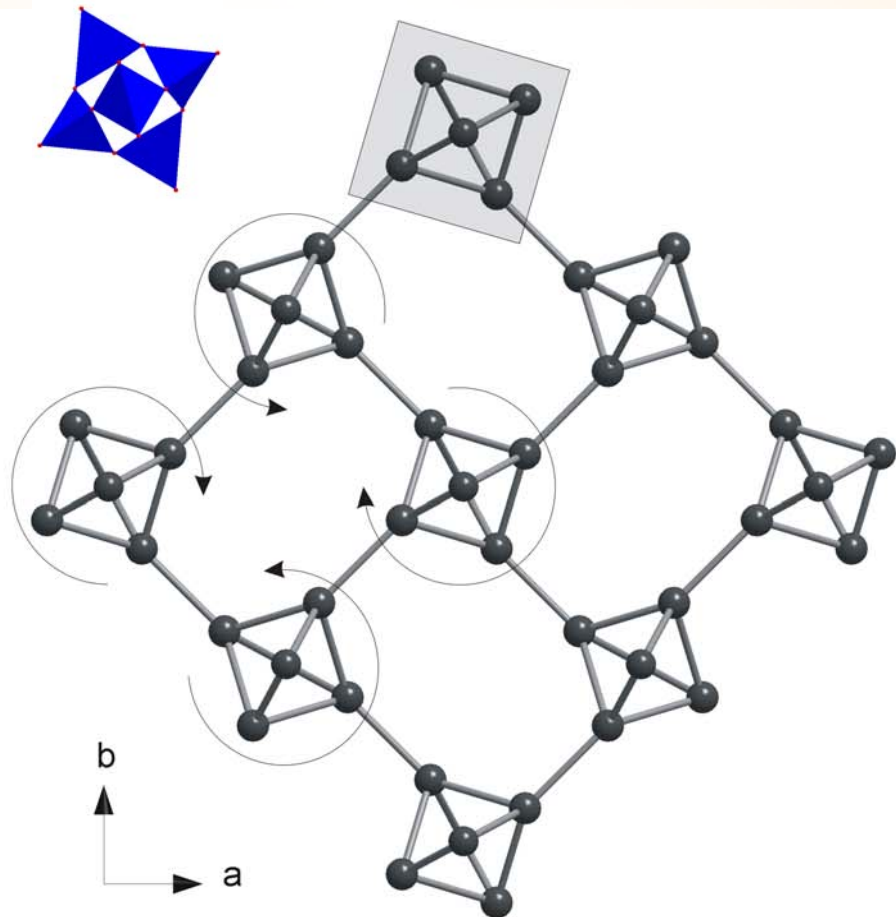
Thomsonite



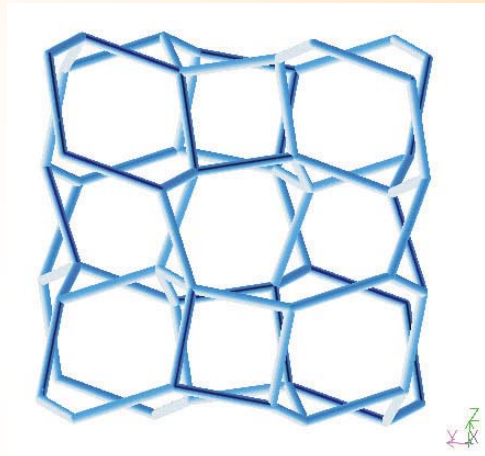
Scolecite



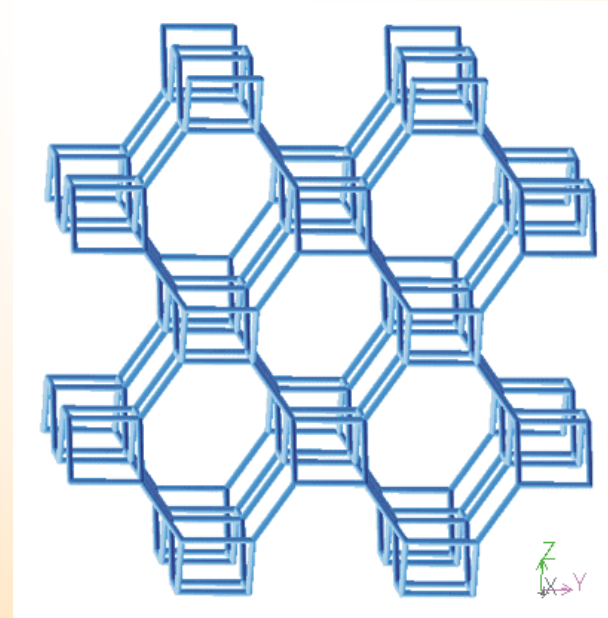
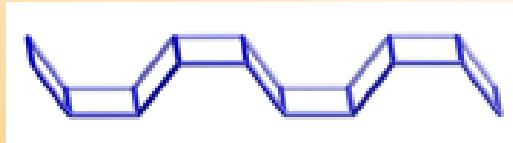
1) Fibrous zeolites – zeolites with T_5O_{10} units



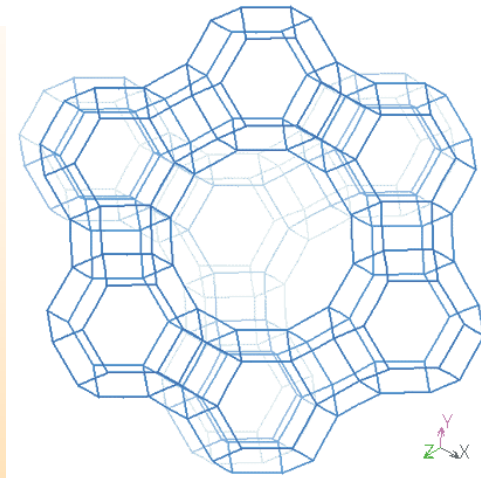
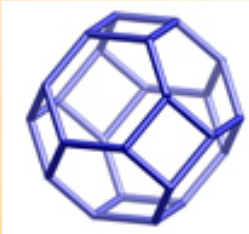
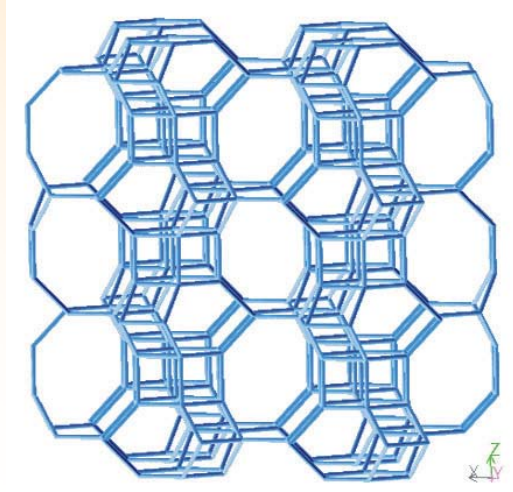
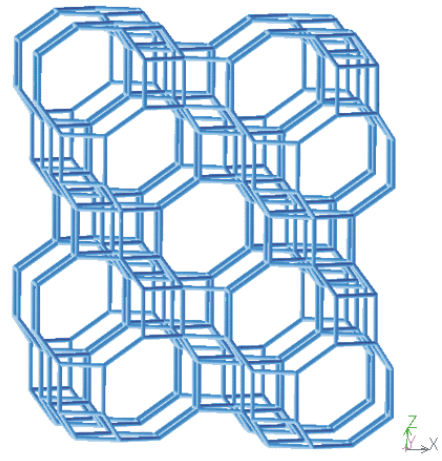
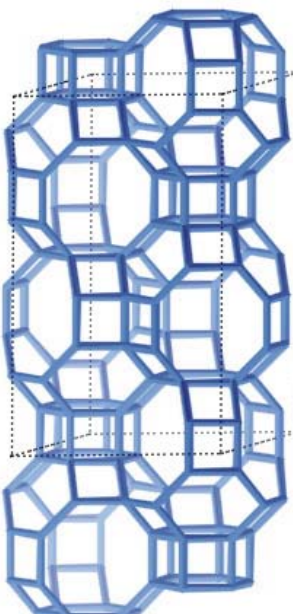
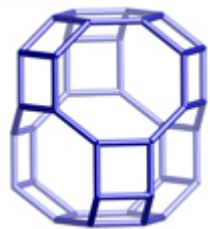
2) Zeolites with singly connected 4-ring chains: analcime, leucite, wairakite, pollucite...



3) Zeolites with edge-sharing 4-ring chains:gismondine, garronite, amicite, gobbinsite...

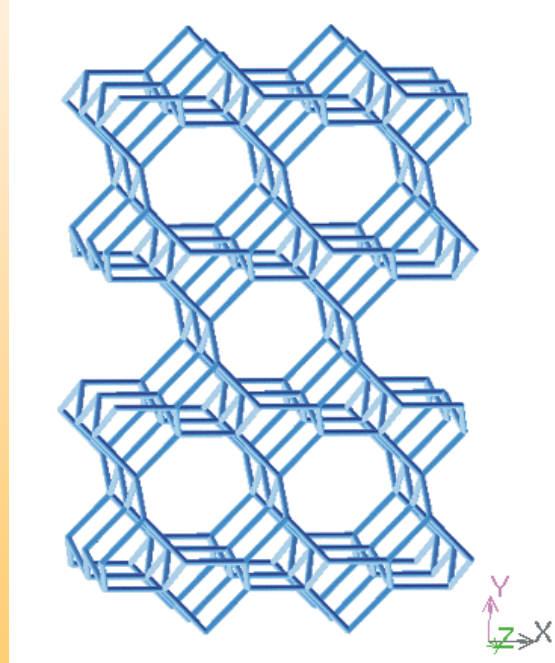
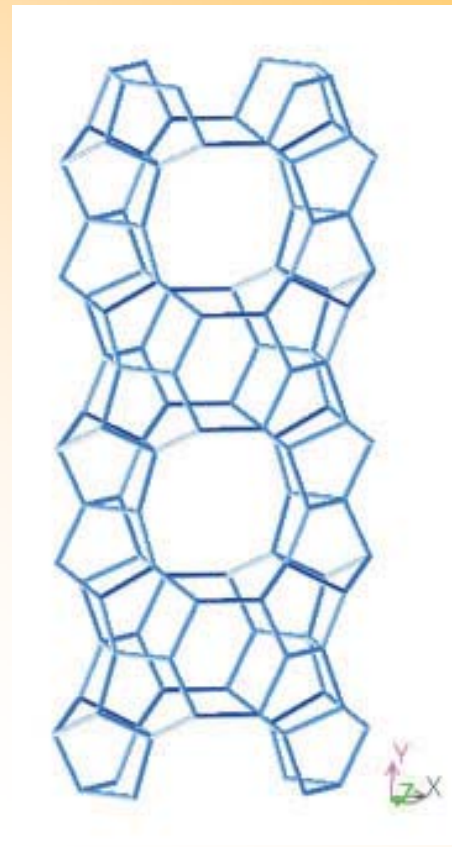
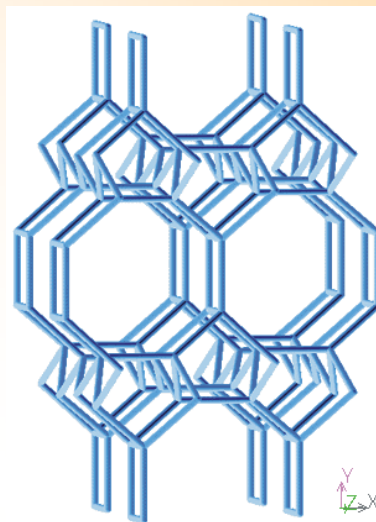
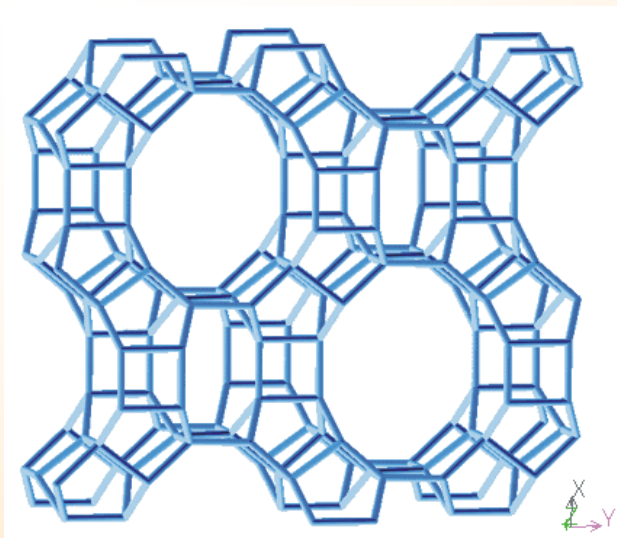


4) Zeolites with 6-rings: chabasite, levyne, erionite, faujasite...

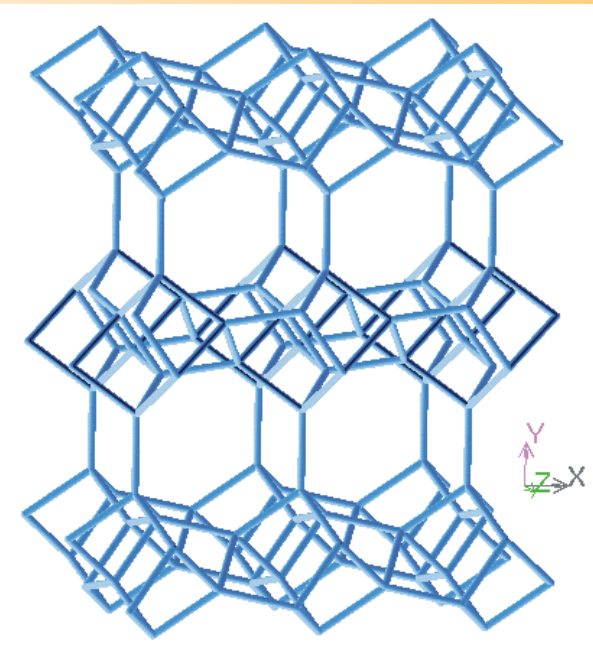
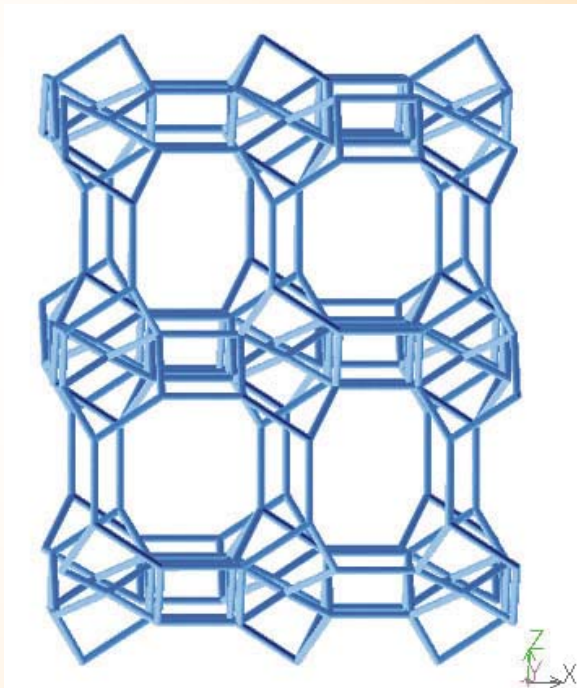
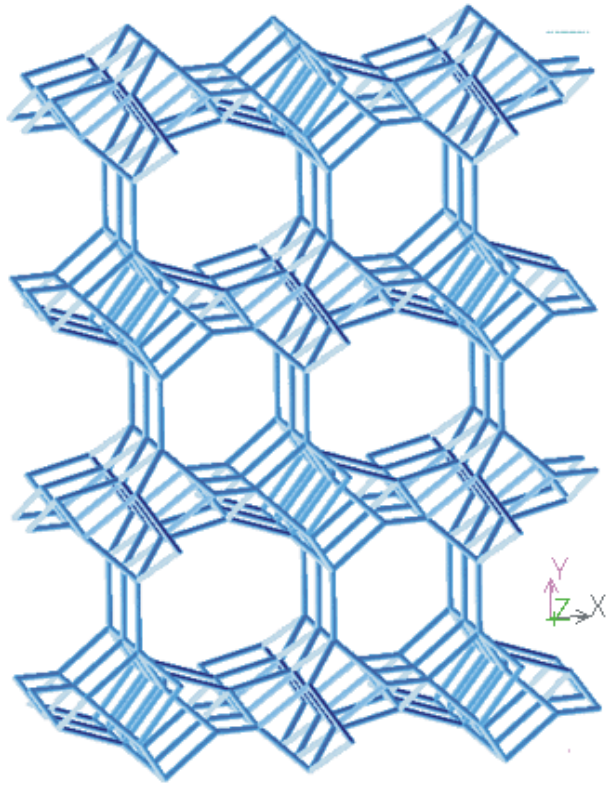


UNIVERSITÀ
DEGLI STUDI
DI MILANO

5) Zeolites of the mordenite group: mordenite, epistilbite, ferrierite, bikitaite...

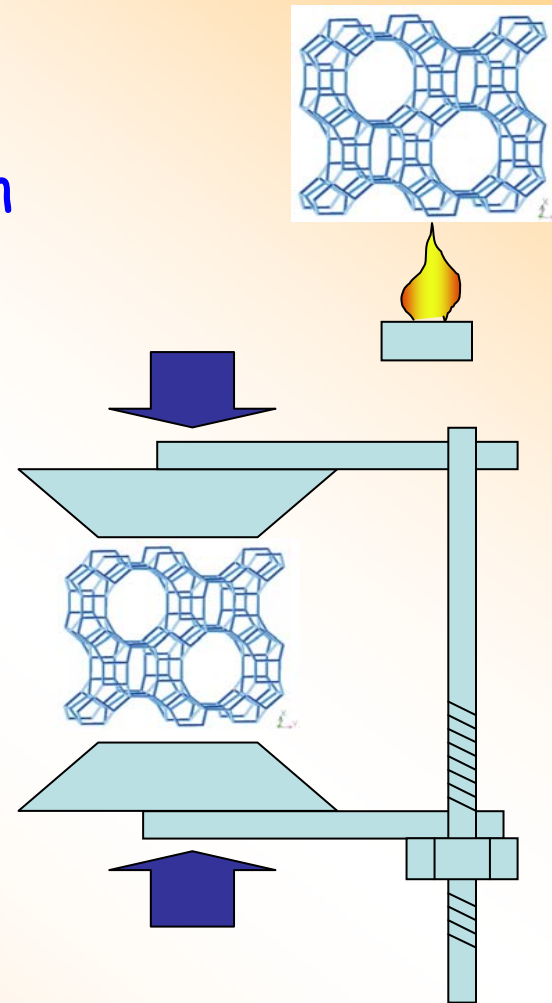


6) Zeolites of the heulandite group: heulandite-clinoptilolite, stilbite, brewsterite...



“Unique” physical/chemical properties of zeolites

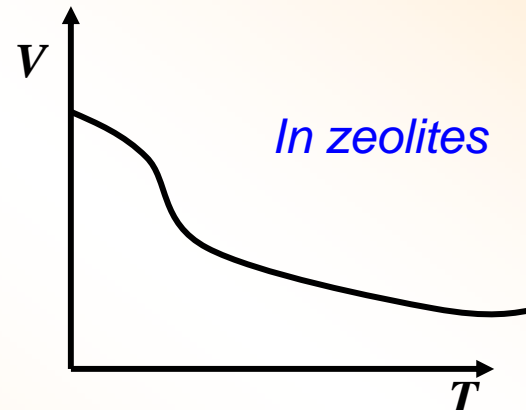
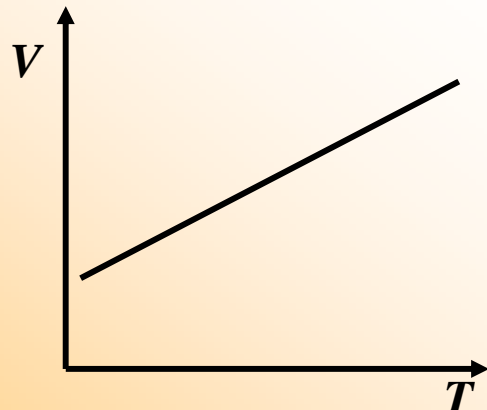
1) Negative thermal expansion



2) P -induced expansion

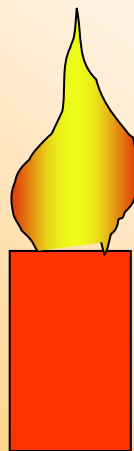
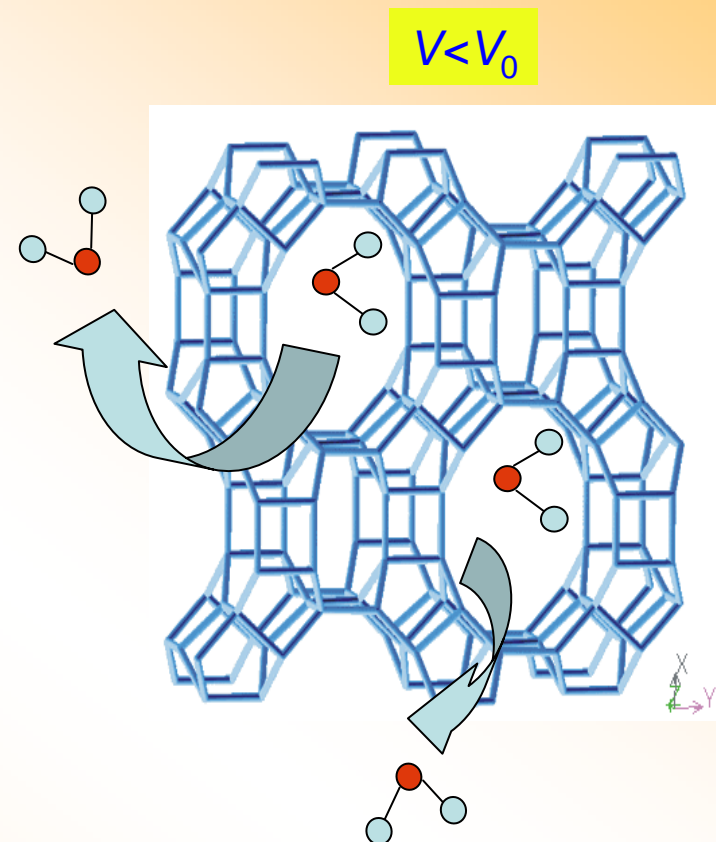
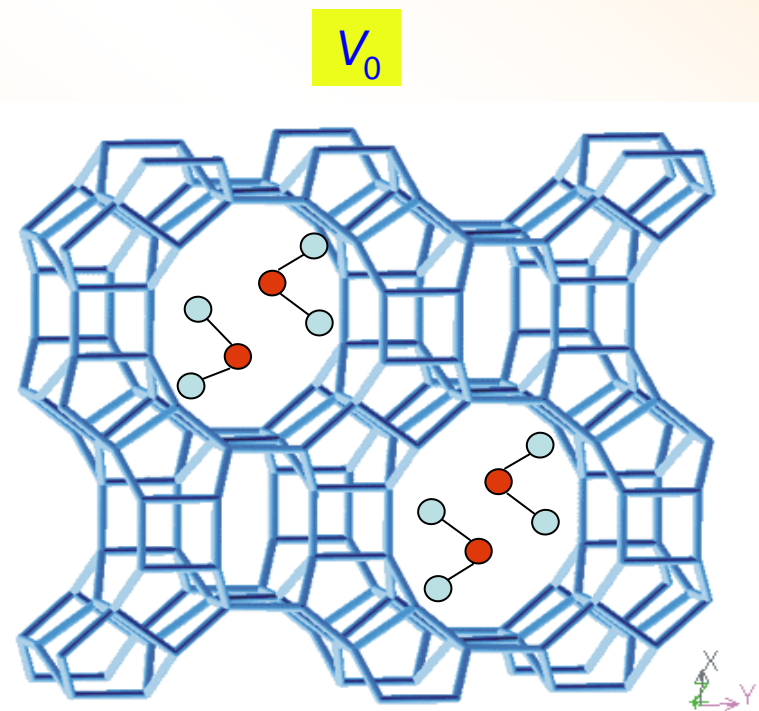
1) Negative thermal expansion

Negative Thermal Expansion is a physicochemical process in which some materials contract upon heating rather than expanding as most materials do. Materials which undergo this unusual process have a range of potential engineering, photonic, electronic, and structural applications. For example, if one were to mix a *negative thermal expansion* material with a "normal" material which expands on heating, it could be possible to make a **zero expansion composite material**.



Zeolites usually dehydrate upon heating. This imply a continuous change of the chemistry with increasing T . The negative thermal expansion is only apparent, and it is basically due to the loss of water molecules with a consequent contraction of the nanopores.

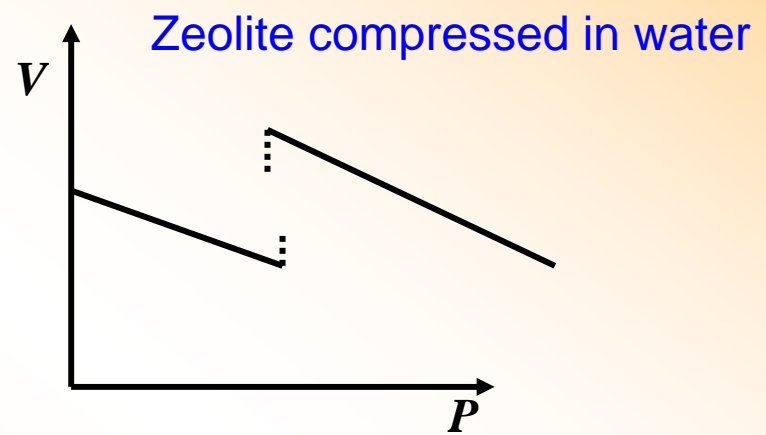
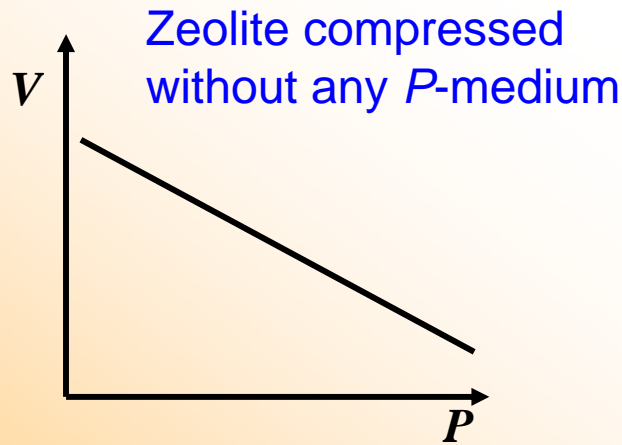
1) Negative thermal expansion



UNIVERSITÀ
DEGLI STUDI
DI MILANO

2) P -induced expansion !!!

When compressed without any P -fluid, all the zeolites show a “normal” elastic behaviour, with a P -induced contraction of the structures. However, when compressed in certain fluids (e.g. H_2O , H_2 , He , N_2 , ...), some zeolites show a P -induced expansion.



Some zeolites compressed in nominally “penetrating fluids” (e.g. H_2O , He , H_2 , N_2 , ...), undergo phase-transitions due to an over-hydration effect through selective sorption of molecules from the P -fluid. This imply a change of the chemistry with increasing P . The P -induced expansion is basically due to new molecules which penetrate in the nanopores with a consequent expansion of the structure.

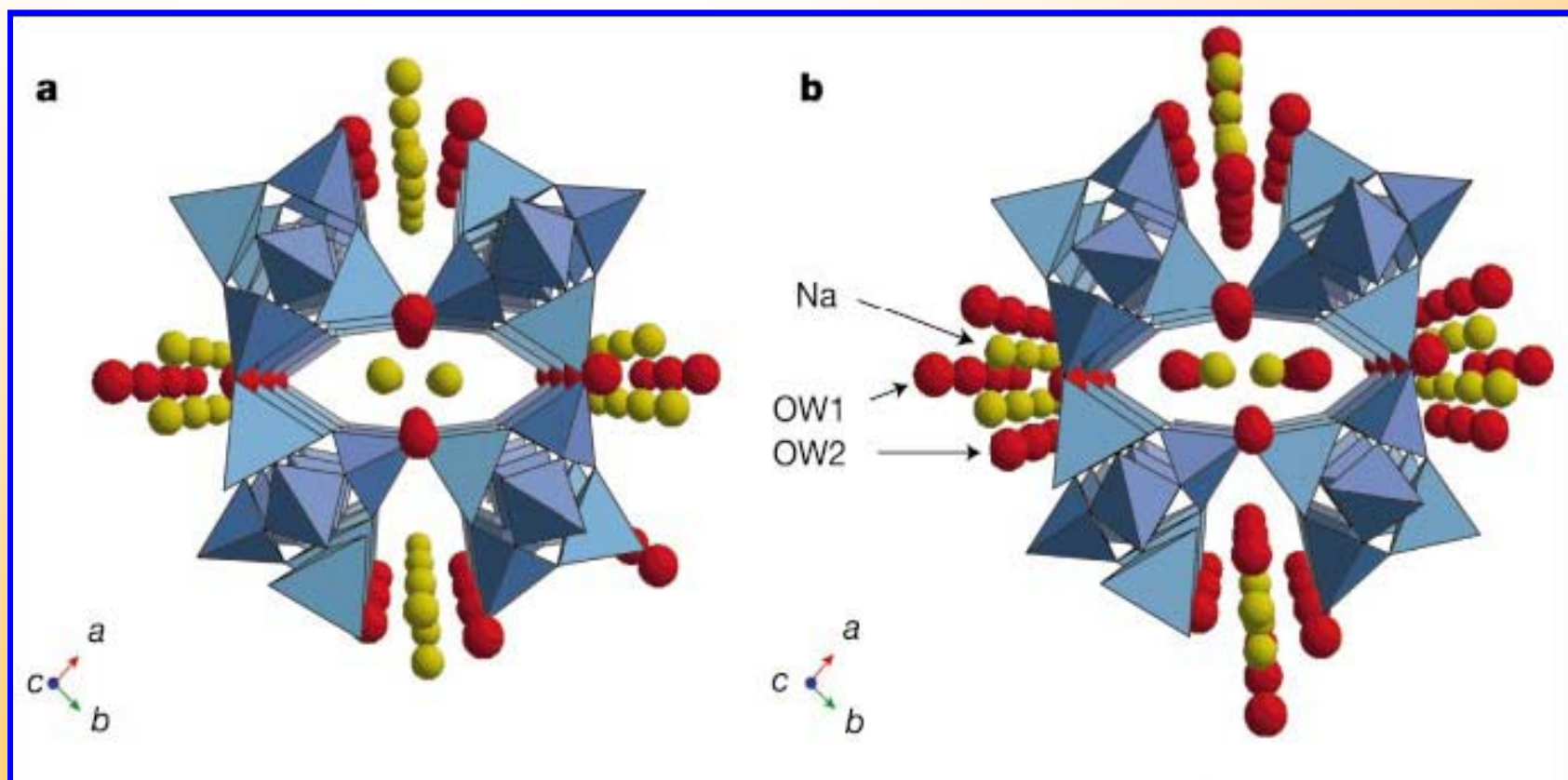
Natrolite compressed in a water-rich P -fluid



$P = 0.0001 \text{ GPa}$



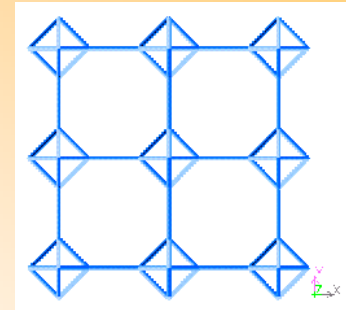
$P = 1.5 \text{ GPa}$



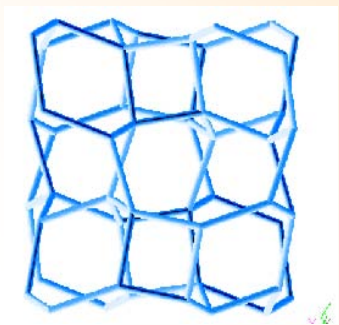
Zeolites at high-pressure

The case of :

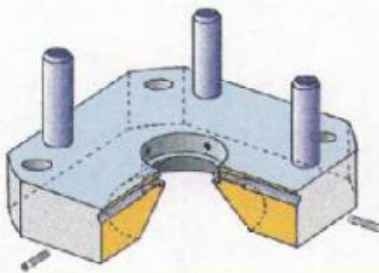
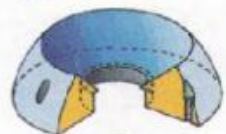
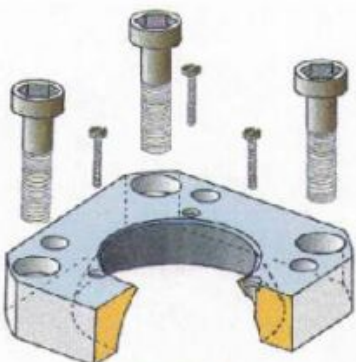
1) Edingtonite ➔ “normal” elastic behaviour



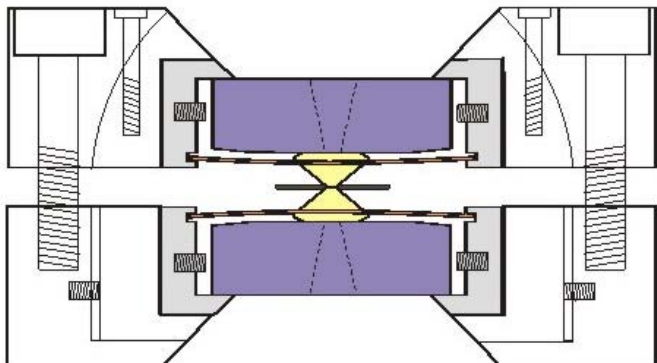
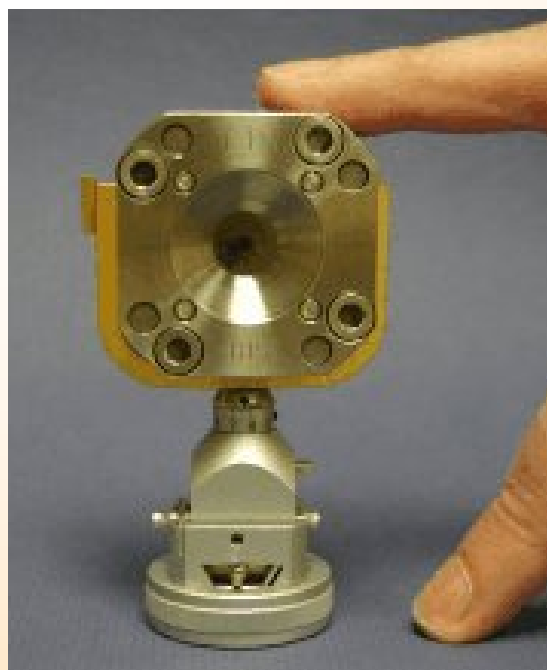
2) Analcime ➔ P -induced first-order
phase transition



UNIVERSITÀ
DEGLI STUDI
DI MILANO



DAC



Experimental

P-transmitting media



(nominally) penetrating:

16:3:1 Methanol:Ethanol:Water

P-calibration

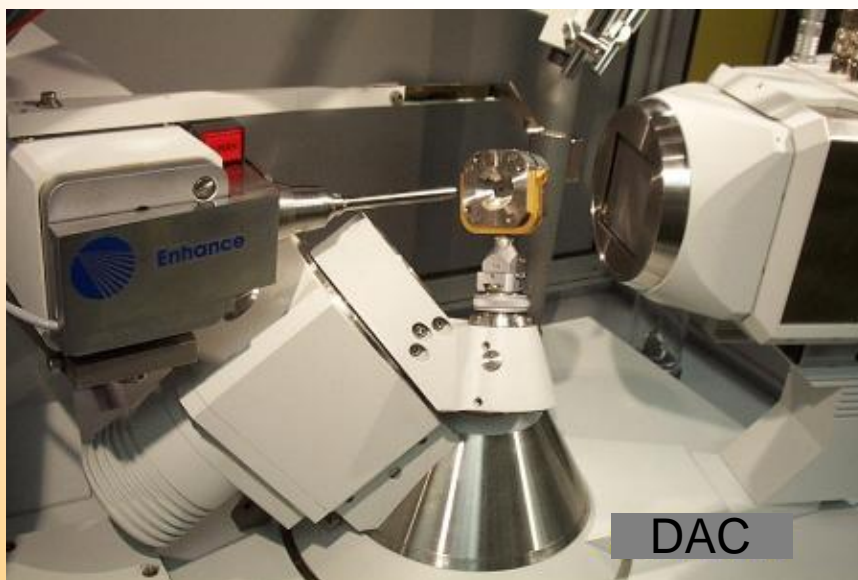


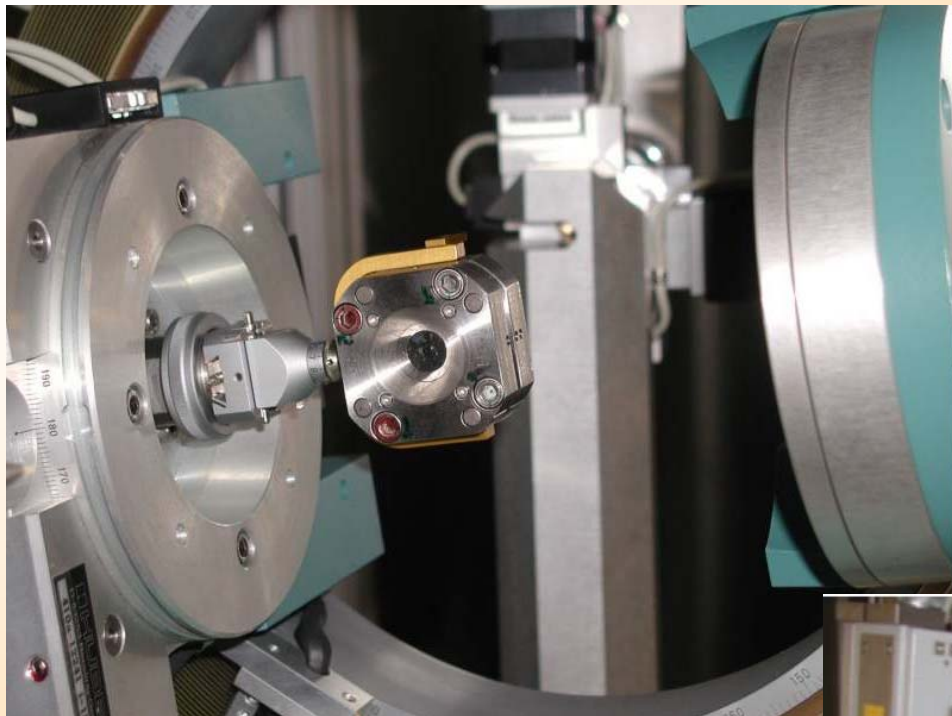
- by the ruby fluorescence method (± 0.05 GPa)
- by the EoS of quartz (± 0.01 GPa)



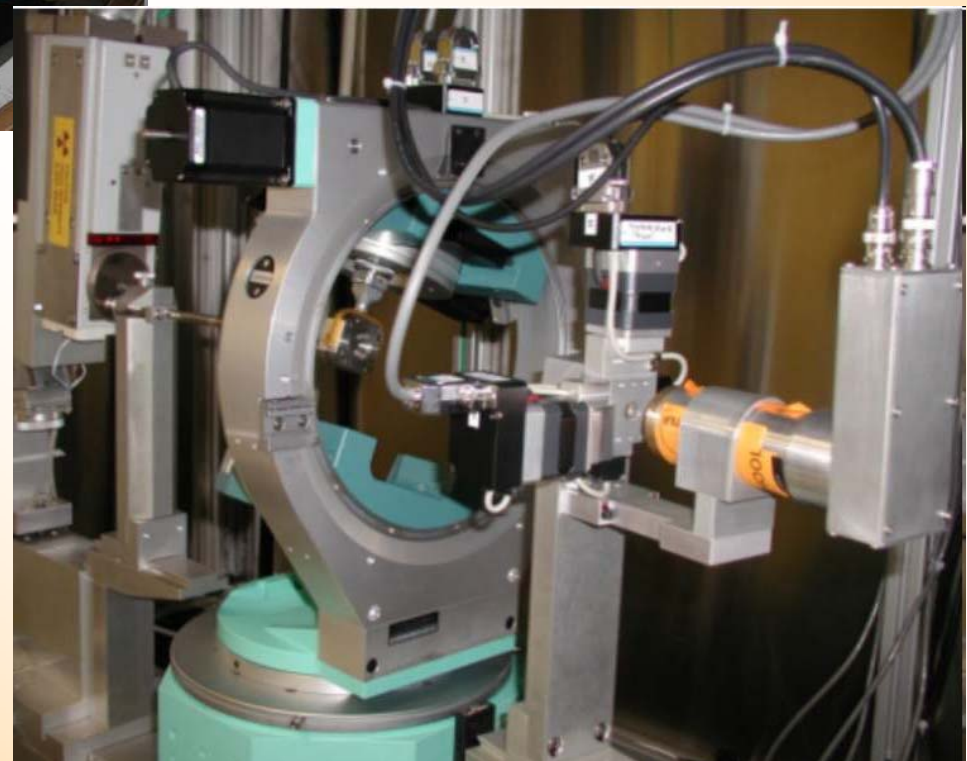
UNIVERSITÀ
DEGLI STUDI
DI MILANO

HP-diffraction experiments...





Huber four-circle diffractometer
driven by SINGLE04 [R.J. Angel]



Edingtonite (EDI)

Ideal formula: $\text{Ba}_2\text{Al}_4\text{Si}_6\text{O}_{20}\cdot 8\text{H}_2\text{O}$

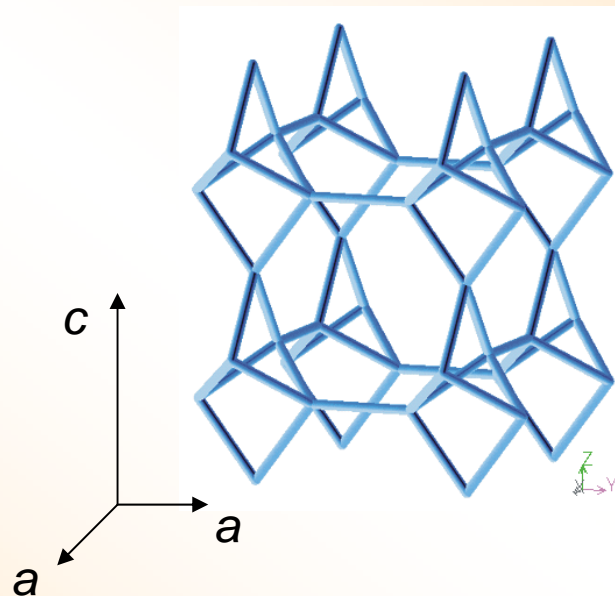
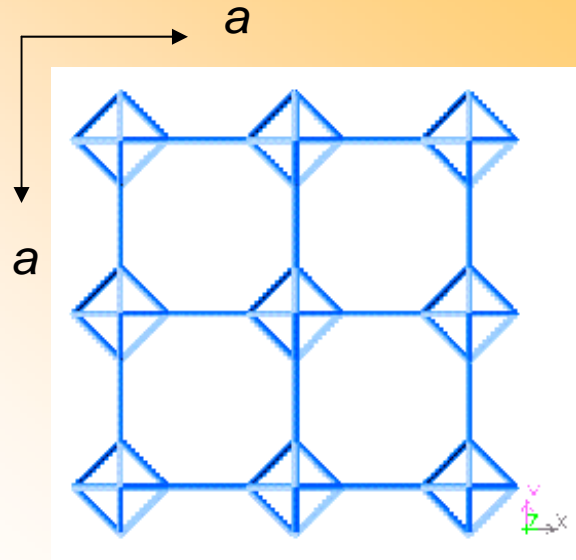
SBU: 4=1

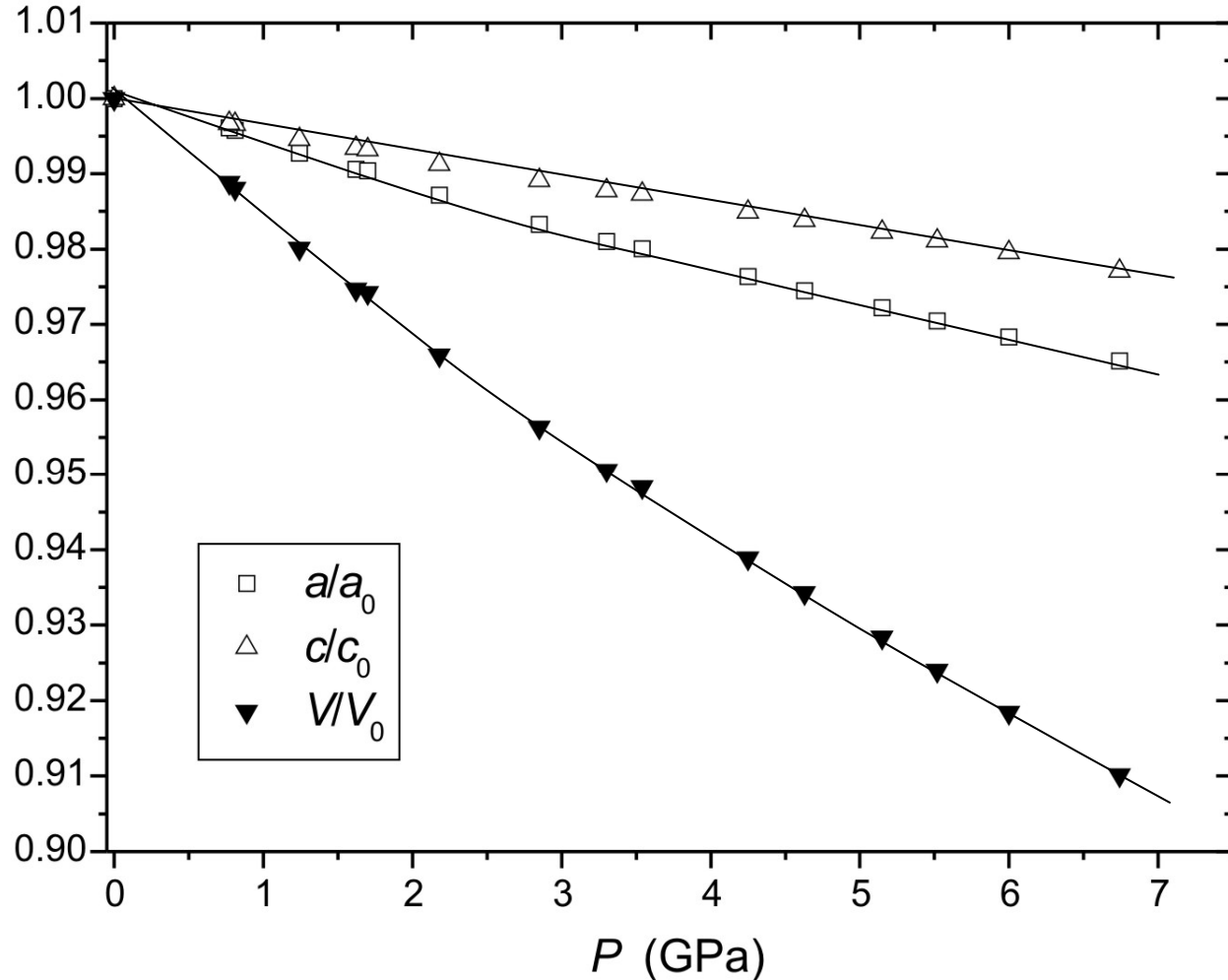
Topological symmetry $P-42_1m$

General symmetry: $P-42_1m$

$a \sim 9.6$, $c \sim 6.5$ Å

FD: 16.6 T/1000Å³





Edingtonite:

II-BM-EoS

$K_0 = 59.3(4)$ GPa

$K' = 4$ (fixed)

III-BM-EoS

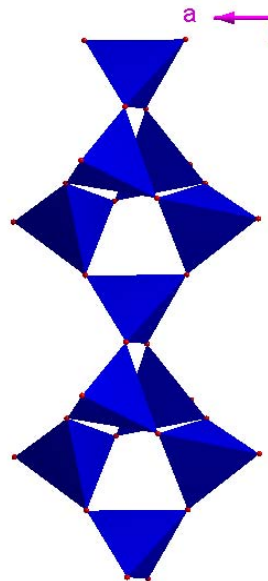
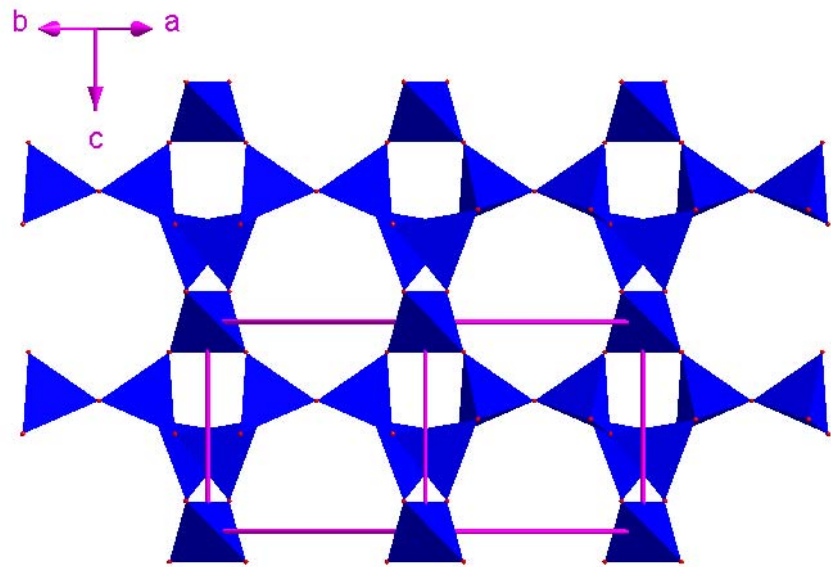
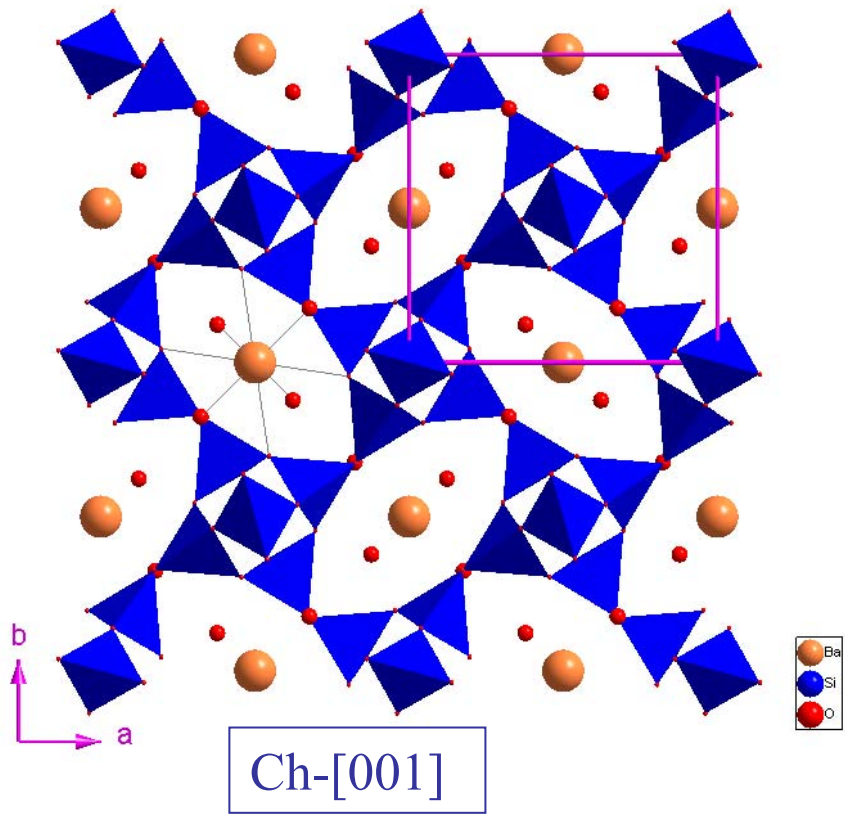
$K_0 = 59(1)$ GPa

$K' = 4.2(5)$

$K(a) = 52(1)$ GPa and $K'(a) = 3.6(4)$
 $K(c) = 82(4)$ GPa and $K'(c) = 6(1)$

Elastic anisotropy

$K(a) : K(c) = 1 : 1.60$

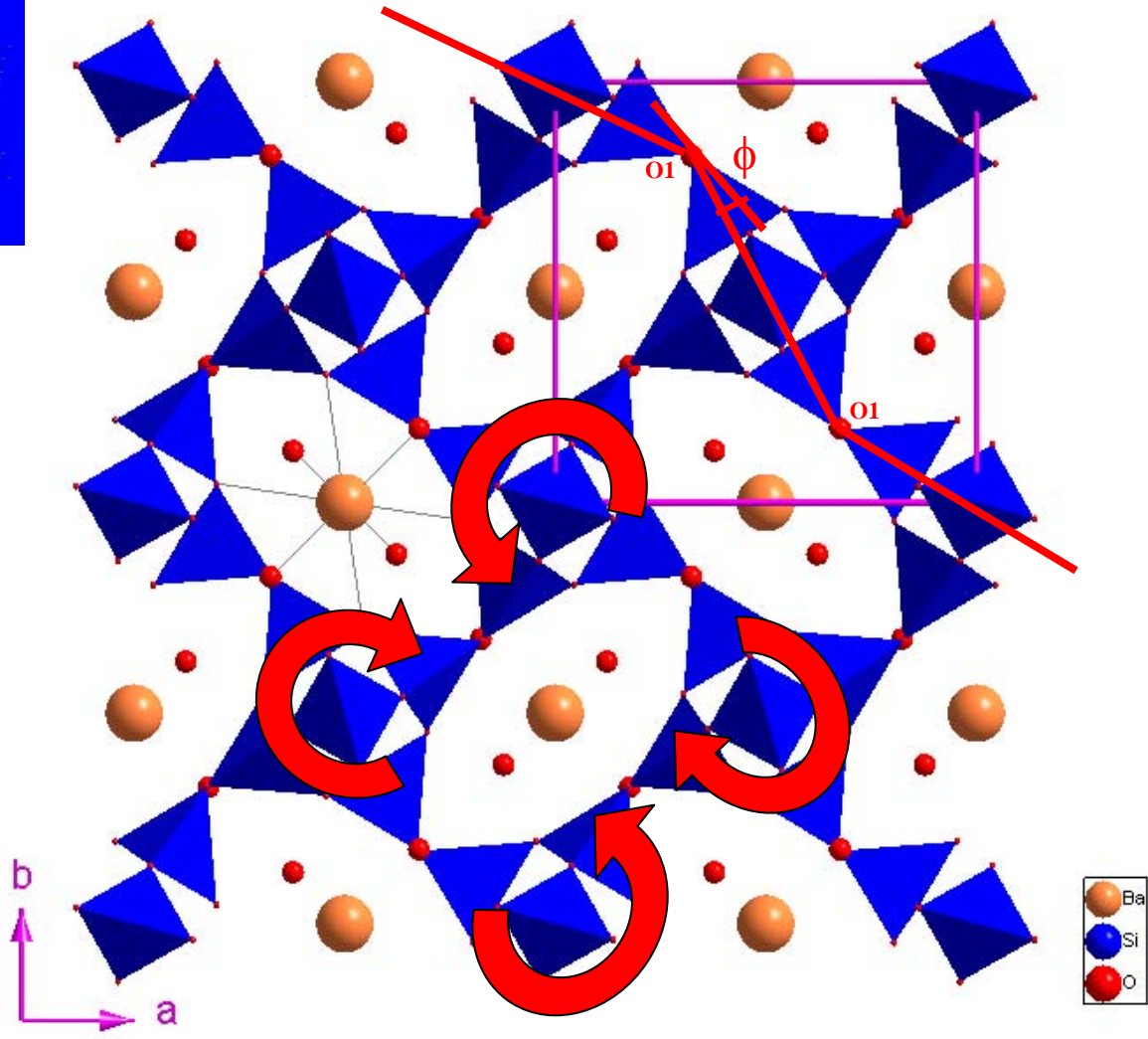
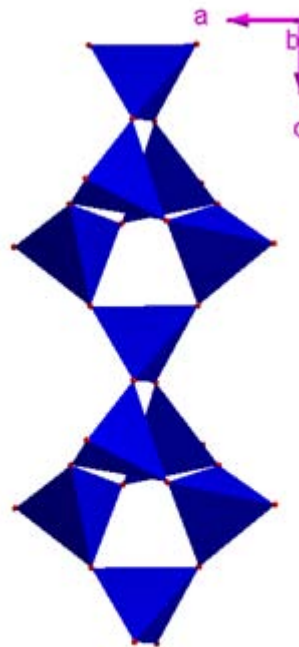


EDI -
Secondary
Building Unit

Crystal structure of edingtonite

EDINGTONITE

Structural behaviour



$$\phi^\circ = [180^\circ - (O1-O1-O1)^\circ]/2 \rightarrow 17.15(4)^\circ \text{ at } P=0.0001 \text{ GPa}$$
$$20.03(3)^\circ \text{ at } P=4.61 \text{ GPa}$$

ORIGINAL PAPER

G. D. Gatta · T. Boffa Ballaran · P. Comodi
P. F. Zanazzi

Comparative compressibility and equation of state of orthorhombic and tetragonal edingtonite

American Mineralogist, Volume 89, pages 633–639, 2004

Isothermal equation of state and compressional behavior of tetragonal edingtonite

**GIACOMO DIEGO GATTA,^{1,*} TIZIANA BOFFA BALLARAN,¹ PAOLA COMODI,² AND
PIER FRANCESCO ZANAZZI²**

¹Bayerisches Geoinstitut, Universitaet Bayreuth, Universitaet Strasse 30, D-95447 Bayreuth, Germany

²Dipartimento di Scienze della Terra, Università di Perugia, Piazza Università, I-06100 Perugia, Italy

Analcime (ANA)

Ideal formula: $\text{NaAlSi}_2\text{O}_6 \cdot \text{H}_2\text{O}$

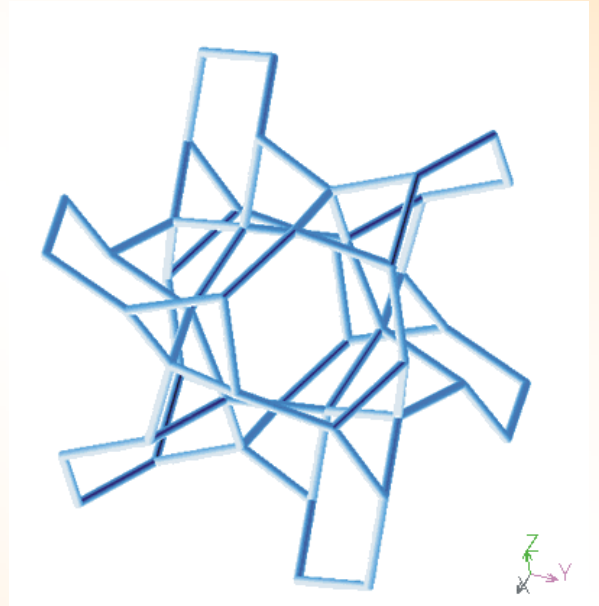
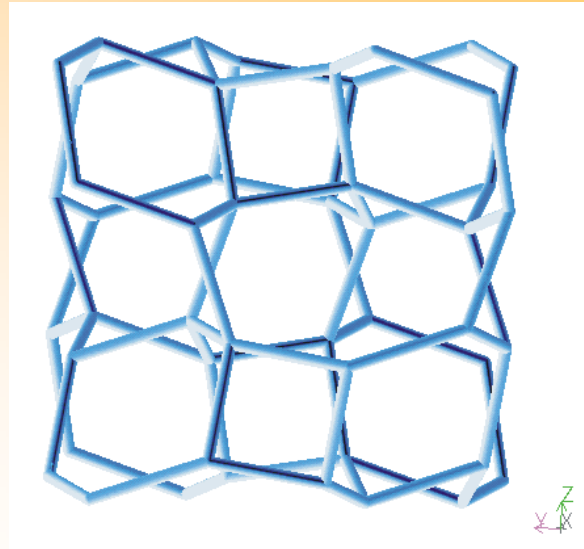
SBU: 4 and 6 (or their combination: 6-2)

Topological symmetry: $Ia-3d$

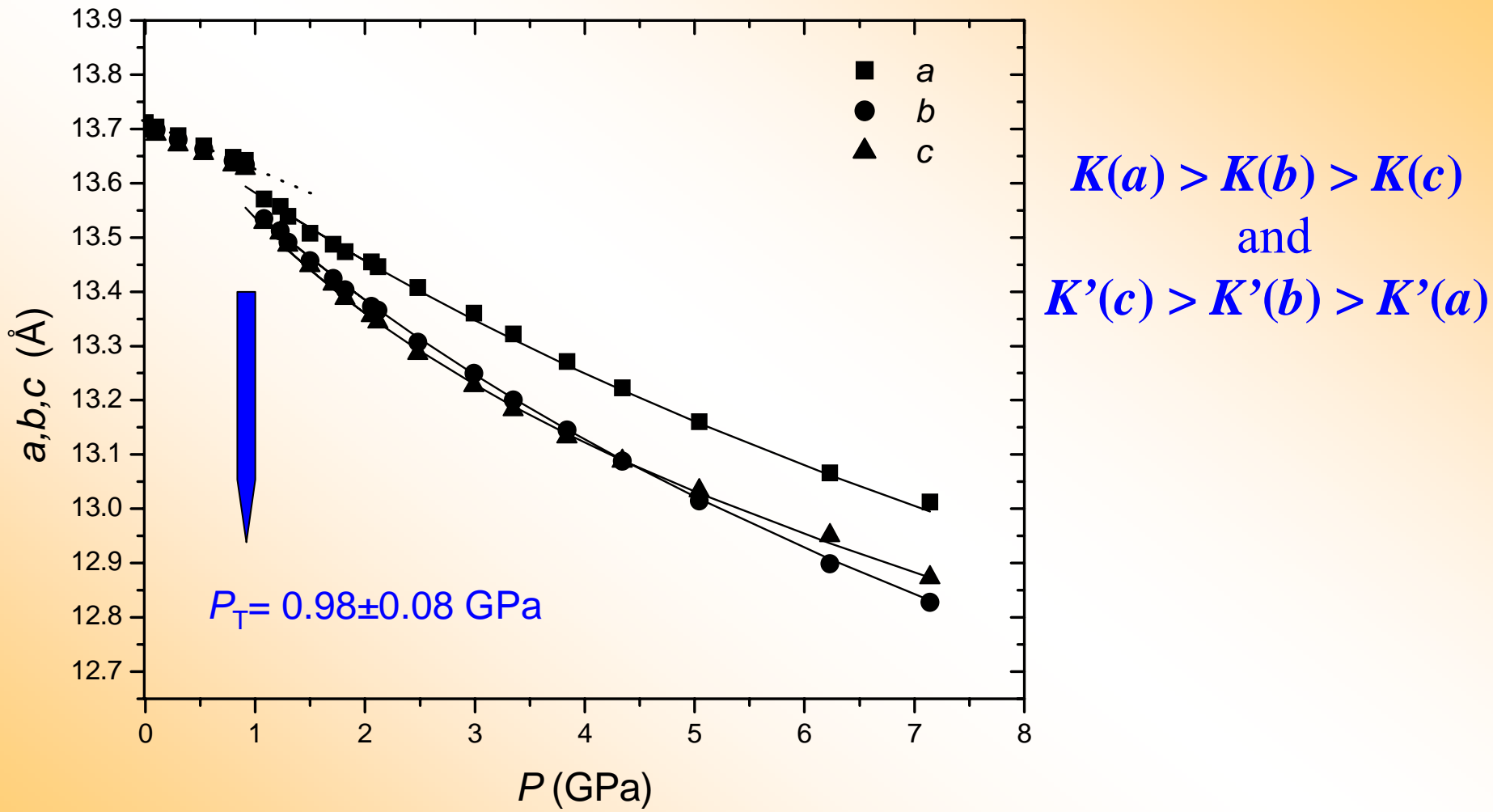
General symmetry: $Ia-3d$

$a \sim 13.7 \text{ \AA}$

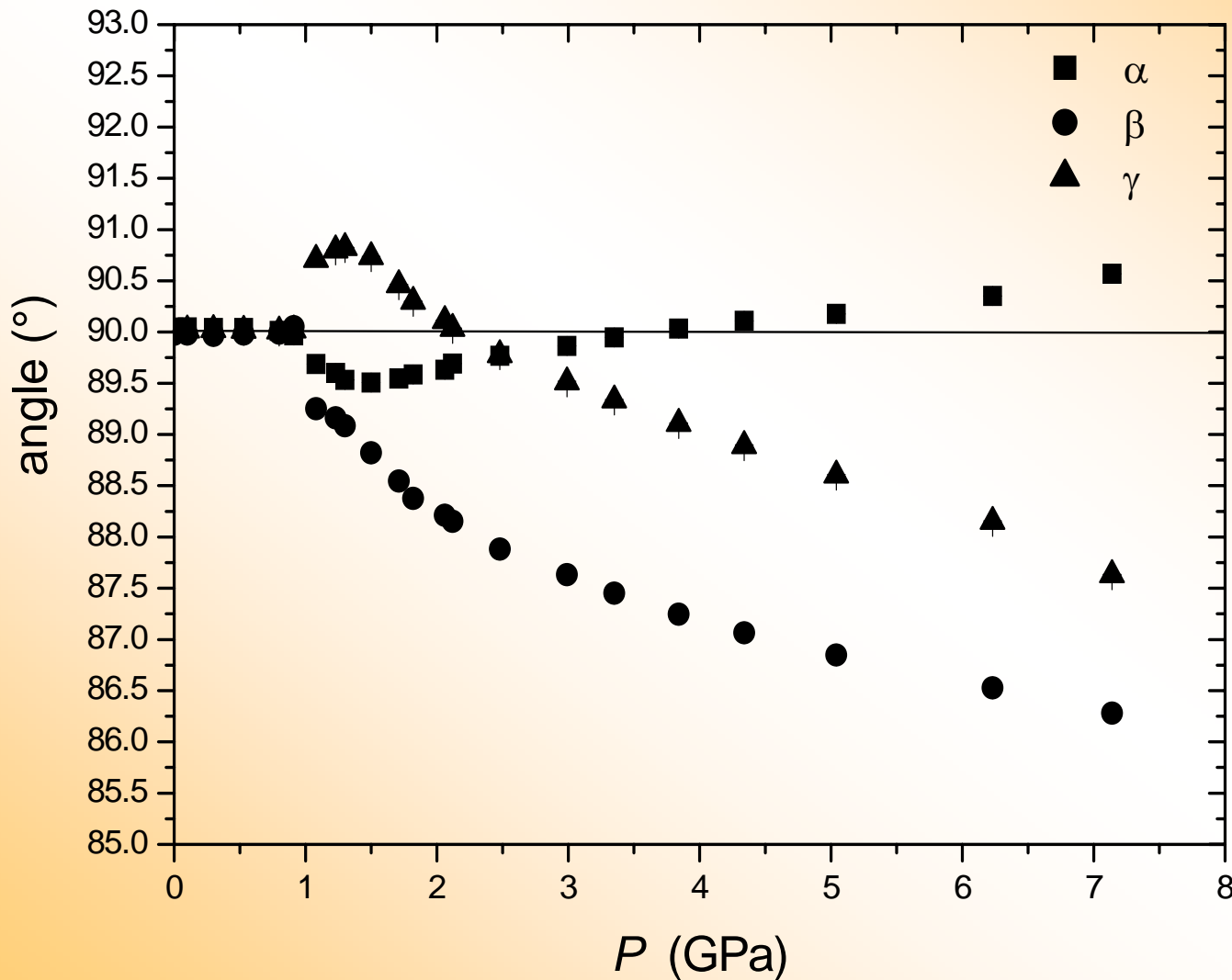
FD: $18.5 \text{ T}/1000\text{\AA}^3$



Analcime at high-pressure...

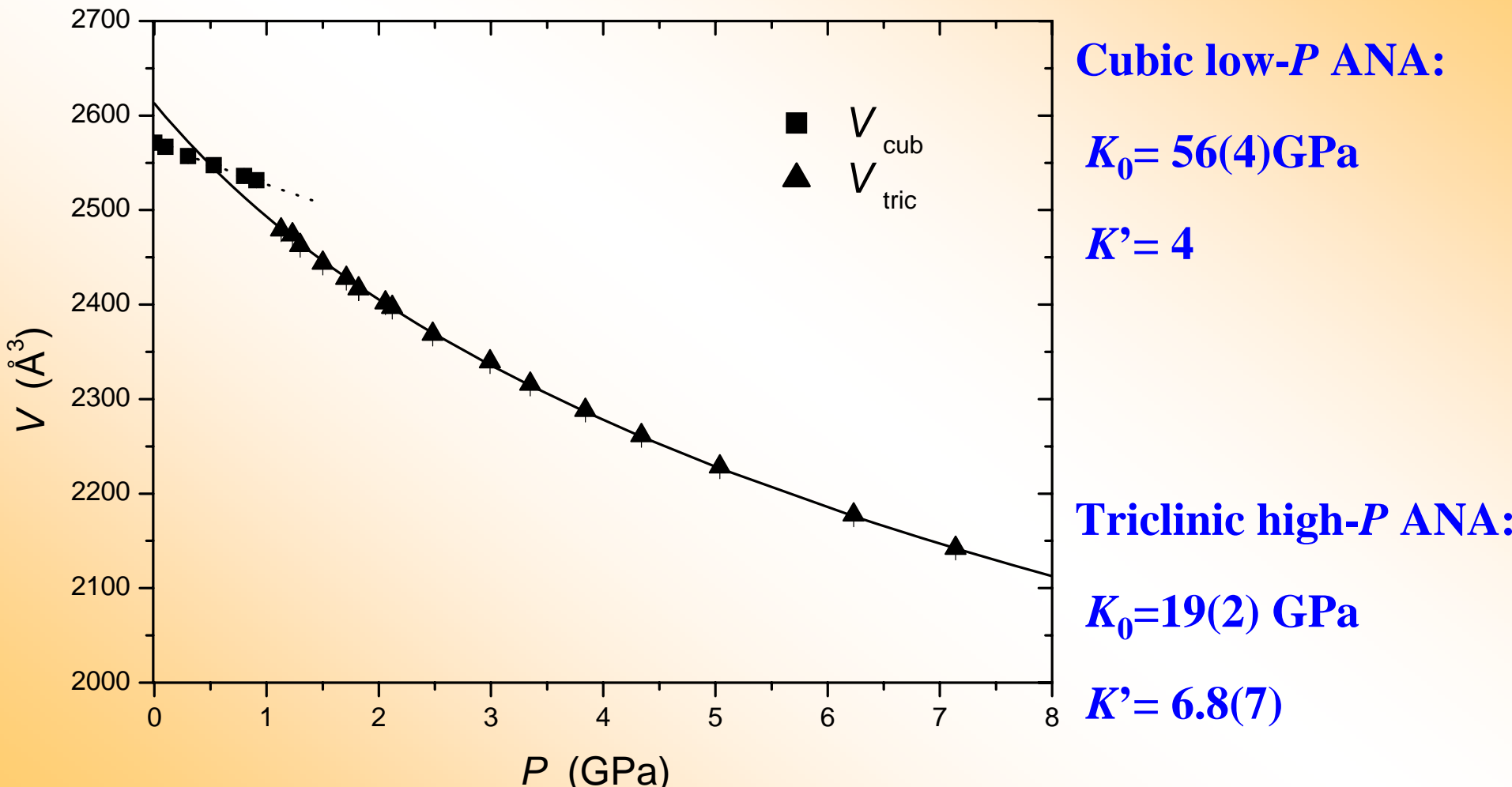


Analcime at high-pressure...



UNIVERSITÀ
DEGLI STUDI
DI MILANO

Analcime at high-pressure...



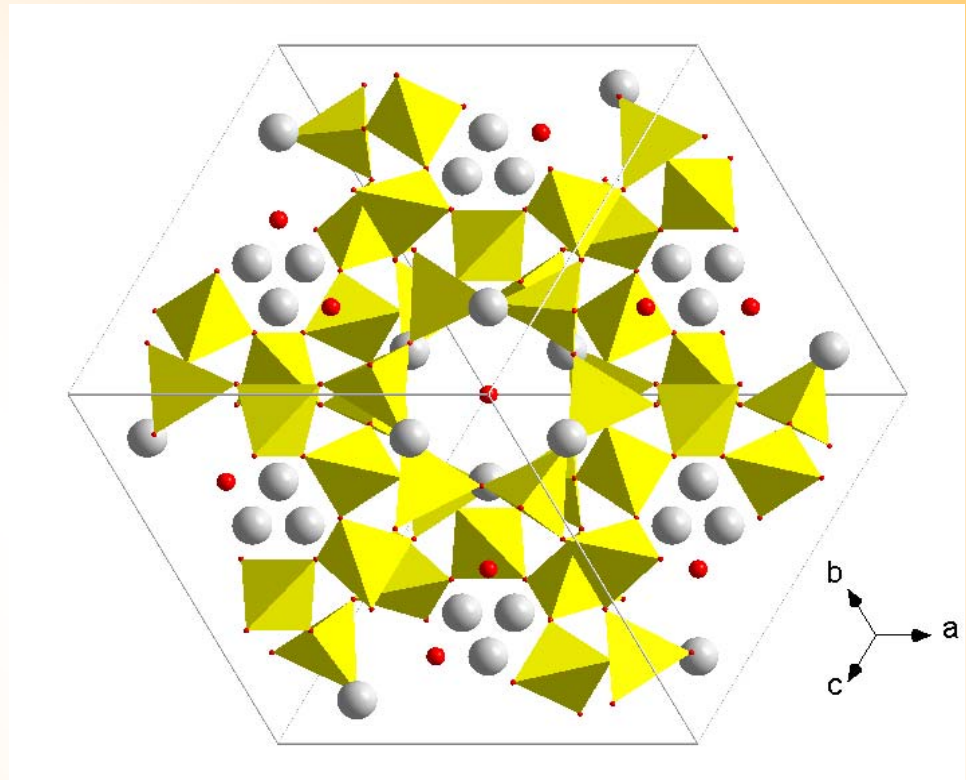
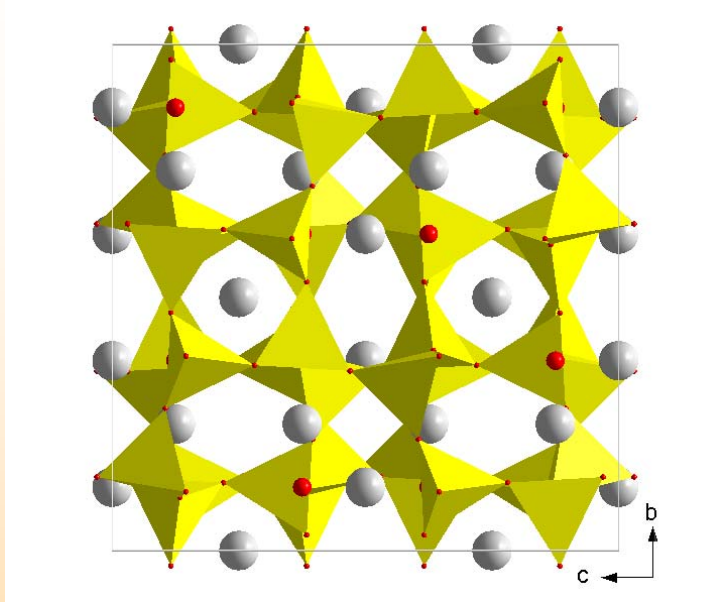
Ia-3d

P-1



UNIVERSITÀ
DEGLI STUDI
DI MILANO

The crystal structure of analcime, $\text{NaAlSi}_2\text{O}_6 \cdot \text{H}_2\text{O}$

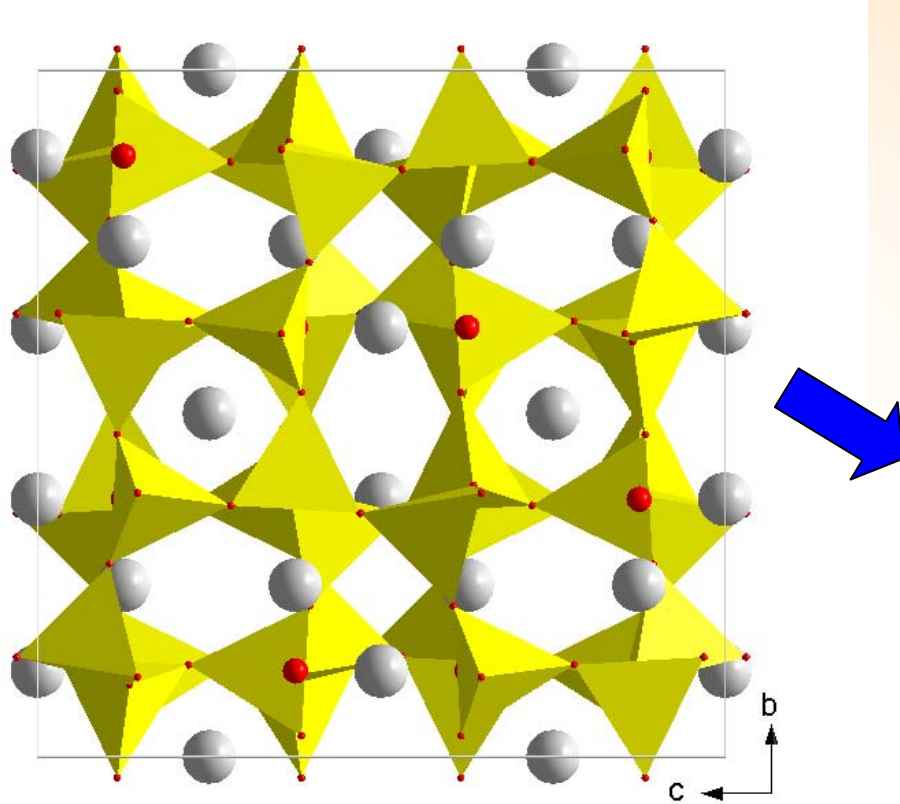


The analcime specimen investigated in this study comes from Su Marralzu, Sardinia, Italy

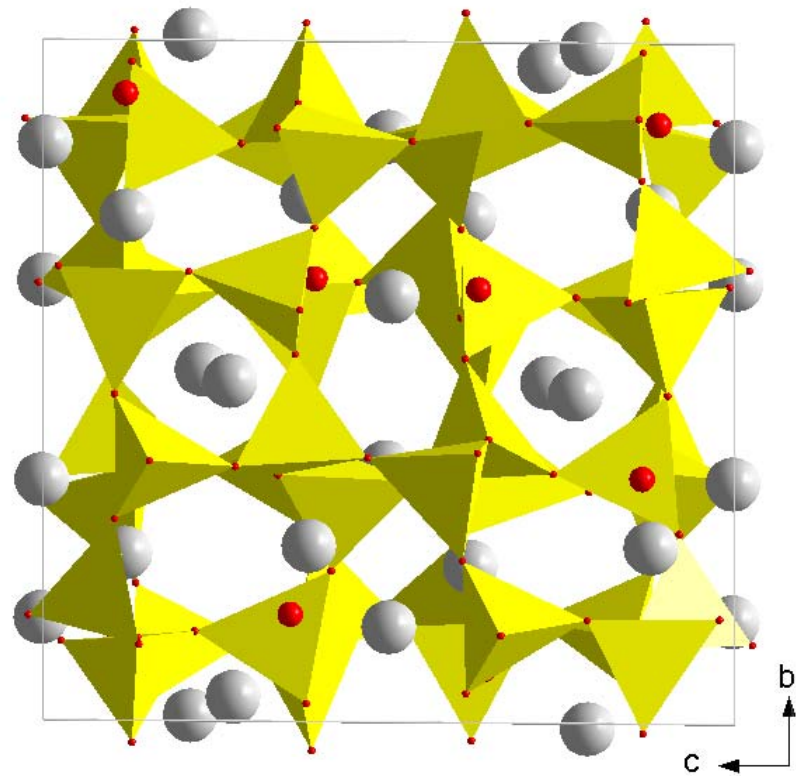


Space group: *Ia-3d*, $a = 13.7065(8)$ Å

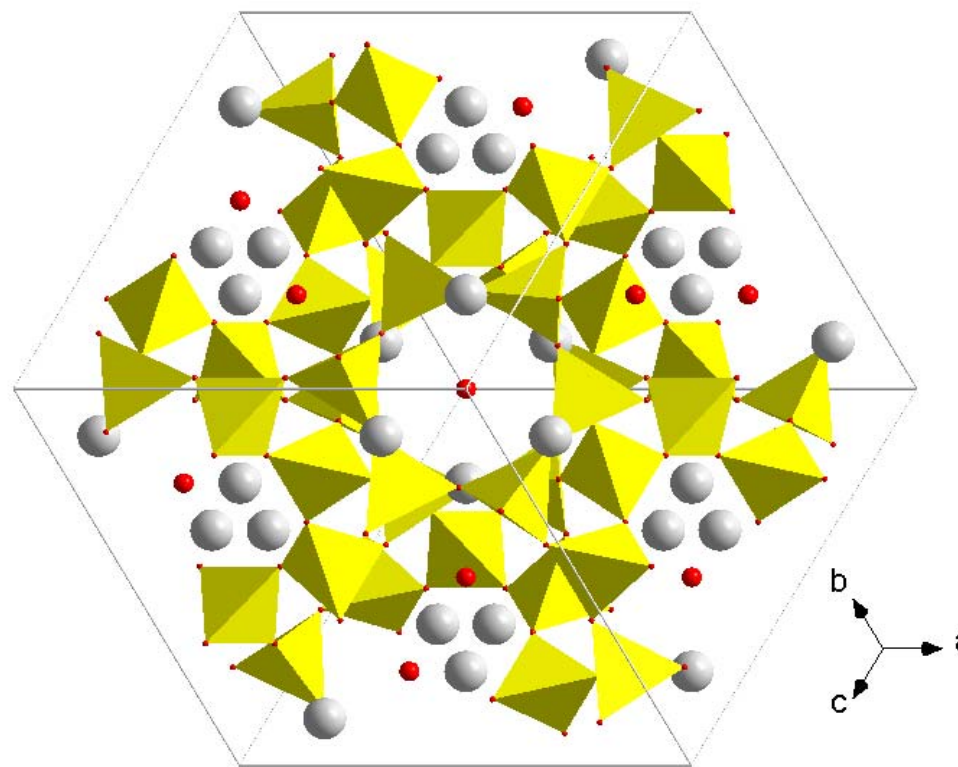
Cubic...



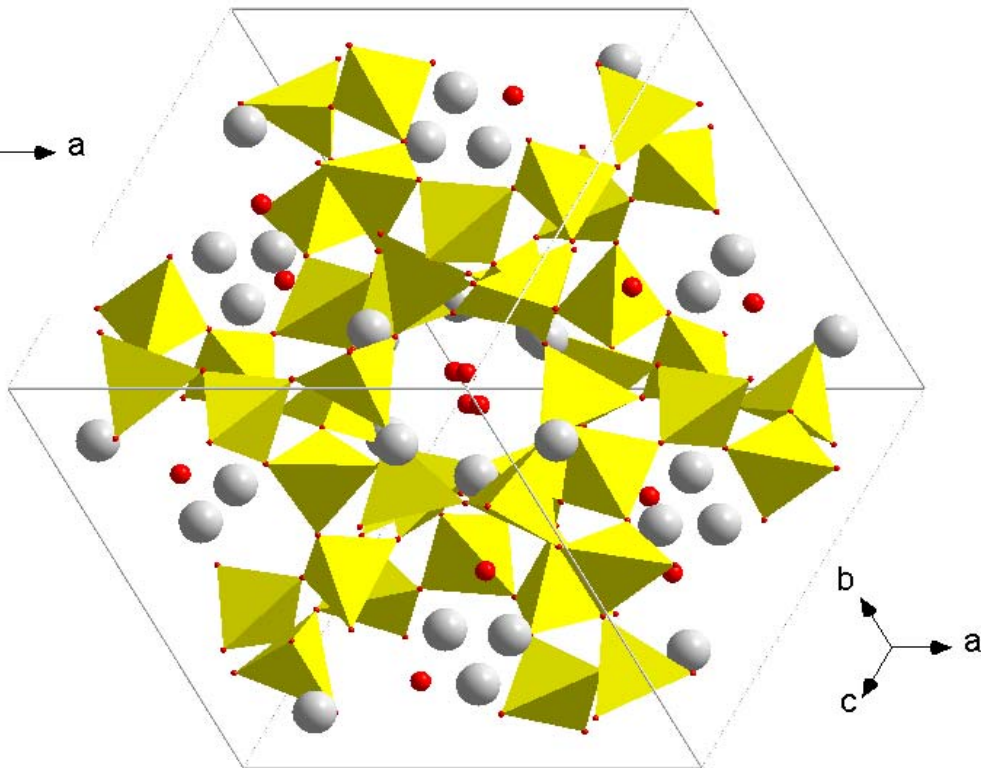
Triclinic...



Cubic...

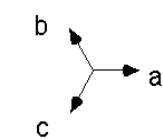
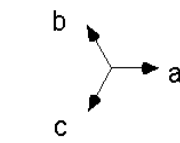
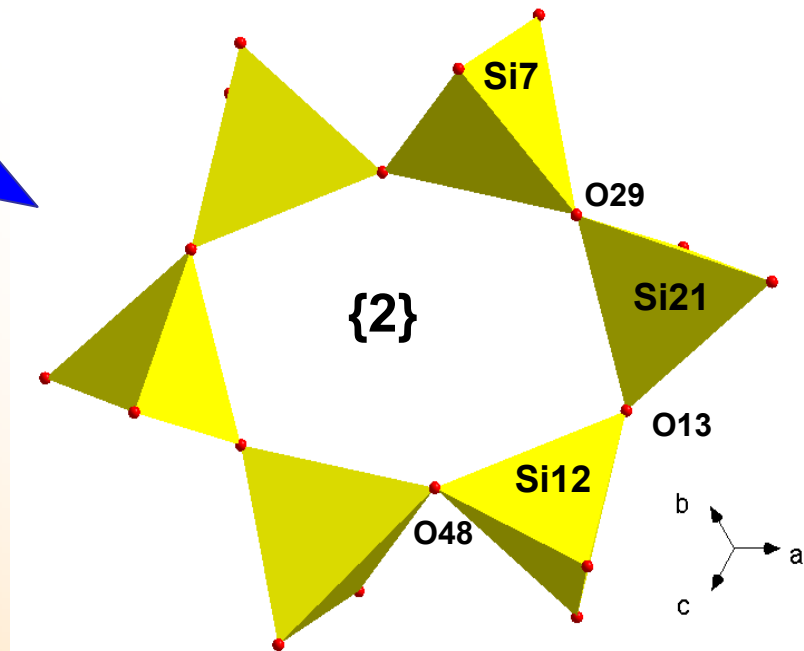
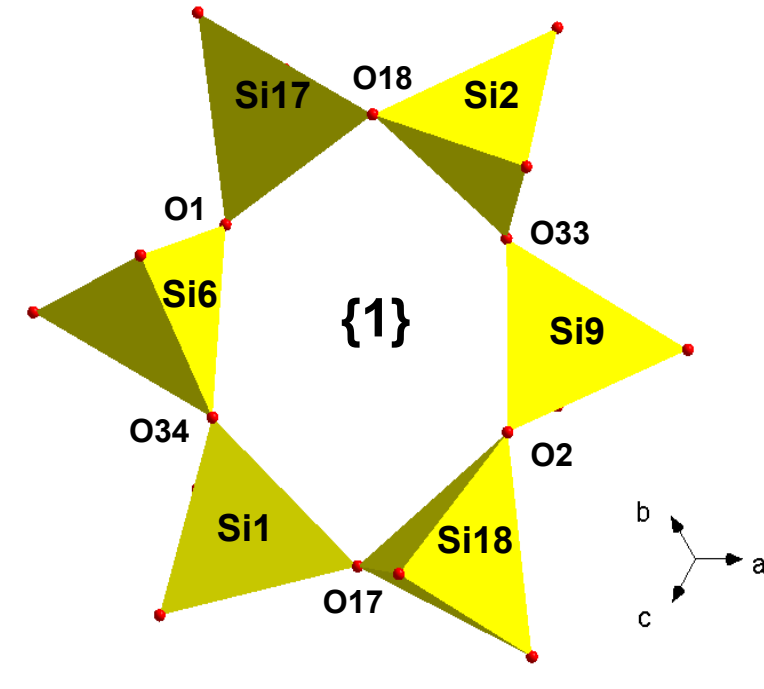
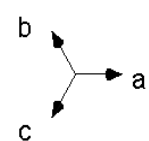
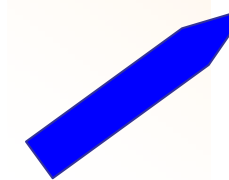
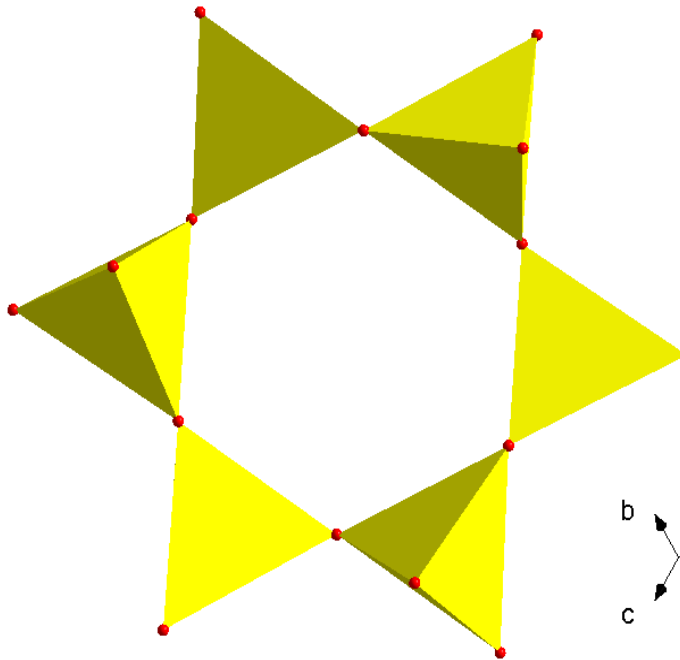


Triclinic...



Cubic to Triclinic phase-transition...

6mR



| <i>P</i> (GPa) | 0.0001 | 0.0001* | 0.91(5) | 1.23(5) | 2.12(5) | 5.04(5) |
|---------------------|-----------|----------|----------|-----------|-----------|-----------|
| 6-ring {1} | | | | | | |
| ϵ (6mR-1) | 1 | 1 | 1 | 0.81 | 0.77 | 0.68 |
| Si-O-Si | 144.79(9) | 143.7(6) | 143.4(7) | | | |
| Si6-O1-Si17 | | | | 138.6(31) | 125.9(35) | 127.0(37) |
| Si17-O18-Si2 | | | | 131.7(36) | 133.4(38) | 140.3(41) |
| Si2-O33-Si5 | | | | 132.6(33) | 132.2(29) | 151.6(45) |
| Si5-O2-Si18 | | | | 128.2(26) | 137.5(35) | 120.0(27) |
| Si18-O17-Si1 | | | | 138.7(42) | 139.1(33) | 121.3(31) |
| Si1-O34-Si6 | | | | 138.5(37) | 139.9(40) | 121.7(33) |
| 6-ring {2} | | | | | | |
| ϵ (6mR-2) | 1 | 1 | 1 | 0.77 | 0.62 | 0.58 |
| Si-O-Si | 144.79(9) | 143.7(6) | 143.4(7) | | | |
| Si21-O13-Si12 (x 2) | | | | 154.8(41) | 135.3(28) | 126.6(31) |
| Si12-O48-Si7 (x 2) | | | | 134.1(33) | 135.9(35) | 140.5(43) |
| Si7-O29-Si21 (x 2) | | | | 135.5(34) | 150.1(47) | 139.6(35) |
| 4-ring SBU | | | | | | |
| ϵ (4mR) | 1 | 1 | 1 | 0.92 | 1.08 | 0.96 |
| Si-O-Si | 144.79(9) | 143.7(6) | 143.4(7) | | | |
| Si9-O38-Si14 | | | | 137.8(28) | 145.7(42) | 119.8(28) |
| Si14-O41-Si1 | | | | 130.3(35) | 143.2(38) | 130.2(35) |
| Si1-O34-Si6 | | | | 138.5(39) | 139.9(35) | 121.7(38) |
| Si6-O45-Si9 | | | | 156.4(41) | 147.2(40) | 148.8(47) |



Elastic behavior, phase transition, and pressure induced structural evolution of analcime

G. DIEGO GATTA,^{1,2,*} FABRIZIO NESTOLA,^{2,3} AND TIZIANA BOFFA BALLARAN²

¹Dipartimento di Scienze della Terra, Universita' degli Studi di Milano, Via Botticelli 23, I-20133 Milano, Italy

²Bayerisches GeoInstitut, Universitaet Bayreuth, Universitaetsstrasse 30, D-95447 Bayreuth, Germany

³Crystallography Laboratory, Department of Geosciences, Virginia Tech, Blacksburg, Virginia 24061, U.S.A.

Eur. J. Mineral.

Fast Track DOI: 10.1127/0935-1221/2009/0021-1923

Fast Track Article

**HP-HT mineral physics:
implication for geosciences**

Compression behaviour and flexibility window of the analcime-like feldspathoids: experimental and theoretical findings

G. DIEGO GATTA^{1,2,*}, ASEL SARTBAEVA³ and STEPHEN A. WELLS⁴

¹ Dipartimento di Scienze della Terra, Universita' degli Studi di Milano, Via Botticelli 23, I-20133 Milano, Italy

*Corresponding author, e-mail: diego.gatta@unimi.it

² CNR-Istituto per la Dinamica dei Processi Ambientali, Milano, Italy

³ Department of Chemistry, Inorganic Chemistry Laboratory, University of Oxford,
South Parks Road, Oxford OX1 3QR, UK

⁴ Department of Physics and Centre for Scientific Computing, University of Warwick,
Gibbet Hill Road, Coventry CV4 7AL, UK

Conclusion...

- The range of compressibility among this class of microporous silicates is large [*i.e.* K_0 ranging between 20 and 65 GPa]. These experimental findings show that microporosity does not necessarily imply high compressibility.

On the whole, **the answer to the question “Does porous mean soft?” is “No”.**

- Any attempt to find a credible relationship between microporosity and compressibility has been, to date, unsuccessful. For example, the compressibility of zeolites is not directly controlled by the microporosity described in terms of “framework density”. In fact, the bulk moduli of some isotypic fibrous zeolites are different even though their FD is similar.

- The flexibility observed in open-framework structures is governed by a few specific deformation modes, based on tetrahedral tilting of stiff tetrahedra around oxygens that behave as hinges.
- When a non-penetrating P -medium is used, P -induced tetrahedral tilting usually leads to a continuous rearrangement of the framework without any phase-transition, but may induce “displacive” phase-transitions, as observed for the zeolites with ANA framework type (Table 1).
- The P -induced main deformation mechanisms are governed by the tetrahedral framework (and its topological configuration) and are independent of the Si/Al-distribution and of the channels content. The extra-framework content controls, however, the compressibility of the channels/cages, implying a different unit-cell compressibility in isotypic structures (*e.g.* fibrous zeolites).



Grazie per la vostra attenzione!
Thanks for your attention!

G. Diego Gatta,

*Department of Earth Sciences,
University of Milan, Italy*

E-mail: diego.gatta@unimi.it



UNIVERSITÀ
DEGLI STUDI
DI MILANO

ADDITIONAL MATERIAL

Macroporous Materials

Microporous materials are a class of solid-state compounds characterized by open framework structures whose pores (as channels or cages) with “free diameters” (Baerlocher et al., 2001) shorter than 20Å. Materials with pores larger than 20Å are defined as “mesoporous materials”. Zeolites, for example, are microporous framework materials. Feldspathoids or clathrates are further classes of microporous materials.

Zeolites

In nature, zeolites are found in several geological environments. Their crystal structure consists of a framework made by linked SiO_4 - AlO_4 - PO_4 -tetrahedra. The tetrahedron is defined as the “primary building unit” of a zeolitic framework. Zeolite frameworks can also be viewed as an assemblage of polytetrahedral units. These units are usually defined as “secondary building units”, or “building block units”. Each zeolitic framework type contains open cavities, in which the channel content (“extra-framework content”) lies. The presence of cavities is responsible for the low framework density (FD) of zeolites, which is defined as the number of tetrahedrally coordinated atoms (T-atoms) per 1000\AA^3 . FD is lower than 20 T/ 1000\AA^3 . In natural zeolites, the channel content is usually represented by water molecules and monovalent or bivalent cations, which are commonly exchangeable. In hydrated zeolites, dehydration occurs at temperatures lower than 400°C and is usually reversible (Coombs et al., 1997; Gottardi and Galli, 1985, Armbruster and Gunter, 2000). The general formula for common Si/Al-zeolites is: $\text{A}^+_{x} \text{B}^{2+}_{y} [\text{Al}_{(x+2y)} \text{Si}_{n-(x+2y)} \text{O}_{2n}] \cdot m\text{H}_2\text{O}$ (usually with $m < n$)

Zeolites at high-pressure

Recent experiments have shown that the high-pressure behavior of microporous materials may be strongly influenced by the nature of the P -transmitting media used for the experiments: *i.e.* “penetrating” or “non-penetrating” P -media. Penetrating media represent a class of fluids that can penetrate into the zeolitic micropores at HP, implying a strong influence on the elastic behavior and on the P -induced structural evolution of the open-framework materials. Water, for example, is able to penetrate micropores. Water-bearing P -media (*e.g.* as the mix ethanol:methanol:water = 16:3:1) or elemental gaseous media (*e.g.* helium, nitrogen, neon, argon, xenon) are potentially penetrating media. Complex and larger molecules than water (methanol, ethanol, isopropanol, glycerol, silicon-oils, perfluorether, fluorinert), or solid media at room conditions (*e.g.* NaCl, KCl), are nominally non-penetrating media. According to Gatta (2008), the P -induced penetrability is controlled by several variables: 1) the “free diameters” (Baerlocher et al., 2001) of the framework channels; 2) the nature of the channel content, and 3) the $P(\text{H}_2\text{O})$, due to the amount of water contained in the P -media.

The P -induced penetration processes opened a new scenario on the use of microporous materials: the sorption selectivity, governed by the channels/cages configurations, makes these materials excellent “nano-reactors”, since space confinement could also lead to the formation of (low-dimensionality) supramolecular systems.

Comparative elastic behaviour of zeolites: general considerations

- The range of compressibility among this class of microporous materials is large [*i.e.* $20 < K_0 < 65$ GPa]. Microporosity does not necessarily imply high compressibility. Several zeolites are less compressible than many rock-forming silicates, such as α -quartz, Na-feldspars, Na-scapolites, and some tri-octahedral and di-octahedral micas. Open-framework structures are intuitively expected to be highly compressible, because the tetrahedral tilting can lead to a channel compression accommodating the effects of pressure. However, the interaction between the tetrahedral framework and the channel content (molecules + cations) may hinder the compression of the channels.
- Any attempt to find a credible relationship between microporosity and compressibility has been, to date, unsuccessful. For example, the compressibility of zeolites is not directly controlled by the microporosity described in terms of “framework density” (Baerlocher et al., 2001). In fact, the bulk moduli of some isotypic fibrous zeolites (*e.g.* natrolite and scolecite) are different even though their FD is similar. Or, more significantly, zeolites with completely different structure topology show drastically different bulk moduli despite their similar FD, as observed for scolecite and heulandite (Gatta 2008).

P-induced structural evolution in zeolites: general considerations

- In zeolites, the flexibility is governed by a few specific deformation modes, based on tetrahedral tilting of stiff tetrahedra around oxygens that behave as hinges;
 - *P*-induced tetrahedral tilting usually leads to a continuous rearrangement of the framework without any phase-transition, but may induce “displacive” phase-transitions, as observed for the zeolites with ANA framework type;
 - The *P*-induced main deformation mechanisms are governed by the tetrahedral framework (and its topological configuration). The extra-framework content controls, however, the compressibility of the channels/cages, implying a different unit-cell compressibility in isotropic structures;
- Open framework structures usually accommodate the effect of pressure with an increase in the ellipticity of the channel systems, while maintaining the original elliptical configuration (*i.e.* without any “inversion” in ellipticity).

References

- Baerlocher, Ch., Meier, W.M., and Olson, D.H., 2001, *Atlas of zeolite framework types*, 5th edn, Elsevier, Amsterdam.
- Gatta, G.D., 2005, A comparative study of fibrous zeolites under pressure. *Eur. J. Mineral.* **17**:411-422.
- Gatta, G.D., 2008, Does porous mean soft? On the elastic behaviour and structural evolution of zeolites under pressure. *Z. Kristallogr.* **223**:160-170.

Structural Chemistry across Phase Boundaries

I. David Brown
Brockhouse Institute for Materials Research
McMaster University,
Hamilton, Ontario

Outline of talk:

[2] Outline of presentation

1. The message
2. The ionic model
3. The bond valence rules of chemistry
4. Constraints causing phase changes
 - Composition
 - Temperature
 - Pressure
5. Structure simulations

[3] In order to explore the crystal chemistry of phases and phase transitions one needs to separate the properties that are responsible for the phase transition from those that are common to all phases. The latter should describe the crystal chemistry using well defined concepts that are quantitatively related. The traditional chemical bond model serves this function for molecular organic chemistry, but acid-base salts and ceramic

The message

**Chemistry does not change
between phases and
across phase boundaries**

**Phase changes are caused by changes
in external constraints such as
composition, temperature, pressure**

compounds, and metal and alloys have not been as well served. This paper describes a chemical bond model for acid-base salts and ceramics, based on an unconventional development of the ionic model.

[4] THE IONIC MODEL Although it gives a poor description of chemical bonding (it contains no information about the distribution of electron density that holds the atoms together), it is remarkably successful in simulating inorganic structures because of its simplicity and robustness. It works for any compound in which the atoms can be divided into cations and anions (with the anions having the larger electronegativity) and in which bonds are found only between cations and anions. This includes a large number of chemical compounds, but there are compounds where it does not work, particularly in organic chemistry.

[5] Setting the charges equal to the atomic valence satisfies this condition and helps to link the model to traditional chemical concepts. The Coulomb interaction ensures that at equilibrium the cations and anions are well mixed. To prevent the charges from collapsing to a point, a repulsive potential must be added. Any repulsive potential can be used, but the best is one that results in the equilibrium positions of the ions being the same as the equilibrium positions of the atoms in the solid. Structures can be predicted by using these potentials to search for the lowest energy. It is the empirical nature of the repulsive force that makes the model so successful, since this is designed to reproduce the observed structure.

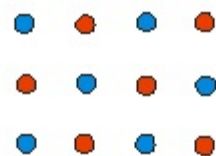
The ionic model

NOT a model of chemical bonding

**a good model of chemical structure
simple and robust**

**The bond valence model
is a chemistry-friendly version
of the ionic model**

The Ionic Model



Cations Anions

The system is globally and locally charge neutral

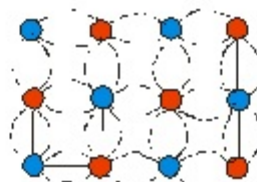
The strengths and weaknesses of the traditional ionic model.

1. It has proved to be remarkably successful in simulating structures of both solids and liquids.
2. The Coulomb force is a long range force and the interaction between every pair of ions in the simulation must be included. Calculations are therefore computer intensive.
3. The model provides few insights for conceptual analysis and planning.
- 4 Traditional chemical concepts such as bond and electonegativity do not arise naturally.

THE BOND VALENCE APPROACH.

[6] Instead of developing the ionic model in terms of the potential field, consider instead developing it in terms of the electrostatic field. It is easy to show that the Faraday lines of field link cations to their neighbouring anions.

**In the bond valence model
the ions are linked by electric
flux**



[7] A bond is defined as existing between ions that are linked by field lines (electrostatic flux). The Coulomb field partitions space into localized bond regions that interact only with their immediate neighbours and involve no long-range forces. The electrostatic field gives a description in terms of localized bonds. The flux linking two ions is a measure of the strength of the bonds. If the charges are set equal to the atomic valences, the flux is called the bond valence. Gauss' theorem states that the total electrostatic flux incident at an ion is equal to its charge. This is the valence sum rule: the sum of bond valences incident on an ion is equal to the valence of the ion.

A bond exists if the ions are linked by flux

**the flux is the bond valence and measures
the strength of the bond**

**The bond valences, like the flux,
add up to
the atomic valence at each atom**

[8] As ions approach more closely, the electrostatic flux linking them increases, thus bond valence correlate with bond length as determined by the repulsive potential.

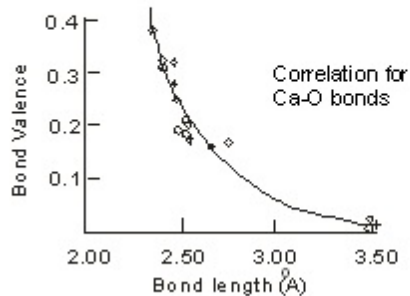
**The closer the atoms,
the greater the flux (valence)
between them**

Chose the correlation between bond valence and bond length to match the ideal bond valences to the observed bond lengths

[9] Like the repulsive potential this correlation is determined empirically and is robustly transferable between bonds of the same type. This allows bond valences to be determined from experimental bond lengths, or bond lengths to be predicted from ideal bond valences. The slide shows electrostatic fluxes calculated for Ca-O bonds in a number of crystals. The bond valences are chosen to be equal to these fluxes.

[10] In this model bonds act as electric capacitors (two equal and opposite charges linked by flux). At equilibrium all the bonds are observed to have the same capacitance (if electronic anisotropies are ignored), hence two Kirchhoff-like network rules can be used to calculate the ideal valence of every bond. The effect of these rules is to make the bond valences as equal as is allowed by the valence sum rule and the topology of the network.

Correlation between Bond Valence and Bond Length



Two rules to predict bond valences

Bond Valence Sum Rule

The sum of bond valences around each atom is equal to its atomic valence

Equal Valence Rule

At equilibrium the valence is distributed as equally as possible between the bonds consistent with the valence sum rule

[11] The bonding strength of an ion is the valence of typical bond it forms, equal to the valence of the ion divided by a typical, or average, coordination number.

BONDING STRENGTH OF AN ION

Each ion has a bonding strength, L , equal to the valence of a typical bond that the ion forms
$$L = V/N$$

Cation (Lewis acid) bonding strength

[12] Examples of cation and anion bond strengths. These also represent Lewis acid and base strengths. The cation bonding strength of an ion can also be used as a measure of its electronegativity.

$$L_a = V_{\text{cation}} / N_{\text{cation}}$$

e.g. $\text{Na}^+ = 1/6 = 0.17$ valence units

Anion (Lewis base) bonding strength

$$L_b = V_{\text{anion}} / N_{\text{anion}}$$

e.g. $\text{O}^{2-} = 2/4 = 0.5$ vu

Each is an estimate of the valence of the bonds the ion forms

THE VALENCE MATCHING RULE

[13] If the bonding strengths of a cation and an anion differ by more than a factor of two it is difficult for them to form a bond.

Bonds can only form if the

Cation bonding strength

is similar to the

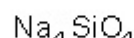
Anion bonding strength

Examples of Valence Matching



$$L_a = 1/8 = 0.11 \quad L_b = 1/12 = 0.08$$

Good match, stable



$$L_a = 1/6 = 0.17 \quad L_b = 4/12 = 0.33$$

poor match, unstable

[14] This allows one to explore which structures (bond topologies) are likely to be stable. The most stable will be those in which the anion and cation bonding strengths are equal. A weak bond between two well matched ions is more stable than a strong bond between two poorly matched ions.

Summary of some bond valence rules

[15] Three of the most important rules of the bond valence model are the valence sum rule, the equal valence rule and the valence matching rule.

Bond valence sum rule

Equal valence rule

Valence matching rule

This set of rules applies
to the local environment of atoms

[no slide] **The distortion theorem: Distorting an ion's environment increases its average bond length.** The concave form of the bond valence - bond length correlation [9] leads to the result that the greater the deviation of the individual bond lengths from their average, the larger the average bond length becomes, providing the valence sum is constant. A corollary is that an atom in a cavity that is too large will increase its effective size by distorting its environment; lengthening some bonds and shortening others.

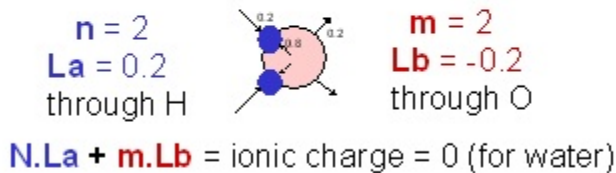
[no slide] **Strengths and weaknesses of the bond valence model.** The above rules and theorems are some of the simple chemical conditions that any acid-base structure, whether solid or liquid, must obey.

1. The model has the same mathematical rigour as the ionic model from which it is developed, but it is expressed in the language of chemical bonds.
2. It is simple, intuitive and requires no more than a pocket calculator.
3. It can therefore be used to discuss, analyze and postulate the structures that might occur under different constraints of composition, temperature or pressure.
4. It has not currently been developed for simulations, though this should be possible.
5. The concept of energy does not arise naturally in this model.

[no slide] The hydrogen atom is so small that the anions to which it is bonded overlap. This anion-anion repulsion destabilizes the symmetric hydrogen bond and, according to the distortion theorem, causes the H^+ ion to move off centre so as to increase its average bond length. The lowest energy hydrogen bond is that found in ice with a bond valence distribution of 0.8 and 0.2 valence units (vu),

[16] The O²⁻ ion is normally four coordinate, and in water therefore forms two donor and two acceptor hydrogen bonds. It acts as both a cation (Lewis acid) with a cation bonding strength of 0.2 vu and as an anion (Lewis base) with an anion bonding strength of 0.2 vu.

The Water Molecule has both
a cation and an anion bonding strength



APPLICATIONS TO PHASES AND PHASE BOUNDARIES

[17] The three factors that normally lead to phase changes are changes in the **composition** between one region and another, changes in **temperature** as a system is heated, and changes in **pressure** as a system is compressed. The bond valences rules apply in all these phases and across the boundaries between them, allowing the structural chemistry to be modelled even as these constraints are changed.

APPLICATIONS TO PHASES

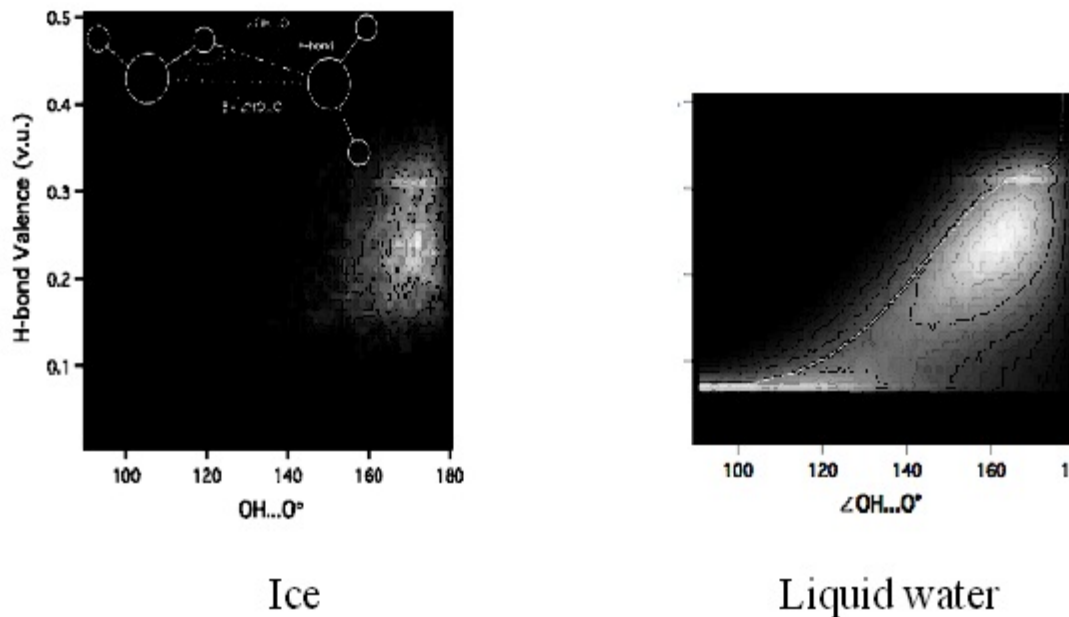
The chemical rules of the bond valence model apply to all phases

Phase differences are driven by
extermal constraints such as
composition
temperature
pressure

[no slide] **Temperature.** The temperature increases as the kinetic energy of the ions is increased and they move away from their equilibrium position. The bond valence model will still provide a good description of the instantaneous local structure, but what is observed using diffraction methods is the average of a large number of different local structures. These average structures may no longer obey the valence rules well, but the model can be used to postulate the different local structures that contribute to the average. The higher the temperature the larger the deviations expected from the valence rules. The valence sum rule can be used to locate the regions that become accessible to the atoms by noting where $\Delta V = \sum_{ij} s_{ij} - V_i$ (s_{ij} = valence of bond ij , V_i = valence of atom i) is less than some limiting value that increases with temperature. This accessible region can be mapped by calculating the bond valence sums in the region around the observed position. As the temperature is increased, the ion has access to larger volumes of space. At higher temperatures the individual bond lengths differ by increasingly large amounts from their mean so that according to the distortion theorem the average bond length increases, giving rise to thermal expansion. However if the region occupied by the ion has several energy minima, the ion

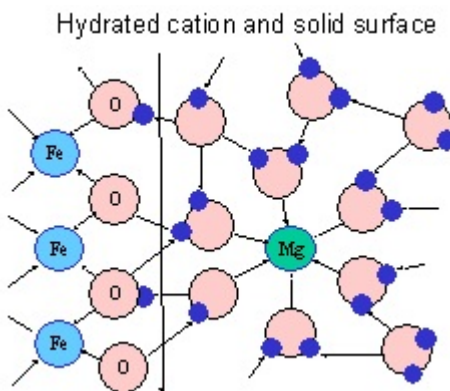
may spend most of its time away from its average (high symmetry) position, leading to bond lengths that are apparently too short. An apparent failure of the bond valence rules can indicate spatial or temporal disorder. The bond valence model gives a correct description of the local structure, and can therefore be used to interpret the high temperature time averaged structure.

Molecular dynamics simulations of ice and water



[18, 19] Ice and water provide an interesting example. The slide shows a histogram of H^+ ion geometries for ice (left) and water (right) calculated using density functional theory. The horizontal axis shows the $\text{O}-\text{H} \dots \text{O}$ angle from 90 to 180 degrees. The vertical axis shows the valence of the $\text{H} \dots \text{O}$ bond ranging from zero (infinite distance) at the bottom to 0.5 vu (symmetrical bond) at the top. In ice all the $\text{O}-\text{H} \dots \text{O}$ angles are close to 180 degrees and the bond valence is close to 0.2 vu. In water most angles are slightly larger, but there is now a significant tail of weaker and bent bonds. The thin line indicates the limiting geometry predicted by the bond valence model. As the ice melts, the cooperative behaviour of the hydrogen bonds breaks down. Most of the bonds are still close to linear with valences of 0.2 vu but a significant proportion are bent and weaker. (Distances corresponding to a valence less than 0.06 vu are not included in this histogram) Figure from B.R. Bickmore, K.M. Rosso, I.D.Brown and S.Kerisit. (2009) J. Phys.

[20] The effects of composition are illustrated in this slide which shows a notional phase boundary in a hypothetical 2-dimensional system. It is designed to show how one can use the bond valence model to discuss possible boundary structures. On the left is an iron oxide solid, on the right a solution containing a hydrated Mg^{2+} ion. The Mg-O bonds have a valence of 0.33 and the hydrogen bonds formed by its hydration sphere are 0.17 vu, close to the valence found in liquid water. The surface of the iron oxide acts as a base. If the Fe is three-valent and six coordinate, the Fe-O bonds have a valence of 0.5 vu. The surface O^{2-} ions, if bonded to two Fe^{3+} ions have a residual valence of 1.0 vu, and if these O^{2-} ions are 4-coordinate, they have a bonding strength of 0.5 vu. The bonding strength of a water molecule bound to Mg^{2+} is 0.83 vu if it has lost one of its H^+ ions. Under these circumstances the H^+ ion will attach to the stronger base, namely the O^{2-} attached to Mg^{2+} . Diagrams like this allow one to explore the different possible structures of the bulk and surfaces to find which best fits the bond valence rules.



[no slide] The effects of pressure have not been much analysed using the bond valence model. It is clear that the external pressure will shorten the bonds, so the bond valence - bond length correlation will be a function of pressure. More work is needed in this field.

[21] The traditional ionic model is used extensively for simulating acid-base structures, by looking for the arrangement of atoms with the lowest energy. The bond valence model has been used to analyze and confirm the correctness of observed and simulated structures but the model could be developed into a simulation tool with a strong chemical flavour. A potential energy simulation of N atoms tries to find the $3N$ atomic coordinates that minimize the single potential energy function, but in a bond valence simulation there are N separate bond valence sum constraints that must be satisfied. In addition there are several softer constraints, e.g., the equal valence rule, that apply around each ion, all expressed directly in chemical language. The bond valence model should bring a different perspective to structure simulation.

Structure Simulations

First principles (quantum mechanical)
2-body potential (ionic model)

The results obey the bond valence rules

Simulations using the bond valence model
should be available within 10 years

[22] A summary of the virtues of the bond valence model.

Bond Valence Model

Chemical version of the ionic model

Describes constraints of acid-base bonding
Combines with external constraints
e.g., composition, temperature and pressure

Simple, robust, insights, computer-lite

Check experimental and simulated structures

Conceptual modelling

Simulations based on chemical criteria (in the future)

IN SITU AFM STUDIES ON THE GROWTH OF CRYSTALS OF BIS(IMIDAZOLIUM 2,6-DICARBOXYLATEPYRIDINE) CU(II) DIHYDRATE

Tzy-Jiun Mark Luo¹, John C. MacDonald², and G. Tayhas R. Palmore^{1,3}

¹*Division of Engineering, Brown Univ., Providence, RI*

²*Dept. of Chemistry and Biochemistry, WPI, Worcester, MA*

³*Division of Biology and Medicine, Brown Univ., Providence, RI*

1. ABSTRACT

The kinetics of growth at the (100) face and the (0-11) of crystals of bis(imidazolium 2,6-dicarboxylatepyridine)Cu(II) dihydrate (**1-Cu**) were compared using atomic force microscopy. The rate at which the (011) step riser advanced across the (0-11) face was found to be consistently faster than that at the (100) face. This difference in kinetics of growth is attributed to the different chemistry exposed at these two surfaces and the manner in which these surfaces assemble.

2. INTRODUCTION

Molecular crystals are pursued widely for use in optical, electronic, and magnetic applications.[1-5] Such applications require careful control over the interface between a crystal and other surfaces.[6-11] The bulk properties of molecular crystals, intrinsically inherited from functional groups, rely on the packing arrangement of individual molecules. The crystal facets that develop during growth determine the surface properties of molecular crystals by reflecting the orientation of molecules exposed at a specific surface.

Atomic force microscopy (AFM) has been an important tool for investigating the rate at which a crystal facet forms and the mechanisms of assembly involved.[12-14] Several crystalline systems have been studied including inorganic solids such as calcite[15] and potassium dihydrogen phosphate (KDP),[16,17] proteins such as lysozyme,[18] canavalin,[19,20] catalase,[21] and insulin,[22] and molecular solids such as diketopiperazines.[13,23] An important finding of these latter studies was that all mechanisms of growth were similar to those described for inorganic crystals and independent of the size or complexity of the growth unit. In addition, studies of crystal surfaces that are anisotropic have provided information about the kinetics of growth and contributing energetic factors.[24] Such information is important for controlling the morphology of crystals as well as controlling the growth of epitaxial layers via solvent-mediated self-assembly.[25]

Despite years of investigation, significant questions remain concerning fundamental aspects of crystal growth from solution. Of particular interest is the pathway by which growth units leave a supersaturated solution to become incorporated in the crystalline solid. This pathway is described as either direct incorporation or surface diffusion of growth units.[26-29] The direct incorporation model is considered appropriate for crystals grown from solution because of the large supply of ions to its surface. Furthermore, the energy of dissolution is small relative to that of evaporation for vapor-phase growth and the diffusion coefficient of growth units in solution is large relative to the diffusion coefficient of growth units across a surface. Nevertheless, the surface diffusion model has been demonstrated in crystals grown from solution.[20]

The purpose of this study is to examine the effect of surface chemistry and molecular packing on the kinetics of assembly of a crystal grown from solution regardless of whether growth occurs by direct incorporation or surface diffusion. Crystals of bis(imidazolium 2,6-dicarboxylatepyridine) Cu(II) dihydrate (**1-Cu**) were used for this study.[30,31] These crystals belong to a unique family of crystals in which the crystal structure is nearly invariant regardless of metal ion present (i.e., M (II) = Cu, Ni, Co, Mn, or Zn), making it an ideal crystal system for studying epitaxial growth via solvent mediated self assembly.[25] The rates at which the (011) step riser advanced across the (100) face (a surface consisting of either a pure layer

of imidazolium cations or Cu (II) complex anions) and the (0-11) faces (surfaces consisting of both imidazolium cations and Cu (II) complex anions) of (**1-Cu**) were measured using atomic force microscopy (AFM).[18, 32] The kinetics of growth at the (0-11) surface was found to be faster than that at the (100) face and becomes increasingly so with increase in supersaturation. This difference in kinetics of growth can be attributed to the different moieties exposed at these two surfaces and the manner in which these surfaces assemble.

3. RESULTS AND DISCUSSION

3.1 Preparation of Crystals of Bis(imidazolium 2,6-dicarboxypyridine) Cu(II) Dihydrate (**1-Cu**)

The preparation of **1-Cu** is shown in **Figure 1**. Typically, an aqueous dimethyl sulfoxide solution containing a 1:4 mixture of metal (II) ion and 2,6-dicarboxypyridine (**DCP**) is mixed with an aqueous dimethyl sulfoxide solution containing imidazole (**Im**) at a concentration equal to that of **DCP**. After leaving the mixture undisturbed for several hours at room temperature, seed crystals in the shape of flat rhombohedrons can be harvested (**Figure 2**, upper inset). Large single crystals subsequently are grown from a seed crystal using a microcrystallizer, which consists of a water-jacketed flask (100 ml) equipped with a rotary stirrer and temperature-controlled water circulator (**Figure 2**). The general procedure for growing crystals in the microcrystallizer is as follows. First, 40 ml of a stock growth solution (e.g., 1:4:4 solution of Cu(II):**Im**:**DCP**) is added to the water-jacketed flask and equilibrated to a desired temperature by the water circulator. Two seed crystals are mounted on top of the crystal stage using silicone grease (**Figure 2**, lower inset). The crystal stage is attached to the end of a stirring rod connected to a motor that reverses the direction of stirring at a controlled rate and duration. Finally, the mounted crystal is placed in the middle of the water-jacketed flask to initiate new growth. Using the microcrystallizer, single crystals with millimeter to centimeter dimensions can be grown for subsequent *in situ* AFM measurements.

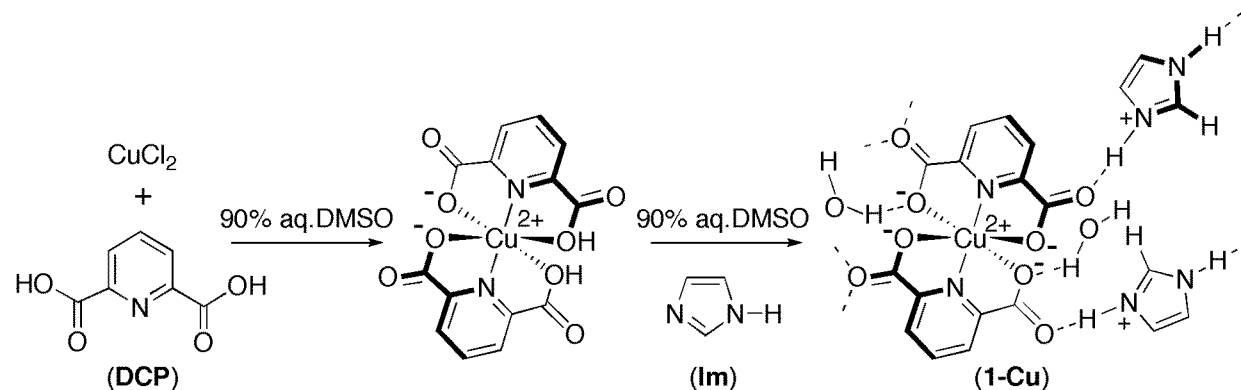


Figure 1. Preparation of bis(imidazolium 2,6-dicarboxypyridine) Cu(II) dihydrate (**1-Cu**) from one equivalent of **CuCl₂** and two equivalents each of 2,6-dicarboxypyridine (**DCP**) and imidazole (**Im**).

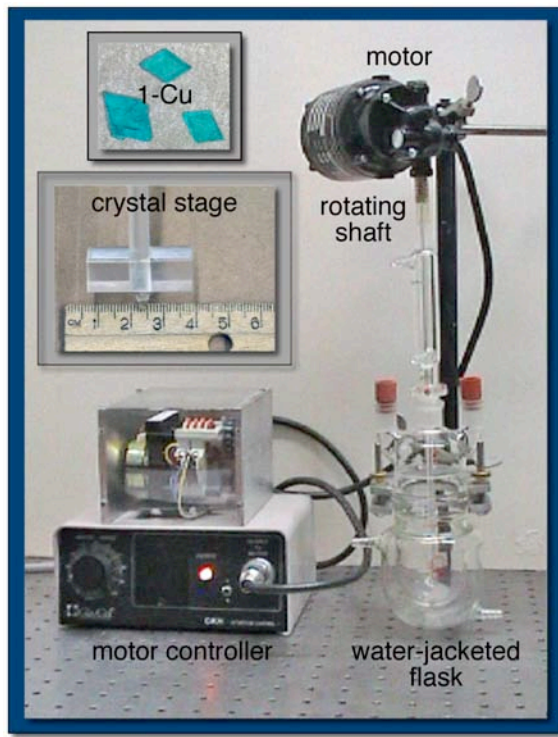


Figure 2. Microcrystallizer used to grow millimeter-sized crystals of **1-Cu**. The upper inset shows three rhombohedral-shaped crystals of **1-Cu**, which were grown from a 1:4:4 solution of Cu(II):Im:DCP. The lower inset shows the crystal stage upon which seed crystals are mounted on either side of the shaft. The direction of rotation and rate of rotation of the stage is set by the motor controller.

3.2 Changing the Size of (011) and (0-11) Facets Relative to the Size of the (100) Facet in Crystals of **1-Cu**

Crystals of **1-Cu** are rhombohedral in shape when grown from a 1:4:4 solution of Cu(II):Im:DCP. The largest surface or most dominant facet in these crystals is the (100) facet. The sides of the rhombohedral-shaped crystals are defined by {011} and {0-11}, which are considerably smaller in size than the (100) facet. To compare the kinetics of step advancement across the (0-11) face to that of the (100) face using *in situ* AFM, it is convenient to work with a crystal with similar sized (100) and (0-11) facets. Because the crystal stage in the microcrystallizer alternates between clockwise and counterclockwise directions of rotation, diffusion of growth units perpendicular to the axis of rotation is enhanced relative to any other direction. Thus, by mounting seed crystals of **1-Cu** with either their (011) or (0-11) faces in contact with the surface of the crystal stage, the size of the (100) face relative to that of the (011) and (0-11) facets can be decreased.

To illustrate, shown in **Figure 3** is a comparison of the aspect ratio of two crystals grown from seed crystals of **1-Cu** mounted with either the (-100) face (**Figure 3a**) or the (0-11) face (**Figure 3b**) in contact with the surface of the crystal stage shown in the lower inset of **Figure 2**. When the seed crystal is mounted with the (-100) face in contact with the crystal stage, diffusion of growth units (green arrows in **Figure 3**) to (011) and (0-11) faces is enhanced by the rotation of the crystal stage. Thus, the (100) face remains the largest (slowest growing) facet in this crystal and the morphology of the crystal is a thin rhombohedron. In contrast, when the seed crystal is mounted with either the (011) face or (0-11) face in contact with the crystal stage, the enhanced diffusion of growth units to the (100) and (-100) faces generated by the rotation of the crystal stage results in a crystal with (011) and (0-11) facets similar in size to the (100) facet. The morphology of the crystal is a thick rhombohedron.

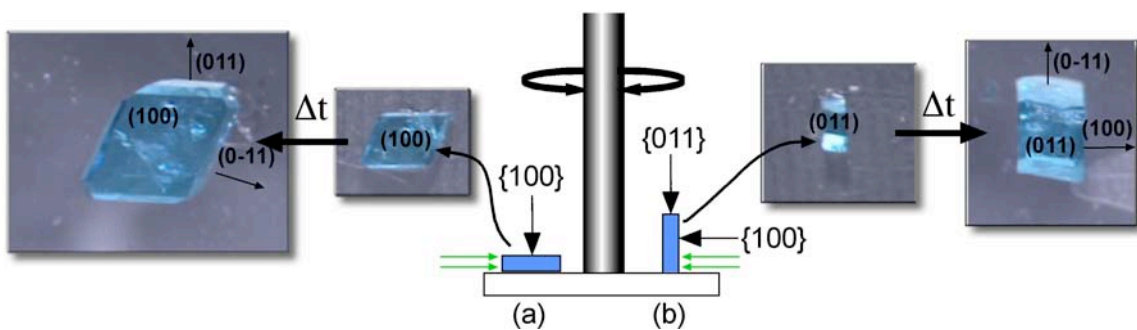


Figure 3. Illustration of seed crystals of **1-Cu** mounted with the (a) (-100) face or (b) (0-11) face in contact with the crystal stage of the microcrystallizer. The relative size of the (100) face to the (011) face of these crystals can be changed according to which surface of the crystal is in contact with the crystal stage. The green arrows indicate the direction in which the diffusion of growth units is enhanced by the rotation of the crystal stage.

3.3 Chemical Composition and Molecular Packing at the Surfaces of **1-Cu** Studied By *in situ* AFM.

As stated previously, the dominant facet in crystals of **1-Cu** is the (100) face when grown from a 1:4:4 solution of Cu(II):Im:DCP.[25] The molecular components exposed at the (100) surface are shown in **Figure 4** and consists of either a pure layer of bis(2,6-dicarboxypyridine) Cu (II) anions (**Figure 4a**) or a pure layer of imidazolium cations (**Figure 4b**).[30,31] In contrast, the molecular components exposed at the (0-11) and (011) surfaces shown in **Figure 4c** and **4d**, respectively, consist of a mixture of both anions and cations with similar patterns of packing. Thus, based solely on the chemical composition and molecular packing at these surfaces, the kinetics of growth at a surface that consists of pure layers of anions or cations (i.e., (100) face) is expected to be different from that at a surface that consists of a mixture of anions and cations [i.e., (0-11) and (011) faces]. The morphology of crystals of **1-Cu** (thin rhombohedrons with a (100) dominant facet) confirms this expectation and *in situ* AFM studies can be used to quantify the difference in rates of growth.

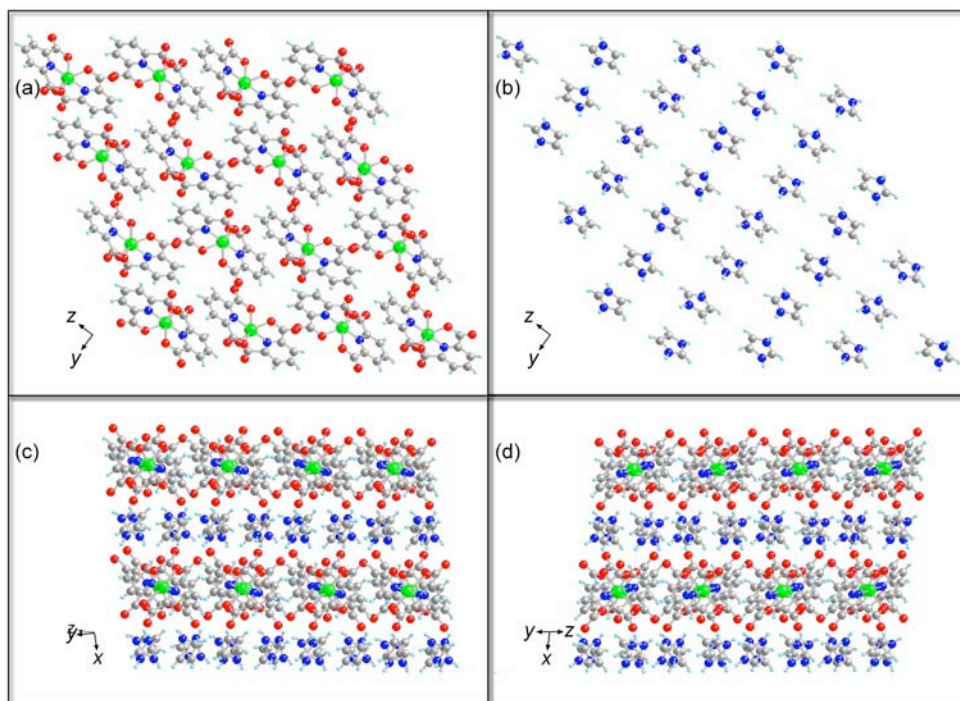


Figure 4. The crystal structure of **1-Cu** viewed perpendicular to three different surfaces. Shown in (a) and (b) is the (100) face, which reveals that either a layer of pure anions or pure cations, respectively, are exposed at this surface. Shown in (c) and (d) is the (0-11) face and (011) face, respectively, revealing that a mixture of anions and cations are exposed at these surfaces.

3.4 Measuring the Kinetics of Growth of Crystals With the AFM

The AFM is a tool with which to image nanoscale features on a surface. In the context of crystals, we have used the AFM to image features that span in size from the nano- to microscale such as the lattice spacing of molecules at the surface of a crystal, molecular steps, dislocations and surface nuclei (**Figure 5**). [13,23, 25] During imaging, the AFM tip is rastered across the surface of a crystal. Rastering occurs in both a net downward direction (i.e., beginning in the upper left corner and ending in the lower right corner of the area to be imaged) and a net upward direction (i.e., beginning in the lower left corner and ending in the upper right corner of the area to be imaged). Under static conditions, features do not move while the surface is being imaged. Consequently, the same image is generated regardless of whether the tip is rastering the surface in the downward or upward direction. Under dynamic conditions (i.e., growing crystals), however, features are moving while the surface is being imaged. Consequently, the images generated by the downward and upward scans are different because of the time-lag between the rastering tip and the dynamic processes (i.e., step advancement) occurring at the surface.[32] This time-lag is illustrated in **Figure 6**.

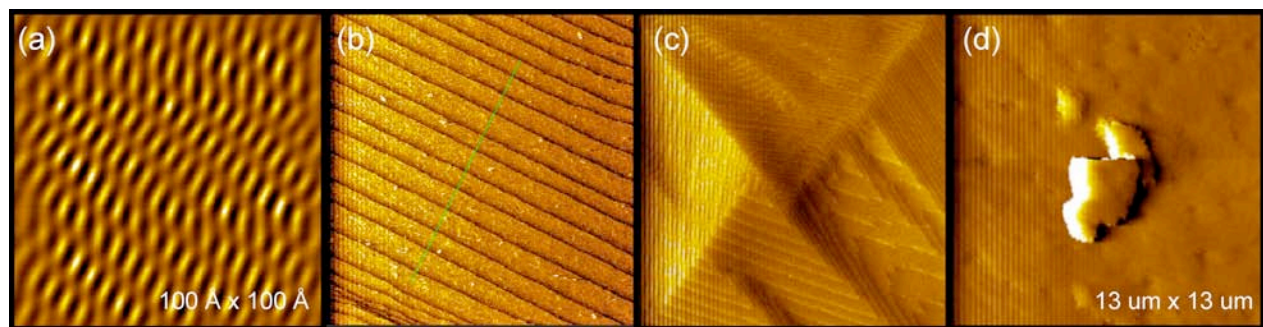


Figure 5. AFM images of the surface of a molecular crystal that reveal (a) lattice spacing, (b) step width, (c) screw dislocation, and (d) surface nuclei.

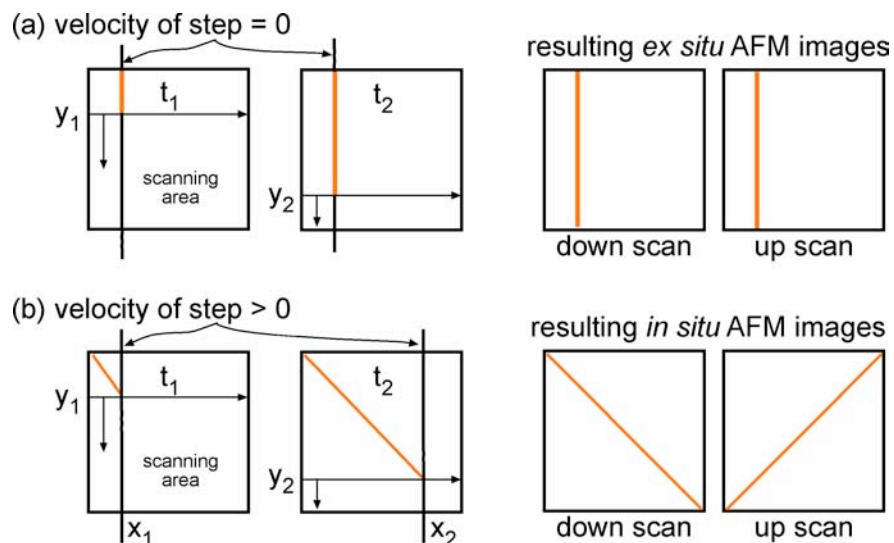


Figure 6. Illustration of what occurs when a static (a) or dynamic (b) surface is imaged with the AFM. For a static surface (*ex situ*), identical images are obtained regardless of the direction of rastering. For a dynamic surface (*in situ*), such as advancing steps in a growing crystal, the downward and upward scans generate different images.

To measure the rate at which a step advances across the surface of a crystal, the surface is imaged while the crystal is immersed in a growth solution of known concentration. Sequential downward and upward scans are collected and a line is drawn parallel to the edge of the advancing steps in both images (**Figure 7**). Using these two images the velocity of step advancement (V) in units of nm s^{-1} is determined by measuring the angle (θ) between the line drawn in an image and a horizontal line drawn across the image for two consecutive images (i.e., θ_d for the downward scan and θ_u for the upward scan). The two values are then substituted into the equation

$$V = \frac{SR}{N} \frac{\cot(q_u) + \cot(q_d)}{\sqrt{(\cot(q_u) - \cot(q_d))^2 + 4}} \quad (1)$$

where S is the scan size (nm), R is scan rate (line s^{-1}), N is number of raster lines in each image. We have observed that the intrinsic error of this equation is avoided if the angle between the step-edges in the downward scan (θ_d) and upward scan (θ_u) is greater than 20° .

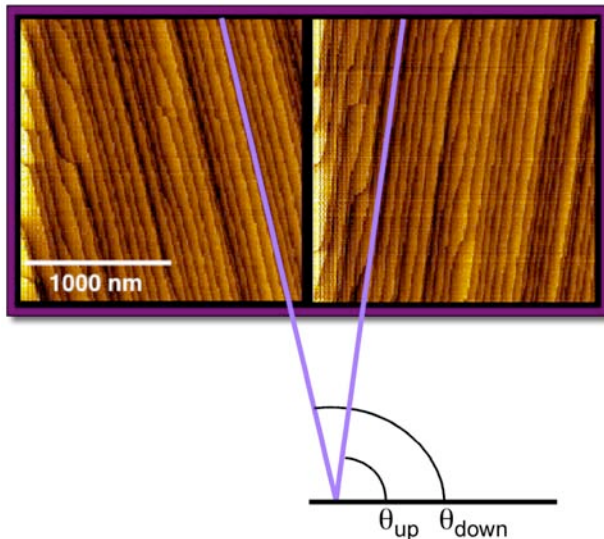


Figure 7. Two consecutive images of the (100) surface of a crystal of 1-Cu from which θ_{down} and θ_{up} are measured for calculating the rate of step advancement.

3.5 Comparison of the Kinetics of Step Advancement Across the (100) Face and the (0-11) Face of Crystals of 1-Cu

Because the chemical composition and molecular packing exposed at the (100) surface is different than that of the (0-11) surface (cf., **Figure 4**), the rate of advancement of (011) step riser across these two surfaces is expected to be different (**Figure 8**). To quantify this difference, the kinetics of growth at these two surfaces was studied *in situ* using atomic force microscopy. Experiments to measure the kinetics of crystal growth were performed in saturated solutions containing an equal volume of each stock solution described above to produce a solution that contained a 1:4:4 ratio of Cu(II):Im:DCP. When the level of supersaturation is such that the crystal is barely growing (i.e., $[\text{Cu}^{2+}] = 30 \text{ mM}$, $[\text{Im}]$ and $[\text{DCP}]$ are each = 120 mM), the average rate at which the (011) riser advances across the (100) face is 7 nm s^{-1} . The average rate at which the (011) riser advances across the (0-11) face is over three times faster at 23 nm s^{-1} . When the concentration of Cu^{2+} ion is increased to 32 mM (and $[\text{Im}]$ and $[\text{DCP}]$ are each = 128 mM), the average rate at which the (011) riser advances across (100) and (0-11) is 23 nm s^{-1} and 37 nm s^{-1} , respectively. At the highest concentration of Cu^{2+} ion used in our kinetic measurements (i.e., 42 mM and $[\text{Im}]$ and $[\text{DCP}]$ are each = 168 mM), the average rate at which the (011) riser advances across (100) and (0-11) is 122 nm

s^{-1} and 153 nm s^{-1} , respectively. Typical AFM images of steps advancing across (100) and (0-11) faces at high supersaturation are shown in **Figure 9**.

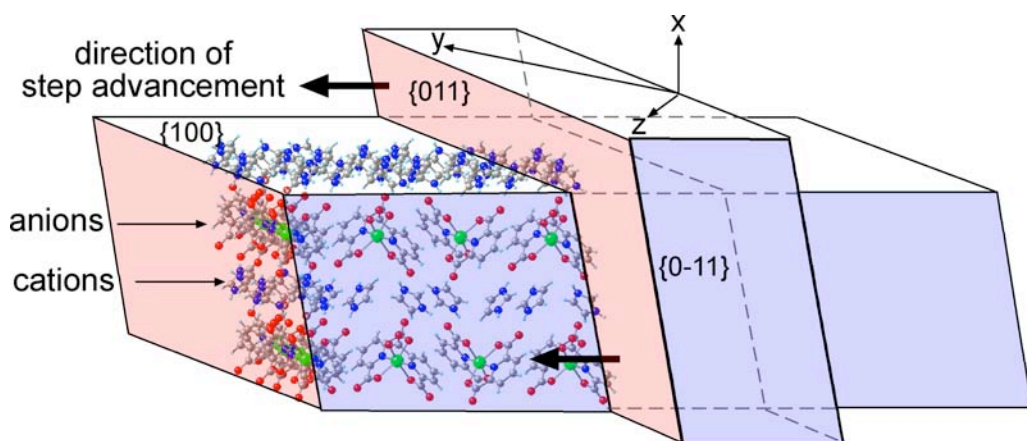


Figure 8. (a) Packing diagram that shows the (011) step riser relative to (100) face and (0-11) face of **1-Cu**.

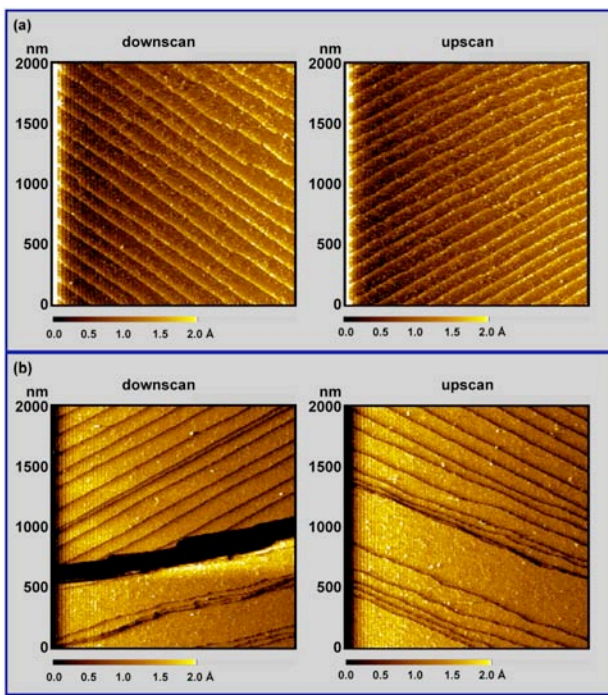


Figure 9. Typical AFM image of steps advancing *in situ* across the (a) (100) and the (b) (0-11) surfaces of **1-Cu** at high supersaturation.

3.6 Why Does the (011) Step-Riser Advance Faster Across the (0-11) Face than the (100) Face?

Figure 10 provides a graphical explanation of the differences in rate at which the (011) step-riser advances across (100) and (0-11) faces. Recall that the (100) surface consists of either a pure layer of anions or a pure layer of cations and the (0-11) surface consists of a mixture of anions and cations that are organized in parallel rows (cf. **Figure 4**). For the (100) face shown in **Figure 10a**, any anion resting on an underlying (100) surface of pure anions will inhibit the attachment and surface diffusion of incoming cations. Consequently, the inhibitory anion, located in a kink site that should be occupied by a cation, must diffuse

out of the kink site to another surface site (a temporary placement) and ultimately dissolve to make the kink site available for incoming cations. This mechanism (i.e., surface diffusion followed by dissolution) enables the incorporation of an incoming cation into the kink site and the resulting advancement of a step-edge. In contrast, a kink site on the (0-11) surface that is occupied incorrectly only requires the inhibitory cation (shown) or anion to diffuse out of the kink site to another surface site to make the kink site available for new growth. Eventually, the inhibitory cation (or anion) will diffuse to a correct surface site and once attached, add to the advancing step-edge.

The observation that the kinetics of growth at the two different faces diverges with increasing supersaturation can be explained by the fact that increasing the supersaturation results in a higher concentration of inhibitors on the surface and in kink sites. For the (100) surface, only dissolution of inhibitors ultimately clears the inhibited kink sites for subsequent growth. Dissolution, however, becomes increasingly difficult with increasing supersaturation. For the (0-11) surface, only surface diffusion is required to clear the inhibited kink sites for subsequent growth. Because the rate of surface diffusion is independent of supersaturation, the inhibitory effect of increasing supersaturation is lower at the (0-11) surface than at the (100) surface, which results in faster kinetics of growth at the (0-11) surface at all levels of supersaturation.

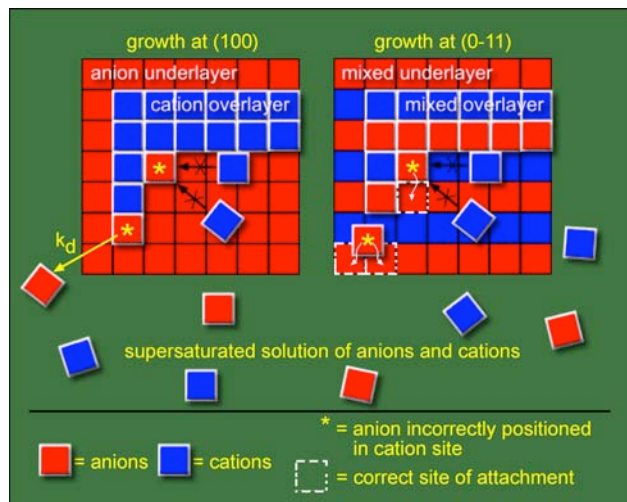


Figure 10. Cartoon illustrating advancement of steps across (a) (100) and (b) (0-11) surfaces of **1-Cu** at high supersaturation. An anion incorrectly positioned in a kink site (*) will either diffuse across the surface or dissolve (k_d) to make the kink site available to an incoming cation. At the (100) surface, both surface diffusion and dissolution are required whereas at the (0-11) surface, only surface diffusion is required.

4. CONCLUSION

We have shown that the AFM can be used to compare the rates at which the same step riser advances across two different crystal surfaces. The effects that molecular packing and supersaturation have on crystal growth kinetics are revealed by this quantitative comparison. Based on these experiments, we conclude that crystal growth is faster when molecular packing at a crystal surface is similar to that of the step-riser (e.g., in this case, both consisting of a mixture of anions and cations) as compared to when the same step-riser advances across a crystal surface with different molecular packing (e.g., in this case, one consisting of a mixture of anions and cations, the other consisting of a pure layer of either anions or cations). The significance of this conclusion is that small changes in supersaturation can lead to significant changes in the kinetics of growth at different crystal surfaces and these changes can be exploited to vary the shape of a crystal, an important capability in the context of batch processing of industrial solids such as pharmaceuticals. Future studies will be directed at exploiting this capability to fabricate complex crystalline solids with varied morphology and composition.

5. ACKNOWLEDGEMENTS

The National Science Foundation and the ACS Petroleum Research Fund provided financial support for this research. The authors thank Jiangfeng Fei for assistance with this manuscript.

6. REFERENCES

- [1] Ashwell, G. J., *Molecular Electronics* Wiley: New York, 1992; 362.
- [2] Bosshard, C.; Sutter, K.; Prêtre, P.; Hulliger, J.; Flörsheimer, M.; Kaatz, P.; Günter, P., *Organic Nonlinear Optical Materials* Gordon and Breach Science Publishers, Switzerland: Postfach, 1995; Vol. 1.
- [3] Gatteschi, D., *Magnetic Molecular Materials* Kluwer Academic Publishers: Lucca, Italy, 1991; 411.
- [4] Fraxedas, J. *Adv. Mater.* **2002**, 14, 1603.
- [5] Vallee, R.; Damman, P.; Dosiere, M.; Toussaere, E.; Zyss, J. *J. Am. Chem. Soc.* **2000**, 122, 6701.
- [6] Hooks, D. E.; Fritz, T.; Ward, M. D. *Adv. Mater.* **2001**, 12, 228.
- [7] Hillier, A. C.; Ward, M. D. *Phys. Rev. B* **1996**, 54, 14037.
- [8] Carter, P. W.; Frostman, L. M.; Hillier, A. C.; Ward, M. D. In *Nucleation and Growth of Molecular-Crystals on Molecular Interfaces - Role of Chemical Functionality and Topography*, ACS Symposium Series, 1994; 186.
- [9] Davey, R. *J. Chem. Soc., Faraday Trans.* **1991**, 87, 3409.
- [10] Davey, R. J.; Black, S. N.; Bromley, L. A.; Cottier, D.; Dobbs, B.; Route, J. E. *Nature* **1991**, 353, 549.
- [11] Sarma, K. R.; Shlichta, P. J.; Wilcox, W. R.; Lefever, R. A. *Journal of Crystal Growth* **1997**, 174, 487.
- [12] Ward, M. D. *Chem. Rev.* **2001**, 101, 1697.
- [13] Palmore, G. T. R.; Luo, T. J.; Martin, T. L.; McBride-Wieser, M. T.; Voong, N. T.; Land, T. A.; De Yoreo, J. J. *Trans. ACA* **1998**, 33, 45.
- [14] Binnig, G.; Quate, C. F.; Gerber, C. *Physical Review Letters* **1986**, 56, 930.
- [15] Hillner, P. E.; Gratz, A. J.; Manne, S.; Hansma, P. K. *Geology* **1992**, 20, 359.
- [16] De Vries, S. A.; Goedtkindt, P.; Bennett, S. L.; Huisman, W. J.; Zwanenburg, M. J.; Smilgies, D. M.; De Yoreo, J. J.; Van Enckevort, W. J. P.; Bennema, P.; Vlieg, E. *Phys. Rev. Lett.* **1998**, 80, 2229.
- [17] De Yoreo, J. J.; Land, T. A.; Rashkovich, L. N.; Onischenko, T. A.; Lee, J. D.; Monovskii, O. V.; Zaitseva, N. P. *J. Cryst. Growth* **1997**, 182, 442.
- [18] Durbin, S. D.; Carlson, W. E.; Saros, M. T. *J. Phys. D-Appl. Phys.* **1993**, 26, B128.
- [19] Land, T. A.; Malkin, A. J.; Kuznetsov, Y. G.; McPherson, A.; De Yoreo, J. J. *Physical Review Letters* **1995**, 75, 2774.
- [20] Land, T. A.; De Yoreo, J. J.; Lee, J. D. *Surface Science* **1997**, 384, 136.
- [21] Malkin, A. J.; Kuznetsov, Y. G.; McPherson, A. *Surface Science* **1997**, 393, 95.
- [22] Yip, C. M.; Brader, M. L.; Defelippis, M. R.; Ward, M. D. *Biophysical Journal* **1998**, 74, 2199.
- [23] Luo, T.-J.; Palmore, G. T. R. *J. Phys. Org. Chem.* **2000**, 13, 870.
- [24] Teng, H. H.; Dove, P. M.; Orme, C. A.; De Yoreo, J. J. *Science* **1998**, 282, 724.

- [25] Luo, T.-J. M.; MacDonald, J. C.; Palmore, G. T. R. *Chem. Mater.* **2004**, 16, 4916.
- [26] Bennema, P. *J. Crystal Growth* **1969**, 5, 29.
- [27] Bennema, P. *J. Crystal Growth* **1967**, 1, 278.
- [28] Vekilov, P. G.; Kuznetsov, Y. G.; Chernov, A. A. *J. Crystal Growth* **1992**, 121, 643.
- [29] Vekilov, P. G.; Alexander, J. I.; Rosenberger, F. *Phys. Rev. E* **1996**, 54, 1.
- [30] MacDonald, J. C.; Dorrestein, P. C. *Trans. ACA* **1998**, 33, 121.
- [31] MacDonald, J. C.; Dorrestein, P. C.; Pilley, M. M.; Foote, M. M.; Lundburg, J. L.; Henning, R. W.; Schutlz, A. J.; Manson, J. L. *J. Am. Chem. Soc.* **2000**, 122, 11692.
- [32] Gratz, A. J.; Manne, S.; Hansma, P. K. *Science* **1991**, 251, 1343.

THE RELATIONSHIP BETWEEN URIC ACID CRYSTALS AND KIDNEY STONE DISEASE

Ryan E. Sours and Jennifer A. Swift
Georgetown Univ., 37th and O Streets NW, Washington, DC 20057, USA

1. ABSTRACT

Uric acid ($C_5H_4N_4O_3$) is one of the final products of protein metabolism in humans. Its concentration balance is maintained in the kidneys, but compromised kidney function can result in its crystallization, either in the renal tract where it can contribute to kidney stone formation and/or in the interstitial fluid of joints of those afflicted with gout. In low pH physiological environments, crystalline uric acid is most frequently found as either an anhydrous (UA) or dihydrate (UAD) phase. Developing a fundamental understanding of the crystal nucleation and growth mechanisms of these uric acid phases at the molecular-level may help to elucidate new strategies for the treatment or prevention of its precipitation *in vivo*. The history, macroscopic crystal growth, and characterization of UA and UAD crystals is described herein.

2. INTRODUCTION

Human kidneys have two basic functions – to excrete metabolic waste products and other foreign chemicals, and to regulate fluid volume, osmolarity, acidity and mineral composition in order to maintain normal concentrations in the extracellular fluid. Impaired kidney function can lead to the deposition of a number of different precipitates throughout the renal tract as well as contribute to kidney stone formation. When this occurs, the functioning of the kidneys is further compromised, and severe blockages may even lead to renal failure in some cases. Although the development of a kidney and/or urinary stone is very rarely fatal, severe pain is associated with the dislodging and passing of a renal stone. In the United States, it is estimated that 10-15% of the population will develop a kidney stone during their lifetime. [1,2] The costs associated with the evaluation and treatment of kidney stone disease were estimated at \$1.83 billion per year in 1993. [3] When adjusted for inflation, keeping all other factors constant, this equates to nearly \$2.4 billion dollars per year in 2004.

Kidney stones are aggregates of crystals held together by an organic matrix. They can consist of principally one crystalline component, or as mixture of two or more components present in significant quantities. Several different urinary components are capable of precipitating in the renal tract and serving as the building blocks of kidney stones. The chemical analysis of the principal stone constituent(s) is clinically valuable, since stones of different composition can sometimes indicate different medical conditions. The most common mineral species identified in renal deposits include calcium oxalates (whewellite, weddelite), calcium phosphates (hydroxyapatite, brushite, octacalcium phosphate, whitlockite) and magnesium phosphates (struvite, newberryite). The most common organic materials found in urinary stones are uric acid and cysteine. The composition of kidney stones shows a geographic dependence, with significant variation between countries around the world. This is most likely due to a combination of local genetics, diet, climate, and customs.

The focus of this manuscript is on the building blocks of uric acid kidney stones, the prevalence of which varies considerably among developed nations. Studies on kidney stone compositions have found different frequencies for uric acid stone occurrence internationally: 4% in Sweden [4], 5.3% in Belgium [5], 5.6% in Australia [6], 6.6% in Great Britain [7], 8.6-16.5% in the United States [8,9], 23.3% in France [10], 17-25% in Germany [11,12], and 39.5% in Israel [13]. Two large-scale studies describing the statistical analysis of over 10,000+ stones from the United States revealed a significant increase in the incidence of uric acid stones over a period of two decades. A 1962 study by Herring [8] reported an 8.6% occurrence for uric acid stones, while a 1989 study by Mandel and Mandel [9] cited a 16.5% occurrence. The exact reasons for the large discrepancy in the two US studies are not certain, as the composition of kidney stones is determined by a variety of factors. Some of the factors that increase the likelihood of uric acid stone

formation include richer diets (and hence the need to process more wastes), increased cell turnover rates (e.g. during chemotherapy) [14], chronic dehydration, and/or other metabolic uric acid regulation problems.

Of the known risk factors, diet and lifestyle have perhaps changed the most significantly in the last century. Uric acid is a waste product of protein metabolism in humans, and two studies have tested the relationship between dietary protein intake and uric acid excretion. [15,16] Fellström, et al. divided patients into two groups, which were fed low protein and high protein diets, respectively. After two weeks on each diet, the urine pH and uric acid concentration of each group were measured. The urine of subjects on the high protein diet was more acidic (by 0.9 pH units) and showed a 90% increase in uric acid concentration. The second study compared the diets of uric acid stone formers and non-stone formers. Coe, et al. found that those patients who had developed uric acid kidney stones consumed 66% more protein than those without stones. Therefore, both studies suggest that increased protein consumption increases the risk for uric acid stone formation. This relationship is especially significant given the current popularity of “low-carb” diets (e.g. Atkins [17], South Beach [18]), which are based on replacing most of the daily carbohydrate intake with protein. This suggests that the incidence rates of uric acid kidney stones may continue to increase in the future unless dietary trends are reversed.

3. STRUCTURE

Investigations into the molecular structure of uric acid date back as far as 1776, when Karl Wilhelm Scheele first isolated a substance from urinary calculi, which he originally named lithic acid. [19] Ten years later, he demonstrated that it was a normal constituent of human urine. George Pearson later renamed the compound uric acid in 1798. [20] The first correct molecular structure of uric acid was put forth by Ludwig Medicus in 1875, although even he lacked definitive evidence at the time. [21] Emil Fischer (Nobel, 1902) provided the first rational synthesis of uric acid twenty years later, proving that the Medicus structure was indeed correct (**Figure 1**). [22-24]

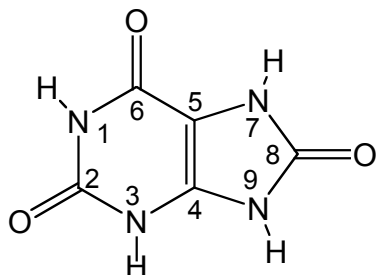


Figure 1. Molecular structure of uric acid with ring atoms numbered according to Fischer.

Under low pH conditions, uric acid is known to crystallize from aqueous solutions in either an anhydrous form (**UA**) or as a less stable dihydrate (**UAD**). Both **UA** and **UAD** phases are found in kidney stones, although the anhydrous form is more common. **UAD** is almost always found in association with the anhydrous phase, in part because the dihydrate phase can transform to the anhydrous phase in solution, presumably through a dissolution-recrystallization mechanism. In neutral or basic pH solutions, uric acid ($pK_a = 5.4$) exists predominantly as urate by deprotonation of the nitrogen at position 3. [25] Urate is significantly more soluble than uric acid, however, a number of different urate salts are also known to crystallize in physiologic environments. The two forms most frequently observed in pathological human deposits are monosodium urate monohydrate and ammonium acid urate. Monosodium urate monohydrate crystal precipitates in the interstitial fluid of joints are also the classic clinical symptom of gouty arthritis.

Although the optical properties of uric acid crystals were investigated at the end of the 19th century, [26-28] the first crystal structure of **UA**, solved by Hans Ringertz, did not appear until 1966. [29] **UA** crystals are monoclinic, with a space group of $P2_1/a$ and four molecules per unit cell. The unit cell dimensions are $a = 14.464(3)$, $b = 7.403(2)$, $c = 6.208(1)$ Å, and $\beta = 65.10(5)^\circ$. Uric acid packs in a layered motif, with

adjacent layers spaced 6.56 Å apart along a^* (see **Figure 2**). Each layer consists of parallel ribbons of uric acid molecules hydrogen-bonded head-to-head ($O_2 \cdots H-N_1$: 1.826 Å, 175.0°) and tail-to-tail ($O_8 \cdots H-N_7$: 1.734 Å, 155.8°), with the ribbon plane perpendicular to the $b-c$ plane. There is no hydrogen-bonding between ribbons within a layer, although ribbons in adjacent layers are hydrogen-bonded to one another and offset by ~ 62°.

The crystal structure of **UAD** continued to remain elusive for thirty more years. The primary obstacle in the structure determination of **UAD** was its ready dehydration in air, and the long data collection times required for small crystals on serial diffractometers. Initial diffraction studies of **UAD** were carried out by Artoli et al. [30] on natural crystal samples (bird droppings found on rock surfaces), which dehydrated less quickly but whose small size prohibited a full data collection. Using a crystal derived from human urinary sediments, the same group later reported the first full structure of **UAD** in 1997. [31] They assigned the crystal to the orthorhombic space group *Pnab*, and refined the structure with a 50:50 disorder of molecules about two positions, although a number of weak reflections violated systematic absences for the space group setting. Parkin and Hope revisited the structure determination of **UAD** a year later, this time using synthetic crystals. The structure was assigned to the monoclinic space group *P2₁/c* with $a = 7.237(3)$, $b = 6.363(4)$, $c = 17.449(11)$, and $\beta = 90.51(1)$ °, based on data collected at 120 K. [32] The monoclinic model was refined with both twinning and disorder, and showed no diffraction peak violations. Side by side analysis of the orthorhombic and monoclinic **UAD** structures shows them to be more or less identical, though the latter is arguably more crystallographically correct. Comparison of the **UAD** and **UA** structures shows their ribbon and layer motifs to be quite similar. The distance and registry between adjacent layers in **UAD** and **UA** are necessarily different, owing to the addition of a 2-dimensional hydrogen-bonded water layer in **UAD**. The interlayer distance in **UAD** is 8.73 Å.

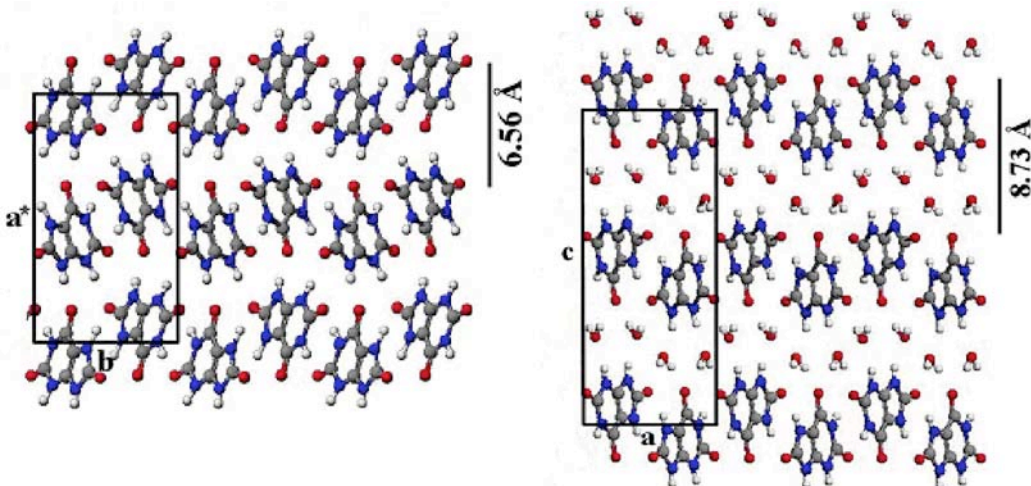


Figure 2. Crystal Structures of uric acid (left) and uric acid dihydrate (right) based on fractional coordinates provided in references [29] and [32], respectively.

4. CRYSTAL GROWTHS AND CHARACTERIZATION

While both **UA** and **UAD** phases grow in biological environments at physiologic temperature, **UA** and **UAD** phases can be grown selectively in a laboratory environment according to the following procedure. Supersaturated uric acid solutions were prepared by dissolving 15-20 mg of uric acid (Aldrich, 99+%) in 100 mL of boiling deionized water. Water was purified by passage through two Barnstead deionizing cartridges followed by distillation. Pure synthetic single crystals (200-300 μm in the largest dimension) of uric acid dihydrate (**UAD**) and uric acid (**UA**) were grown upon standing at ambient (24 ± 1 °C) and physiologic (37 ± 0.1 °C) temperatures, respectively. While pH can be an important factor in uric acid crystal growth, solutions prepared under the specified conditions were of pH = 4-5 and no further pH adjustment was made. Crystals of **UA** deposit as clear, colorless rectangular plates with large (100) faces bounded by (210), (201), (001), and sometimes (121). **UAD** also crystallizes as clear colorless

rectangular plates with large (001) faces bounded by (011) and (102) and infrequently (210) faces. Optical micrographs of **UA** and **UAD** crystals with their Miller indexes labeled are provided in **Figure 3**. In related crystal growth studies, we have also observed that the presence of known quantities of some synthetic dyes in the uric acid growth solutions can lead to alternative **UA** and **UAD** crystal habits. Details on the selective recognition of synthetic dye probes and habit modification of **UA** and **UAD** are elaborated in references 33–35.

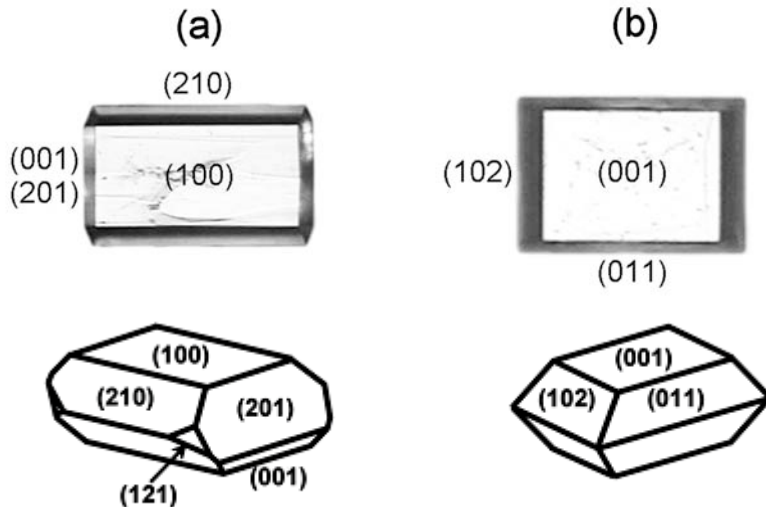


Figure 3. (a) Anhydrous uric acid (**UA**) and (b) uric acid dihydrate (**UAD**) crystals grown from aqueous solutions. Crystals are typically ~200–300 μm in their largest dimension.

Though both **UA** and **UAD** have similar structural features and general plate-like morphologies, differentiating between the two forms is relatively straightforward. The most obvious method for unambiguously determining the crystal form (besides X-ray diffraction) is infrared spectroscopy. The FTIR-ATR spectra of **UAD** exhibits a strong water absorption band at $\sim 3440 \text{ cm}^{-1}$ which is absent in **UA**. The main drawback of using this technique for routine characterization is that the crystals are frequently destroyed in the ATR press. An alternative and non-destructive method uses conoscopic light interference patterns. [36] Anhydrous uric acid crystals are biaxial positive, while dihydrate crystals are biaxial negative. [28] For monoclinic crystals, the refractive indexes do not all necessarily lie along crystallographic directions. This is true for **UA**, in which n_α (1.588) lies along b , while n_β (1.739) and n_γ (1.898) are offset by 45.6° from a^* and c . The refractive indices for **UAD** are more straightforward, as n_α (1.508) lies along a , n_β (1.691) along c , and n_γ (1.728) along b . [28,37] Therefore, the optic plane for **UA** is tilted 45.6° from the large (100) plate face, whereas the optic plane for **UAD** is perpendicular to the large (001) plate face.

Conoscopic interference patterns were obtained using an Olympus BX-50 polarizing microscope and a 505 nm interference filter (**Figure 4**). The optic plane is perpendicular to (001) for **UAD**, although the melatopes (the points of emergence of the optic axes) are spaced too far apart to be observed by our objective lens (N.A. = 0.80, $2V_o = 140^\circ$). The optic plane in **UA** is inclined relative to (100), as indicated by the asymmetry of the interference pattern. The inclination combined with the large angle between the optic axes also made it impossible for us to observe the melatopes for **UA** ($2V_a = 84^\circ$). In any case, the difference between **UA** and **UAD** patterns is unmistakable (**Figure 4**), and this method proved to be the easiest for rapidly distinguishing the two phases.

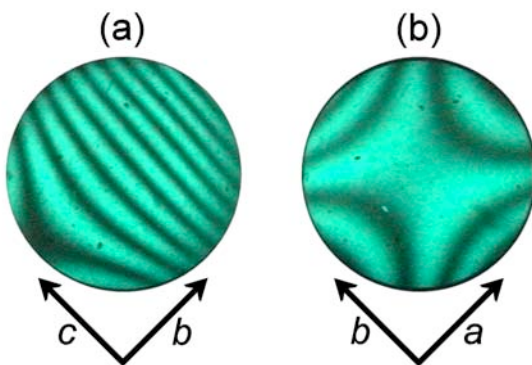


Figure 4. Conoscopic interference patterns obtained on the large plate faces of (a) **UA** and (b) **UAD** with crystallographic directions indicated.

5. EPITAXIAL GROWTH

The common coexistence of these uric acid phases and their frequent association with assorted mineral species in kidney stone deposits led Lonsdale [38] in 1968 to suggest that epitaxial relationships between biological crystalline phases may be an important factor contributing to their pathological formation. Epitaxy is defined as the growth of one crystal on the substrate of another, such that there is at least one preferred orientation and a near geometrical fit between the contacting surface lattices. When seed crystals with geometrically matched surface lattices are present in solution, the barrier to nucleation can be significantly reduced, such that crystallization occurs in environments that have otherwise not met critical supersaturation conditions. A seed crystal of the same material is usually regarded as the best-matched epitaxial surface, though surfaces of two different crystalline materials may also be related by epitaxy if their 2D surface lattice spacings are similar. A geometric lattice-matching protocol, EpiCalc [39], was used as a screening tool to identify all possible epitaxial interfaces between surfaces of **UA** and **UAD**. [40] The program rotates an overlayer (with lattice parameters b_1 , b_2 , and β) with respect to a substrate (with lattice parameters a_1 , a_2 , and α), through a series of azimuthal angles (θ). Because overlayer structures are particularly sensitive to competition between energy lowering interfacial interactions and energetic penalties associated with even minor reconstruction, geometric calculations allowed for the overlayer lattice parameters to be systematically varied by up to $\pm 5.0\%$ of the unit cell dimensions. This screening method is mechanistically different from previous epitaxy searches, which typically examine the percentage of misfit (up to 15%) of various interfacial lattice alignments. [38,41]

When all possible pairs of the various natural faces of **UA** and **UAD** were subjected to EpiCalc screening, ten epitaxial relationships were identified. The best match between the plate faces of the two materials, **UAD** (001) / **UA** (100) ($\theta = 0^\circ$), can be considered a near perfect commensurate relationship. The nine other matches identified were related by coincident epitaxy. Coincident matches include **UAD** (001) / **UA** (201) ($\theta = 0^\circ$), **UAD** (001) / **UA** (210) ($\theta = 0^\circ$), **UAD** (001) / **UA** (121) ($\theta = 0^\circ, 55^\circ$), **UAD** (001) / **UA** (001) ($\theta = 27^\circ$), **UAD** (011) / **UA** (201) ($\theta = 1^\circ$), **UAD** (011) / **UA** (210) ($\theta = 0^\circ$), **UAD** (102) / **UA** (201) ($\theta = 25^\circ$), **UAD** (102) / **UA** (210) ($\theta = 4^\circ$). In our laboratory and also in others [42], the epitaxial growth of **UA** (100) on **UAD** (100) has been frequently observed (**Figure 5**) at the commensurate angle predicted by lattice-matching calculations. Crystals of **UAD** can also be grown on **UA** substrates with the same interfacial orientation. During the epitaxial growth of **UA** on **UAD**, which can occur over a period of days to weeks, the **UAD** substrate slowly becomes pitted or opaque. However, the exact molecular-level mechanism of this epitaxial growth process is not well understood at this time and requires further elucidation.

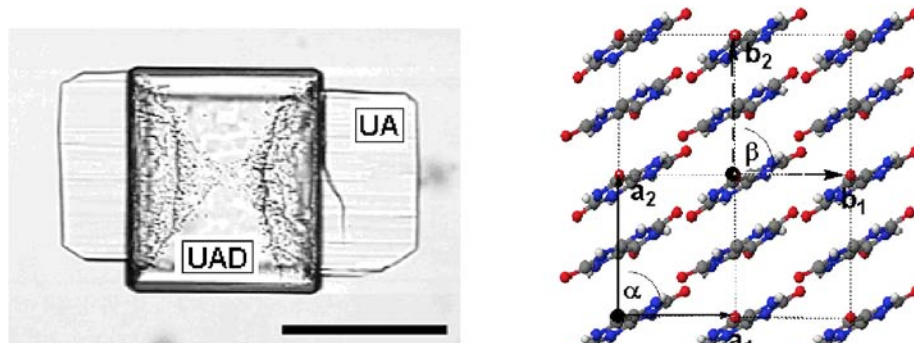


Figure 5. (left) Photomicrograph showing the epitaxial growth of UA (100) on a UAD (001) substrate. Scale bar = 100 μm . (right) Epitaxial relationship between the same UAD substrate (a_1 , a_2 , α) and UA overlayer (b_1 , b_2 , β).

The same EpiCalc screening procedure was applied to uric acid surfaces and the natural surfaces of minerals found in kidney stones. [40] Several potential coincident and commensurate epitaxial matches were also identified for these different uric acid / mineral interfaces. Ongoing experimental studies seek to establish epitaxy between these phases as a potential factor in pathological stone formation.

6. ACKNOWLEDGEMENTS

The authors gratefully acknowledge the financial support of Georgetown University, the Henry Luce Foundation, the Henry Dreyfus Foundation, and the ARCS Foundation.

7. REFERENCES

- [1] Johnson, C.M., D.M. Wilson, W.M. O'Fallon, et. al., *Kidney Int.* **16** (1979) 624.
- [2] Sierakowski, R., B. Finlayson, R.R. Landes, et. al., *Invest. Urol.* **15** (1978) 438.
- [3] Clark, J.Y., I.M. Thomson, and S.A. Optenberg, *J. Urol.* **154** (1995) 2020.
- [4] Grenabo, L., H. Hedelin, and S. Pettersson, *Scand. J. Urol.* **19** (1985) 285.
- [5] Fuss, M., J. Simon, D. Verbeelen, et. al., *Eur. Urol.* **4** (1978) 90.
- [6] Wardlaw, H.S.H., *Med. J. Australia* **1** (1952) 180.
- [7] Sutor, D.J., S.E. Wooley, and J.J. Illingworth, *Br. J. Urol.* **46** (1974) 275.
- [8] Herring, L., *J. Urol.* **88** (1962) 545.
- [9] Mandel, N.S. and G.S. Mandel, *J. Urol.* **142** (1989) 1516.
- [10] Cottet, J. and A. Weber, *Pathol. Biol.* **7** (1959) 1975.
- [11] Scholz, D., P.O. Schwille, D. Ulrich, et. al., *Urol. Res.* **7** (1979) 161.
- [12] Hesse, A., H.-J. Schneider, W. Berg, et. al., *Invest. Urol.* **12** (1975) 405.
- [13] Atsmon, A., A. de Vries, and M. Frank, *Uric Acid Lithiasis*, (Elsevier, Amsterdam, 1963)
- [14] Rieselbach, R.E. and M.B. Garnick, *Cancer and the Kidney*, (Lea & Febiger, Philadelphia, 1982)
- [15] Fellström, B., B.G. Danielson, B. Karlstrom, et. al., *Clin. Sci.* **64** (1983) 399.
- [16] Coe, F.L., E. Moran, and A.G. Kavalich, *J. Chronic Dis.* **29** (1976) 793.
- [17] Atkins, R.C., *Dr. Atkins' New Diet Revolution; 3rd ed*, (M. Evans and Co., New York, 2002)
- [18] Agatston, A., *The South Beach Diet: The Delicious, Doctor-Designed, Foolproof Plan for Fast and Healthy Weight Loss*, (Rodale, New York, 2003)
- [19] Scheele, K.W., *Opuscula* **2** (1776) 73.
- [20] Pearson, G., *Philos. Trans. R. Soc. London* **88** (1798) 15.

- [21] Medicus, L., *Justus Liebigs Ann. Chem.* **175** (1875) 230.
- [22] Fischer, E. and L. Ach, *Ber. Dtsch. Chem. Ges.* **28** (1895) 2473.
- [23] Fischer, E., *Ber. Dtsch. Chem. Ges.* **30** (1897) 549.
- [24] Fischer, E., *Ber. Dtsch. Chem. Ges.* **32** (1899) 435.
- [25] Mandel, N.S. and G.S. Mandel, *J. Am. Chem. Soc.* **98** (1976) 2319.
- [26] Brun, A., *Arch. Sci. Phys. Nat.* **7** (1899) 284.
- [27] Winchell, A.N., *The Optical Properties of Organic Compounds. 2nd ed.*, (Academic Press, New York, 1954)
- [28] Ringertz, H., *Acta. Cryst.* **19** (1965) 286.
- [29] Ringertz, H., *Acta. Cryst.* **20** (1966) 397.
- [30] Artoli, G., E. Galli, and M. Ferrari, *Riv. Mineral. Ital.* **2** (1993) 91.
- [31] Artioli, G., N. Masciocchi, and E. Galli, *Acta. Cryst.* **B53** (1997) 498.
- [32] Parkin, S. and H. Hope, *Acta. Cryst.* **B54** (1998) 339.
- [33] Sours, R.E., D.A. Fink, and J.A. Swift, *J. Am. Chem. Soc.* **124** (2002) 8630.
- [34] Fink, D.A., R.E. Sours, and J.A. Swift, *Chem. Mater.* **15** (2003) 2718.
- [35] Sours, R.E., D.A. Fink, K.A. Cox, and J.A. Swift, *Mol. Cryst. Liq. Cryst.* **440** (2005) 187.
- [36] Wood, E.A., *Crystals and Light, 2nd ed.*, (Dover, New York, 1977)
- [37] Shirley, R., *Science* **152** (1966) 1512.
- [38] Lonsdale, K., *Nature* **217** (1968) 56.
- [39] Hillier, A. and M.D. Ward, *Phys. Rev. B* **54** (1996) 14037.
- [40] Frincu, M.C., C.E. Fogarty, and J.A. Swift, *Langmuir*, **20** (2004) 6524.
- [41] Mandel, N.S. and G.S. Mandel, in: *Urolithiasis: Clinical and Basic Research*, eds. L.H. Smith, W.G. Robertson, and B. Finlayson (Plenum Press, New York, 1981), p. 469.
- [42] Boistelle, R. and C. Rinaudo, *J. Cryst. Growth* **53** (1981) 1.

DESIGNING MOLECULAR INTERFACES

Colin C. Seaton and Nicholas Blagden
*Drug Delivery Group, Inst of Pharmaceutical Innovation
School of Pharmacy, Univ. of Bradford, Bradford BD7 1DP, UK*

1. ABSTRACT

A key aim of crystal engineering is the design and synthesis of new materials with defined functionality through the control of intermolecular interactions. The formation of composite materials, created from two separate crystalline components bound through some epitaxial interface, are of interest since the properties can be controlled through selection of components. To gain an understanding of the intermolecular interactions occurring across the boundary, the differential evolution (DE) algorithm was applied to problem of optimising the position and orientation of two crystal blocks together. An investigation in the effect of the limited number of control parameters highlights the fact that a small range of values is required for optimal performance of the method. A test system of benzoic acid and benzamide was investigated and the computational results indicate the formation of hydrogen bonding between the {100} face of benzoic acid with the {010} face of benzamide.

2. INTRODUCTION

Composite materials play an increasingly important part in contemporary life with their properties inevitably being determined by their component materials and inherent interfacial characteristics. For example: concrete, polymers, paper and paint all depend on the integrity of solid/solid interfaces for their mechanical strength, while anti-corrosive treatments and adhesives depend on their integrity with a substrate for successful application [1,2]. Recently there has been increased emphasis on the development of sophisticated products and processes in which the design of multi-component systems is essential. Examples include; herbicides, fungicides and pharmaceutical drug delivery systems [3,4], all of which rely on multi-components to give optimum efficacy and controlled release. However, manipulation of epitaxy without mechanical processing of the host substrate remains an unresolved challenge.

Developments in the field of crystal engineering have highlighted the role that molecular recognition plays in the process of crystal growth [5,6] and imply the possibility of engineering epitaxial relationships between materials through purely molecular means. The understanding of molecular processes and structural nature of interactions at the interface has been boosted by the application of the vast accumulation of structural data that exists for molecular materials. These studies have been directed to a molecular level understanding of such processes as nucleation [7], growth of twinned crystals [8], polymorphism in crystals [9], formation of solid solutions [10,11], and the nature of the inorganic-organic interface in biominerals [12]. This understanding has lead to a tremendous progress in the ability to manipulate crystal properties such as morphology, structure and extent of crystal aggregation and the orientation of nuclei [13].

2.1 Interfaces And Epitaxy

At the interface between two materials both the composition and the arrangement of molecules or ions change from that corresponding to one pure phase to that of a second. When the structural registry (geometric and stereochemical) between the two phases lies within a narrow limit, the materials are said to display an epitaxial relationship to each other. In this configuration of the interface, stress is minimised and intermolecular/interionic attractive interactions are maximised, leading to optimum stability, strength and chemical integrity across the interface. Historically epitaxy was widely reported as occurring in mineral samples [14], for example rutile on hematite, marcasite on pyrite and staurite on kainite [15,16]. The role of lattice match between the host substrate and the guest overlayer as a contributing factor to epitaxy was experimental verified by the study of a series of inorganic systems [17] and relating the occurrence of epitaxy to the degree of lattice mismatch. These system included silver and gold deposition on calcite, mica and sodium chloride [18], urea on ammonia chloride [17]. Further studies have identified that the interfacial mixing relies not only on a lattice match at the interface [19] but also on the lattice relaxation away from the surfaces, which governs the azimuthal alignment achieved [20-22].

Currently the study of epitaxy relies on macroscopic analysis of the phenomena [23] with nucleation described in terms of heterogeneous nucleation [24] modified by terms that account for a contribution from surface wetting [25] and the free energy of the guest host interaction [26-28]. Generally a mechanically cleaved surface is used to support the epitaxy and molecular organisation, for example in selection of polymorphs by molecular solids [29,30] and investigations into the role that the molecular topography and chemical functionality of the substrate plays in the deposition of molecular solids [31].

As noted above, historically epitaxy has been investigated with respect to inorganic systems and little work has focused on the epitaxial growth of organic molecular materials onto an organic molecular substrate or the understanding of the intermolecular interactions within these interfaces. Much of this work focuses on the problem of twinning, the situation where two or more individual single crystals are joined in a single particle such that the components are related by a symmetry element that does not exist in the single crystal [32], which can be considered as the epitaxy of one material with itself. Though an understanding of the symmetry relationships between the component parts of the twinned crystal can generally be obtained, exact understanding of the molecular relationship and intermolecular interactions between the components is often harder to obtain. In the case of saccharin [32], the application of energy calculations to a series of molecular juxtapositions about the known twin plane allowed the determination of a feasible molecular configuration.

Another area of interest is the selective growth of polymorphs upon a molecular solid [29,30]. Here a mechanically cleaved surface of a selected compound acts as a nucleating point for a secondary material, if this secondary material is polymorphic then the polymorph with the more favourable lattice match will grow. This work shows that the crystalline and intermolecular relationships between the substrate and overlayer must be fully understood if a substrate is to be designed to selectively grow a chosen polymorph.

To fully develop a method of molecular based epitaxy, a full understanding of both the lattice matching and potential molecular recognition of the substrate and the overlayer must be achieved. Computational modelling of the structural registry is required to give an insight into the interactions occurring between the interfacing components.

3. MODELLING THE INTERFACE

As a first step to model the creation of an interface between two organic crystal systems on an atomic scale, it was assumed that the known crystal structure sufficiently represented the system and that there was no molecular relaxation and negligible strain at the molecular interface. Therefore the substrate and overlayer crystal blocks are generated from the known crystal structures by combining a fixed number of unit cells in each direction.

For any face $\{hkl\}$ of the substrate system, a vector system may be defined such that the mutually perpendicular unit vectors \mathbf{u} , \mathbf{v} , lie in the plane of the substrate face and a unit vector, \mathbf{w} , is perpendicular to the face. The position of the overlayer crystal block may then be defined by reference to this coordinate system (u , v , w). The orientation of the overlayer crystal block is defined by three angles (θ, ϕ, γ) , which allows the positioning of any crystal face onto the interface and reduces the number of assumptions about the nature of the interface (**Figure 1**). Once the overlayer is positioned and rotated, the energy between the components may then be calculated by use of a force field. Since the interactions between molecules in the same crystal block are independent of the position of the two components, they will be constant for all potential crystal packings. Thus, for computational efficiency, only those interactions between separate crystal blocks are considered in the calculation of the system energy.

Thus, the system is modelled by nine problem parameters (h , k , l , u , v , w , θ , ϕ , γ) and for a given set of parameters the energy is calculated. The location of the global minima for the nine dimensional hypersurface should correspond with the feasible interactions across the interface, which may be located by use of a global optimisation algorithm. This optimisation problem may also be simplified by noting that the number of potential faces for growth will be very limited and so running a separate search for face pairs based on crystal criteria will be more efficient than searching over a large number of unfeasible faces, thus reducing the dimensionality of the optimisation problem. The potential faces for growth may be selected initially through consideration of experimental details (crystal morphology, habit modification studies) or by computation of the crystal morphology by habit prediction methods.

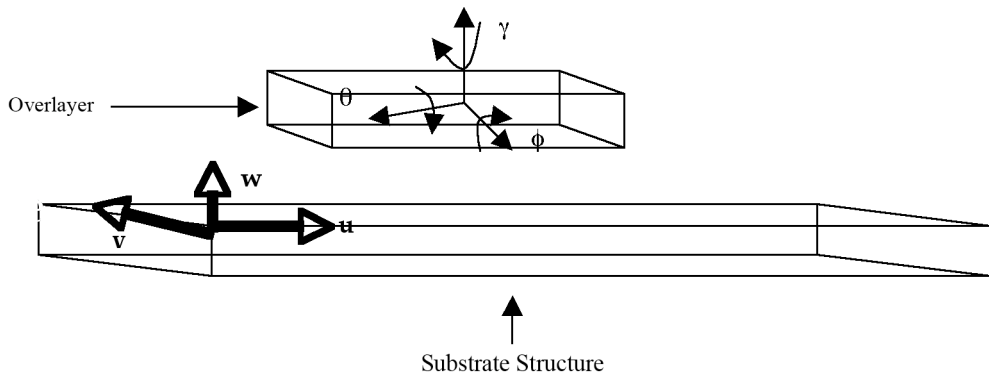


Figure 1. Representation of the formation of an interface between a substrate and an overlayer. The problem parameters ($\mathbf{u}, \mathbf{v}, \mathbf{w}, \theta, \phi, \gamma$) are shown.

A number of global optimisation algorithms have been developed to solve a range of problems such as evolutionary algorithms, simulated annealing, tabu search and particle swarm [33-37]. Since the size of the optimisation problem prohibits the use of a systematic grid search of the hypersurface, the differential evolution algorithm was selected as the searching method for this work.

4. DIFFERENTIAL EVOLUTION

Differential Evolution (DE) is a recently developed evolutionary algorithm for the optimisation of real-valued problems. It was developed initially to solve the Chebychev polynomial fitting problem [38], though it has since been adapted to a broader range of optimisation problems; including digital filter design [39], modelling of disordered materials [40] and structure solution from powder X-ray diffraction data [41,42].

As with other evolutionary algorithms, DE operates on a population of trial solutions with new solutions being created through recombination and mutation. Each trial structure represents a potential solution to the problem to be solved and is represented as a vector of real numbers. Unlike traditional genetic algorithms the recombination and mutation steps are combined into a single step in the DE methodology. Initial implementations utilised a *uniform crossover* with fixed mutation (a) [38] however, due to problems with correlations between the control parameters [43], a modification based on *arithmetic crossover* was introduced (b). This arithmetic crossover form was utilised throughout the work reported here.

(a) Uniform Crossover

$$\begin{aligned} k &= \text{int}(\text{random}(0,1)*D) \\ t_{i,k} &= \begin{cases} P_{r_3,k} + F(P_{r_2,k} - P_{r_1,k}) & \text{if } \text{random}(0,1) < C_R \text{ or } j = k \\ P_{i,j} & \text{otherwise} \end{cases} \\ k &= (k+1) \bmod D \end{aligned}$$

(b) Arithmetic Crossover

$$t_{i,j} = P_{i,j} + K(P_{r_3,j} - P_{i,j}) + F(P_{r_2,j} - P_{r_1,j})$$

where N = population size,

D = Number of parameters to solve,

C_R = crossover probability

$t_i = i^{\text{th}}$ trial structure to be generated

$r_1 \neq r_2 \neq r_3 \neq \text{random}(0,1)*N \neq i$

$P_i = i^{\text{th}}$ member of DE population.

$i = 1 \dots N, j = 1 \dots D$

The DE operation is applied to each member of the DE population to create a new trial solution, which replaces the

parent in the population if it is a better solution than its parent. This process is repeated until a fixed number of generations have been processed or until the population converges upon a single solution. The DE algorithm is summarised below.

```

Create a random initial population of size  $N$ 
Evaluate initial population
Until  $G_{max}$  generations or convergence
For each member of population ( $P_i$ )
    Generate a trial structure ( $\underline{T}_i$ )
    Check boundary conditions - adjust if necessary
    Evaluate trial solution (trial  $E$ )
    If trial  $E \leq$  parent  $E$ 
        Replace  $P_i$  by  $\underline{T}_i$ 

```

With a simplified method of creating trial structures and the use of a deterministic selection for the new population ensures that the DE method is simpler to implement than many traditional genetic algorithms, where a number of recombination and mutation steps are performed on randomly selected members of the population before the new population is probabilistically selected [44,45]. This simplification also results in fewer user-defined control parameters (population size N , maximum number of generations G_{max} , K and F) compared to other evolutionary algorithms and so greater understanding of the role each control parameter plays in controlling the dynamics of the search may be achieved. To this end a systematic study on these control parameters was performed.

An initial test system of benzamide as a substrate and benzoic acid as the overlayer was selected; since the crystal structures are very similar for both systems (**Figure 2** and Table 1). The similarities of the crystal structures is the basis for habit modification of benzamide by benzoic acid [46], which is a result of the benzoic acid blocking growth along the [010] axis of the benzamide. Consequently this face was selected as the initial face for these computational studies. A block of 3x3x1 unit cells of benzamide was generated as the substrate, while a single unit cell of benzoic acid was used as the overlayer. The force field detailed in No *et al* [47] was used to calculate the lattice energy of the generated structures with the partial charges calculated in Gaussian [48] at the HF3-21G level and a cut off value of 15Å.

Table 1
Unit cell parameters for benzoic acid and benzamide

| Compound | a/Å | b/Å | c/Å | $\beta/^\circ$ | Volume/Å ³ | Space Group |
|--------------|--------|--------|--------|----------------|-----------------------|--------------------|
| Benzoic Acid | 5.4996 | 5.1283 | 21.95 | 97.37 | 613.95 | P2 ₁ /c |
| Benzamide | 5.5657 | 5.0353 | 21.698 | 90.39 | 608.07 | P2 ₁ /c |

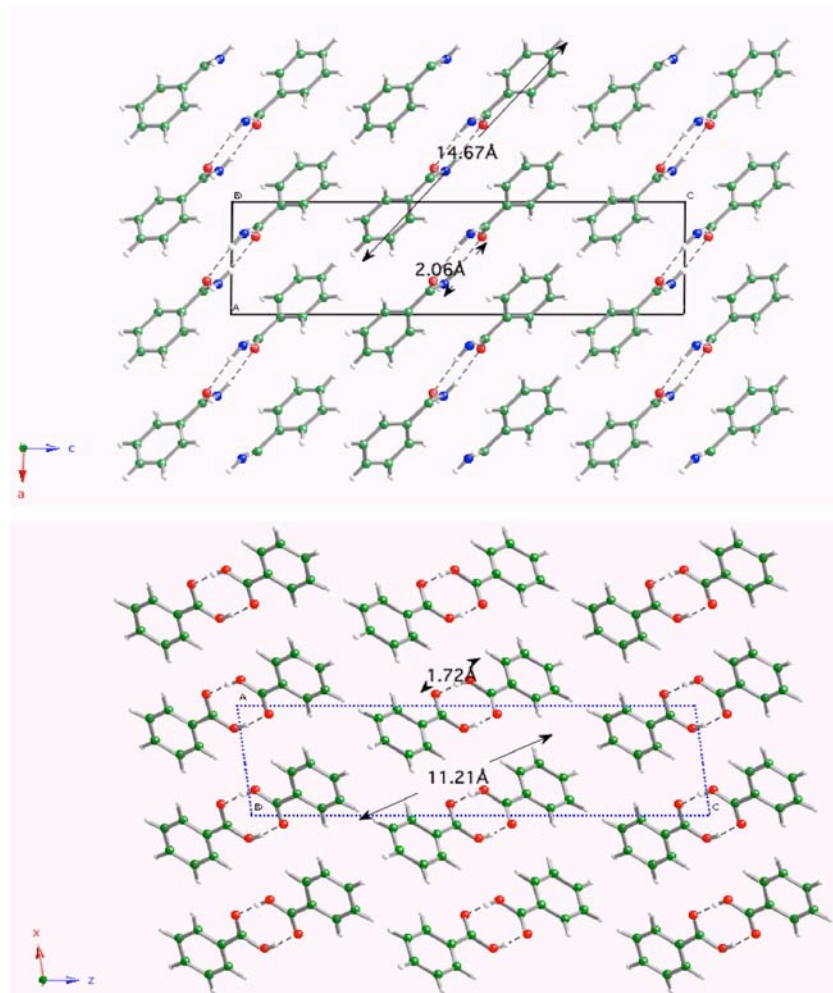


Figure 2. Crystal Packing for (a) benzamide (b) benzoic acid. Both systems are viewed along the b-axis and the lengths of the dimer unit and O...H hydrogen bond are indicated. C atoms are shown as green, N as blue, O as red and H as light grey.

The DE parameters K , F were varied from 0.1 to 1.0 in steps of 0.1 for population sizes $N = 30, 60$. Each of the DE calculations were performed for a maximum of 500 generations or until the difference between the mean energy and the best solution energy was less than 1×10^{-5} kcal mol⁻¹ and convergence was assumed to have occurred. Ten individual DE calculations were performed for each set of parameters. The boundaries for each variable were [0, 360°] for θ, ϕ, γ , [7, -7 Å] for u, v and [0, 360 Å] for w . Generated values that exceeded a boundary were replaced by the median point between the parent and the exceeded boundary.

The mean energy located for each parameter set is shown in **Figure 3** for both population sizes. Similar features are shown in the surface for both experiments; a broad minima in the region bounded by 0.6, 1.0 for K and 0.5, 0.8 for F , a large maxima for high values of K with low values of F , while the rest of the surface is generally flat. A local maximum is also evident in the region bounded by 0.5 to 0.8 for K and 0.8 to 0.9 for F , which is greatly reduced by increasing the population size. Subsequent increases of the population size also leads to an increase in the size of the minima and reduction in the range of energies located.

Consequently, an effective search by the DE algorithm relies on balancing the convergence from the deterministic selection and the recombination with exploration by mutation through selection of K and F . These results show, for this problem, that small values of F with large values of K cannot balance the inward selection pressure and the population converges quickly into local minima, which is supported by consideration of the number of generations required for each DE calculation (**Figure 4**). The majority of calculations ran until the maximum limit was reached

though a minima closely related to the maxima in the solution plot can clearly be seen. The lack of convergence is either due to very slow convergence or stagnation in the DE population. Stagnation is when the DE population, despite having diversity within the population, is unable to create any new trial structures that are superior to the old population. Small values of both K and F generally result in slow convergence, shown by the evolutionary progress plot (EPP) for K and F equal to 0.1 (**Figure 5a**). In this case the DE performs as a population of random searches in the neighbourhood of each member of the initial population. The convergence properties for large values of K appear to form a similar pattern (**Figures 5b** and **5c**) with the value of F controlling the rate of convergence and so small values of F results in premature convergence while the large F values generally locate the global minima. The final case of median values for both K and F appear to result in stagnation (**Figure 5d**), though often the population has predominately converged upon a solution and only a small percentage remain unique.

The process of stagnation, slow convergence and premature convergence all inhibit the ability of the DE calculation to perform successfully and so a further investigation into the dynamics of the DE population was undertaken, as this may help to optimise the selection of control parameters to the problem. To ensure effective searching, diversity must be maintained within the DE population during the search. To quantify this concept the population entropy as defined by Bessaou and Siarry [49] was evaluated for each population during each DE calculation. This measure is also an indicator of population stagnation, as these cases would exhibit a large stationary value for the population entropy, while the best and mean energies would remain constant.

The entropy (S_j^g) for the j^{th} parameter in generation g is defined by equation 1.

$$S_j^g = \sum_{i=1}^N \sum_{k=i+1}^N -P_{i,k} \log(P_{i,k}) \quad (1)$$

$$P_{ik} = 1 - \frac{|x_{i,j}^g - x_{k,j}^g|}{H_{i,j} - L_{o,j}}$$

Where $H_{i,j}$ = upper bound on the j^{th} parameter
 $L_{o,j}$ = lower bound on the j^{th} parameter.
 $x_{i,j}$ = value of the j^{th} parameter of the i^{th} member of the population.

Thus, entropy is defined to be large when the values for the parameter differ widely and tends to zero as the values converge upon a single value. The mean entropy for the population can be determined by averaging over the entropies for each parameter. The entropies for four selected systems are included in the evolutionary progress plots given in **Figure 5**. Note that the entropy, unlike the best and mean energy, can increase during a DE calculation, indicating that the diversity of the population is increasing. Consideration of the entropy change during the DE calculation can therefore be used as an indicator of the variation of diversity within the population and so the rate of convergence, therefore it could be used to control the selection of K and F during the DE calculation, thus optimising the DE performance.

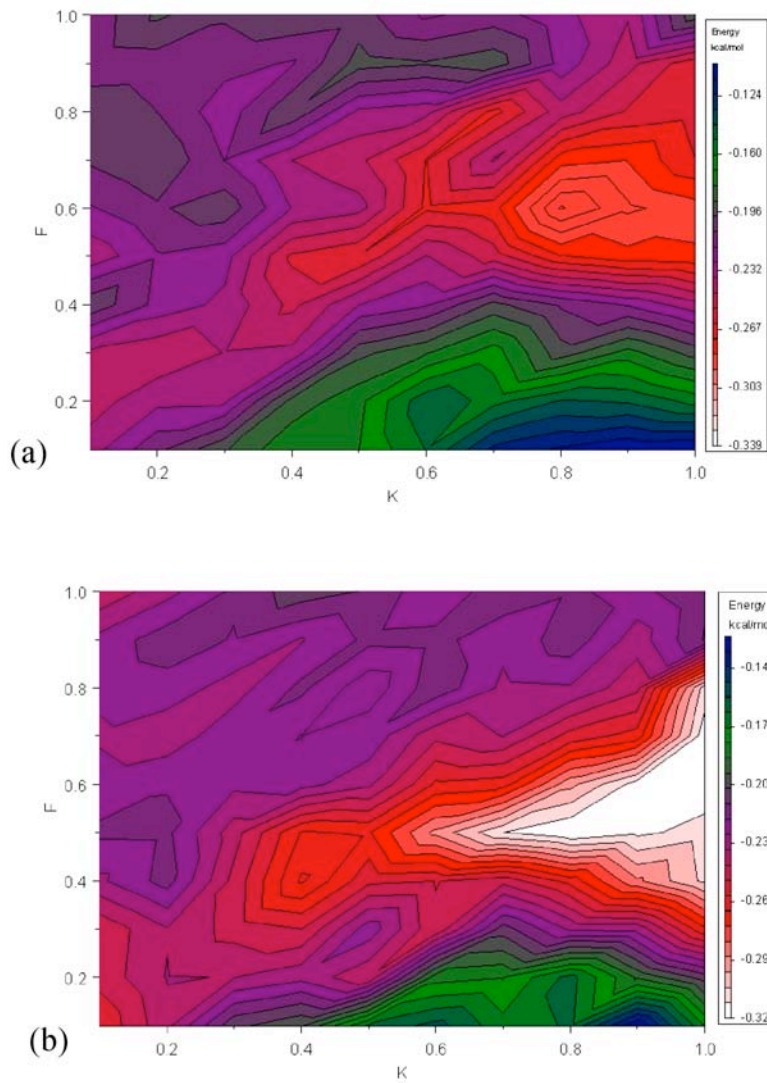


Figure 3. Contour Plots of the mean energy located by a given set of K , F over 10 DE calculations. (a) Calculation with $N = 30$ (b) Calculation with $N = 60$.

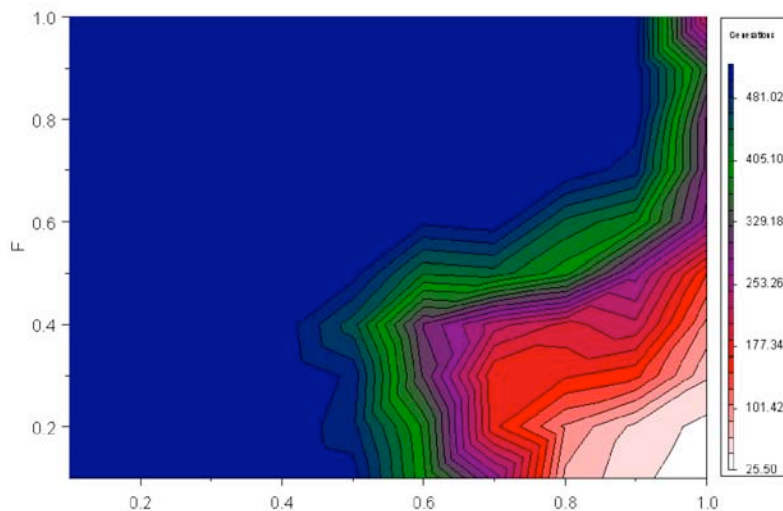


Figure 4. The mean number of generations performed for each set of K and F for population size 30.

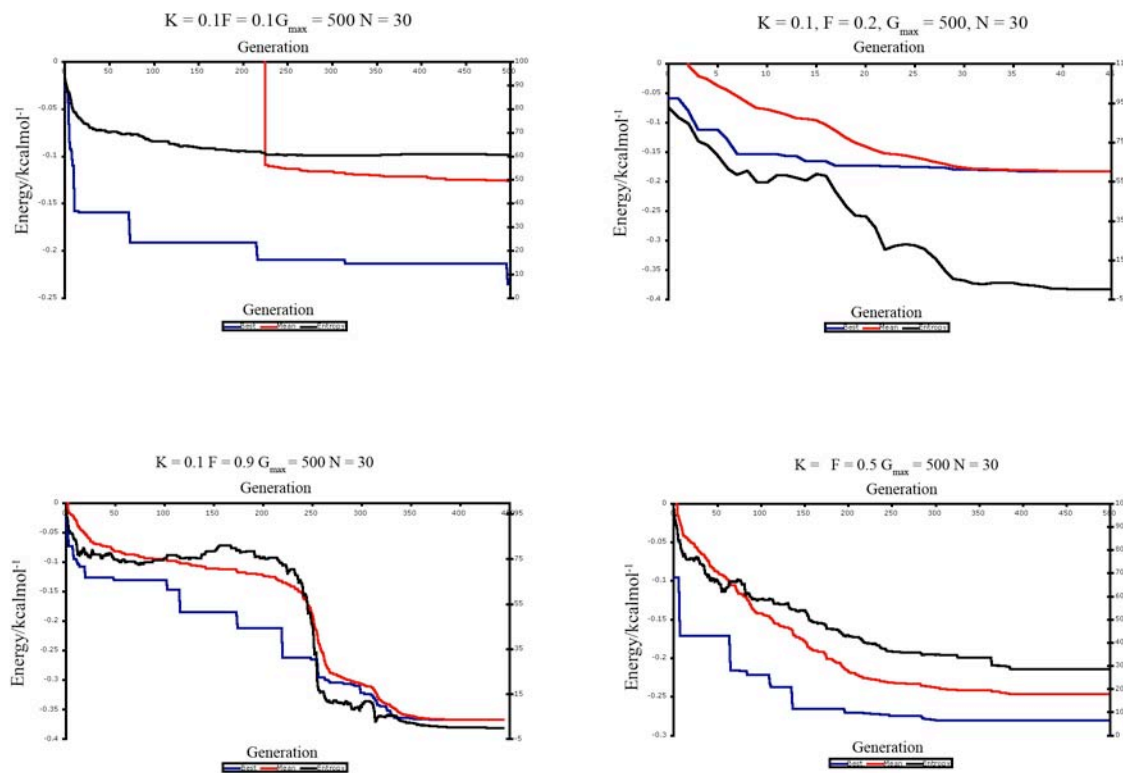


Figure 5. Evolutionary progress plots for four randomly selected DE calculations. In all cases $G_{\max} = 500$ and $N = 30$. For (a) $K = 0.1$, $F = 0.1$ (b) $K = 1.0$, $F = 0.2$, (c) $K = 1.0$, $F = 0.9$, (d) $K = 0.5$, $F = 0.5$. The blue line is the energy of the lowest structure in the population, the red line the mean energy of population and the black line the entropy of the population.

Another problem with identifying stagnation is that the selection of population members for mutation and recombination are randomly selected and so a favourable selection may not have been made in the time the DE was run. To ensure that the DE calculations were allowed sufficient time to search, an investigation in the effect of increasing the value of G_{\max} to 5000 was undertaken with the parameters: K equal to 1.0, F varied from 0.1 to 1.0 and N set to 30, 60 and 90. Ten DE calculations for each parameter set were performed and the mean number of generations required to converge calculated (**Figure 6**). This shows that longer convergence times are achieved with both larger populations and larger values of F , except in the case of $K = F$ where convergence is enhanced. This can be explained by consideration of the DE method of generating trial structure, when $K = F$ this can be rearranged to be

$$t_{i,j} = (1 - K)P_{i,j} + K(P_{r_3,j} + P_{r_2,j} - P_{r_1,j}) \quad (2)$$

so the values of r_2 and r_3 are interchangeable, therefore the number of potential new trial structures is reduced. This is highlighted by performing the same DE calculations with K set to 0.99 (**Figure 7**), again there is a drop in number of generations required when F is 1.0 but it is much smaller than when K is also 1.

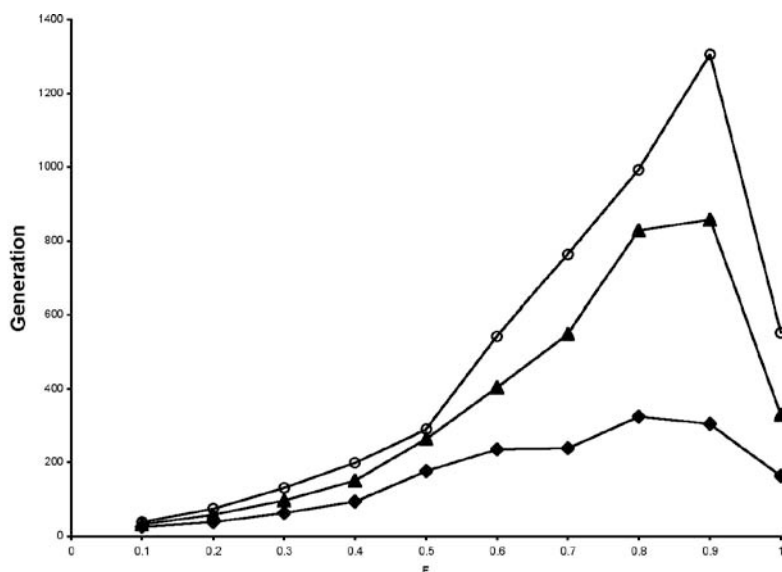


Figure 6. The mean number of generations required for convergence for increasing population sizes, 30 (diamonds), 60 (triangles), 90 (open circles). The DE parameters are $K = 1.0$, $G_{\max} = 5000$.

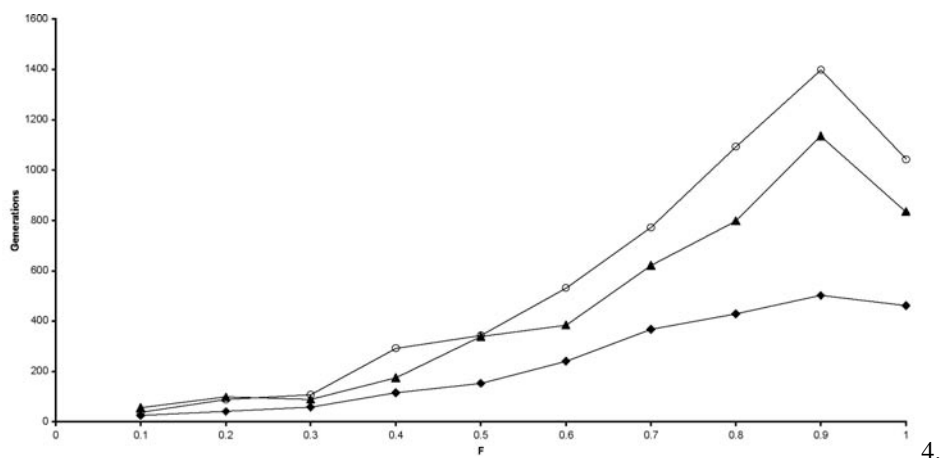


Figure 7. The mean number of generations required for convergence for increasing population sizes, 30 (diamonds), 60 (triangles), 90 (open circles). The DE parameters are $K = 0.99$, $G_{\max} = 5000$.

5. COMPUTATIONAL CRYSTAL PACKINGS

The interface packings obtained from the DE calculations show a number of similarities within a small range of energies (Appendix 1), though due to the distance cut off in the energy calculation many of the lowest energy structures favoured overlayers positioned at the edges of the substrate (**Figure 8a**). This is also enhanced by the boundary reset function used, which asymptotically approaches the boundary values during the calculation. Initial investigations into the application of a periodic boundary reset results in a lower mean energy located but with more of the solutions located over the substrate (Appendix 2). Analysis of the crystal packings for the remaining low energy solutions (**Figure 8b**) with the crystal faces of the component systems shows that the {100} benzoic acid face is interacting the {010} face of the benzamide and clearly shows a hydrogen bonding interaction between the two components of the system. The crystal structures and composite packings were visualised using Cerius² and CrystalMaker [50,51].

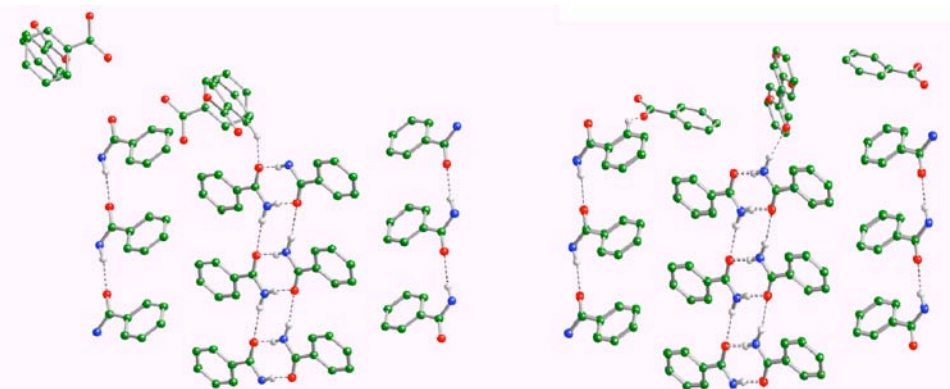


Figure 8. Crystal packings for a low energy solutions of the DE calculation. (a) The lowest energy solution located ($E = -0.4182 \text{ kcal mol}^{-1}$). (b) A solution of low energy ($E = -0.372 \text{ kcal mol}^{-1}$). C atoms are shown as green, N as blue, O as red and H as light grey. Only those Hs involved in Hydrogen bonding are shown.

6. EXPERIMENTAL RESULTS

The synthesis of composite benzoic acid and benzamide crystal was undertaken. Both samples were purchased from Aldrich. Seed crystals of benzoic acid were obtained through slow cooling of a saturated aqueous solution, which resulted in thin white plate-like crystals [52]. The seed crystals were then suspended into a saturated aqueous solution of benzoic acid and benzamide, which was slowly cooled. After three days the seed crystals were removed and inspected by polarizing optical microscopy, which indicated the existence of interfacial layer (**Figure 9**). The expected binding face from the computational studies, {100}, exists as a small facet on the side of the crystal and so the potential level of binding may be small. Initial Raman spectroscopy studies, appear to suggest this since similar spectrums are obtained either side of the interface, though if only low levels of benzamide exist then the signal may be too weak to be seen. Therefore further work is required to fully characterise and validate the computational results, and further investigation into the manipulation of the crystal growth conditions to improve the quality of the material obtained is also required, for example habit modification of the seed crystals to enlarge the binding faces, variation of the temperature, rate of cooling and pH of the solutions during crystal growth.

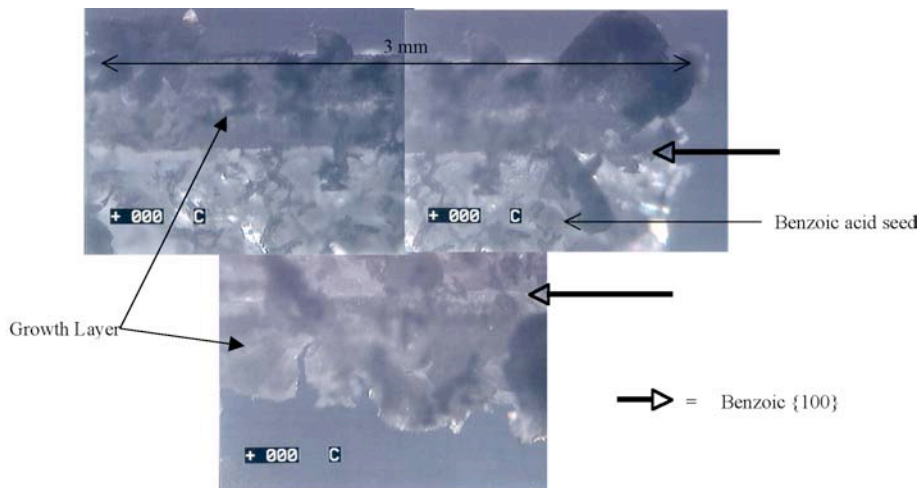


Figure 9. Cross-polarized microscopy image of the grown composite crystal.

7. CONCLUSIONS

In this paper we have demonstrated the application of global optimisation methods to the problem of designing composite molecular materials. The differential evolution algorithm has been shown to offer robust searching of minima, yet relatively simple to implement. The reduced number of control parameters associated with the method, means that optimisation of the search process is computational feasible. Initial investigation in the role of the control parameters K and F appears to show that a relatively small of values is required for optimal performance and these values are independent of the population size selected. Further investigations into the remaining parameters, population size (N) and the number of generation the calculation is run (G_{max}), need to be undertaken. The concept of the entropy of DE population offers a valuable tool in the understanding of the dynamics of the DE performance and consideration of the level of entropy during the calculation will improve the performance of the DE algorithm. Further experimental work is required to fully validate the computational results obtained and number of potential optimisations of the experimental set up are to be undertaken.

8. ACKNOWLEDGEMENTS

We acknowledge the EPSRC for the financial support for this project and Luciana De Matos for assistance with Raman spectroscopy.

9. REFERENCES

- [1] P. Somasundaran & A. Hubbard (Eds.), *Encyclopedia of Surface and Colloid Science*, (Dekker, 2002)
- [2] W. Jones & C. N. R. Rao (Eds.), *Supramolecular Organization and Materials Design*, (Cambridge University Press, 2001).
- [3] C. T. Vogelson, *Modern Drug Delivery*, **4**, (2001), 49.
- [4] J. Yang, J. M. F. Ferreira, S. Mei, W. Weng, *Composite Fine Particles* in *Encyclopedia of Surface and Colloid Science*, Eds, P. Somasundaran & A. Hubbard, (Dekker, 2002).
- [5] J.M. Lehn, *Angew. Chem. Int. Ed.*, **27**, (1988), 89.
- [6] A.D. Burrows, C-W. Chen, M. Chewophry, J.E. McGrady, D. Micheal, P. Mingos, *Chemical Reviews*, **24**, (1995), 329.
- [7] L. Leiserowitz, *Industrial Crystallization*, (Elsevier, 1991).
- [8] R.J. Davey, L. Williams-Seton, H. F. Lieberman, N. Blagden, *Nature*, **402**, (1999), 797.
- [9] N. Blagden, R.J. Davey, *Chemistry in Britain*, March, (1999), 44.
- [10] L. Leiserowitz, L.J.W. Shimon, M. Vaide, F. Frolow, M. Lahav, *Faraday Dis.*, **95**, (1993), 307.
- [11] L. Leiserowitz in: *The Lock and Key Principle*, ed. J.P. Behr, (Wiley, 1994).
- [12] B.R. Heywood and S. Mann, *J. Am. Chem. Soc.*, **114**, (1992), 4681.
- [13] R.J. Davey, B.R. Heywood, *Particle Tech. Forum, A.M.I. Ch Eng*, **1**, (1994), 362.
- [14] M. Gebhart, *Crystal Growth: An Introduction*, (Wiley, 1973).
- [15] H. E. Buckley, *Crystal Growth*, (Wiley, 1951).
- [16] T. V. Barker, *Trans. Chem. Soc. London*, **89** (1906), 1120.
- [17] C.W. Bunn, *Proceedings of the Royal Society*, **141**, (1933), 567.
- [18] O. Rudgiger, *Ann. Physik*, **30**, (1937), 505.
- [19] G.H. van der Merve, *Surf. Sc.*, **31**, (1972), 1988.
- [20] M. J. Stowell, *Thin Films*, **1**, (1968), 55.
- [21] R. Kern, *Current Topics in Material Science*, **12**, (1985), 81.
- [22] R. Kern, *NATO ASI series B, Physics*, **201**, (1987), 143.
- [23] G. B. Stringfellow, *Advanced Crystal Growth*, (Elsevier, 1988).
- [24] W.K. Burton, N. Cabrera, F. C. Frank, *Trans. Roy. Soc*, **A243**, (1951), 299.

- [25] J. Otsaki, T. Oga, S-H. Lee, *Chem. Comm.*, **21**, (1995), 2193.
- [26] N. Aleksandra in: *Epitaxi-Endotaxi*, ed., H.G. Scheider, (VEB, 1968)
- [27] E. Bauer, *Z. Krist.*, **110**, (1958), 372.
- [28] S. Feng, T. Bein, *Science*, **256**, (1994), 1839.
- [29] S. J. Bonafede, M.D. Ward, *J. Am. Chem. Soc.*, **117**, (1995), 7853.
- [30] C. A. Mitchell, L. Yu, M.D. Ward, *J. Am. Chem. Soc.*, **123**, (2001), 10830.
- [31] D.E. Hookes, T. Fritz, M.D. Ward, *Adv. Mater.*, **13**, (2001), 227.
- [32] H.F. Lieberman, L. Williams, R.J. Davey, R.G. Pritchard, *J. Am. Chem. Soc.*, **120**, (1998), 686.
- [33] A. P. Engelbrecht, *Computational Intelligence: An Introduction*, (Wiley, 2002)
- [34] S. Kirkpatrick, C.D. Gelatt, H. P. Vecchi, *Science*, **220**, (1983), 671.
- [35] J. H. Holland, *Adaptation in Natural and Artificial Systems*, (University of Michigan Press, 1975)
- [36] F. Glover, *ORSA Journal of Computing*, **1**, (1989), 190.
- [37] J. Kennedy and R. C. Eberhart in: *New Ideas in Optimisation*, eds. D. Corne, M. Dorigo and F. Glover (McGraw-Hill, 1999), p 379.
- [38] R. Storn and P. V. Price, *Journal of Global Optimisation*, **11** (1997), 341.
- [39] R. Storn in: *New Ideas in Optimisation*, eds. D. Corne, M. Dorigo and F. Glover (McGraw-Hill, 1999), p 108.
- [40] T. Weber, H-B. Bürgi, *Acta Cryst.*, **A58**, (2002), 536.
- [41] C.C. Seaton and M. Tremayne, *Chem. Comm.*, **8**, (2002), 880.
- [42] M. Tremayne, C.C. Seaton, C. Glidewell, *Acta Cryst.*, **B58**, (2002), 823.
- [43] P. V. Price in: *New Ideas in Optimisation*, eds. D. Corne, M. Dorigo and F. Glover (McGraw-Hill, 1999), 80.
- [44] D. L. Goldberg, *Genetic Algorithms in Search, Optimization and Machine Learning*, (Addison-Wesley, 1989).
- [45] T. Bäck, D.B. Fogel, T. Michalewicz (Ed.), *Evolutionary Computation 1: Basic Algorithms and Operators*, (Institute of Physics Publishing, 2000).
- [46] F. Vögtle, *Supramolecular Chemistry*, (Wiley, 1991).
- [47] K. T. No, O. Y. Kwon, S. Y. Kim, K. H. Cho, C. N. Yoon, Y. K. Kang, K. D. Gibson, M. S. Jhon, H. A. Scheraga, *J. Phys. Chem.*, **99**, (1995), 13019.
- [48] M. J. Frisch, G. W. Trucks, H. B. Schlegel, G. E. Scuseria, M. A. Robb, J. R. Cheeseman, J. A. Montgomery, Jr., T. Vreven, K. N. Kudin, J. C. Burant, J. M. Millam, S. S. Iyengar, J. Tomasi, V. Barone, B. Mennucci, M. Cossi, G. Scalmani, N. Rega, G. A. Petersson, H. Nakatsuji, M. Hada, M. Ehara, K. Toyota, R. Fukuda, J. Hasegawa, M. Ishida, T. Nakajima, Y. Honda, O. Kitao, H. Nakai, M. Klene, X. Li, J. E. Knox, H. P. Hratchian, J. B. Cross, C. Adamo, J. Jaramillo, R. Gomperts, R. E. Stratmann, O. Yazyev, A. J. Austin, R. Cammi, C. Pomelli, J. W. Ochterski, P. Y. Ayala, K. Morokuma, G. A. Voth, P. Salvador, J. J. Dannenberg, V. G. Zakrzewski, S. Dapprich, A. D. Daniels, M. C. Strain, O. Farkas, D. K. Malick, A. D. Rabuck, K. Raghavachari, J. B. Foresman, J. V. Ortiz, Q. Cui, A. G. Baboul, S. Clifford, J. Cioslowski, B. B. Stefanov, G. Liu, A. Liashenko, P. Piskorz, I. Komaromi, R. L. Martin, D. J. Fox, T. Keith, M. A. Al-Laham, C. Y. Peng, A. Nanayakkara, M. Challacombe, P. M. W. Gill, B. Johnson, W. Chen, M. W. Wong, C. Gonzalez, and J. A. Pople, *Gaussian 03, Revision 6.0*, (Gaussian, Inc., Pittsburgh PA, 2003).
- [49] M. Bessaou and P. Siarry, *Adv. Eng. Soft.*, **32** (2001), 363.
- [50] *Cerius², Version 4.6*, (Accelrys Inc., Cambridge, UK,)
- [51] D. Palmer, *CrystalMaker, Version 6.3.6*, (CrystalMaker Software, Oxford, UK, 2003)
- [52] X. Holmback and Å.C. Ramuson, *J. Cryst. Grow.*, **198/199**, (1999), 780.

10. APPENDIX 1

The energies and model parameters of the fifteen lowest energy solutions located by the DE calculations with control parameters: $G_{max} = 500$, $N = 30$ using the asymmetric boundary reset.

| θ | ϕ | γ | u | v | w | Energy | K | F |
|----------|----------|----------|---------|---------|--------|---------|-----|-----|
| 43.1139 | 181.4188 | 124.2822 | 6.9983 | -6.9988 | 8.4653 | -0.4182 | 0.7 | 0.8 |
| 223.3406 | 0.0278 | 303.0045 | 6.9729 | -6.9755 | 8.4996 | -0.4132 | 0.8 | 0.6 |
| 224.0255 | 0.4766 | 302.5999 | 6.9763 | -6.9823 | 8.5321 | -0.4113 | 1 | 0.6 |
| 222.2705 | 0.1511 | 302.0412 | 6.9751 | -6.9939 | 8.3633 | -0.4068 | 0.9 | 0.7 |
| 338.2288 | 346.7209 | 69.844 | -3.7514 | 3.0639 | 8.3048 | -0.3723 | 0.9 | 0.6 |
| 140.8144 | 200.8251 | 242.1966 | -1.9241 | -2.2341 | 8.2951 | -0.3668 | 1 | 0.9 |
| 181.0654 | 185.089 | 251.1345 | -3.2224 | 4.7522 | 8.3529 | -0.3652 | 0.9 | 0.7 |
| 317.1483 | 358.9626 | 76.5565 | -0.7146 | -2.2112 | 8.9263 | -0.361 | 1 | 0.7 |
| 157.8049 | 190.9717 | 252.6098 | -3.653 | 3.2946 | 8.4341 | -0.3589 | 0.5 | 0.7 |
| 183.9766 | 183.7777 | 248.8152 | -3.0094 | 4.5959 | 8.5406 | -0.3579 | 0.7 | 0.7 |
| 61.633 | 197.9187 | 130.1989 | 5.6925 | -3.3446 | 9.3372 | -0.3579 | 1 | 0.9 |
| 219.8356 | 2.4319 | 300.8803 | 6.7132 | -6.9462 | 8.5025 | -0.3557 | 0.6 | 0.7 |
| 316.5667 | 1.156 | 78.1893 | -0.4703 | -2.1489 | 8.9979 | -0.354 | 0.9 | 0.5 |
| 357.5303 | 351.2201 | 79.4851 | -3.3438 | 5.3436 | 8.2397 | -0.3535 | 0.6 | 0.7 |
| 61.4582 | 196.6407 | 130.8331 | 5.7922 | -3.2436 | 9.475 | -0.3535 | 0.9 | 0.9 |

11. APPENDIX 2

The energies and model parameters of the fifteen lowest energy solutions located by the DE calculations with control parameters: $G_{max} = 1000$, $N = 30$ using a periodic boundary reset.

| θ | ϕ | γ | u | v | w | Energy | K | F |
|----------|----------|----------|---------|---------|--------|---------|-----|-----|
| 158.238 | 193.2731 | 249.8365 | -3.7512 | 3.0644 | 8.3049 | -0.3723 | 0.9 | 0.8 |
| 186.0786 | 182.1966 | 239.7925 | -2.8189 | 4.1042 | 8.5862 | -0.3562 | 0.8 | 0.5 |
| 178.1329 | 188.4357 | 258.1398 | -3.2619 | 5.4611 | 8.0162 | -0.3482 | 0.9 | 0.9 |
| 139.9251 | 176.6658 | 257.9797 | -0.9926 | -2.3955 | 9.1961 | -0.3412 | 0.4 | 0.5 |
| 222.8271 | 161.9671 | 51.6002 | 1.9904 | -0.0225 | 9.4944 | -0.3315 | 0.9 | 0.7 |
| 42.4558 | 18.5218 | 230.9883 | 1.9809 | -0.0441 | 9.5115 | -0.3307 | 0.9 | 0.6 |
| 141.3574 | 174.3229 | 259.808 | -1.0084 | -2.5184 | 9.3674 | -0.3299 | 0.5 | 0.1 |
| 223.2379 | 161.4847 | 51.674 | 2.0183 | 0.0224 | 9.5293 | -0.3295 | 0.9 | 0.5 |
| 212.5143 | 7.1264 | 300.1183 | 6.9599 | -6.5524 | 8.7754 | -0.3293 | 0.9 | 0.9 |
| 160.4309 | 194.811 | 257.4507 | -3.8274 | 3.6735 | 8.599 | -0.3287 | 0.6 | 0.6 |
| 222.5658 | 162.295 | 49.9119 | 1.961 | -0.1307 | 9.6029 | -0.3275 | 0.9 | 0.7 |
| 223.5758 | 162.3078 | 50.956 | 2.0199 | -0.0594 | 9.6096 | -0.3271 | 0.9 | 0.7 |
| 141.1663 | 177.8432 | 255.4193 | -1.3296 | -2.6766 | 9.3917 | -0.3238 | 0.4 | 0.5 |
| 138.9523 | 182.8565 | 253.7138 | -1.0847 | -2.6969 | 9.2414 | -0.3227 | 0.2 | 0.4 |
| 167.7148 | 194.7255 | 259.3945 | -4.0432 | 4.5612 | 8.6741 | -0.3197 | 0.4 | 0.6 |

MOLECULAR TECTONICS: DESIGN OF 1-D COORDINATION NETWORKS BASED ON RIGID METACYCLOPHANE BACKBONE

Cédric Klein, Ernest Graf, Mir Wais Hosseini and Nathalie Kyritsakas-Gruber

*Laboratoire de Chimie de Coordination Organique, UMR-CNRS 7140 (Tectonique Moléculaire du Solide),
University Louis Pasteur, Inst Le Bel, 4, rue Blaise Pascal, 67000 Strasbourg France
hosseini@chimie.u-strasbg.fr*

1. ABSTRACT

Upon combining the rigid bis monodentate organic tectons **2** and **3** based on the [1.1.1.1] paracyclophane backbone and possessing a « V-type » shape with silver cation and mercury chloride, 1-D coordination networks were generated and structurally characterized by X-ray diffraction methods on single crystals. Whereas the tecton **2** leads in the presence of HgCl_2 to the formation of a 1-D network with « zigzag » geometry, the combination of the tecton **3** with Ag^+ generates a 1-D network which may be described as fused metallamacrocycles.

2. INTRODUCTION

Molecular tectonics [1-3] deals with the generation of molecular networks in the solid state. This approach is based on iterative molecular recognition processes [4] using molecular building block called tectons [2]. Molecular networks are in principle infinite structures obtained upon self-assembly of complementary tectons capable of mutual recognition. These types of molecular architectures possess translational symmetry and are defined by their dimensionality, their geometry and the nature of interactions involved in the recognition event. The dimensionality of molecular networks is defined by the number of translations operating on the recognition patterns formed between complementary or self-complementary tectons. Thus, 1-, 2- and 3-D networks are generated upon one, two and three translations of recognition patterns respectively. Within each dimensional category, molecular networks may be further described by their geometry. For 1-D networks one may define different geometries such as linear, stair type, "zigzag" type and helical. 2-D networks may be of the flat or puckered type. Finally, 3-D networks may be of the cubic or diamondoid or gyroid type. Dealing with the nature of interactions involved in the molecular recognition processes, in principle any type of reversible intermolecular interactions may be used. In particular, inclusion molecular networks based mainly on Van der Waals interactions [5], H-bonded molecular networks based on H-bonds [6] or a combination of H-bonds and charge-charge electrostatic interactions (charge-assisted H-bond) [7] and finally coordination networks based on coordination bonds between organic and metallic tectons [8] have been reported.

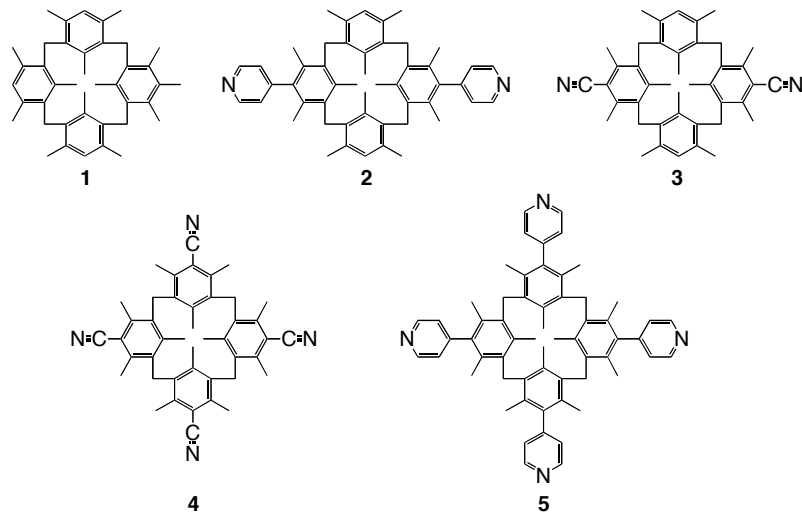
In this contribution, we will focus on the design of rigid organic coordinating tectons and on the formation of coordination networks upon their combination with metallic tectons.

3. RATIONAL

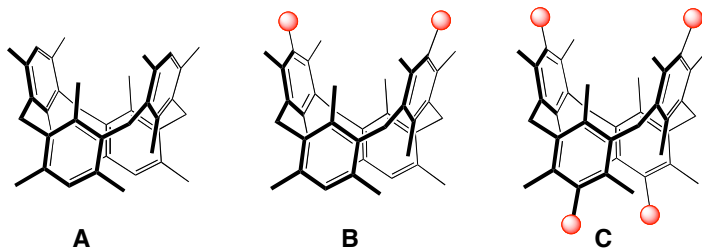
3.1 Design of Organic Tectons

Coordination networks or polymers are infinite molecular assemblies generated upon mutual bridging between organic coordinating tectons and metallic centers. Continuing our effort in this area [9], we designed the rigid tectons **2** and **3** that are of the bis monodentate type (Scheme 1) [10]. Both tectons **2** and **3** are based on the [1.1.1.1]metacyclophane backbone **1** [11] which adopts the 1,3-alternate conformation over a wide range of temperature (Scheme 2 A) [12]. A further interesting feature associated with this backbone is its rigidity which allows to set-up 1-4 coordinating sites upon further functionalization [13]. Both tectons **2** and **3** [10] bearing two coordination sites as well as tectons **4** and **5** [14] bearing four coordination sites have been designed and prepared previously. Two other tectons based on the

metacyclophane backbone bearing two chelating units such as quinoline or 2,2'-bipyridine have been also reported [15].



Scheme 1.



Scheme 2.

Whereas for both tectons **2** and **3** the two coordination sites (nitrile for **2** and pyridyle for **3**) are located at the extremities of a "V" (**Scheme 2 B**), for the other two tetra functionalized tectons **4** and **5**, the coordinating site occupy the apices of a tetrahedron (**Scheme 2 C**). We have previously demonstrated that the compounds **4** and **5** may behave as tetrakis monodentate tectons. Indeed, whereas a combination of **4** with silver cation leads to the formation of a 1-D tubular coordination network [16], the combination of **5** again with silver cation generates a doubly interpenetrated 3-D diamandoid type coordination network [17]. For both tectons **2** and **3**, depending on the nature of the metal centre used, one may expect either discrete entities such as metallamacrocycles (**Figure 1a**) or infinite coordination networks (**Figure 1b** and **c**). We have previously shown that the compound **2** in the presence of zinc halides, a neutral metallatecton possessing a tetrahedral coordination geometry and offering two free coordination sites, behaves as a bis monodentate ligand and forms metallamacrocycles of the type shown on **Figure 1a** [18]. Dealing with the infinite 1-D networks, one may envisage the formation of two types of connectivity. Whereas in the case of metallatectons offering two available coordination sites, one would expect the formation of 1-D networks of the type b (**Figure 1**), for metallatectons offering four free coordination sites, one would envisage the formation of networks of the type c (**Figure 1**). The latter case may be regarded as fused metallamacrocycles.

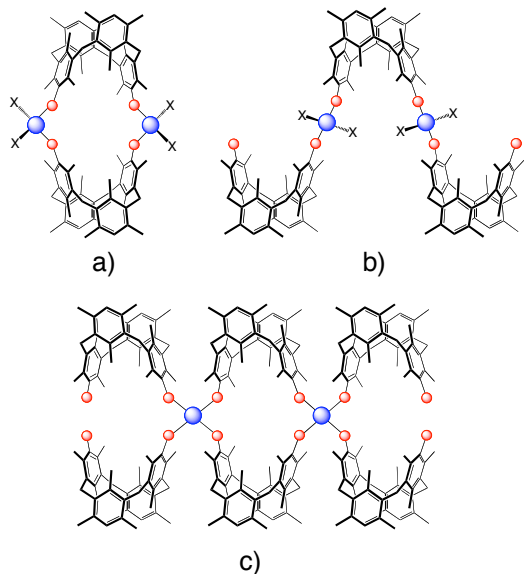


Figure 1. Schematic representation of combinations of a bis-monodentate organic tecton possessing a V-shape such as compounds **2** and **3** with metallic centers with coordination number 4 and adopting tetrahedral coordination geometry. A) discrete metallamacrocycles, b) and c) infinite 1-D coordination networks.

3.2 Choice of Metallic Tectons

As stated above, coordination networks are generated upon combining organic tectons with metallic centers. Thus, for their design, the nature of the metal complex used is of prime importance. First of all, since coordination networks are formed under self-assembly conditions, the interaction between the metal and the coordinating sites of the organic tecton must be reversible. For the choice of the metal cation, one may either use weakly coordinating anions such as SbF_6^- , PF_6^- etc. or strongly coordinating anionic ligands such as halides. Whereas for the first case, all coordination sites of the metal would be available for the generation of the network, in the second case, some of the coordination sites will be occupied by the anionic ligands and thus only a restricted number of coordination sites may be available for the formation of the network. Silver cation is certainly one of the most used metal cation for the formation of coordination networks. The reason for that is related to his rather loose coordination geometry (linear, trigonal, T type, tetrahedral) and coordination number (2, 3, 4) requirements. For the same reasons, mercury dication is another interesting candidate. In particular, mercury halides may be used as neutral metallatectons. We have previously demonstrated the ability of mercury halides to generate discrete metallamacrocycles [19] as well as 1-D helical [20-21], linear [22-23] as well as 2-D [23] coordination networks.

4. EXPERIMENTAL

4.1 Synthesis and Crystallization

$[\mathbf{2} \cdot \text{HgCl}_2]_n$: Suitable colorless crystals for X-ray diffraction analysis on single crystal were obtained after 7 days in the dark and at room temperature in a crystallizing tube ($L = 15 \text{ cm}$, $\varnothing = 0.4 \text{ cm}$) upon slow diffusion of a EtOH solution (1.5 ml) of HgCl_2 (5 mg, 0.018 mmol) into a 1,1,2,2-tetrachloroethane solution (0.5 ml) of compound **2** (5 mg, 0.0073 mmol).

$[\mathbf{3} \cdot \text{AgSbF}_6]_n$: Suitable colorless crystals for X-ray diffraction analysis on single crystal were obtained after 4 days in the dark and at room temperature in a crystallizing tube ($L = 15 \text{ cm}$, $\varnothing = 0.4 \text{ cm}$) upon slow diffusion of a EtOH solution (1.5 ml) of AgSbF_6 (3 mg, 0.0087 mmol) into a chlorobenzene solution (0.5 ml) of compound **3** (3 mg, 0.0052 mmol).

5. X-RAY CRYSTALLOGRAPHY

X-ray diffraction data collection was carried out on a Kappa CCD diffractometer equipped with an Oxford Cryosystem liquid N₂ device, using graphite-monochromated Mo-K α radiation. For all structures, diffraction data were corrected for absorption and analyzed using OpenMolen package [24]. All non-H atoms were refined anisotropically. CCDC 245945 and 245946 contains the supplementary crystallographic data for this paper. These data can be obtained free of charge at www.ccdc.cam.ac.uk/conts/retrieving.html or from the Cambridge Crystallographic data Center, 12 Union Road, Cambridge CB2 1EZ, UK; Fax: (Internat.) +44-1223/336-033; E-mail: deposit@ccdc.cam.ac.uk.

Crystallographic data for (2-HgCl₂)_n: (colorless crystals, 173 K): C₅₀H₅₄N₂Hg Cl₂•C₂H₂Cl₄ $M = 1122.35$, monoclinic, $a = 18.0016(4)$, $b = 20.6568(5)$, $c = 13.0728(4)$ Å, $\beta = 109.488(5)$, $U = 4582.7(2)$ Å³, space group C2/c, Z = 4, $D_c = 1.63$ g cm⁻³; $\mu = 3.748$ mm⁻¹, 3341 data with I > 3σ(I), $R = 0.038$, $R_w = 0.074$.

Crystallographic data for (3-AgSbF₆)_n: (colourless crystals, 173 K): C₈₄H₉₂N₄Ag•SbF₆•2H₂O•C₂H₅OH, $M = 1583.41$, monoclinic, $a = 26.1634(4)$, $b = 22.3454(4)$, $c = 16.7789(3)$ Å, $\beta = 120.396(5)$, $U = 8461.2(2)$ Å³, space group C2/c, Z = 4, $D_c = 1.24$ g cm⁻³; $\mu = 0.611$ mm⁻¹, 4810 data with I > 3σ(I), $R = 0.086$, $R_w = 0.118$.

6. RESULTS AND DISCUSSION

Upon slow diffusion, in the dark and at room temperature, of an EtOH solution of HgCl₂ into a 1,1,2,2-tetrachloroethane solution containing the tecton **2**, colorless crystals were obtained after several days. Structural analysis by X-Ray diffraction on single crystals (monoclinic, space group C 2/c) revealed that the solid was composed of the tecton **2**, HgCl₂ and 1 molecule of 1,1,2,2-tetrachloroethane.

As expected from the design, the combination of neutral tecton **2** and neutral HgCl₂ complex leads to the formation of a neutral "zigzag" type 1-D coordination network of the type b (**Figure 1b**). The network is generated by mutual bridging between the organic tectons **2** and the metallatectons HgCl₂ (**Figure 2a**).

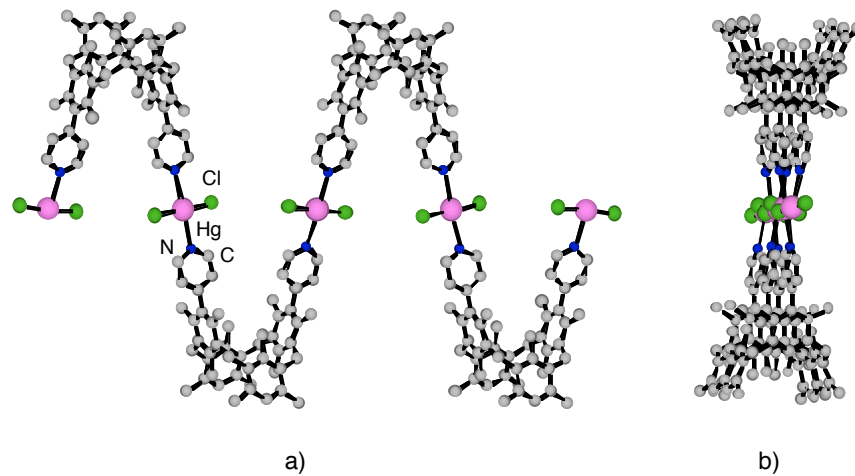


Figure 2. A portion of the X-ray structure showing the cationic coordination network formed between **2** and HgCl₂. a) View perpendicular to the axis of the network. b) View along the axis of the network. For clarity, H atoms and solvent molecules (1,1,2,2-tetrachloroethane) are omitted.

The organic tecton adopts the expected 1,3-alternate conformation imposing thus the localization of the two coordinating pyridyl groups on the same face of the backbone and affording a bis monodentate ligand possessing a "V-shape". The two pyridine units are tilted with respect to the phenyle moieties of **2** (CCCC dihedral angles of -89.0° and -90.3°). For the mercury (II) centers the coordination number is four and the

coordination sphere is composed of two Cl^- anions ($d_{\text{Hg-Cl}} = 2.327 \text{ \AA}$) and two N atoms of two pyridine units belonging to two consecutive tectons **2** ($d_{\text{Hg-Cl}} = 2.606 \text{ \AA}$). The coordination geometry around the metal centre is square planar (both ClHgCl and NHgN angles are 180°). The network may be regarded as an aligned arrangement of mercury cations with 9.19 \AA distance between consecutive metal centers interconnected by tectons **2** (**Figure 2b**). The packing of the 1-D networks leads to the presence of cavities which are occupied by solvent molecules with no specific interactions with the networks.

Upon slow diffusion, in the dark and at room temperature, of an EtOH solution of $\text{Ag}(\text{SbF}_6)$ into a chlorobenzene solution containing the tecton **3**, colorless crystalline material was obtained after few days. X-Ray diffraction on single crystals (monoclinic, space group $C 2/c$) revealed that in addition to **3**, Ag^+ , and SbF_6^- anions, 2 molecules of H_2O and 1 molecule of EtOH are present in the lattice.

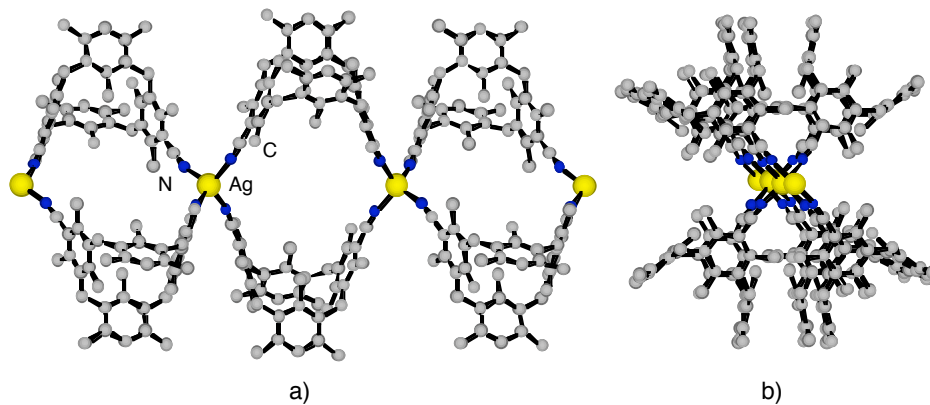


Figure 3. A portion of the X-ray structure showing the cationic coordination network formed between **3** and silver cations. a) View perpendicular to the axis of the network. b) View along the axis of the network. For clarity, H atoms, solvent molecules (chlorobenzene, ethanol) and SbF_6^- anions are omitted.

As expected from the design, the organic tecton **3** indeed adopts the V-shape conformation thus leading to the localization of the two nitrile groups ($d_{\text{C-N}} = 1.15$ and 1.16 \AA) on the same face of the molecule. Tectons **3** are bridged by silver cations leading thus to a cationic 1-D coordination network (**Figure 3**). The Ag^+ cation is surrounded by four nitrogen atoms belonging to four different tectons **3** ($d_{\text{Ag-N}}$) varying between 2.18 \AA and 2.24 \AA) and adopts a distorted tetrahedral coordination geometry with NAgN angle varying between 104.4° and 115.0° (**Figure 3a**). Within the 1-D network, the cations are arranged in a linear fashion (**Figure 3b**) with a distance of 11.42 \AA between consecutive silver cations. The parallel packing of consecutive networks generates space which are occupied by anions (SbF_6^-) and solvent molecules (H_2O and EtOH). No specific interactions between the cationic networks and anions or solvent molecules can be spotted.

The 1-D network formed between **3** and Ag^+ cation may be described as fused metallamacrocycles (**Figure 1c**).

7. CONCLUSIONS

The combination of the rigid bis monodentate tectons **2** and **3** possessing a "V-shape" with metal centers leads as expected to the formation of 1-D coordination networks. The type of network generated depends on the nature of the metal centre used to bridge consecutive organic tectons. Whereas the use of neutral mercury chloride complex offering two free coordination sites leads to the formation of a neutral "zigzag" type 1-D network in the presence of tecton **2** bearing two pyridine units as coordinating sites, the combination of silver cation with the tecton **3** bearing two nitrile groups generates a cationic 1-D network which may be described as an array of fused metallamacrocycles. We are currently investigating the ability

of tectons **2** and **3** as well as other derivatives bearing other coordinating sites such as thiols, thioethers, phosphines and phine oxide [10] to form coordination networks with a variety of metal centers.

8. ACKNOWLEDGEMENTS

We would like to thank the Université Louis Pasteur, the French National Research Centre (CNRS) and the Ministry of Research and Technology and for financial support and scholarship to C.K.

9. REFERENCES

- [1] S. Mann. *Nature*, **365** (1993), 499.
- [2] M. Simard, D. Su, J. D. Wuest, *J. Amer. Chem. Soc.*, **113** (1991), 4696.
- [3] M. W. Hosseini, Cryst. Eng. Comm., **2004**, 6, 318; G. Brand, M. W. Hosseini, O. Félix, P. Schaeffer, R. Ruppert, in *NATO ASI Series*, O. Kahn, Ed, Serie c, Kluwer, Dordrecht, **484** (1995), 129; M. W. Hosseini in *NATO ASI Series*, G. Tsoucaris, Ed, Serie c, Kluwer, Dordrecht, **518** (1998), 209; M. W. Hosseini, in *NATO ASI Series*, Eds. D. Braga, F. Grepioni, G. Orpen, Serie c, Kluwer, Dordrecht, Netherlands, **538** (1999), 181.
- [4] J.-M. Lehn, *Supramolecular Chemistry, Concepts and Perspectives*, VCH, Weinheim, **1995**.
- [5] M. W. Hosseini, A. De Cian, *Chem. Comm.*, (1998), 727; J. Martz, E. Graf, A. DE Cian, M. W. Hosseini, in *Perspectives in Supramolecular Chemistry*, Ed. G. Desiraju, Wiley, (2003), 177.
- [6] M.C. Etter, *Acc. Chem. Res.*, **23** (1990), 120; G. D. Desiraju, *Crystal Engineering: The Design of Organic Solids*, Elsevier, New York, **1989**; G. M. Whitesides, J. P. Mathias, T. Seto, *Science*, **254** (1991), 1312; C. B. Aakeröy, K. R. Seddon, *Chem. Soc. Rev.*, **22** (1993), 397; S. Subramanian, M. J. Zaworotko, *Coord. Chem. Rev.*, **137** (1994), 357; D. S. Lawrence, T. Jiang, M. Levett, *Chem. Rev.*, **95** (1995), 2229; J. F. Stoddart, D. Philip, *Angew. Chem. Int. Ed. Engl.*, **35** (1996), 1155.
- [7] M.D. Ward, P.J. Fagan, J.C. Calabrese, D.C. Johnson, *J. Am. Chem. Soc.*, **111** (1989), 1719; E. Fan, J. Yang, S. J. Geib, T. C. Stoner, M. D. Hopkins, A. D. Hamilton, *Chem. Commun.*, (1995), 1251; K. E. Schwiebert, D. N. Chin, J. C. MacDonald, G. M. Whitesides, *J. Am. Chem. Soc.*, **118** (1996), 4018; K. T. Holman, A. M. Pivovar, J. A. Swift, M. D. Ward, *Acc. Chem. Res.*, **34** (2001), 107; M. W. Hosseini, *Coord. Chem. Rev.*, **240** (2003), 157.
- [8] S. R. Batten, R. Robson, *Angew. Chem. Int. Ed.*, **37** (1998), 1460; A. J. Blake, N. R. Champness, P. Hubberstey, W.-S. Li, M. A. Withersby, M. Schröder, *Coord. Chem. Rev.*, **193** (1999), 117; M. Eddaoudi, D. B. Moler, H. Li, B. Chen, T. M. Reineke, M. O'Keeffe, O. M. Yaghi, *Acc. Chem. Res.*, **34** (2001), 319; B. Moulton, M. J. Zaworotko, *Chem. Rev.* **101** (2001), 1629.
- [9] C. Kaes, M. W. Hosseini, C. E. F. Rickard, B. W. Skelton, A. White, *Angew. Chem. Int. Ed. Engl.*, **37** (1998), 920; G. Mislin, E. Graf, M. W. Hosseini, A. De Cian, N. Kyritsakas, J. Fischer, *Chem. Comm.*, (1998), 2545; M. Loï, M. W. Hosseini, A. Jouaiti, A. De Cian, J. Fischer, *Eur. J. Inorg. Chem.*, (1999), 1981; M. Loï, E. Graf, M. W. Hosseini, A. De Cian, J. Fischer, *Chem. Comm.*, (1999), 603.; H. Akdas, E. Graf, M. W. Hosseini, A. De Cian, J. McB. Harrowfield, *Chem. Comm.*, (2000), 2219; A. Jouaiti, M. W. Hosseini, A. De Cian, *Chem. Comm.*, (2000), 1863; B. Schmaltz, A. Jouaiti, M. W. Hosseini, A. De Cian, *Chem. Comm.*, (2001), 1242; A. Jouaiti, V. Jullien, M. W. Hosseini J.-M. Planeix, A. De Cian, *Chem. Comm.*, (2001), 1114; S. Ferlay, S. Koenig, M. W. Hosseini, J. Pansanel, A. De Cian, N. Kyritsakas, *Chem. Comm.*, (2002), 218; B. Zimmer, M. Hutin, V. Bulach, M. W. Hosseini, A. De Cian, N. Kyritsakas, *New. J. Chem.*, **26** (2002), 26, 1532; A. Jouaiti, M. W. Hosseini, N. Kyritsakas, *Eur. J. Inorg. Chem.* 2002, 57; A. Jouaiti, M. W. Hosseini, N. Kyritsakas, *Chem. Comm.*, (2002), 1898; B. Zimmer, V. Bulach, M. W. Hosseini, A. De Cian, N. Kyritsakas, *Eur. J. Inorg. Chem.*, (2002), 3079; A. Jouaiti, M. W. Hosseini, N. Kyritsakas, *Chem. Comm.*, (2003), 472; P. Grosshans, A. Jouaiti, M. W. Hosseini, N. Kyritsakas, *New. J. Chem.*, **27** (2003), 793.
- [10] C. Klein, E. Graf, M. W. Hosseini, A. De Cian, N. Kyritsakas-Gruber, *Eur. J. Org. Chem.* (2003), 395.

- [11] F. Bottino, G. Montaudo, P. Maravigna, *Ann. Chimica*, **57** (1967), 972.
- [12] S. Pappalardo, F. Bottino, *Phosphorus and Sulfur*, **19** (1984), 327.
- [13] S. Pappalardo, G. Ferguson, J. F. Gallagher, *J. Org. Chem.*, **57** (1992), 7102.
- [14] C. Klein, E. Graf, M. W. Hosseini, A. De Cian, N. Kyritsakas, *Eur. J. Org. Chem.*, (2002), 802.
- [15] C. Klein, E. Graf, M. W. Hosseini, G. Mislin, A. De Cian, *Tetrahedron Lett.* **41** (2000), 9043.
- [16] C. Klein, E. Graf, M. W. Hosseini, A. De Cian, J. Fischer, *Chem. Comm.*, (2000), 239.
- [17] C. Klein, E. Graf, M. W. Hosseini, A. De Cian, *N. J. Chem.* **25** (2001), 207.
- [18] C. Klein, E. Graf, M. W. Hosseini, A. De Cian, N. Kyritsakas-Gruber, *Eur. J. Inorg. Chem.* (2003), 1299.
- [19] P. Grosshans, A. Jouaiti, V. Bulach, J.-M. Planeix, M. W. Hosseini, N. Kyritsakas, *Eur. J. Inorg. Chem.*, (2004), 453.
- [20] P. Grosshans, A. Jouaiti, V. Bulach, J.-M. Planeix, M. W. Hosseini, J.-F. Nicoud, *Chem. Comm.*, (2003), 1336.
- [21] Grosshans, A. Jouaiti, V. Bulach, J.-M. Planeix, M. W. Hosseini, J.-F. Nicoud, *C. R. Chimie*. **7** (2003), 189.
- [22] M. Henry, M. W. Hosseini, *New J. Chem.*, **28** (2004), 897.
- [23] P. Grosshans, A. Jouaiti, N. Kardouh, M. W. Hosseini, N. Kyritsakas, *New J. Chem.*, **27** (2003), 1806.
- [24] OpenMolen, Interactive Structure Solution, Nonius B.V., Delft, The Netherlands, **1997**.

AN INFINITE HYDROGEN-BONDED MOLECULAR ASSEMBLY BASED ON CATECHOL AND A BIFUNCTIONAL OLEFIN

Giannis S. Papaefstathiou,[†] Tomislav Friščić[†] and Leonard R. MacGillivray

Dept. of Chemistry, Univ. of Iowa, Iowa City, IA 52242, USA
len-macgillivray@uiowa.edu

1. ABSTRACT

Catechol (cat) and *trans*-1,2-bis(4-pyridyl)ethylene (4,4'-bpe) form a 1:1 co-crystal, of composition (cat)·(4,4'-bpe) 1, that consists of infinite one-dimensional (1D) undulating chains held together by O-H···N hydrogen bonds. The chains are based on an alternating sequence of five crystallographically independent molecules, two that involve cat and three that involve 4,4'-bpe, and an eight-component repeat unit. The cat molecules adopt an *anti-anti* conformation, while the olefins adopt either a co-planar or twisted conformation. The chains self-assemble *via* a combination of face-to-face π - π interactions, C-H··· π forces, and C-H···O hydrogen bonds.

2. INTRODUCTION

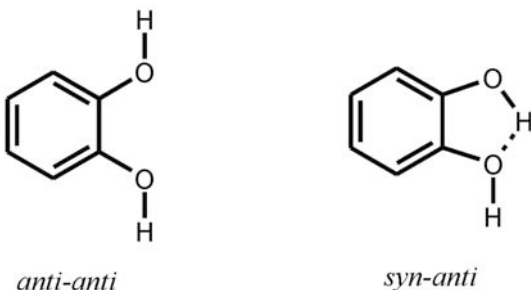
The engineering of molecular crystalline solids with components assembled in predefined geometries and packing arrangements is a central goal of the crystal engineer.[1] Such control of geometry and packing, when combined with the myriad of chemical functionalities offered by a molecular approach, provides a means to design a vast array of solids with predictable and controllable properties (e.g. porosity, reactivity). This goal, however, is underscored by the fact that geometry and packing in the solid state are sensitive to subtle changes to molecular structure such that structurally similar molecules typically do not exhibit similar geometry and packing arrangements.[2] Thus, to confront such apparent disparity between molecular and solid-state structure, we,[3] and others,[1] are focused upon identifying geometries and packing patterns that may be used as synthons[4] to reliably control the organization of molecules in solids to achieve and control desired properties.

In this context, a property of the organic solid state that we aim to control is reactivity.[3] Specifically, we have revealed the ability of ditopic molecules, in the form of linear templates, to orient olefins in the solid state, *via* hydrogen bonds, in geometries suitable for single and multiple [2+2] photodimerizations.[2] Thus, co-crystallization of 1,3-benzenediol, or resorcinol (res), with *trans*-1,2-bis(4-pyridyl)ethylene (4,4'-bpe) produced a discrete four-component molecular assembly, 2(res)·2(4,4'-bpe),[5] held together by four O-H···N hydrogen bonds wherein two olefins were juxtaposed in a geometry suitable[2] for photoreaction. Ultraviolet (UV) irradiation of the crystalline solid produced *rctt*-tetrakis(4-pyridyl)cyclobutane in quantitative yield.[3] We have also demonstrated that the arrangement adopted by the templates and reactants is robust such that the geometry can be ‘transferred’ to additional solids to construct targets such as a [2.2]paracyclophane[6] and [n]-ladderanes (where n = 3 and 5).[7]

Having demonstrated the ability of res to force stacking of 4,4'-bpe in the solid state, we turn to structurally related 1,2-dihydroxybenzene, or catechol (cat). In particular, we wish to describe the formation of an infinite solid-state molecular assembly based on cat and 4,4'-bpe of composition (cat)·(4,4'-bpe).[8] Similar to resorcinol, cat can adopt more than one conformation based on the orientation of the two hydroxyl groups.[9] Specifically, two stable conformations can form: *anti-anti* and *syn-anti* (Scheme 1). In the former, the hydrogen atoms of the hydroxyl groups of the hydroxyl groups point away from each other, while in the latter one hydroxyl group participates in an intramolecular O-H···O hydrogen bond. *Ab initio* calculations indicate that the *syn-anti* conformation is more stable by approximately 5 kcal mol⁻¹,[9]

[†] Authors contributed equally to the manuscript.

which suggested to us that cat may assemble with 4,4'-bpe in the solid state to produce, similar to 2(res)·(4,4'-bpe), a discrete hydrogen-bonded assembly that is photoactive.[10]



Scheme 1.

3. EXPERIMENTAL

Addition of cat (0.12 g, 1.1 mmol) to acetone (10 mL) in the presence of 4,4'-bpe (0.182 g, 1.0 mmol) yielded, upon standing for a period of approximately 2 days, yellow crystals of **1** (yield: 100%) suitable for X-ray analysis. The formulation of **1** was confirmed by ¹H NMR spectroscopy, as well as single-crystal X-ray diffraction.[11]

4. RESULTS AND DISCUSSION

The asymmetric unit of **1** consists of two full molecules of cat [based on O-atoms O1/O2 (cat_A) and O3/O4 (cat_B)], one full molecule of 4,4'-bpe [based on N-atoms N1/N2 (4,4'-bpe_A)], and two half-molecules of 4,4'-bpe [based on N-atoms N3/N3ⁱ (4,4'-bpe_B) and N4/N4ⁱⁱ (4,4'-bpe_C)] (**Fig. 1a**). The components have assembled *via* O-H···N hydrogen bonds, in the sequence 4,4'-bpe_C···cat_A···4,4'-bpe_A···cat_B···4,4'-bpe_B (**Fig. 1b**), to form a one-dimensional (1D) chain based on alternating cat and 4,4'-bpe molecules.

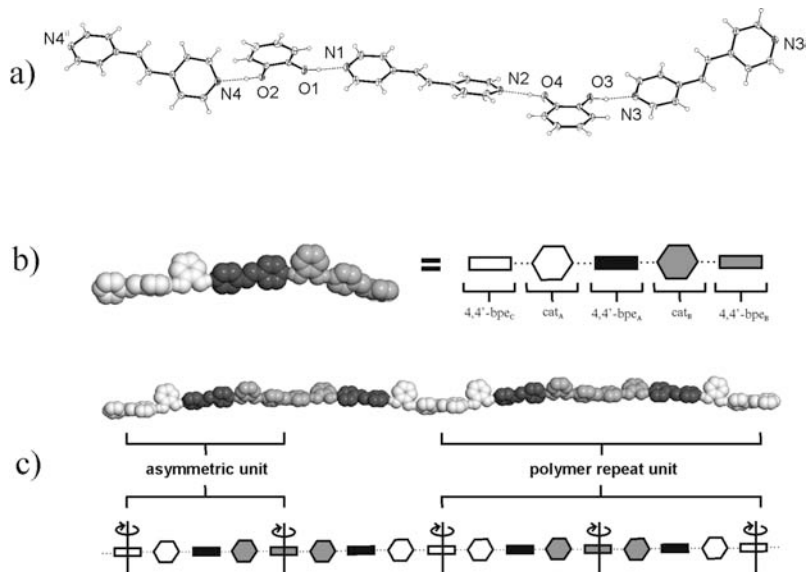


Figure 1. Perspectives of **1**: (a) ORTEP of the asymmetric unit (all non-hydrogen atoms at 30 % probability level), (b) space-filling model of the asymmetric unit along with a schematic representation, and (c) space-filling model of the eight-component repeat unit along with a schematic representation. Selected interatomic distances (Å) and angles (°): O1···N1 = 2.733(2), O1-H1O···N1 = 171.0(1), O2···N4 = 2.756(2), O2-H2O···N4 = 174.37(9); O3···N3 = 2.710(2), O3-H3O···N3 = 167.00(9); O4···N2 = 2.749(2), O4-H4O···N2 = 172.67(9). Symmetry operators: *i* = -*x*+3, *y*, -*z* + 3/2; *ii* = -*x*, *y*, -*z* + 1/2.

Each cat molecule adopts the *anti-anti* conformation, while the pyridyl groups of each 4,4'-bpe molecule deviate from co-planarity [pyridine···pyridine twist angles ($^{\circ}$): 41 (4,4'-bpe_B); 39 (4,4'-bpe_C); 22.7(1) (4,4'-bpe_A)]. In this arrangement, the aromatic units of each hydrogen bond are either twisted or lie approximately co-planar, the twist angles involving cat_A and cat_B being 71 $^{\circ}$ (4,4'-bpe_A) and 67 $^{\circ}$ (4,4'-bpe_C), and 10 $^{\circ}$ (4,4'-bpe_A) and 11 $^{\circ}$ (4,4'-bpe_B), respectively. The components of the hydrogen-bonded sequence are propagated along the crystallographic [100] direction, *via* two-fold rotation axes, to give a polar, undulating chain (wavelength: 6.8 nm) based on the eight-component repeat unit 4,4'-bpe_C···cat_A···4,4'-bpe_A···cat_B···4,4'-bpe_B···cat_B···4,4'-bpe_A···cat_A (**Figure 1c**).

The chains of **1** have self-assembled in the solid state to form centrosymmetric dimers (**Figure 2a**). The dimers are held together by a combination of face-to-face π - π interactions, involving the pyridyl units and cat molecules, and C-H··· π forces.[12] These interactions occur between peaks and troughs of adjacent polymers (**Figure 2b**). Neighboring dimers interact *via* a combination of two-point C-H···O forces and face-to-face π - π interactions (**Figure 2c**) involving nearest-neighbor pyridyl units and cat molecules.[13] The shortest distance between neighboring carbon-carbon double bonds of **1** is 6.85 Å, involving molecules 4,4'-bpe_A and 4,4'-bpe_Bⁱⁱⁱ (symmetry operator *iii* = -*x*+2, -*y*+2, -*z*+1). This distance extends beyond the separation criteria of Schmidt for [2+2] photodimerization.² Moreover, the olefins of **1**, as determined by irradiating a powdered crystalline sample of **1** with UV-radiation (broadband Hg lamp), are photostable.

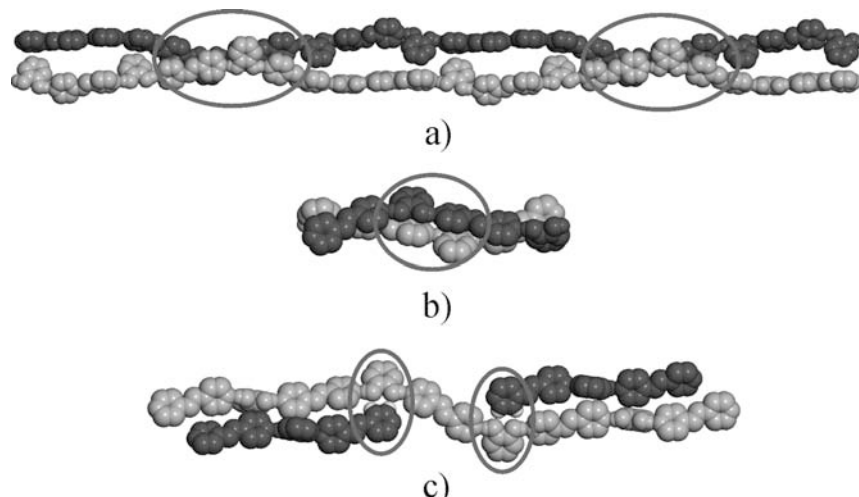


Figure 2. Space-filling views of: a) self-assembled chain dimers highlighting the peak and trough interaction, (b) interactions between the chains highlighting the π - π interactions in the central region of the fragment, and (c) interactions between the dimers highlighting the C-H···O forces (hydrogen atoms colored white).

5. CONCLUSION

In conclusion, we have revealed that cat assembles with 4,4'-bpe in the solid state to form a 1D hydrogen-bonded chain of composition (cat)·(4,4'-bpe) **1**. The cat molecules of the chain adopt the *anti-anti* conformation.[9] Efforts are currently underway to engineer cat derivatives[14] that may provide access to photoactive solids based on discrete hydrogen-bonded assemblies akin to 2(res)·2(4,4'-bpe).[15]

6. REFERENCES

- [1] Braga, D. *Chem. Comm.* **2003**, 2751; (b) Hosseini, M.W. *Coord. Chem. Rev.* **2003**, 240, 157; (c) Hollingsworth, M.D. *Science* **2002**, 295, 2410; (d) Holman, K.T.; Pivoval, A.M.; Swift, J.A.; Ward, M.D. *Acc. Chem. Res.* **2001**, 34, 107; (e) Aakeröy, C.B.; Beatty, A.M. *Aust. J. Chem.* **2001**, 54, 409; (f) Moulton, B.; Zaworotko, M.J. *Chem. Rev.* **2001**, 101, 1629; (g) Blake, A.J.; Champness, N.R.; Hubberstey, P.; Li, W.-S.; Withersby, M.A. Schröder, M. *Coord. Chem. Rev.* **1999**, 183, 117.

- [2] Schmidt, G.M.J. *Pure Appl. Chem.* **1971**, *27*, 647.
- [3] MacGillivray, L.R. *CrystEngComm*, **2002**, *4*, 37.
- [4] Desiraju, G.R. *J. Mol. Struc.* **2003**, *656*, 5.
- [5] MacGillivray, L.R.; Reid, J.L.; Ripmeester, J.A. *J. Am. Chem. Soc.* **2000**, *122*, 7817.
- [6] Friščić, T.; MacGillivray, L.R. *Chem. Commun.* **2003**, 1306.
- [7] Gao, X.; Friščić, T.; MacGillivray, L.R. *Angew. Chem. Int. Ed.* **2004**, *43*, 232.
- [8] St Pourçain, C.B. *J. Mater. Chem.* **1999**, *9*, 2727.
- [9] Puebla, C.; Ha, T.-K. *J. Mol. Struc. (Theochem)* **1990**, *204*, 337.
- [10] Such an assembly would involve a bifurcated interaction involving the hydroxyl group of cat that participates in the intramolecular O-H···O hydrogen bond such that cat serves as a ditopic U-shaped moiety.
- [11] Crystal data for **1**: monoclinic, *P2/c* (No. 13), $Z = 4$, $a = 23.927(2)$ Å, $b = 7.4219(7)$ Å, $c = 17.631(2)$ Å, $\beta = 109.006(5)$ °, $V = 2960.4(5)$ Å³, 6729 unique reflections, $R = 0.0455$ [for 4512 reflections with $I \geq 2\sigma(I)$], $R = 0.0827$ (all data) and $wR^2 = 0.1627$ (all data). Crystallographic data has been deposited with the Cambridge Crystallographic Data Centre and has been allocated with deposition number CCDC 244922.
- [12] Jorgensen, W.L.; Severance, D.L. *J. Am. Chem. Soc.* **1990**, *112*, 4768.
- [13] The *anti-anti* conformation adopted by cat in **1** may be attributed to the intermolecular forces (*i.e.* face-to-face π···π stacking, C–H···π, and C–H···O hydrogen bonds) that occur between the chains.
- [14] Papaefstathiou, G.S.; Friščić, T.; MacGillivray, L.R. *J. Supramol. Chem.* **2003**, *2*, 227.
- [15] For a related strategy, see: Papaefstathiou, G. S.; MacGillivray, L. R. *Org. Lett.* **2001**, *3*, 3835.

COMPLEMENTARY FEATURES OF INORGANIC AND ORGANIC HALOGENS: APPLICATION TO CRYSTAL ENGINEERING

Lee Brammer, Fiorenzo Zordan, Guillermo Mínguez Espallargas, Stephen L. Purver, Luis Arroyo Marin
and Harry Adams

Dept. of Chemistry, Univ. of Sheffield, Brook Hill, Sheffield S3 7HF, UK
lee.brammer@sheffield.ac.uk

Paul Sherwood

*Computational Science and Engineering Dept., CLRC Daresbury Laboratory, Daresbury,
Warrington WA4 4AD, UK*

1. ABSTRACT

Inorganic ($M-X$) and suitably chosen organic ($C-X$) halogens exhibit anisotropic electrostatic potentials whose complementary aspects can be exploited to permit supramolecular assembly of molecules or ions based upon attractive $M-X \cdots X'-C$ interactions. Electrostatic potential calculations and crystal syntheses are presented to illustrate this approach to the design of crystalline materials.

2. INTRODUCTION

Halogens (X) are present at the periphery of a large number of organic and inorganic molecules. As such they provide a potential site for intermolecular interactions in condensed phases. In recent years we have examined the geometric aspects of intermolecular interactions involving halogens and sought to understand the electronic factors that govern the observed geometries and the interaction energies. In this article we examine the similarities and, particularly, the differences in the electronic nature of organic halogens ($C-X$) and inorganic halogens ($M-X$) and show how the complementary electronic features of halogens in these two environments can be harnessed to provide a class of non-covalent interactions of the type $M-X \cdots X'-C$.

3. GEOMETRIC AND ELECTROSTATIC MODELS

Examination of the electrostatic potential in the vicinity of organic and (terminal) inorganic halogens shows a marked anisotropy that is a manifestation of the charge density distribution about the halogens. Specifically halogens in both environments show far greater negative electrostatic potential in directions inclined at $90\text{--}130^\circ$ to the $C-X$ or $M-X$ bond relative the direction axial to the bond (180°) [1]. **Figure 1** illustrates this point and highlights the far greater potential associated with the inorganic halogens, consistent with the $M-X$ bond being the more polar of the two. It is also evident that as bond polarity decreases with decreasing electronegativity of the halogen ($F > Cl > Br > I$) then so does the magnitude of the negative electrostatic potential.

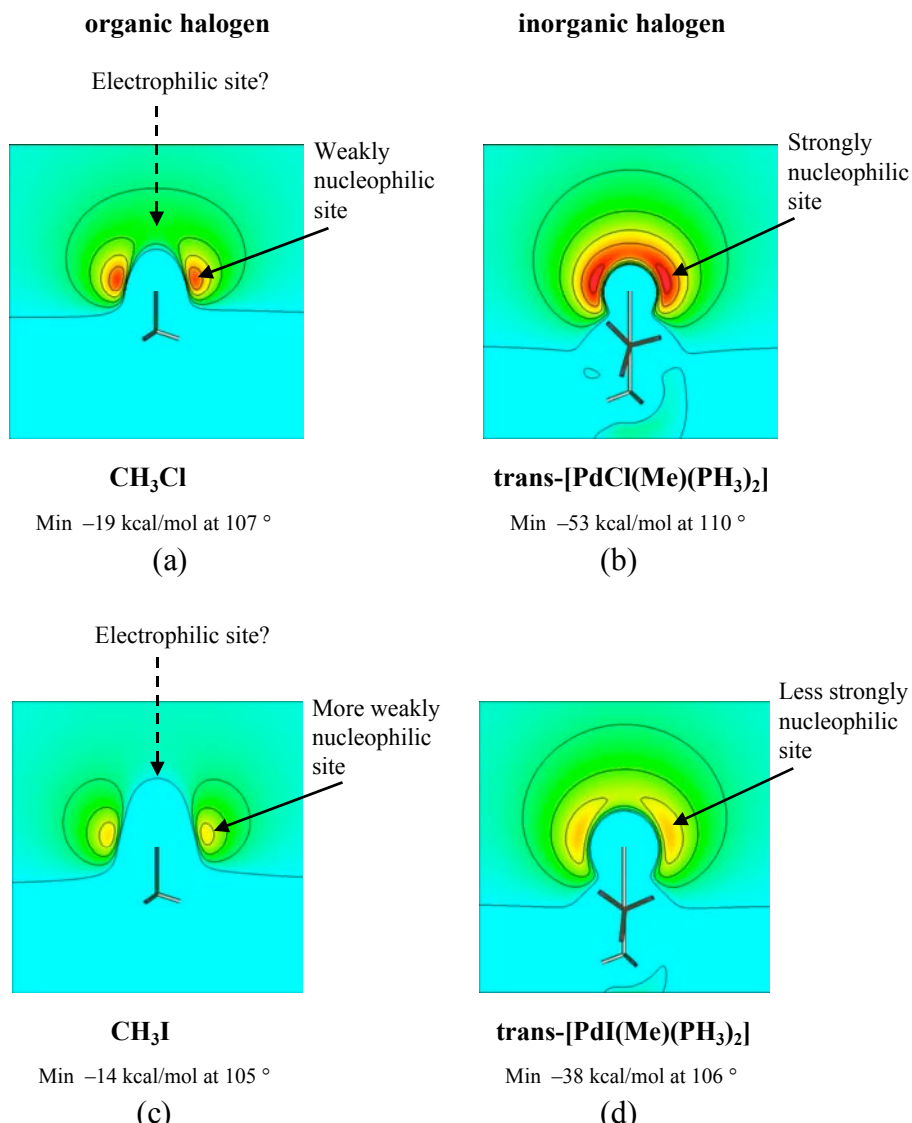


Figure 1. Calculated negative electrostatic potentials for model compounds (a) CH_3Cl , (b) $\text{trans-}[\text{PdCl}(\text{Me})(\text{PH}_3)_2]$, (c) CH_3I , (b) $\text{trans-}[\text{PdI}(\text{Me})(\text{PH}_3)_2]$, contoured at intervals of 4 kcal/mol for organic halogens and 10 kcal/mol for inorganic halogens. The calculations are presented and described in full in ref. 1. Figures are adapted from ref 1 with permission of the American Chemical Society.

3.1 Halogens As Nucleophiles

These electrostatic potential distributions provide a rationalization for the interaction of halogens with electrophiles such as hydrogen bond donors or metal ions. Thus, the negative potential at the halogen contributes to an attractive interaction with electrophiles. Furthermore, use of the Cambridge Structural Database [2] has shown that the geometric distribution of hydrogen bond donors in the vicinity of terminal halogens (**Figure 2**) is quite consistent with an electrostatic driving force for hydrogen bond formation since there is a significant preference for interactions occurring along the directions at which the halogen potential is most negative [1]. $\text{H}\cdots\text{X}$ distances are found to lengthen over the sequence $\text{F} < \text{Cl} < \text{Br} < \text{I}$ and are typically longer for organic halogens ($\text{C}-\text{X}$) than for comparable inorganic ($\text{M}-\text{X}$) halogens (Table 1), again consistent with the importance of the electrostatic component in these hydrogen bonds.

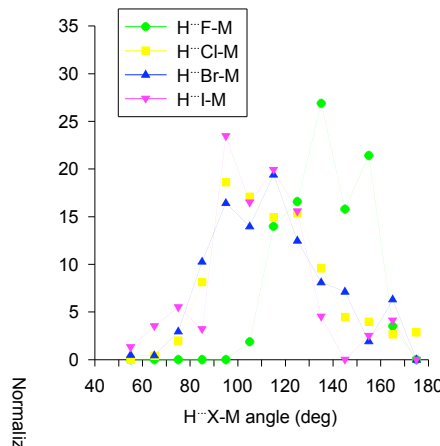


Figure 2. Normalized [3] angular distribution of N–H···X–M hydrogen bonds. Reproduced from ref 1 with permission of the American Chemical Society.

The directional preference of N–H···X–M hydrogen bonds has been used in design strategies for synthesis of hydrogen-bonded crystals of perhalometallate salts [4–8]. C–X hydrogen bond acceptors are generally considered too weak for use in a hydrogen bonding strategy for crystal synthesis, though the importance of such hydrogen bonds has been the subject of some recent attention [9–11].

Table 1
Mean normalized HX distances for N–H···X–M and N–H···X–C hydrogen bonds [1]

| Nucleophile (Lewis base) | L _n M—X | R _n C—X |
|--|--|--|
| Electrophile (Lewis acid) | | |
| Mean normalized H···X distance, R _{HX} | R _{HX} [d(H···X)] | R _{HX} [d(H···X)] |
| R _{HX} = d(H···X)/(r _{vdW} H + r _{vdW} X) | 0.776 [2.072 Å] (X = F) 0.853 [2.516 Å] (X = Cl) 0.879 [2.681 Å] (X = Br) 0.923 [2.917 Å] (X = I) | 0.923 [2.464 Å] 0.963 [2.841 Å] 0.973 [2.968 Å] ca. 0.99 [3.13 Å] |
| [using data for R _{HX} < 1.05] | Stronger hydrogen bond M–X bond very polar | Very weak hydrogen bond C–X bond somewhat polar |

3.2 Organic Halogens As Electrophiles

Evidence from crystal structure data has clearly established that organic halogens (C–X) are involved in short contacts with nucleophiles such as oxygen and nitrogen bases via an axial approach geometry, i.e. approximately linear C–X···O/N geometries [12,13] (**Figure 3**). *Ab initio* intermolecular perturbation theory (IMPT) calculations on model dimers by Lommersse et al have permitted a detailed analysis of the contributions to the interaction energies of C–Cl···O interactions [13]. It is illustrative to consider their analyses of the chloromethane···formaldehyde (I) and chloro-cyanoacetylene···formaldehyde (II) systems (**Figure 4**). For both I and II the geometry with the minimum energy involves a linear C–Cl···O arrangement. However, there is no net attractive interaction for I while the interaction in II is attractive. In

both systems the exchange repulsion is quite anisotropic and is at a minimum for a linear C–Cl···O arrangement. This is consistent with an earlier theoretical study on C–Cl···Cl–C interactions by Price [14] and has led to the suggestion that chlorine (and the heavier halogens) should be considered to have aspherical van der Waals radii [15].

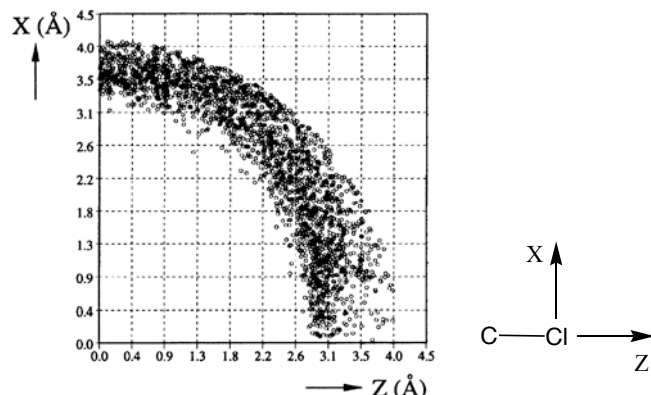


Figure 3. Plot of C–Cl···O contacts in crystal structures (Cl at origin) illustrating that the shortest interactions lie along the C–Cl bond axis. Adapted from ref. 13 with permission of the American Chemical Society.

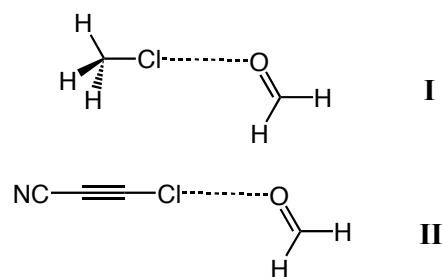


Figure 4. The chloromethane–formaldehyde (**I**) and chloro-cyanoacetylene–formaldehyde model systems for C–Cl···O interactions [13].

The electrostatic component of the interaction energy in **I** and **II** is also anisotropic, being most attractive (or least repulsive) for a linear C–Cl···O geometry. For **I** the electrostatic term is repulsive for all geometries, but least repulsive for the axial interaction, consistent with the small but negative electrostatic potential associated with an axial approach to CH₃Cl (**Figure 1a**). However, the electrostatic contribution to the interaction energy in **II** is attractive for a linear C–Cl···O geometry. Here the electron distribution associated with the C–Cl group is influenced by the electron-withdrawing effect of the alkyne and nitrile groups, presumably diminishing the negative electrostatic potential associated with the chlorine atom (relative to that in CH₃Cl) and leading to a slightly positive potential in the direction of the axial approach. The charge transfer, polarization and dispersion energy terms are all attractive but small in comparison to the exchange repulsion and electrostatic contributions to the interaction energy. The situation regarding the contribution of the exchange repulsion, electrostatic and charge transfer components of the interaction energy are summarized in **Figure 5**. Lommers et al. have also noted that (heavier) more polarizable halogens form stronger/shorter interactions with nucleophiles [13]. This arises primarily from an enhanced electrostatic term: I > Br > Cl [> F], though the (smaller) charge transfer energy term should also be significantly enhanced. Finally, it should be noted that in a CSD search C–F groups were found to exhibit very few short contacts with nucleophiles and to show no directional preferences within such interactions [13].

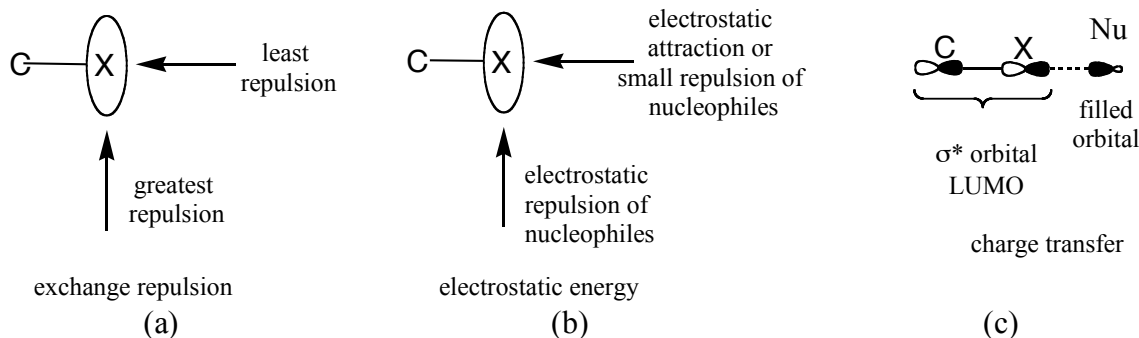
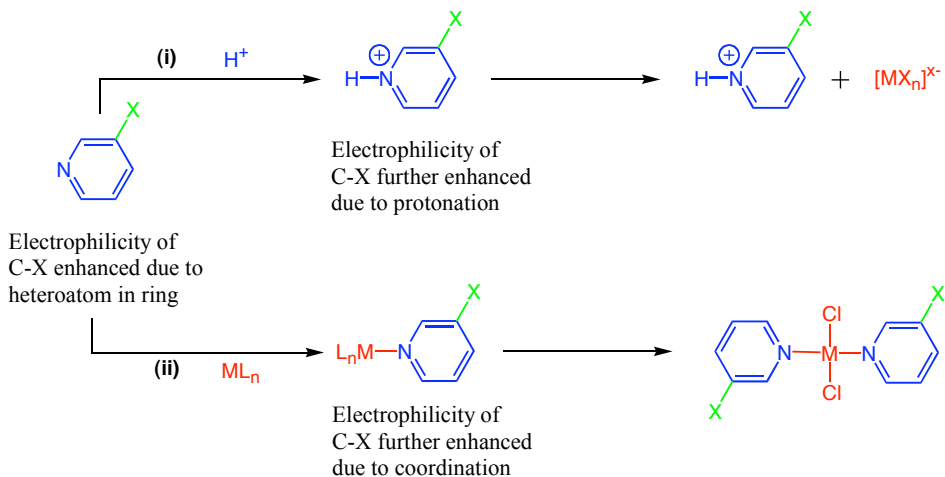


Figure 5. Schematic representation of the contributions to the C–X···O interaction energy from (a) exchange repulsion, (b) electrostatic energy and (c) charge transfer.

4. APPLICATION TO CRYSTAL DESIGN

4.1 Design Strategy Using M–X···X'–C Interactions As Synths

The calculations summarized above, but those considering the electrostatic potential in particular, have led us to anticipate that inorganic halogens have electronic features complementary to suitably "activated" organic halogens such that interactions of the type M–X···X'–C should have an attractive electrostatic energy contribution and in all likelihood should be attractive interactions. It is on this basis that we have pursued a two-pronged approach to crystal synthesis based upon such intermolecular interactions as supramolecular synthons (**Scheme 1**). Halopyridines have been chosen to include the organic halogen as part of a rigid and geometrically well-defined molecular component. The presence of ring nitrogen atom also exerts an electron withdrawing effect on the halogen substituent enhancing its electrophilicity. This effect has then been accentuated by either (i) protonation of the ring nitrogen atom or (ii) coordination through nitrogen to a metal center, and is expected to lead to a positive electrostatic potential along the axial approach to the C–X group, with the greatest effect being seen for the heavier halogens. In the first approach, the inorganic halogen with which the C–X group is intended to interact is provided by a perchlorometallate anion to accompany the halopyridinium cations. The second strategy allows coordinated chloride ligands to be present on the same (neutral) building blocks as the halopyridine ligand.



Scheme 1. Two approaches for combining nucleophilic inorganic halogens (M–X) with electrophilic organic halogens (C–X') for construction of network propagated via M–X···X'–C interactions. Reproduced from ref. 20 with permission of the American Chemical Society.

A family of ionic compounds $[\text{HpyX-3}]_2[\text{CoCl}_4]$ (pyX-3 = 3-halopyridine, X = I, Br, Cl, F) have been prepared and crystallographically characterized [16] (**Figure 6**). All exhibit N–H···Cl–Co hydrogen bonds

linking cations and anions. All but the fluoropyridinium salt also show Co–Cl···X–C interactions with geometries that are approaching linearity at the organic halogen, but markedly angular at the inorganic halogen. Analogous interactions have been observed for [HpyX-n]₂[CoX'₄] (X = Cl, Br; X' = Cl, Br; n = 2, 3, 4) [17]. The M–Cl···X–C interaction geometry is consistent with that anticipated from our analysis of the likely behavior of the inorganic and organic halogens used as nucleophiles and electrophiles, respectively and the interaction can be referred to as a halogen bond [18,19]. The absence of Co–Cl···F–C interactions in the crystal structure of [HpyF-3]₂[CoCl₄] suggests that such an interaction may be repulsive, probably due to a repulsive electrostatic component. This is consistent with the findings of Lommerse et al. regarding possible C–F···O interactions [13] and is confirmed by our own calculations on the electrostatic potential surrounding C–F groups [1,20].

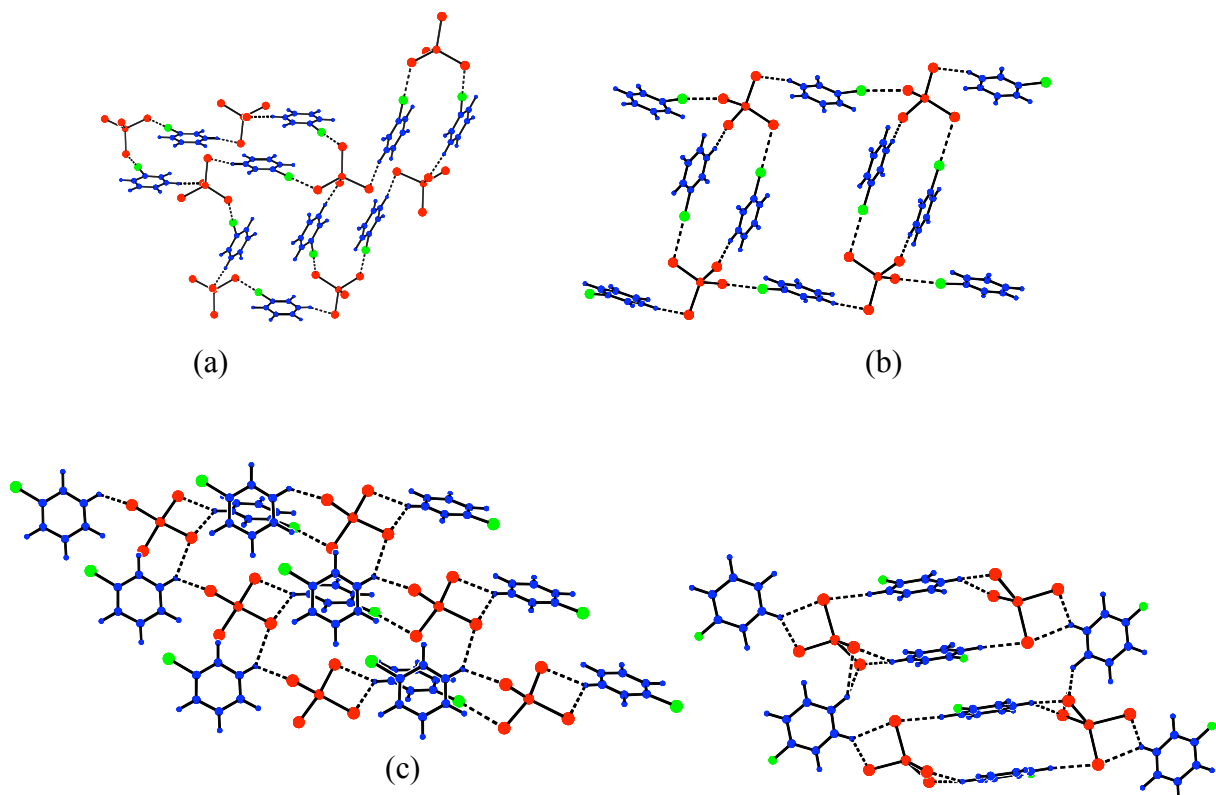


Figure 6. (a) A (4,4) grid network formed by [HpyI-3]₂[CoCl₄], (b) a ladder network formed by [HpyBr-3]₂[CoCl₄] and (c) a (4,4) grid network formed by [HpyCl-3]₂[CoCl₄], each involving N–H···Cl–Co hydrogen bonds and Co–Cl···X–C halogen bonds linking cations and anions. (d) Network formed by [HpyF-3]₂[CoCl₄] involving N–H···Cl–Co and C–H···Cl–Co hydrogen bonds, but no Co–Cl···F–C interactions. Color scheme: anions (red), cations (blue), organic halogen (green). Figures (a)–(c) reproduced from ref.16 with permission of the Royal Society of Chemistry.

In adopting the second strategy shown in Scheme 1, we have prepared a family of compounds *trans*-[MCl₂(pyX-3)₂] (M = Pd, Pt X = I, Br, Cl, F) [20]. Like their ionic counterparts (vide supra) the crystal structures of these compounds (for X ≠ F) comprise networks based upon M–Cl···X–C interactions with geometries that are quite angular at inorganic halogen, but approaching linearity at the organic halogen. The structures fall into two main types, namely those in which the molecules are connected via M–Cl···X–C interactions to two neighbors and those in which such interactions provide links to four neighbors (**Figure 7**). The fluoropyridine-containing compounds again do not form M–Cl···F–C interactions, and calculations on *trans*-[PdCl₂(pyF-3)₂] suggest that the electrostatic contribution to a putative M–Cl···F–C interaction would be repulsive. Rather, the *trans*-[MCl₂(pyF-3)₂] crystal structures are based predominantly upon C–H···Cl–M hydrogen bonds and π-stacking interactions between fluoropyridine rings.

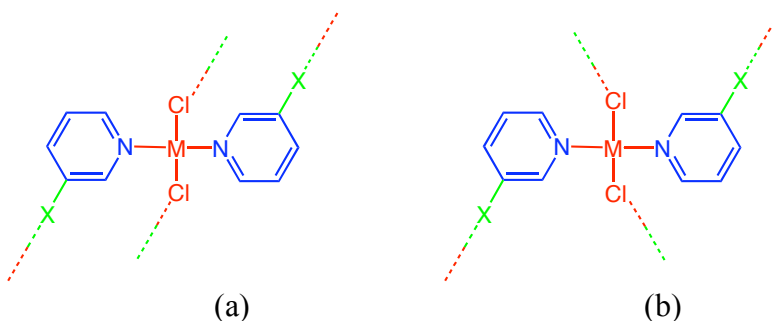
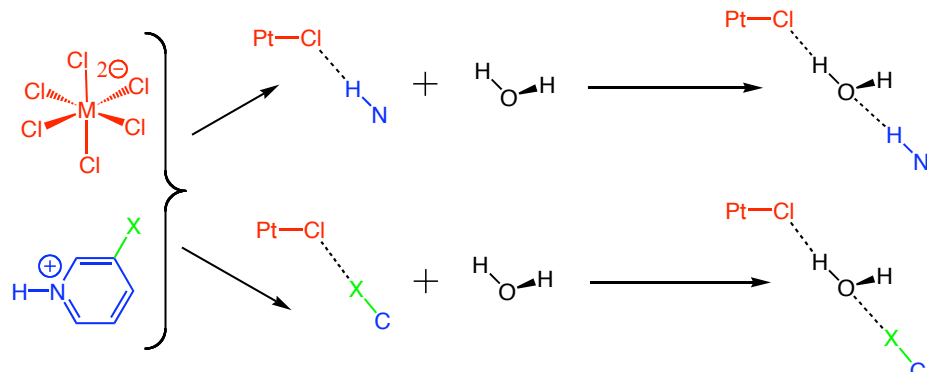


Figure 7. Two types of networks found for *trans*-[MCl₂(pyX-3)₂] compounds, involving (a) two M-Cl···X-C interactions to each of two neighbors and (b) one M-Cl···X-C interaction to each of four neighbors.

4.2 Resistance of M-X···X'-C Interactions To Water Molecule Insertion

A third set of compounds has allowed us to examine solvent incorporation in crystal growth, an almost universal issue in crystal engineering. Specifically we have examined the effect of water incorporation in the salts [HpyX-3]₂[PtCl₆] (X = I, Br), which in the absence of water would be expected to form networks based upon N-H···Cl-Pt hydrogen bonds and Pt-Cl···X-C halogen bonds by analogy to the perchlorocobaltate and perchlorocuprate systems previously mentioned [21]. In principle the water molecules have the necessary donor and acceptor functions to insert into either the hydrogen bonds or halogen bonds as shown in Scheme 8. In the three structures studied (including two polymorphs for [HpyI-3]₂[PtCl₆].2H₂O) insertion of water molecules occurs exclusively into the hydrogen bonds leaving the halogen bonds intact, as illustrated in **Figure 8** for [HpyBr-3]₂[PtCl₆].2H₂O.



Scheme 2. The two types of interaction, N-H···Cl-Pt hydrogen bonds (top) and Pt-Cl···X-C halogen bonds (bottom) expected to be present in the crystal structures of [HpyX-3]₂[PtCl₆] (X = I, Br) and the possible means of insertion of a water molecule into each type of interaction.

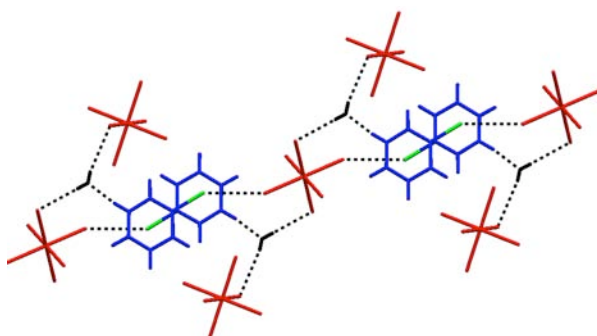


Figure 8. View of the crystal structure [HpyBr-3]₂[PtCl₆].2H₂O showing N-H···O and O-H···Cl-Pt hydrogen bonds along with Pt-Cl···Br-C interactions [21].

5. CONCLUSIONS

The anisotropic electron distributions around terminally bonded halogens manifest themselves in similarly anisotropic electrostatic potential distributions. While the potential is negative in all directions for inorganic halogens ($M-X$), the potential distribution can range from negative to positive for suitably chosen (or "activated") organic halogens ($C-X$). Thus, pairings of inorganic and organic halogens can be used in forming directional $M-X\cdots X'-C$ interactions (halogen bonds) for supramolecular assembly. We have developed such an approach and illustrated it herein with examples using neutral and ionic molecular units to construct crystals in which $M-Cl\cdots X-C$ halogen bonds play a structure directing role. In each case the organic halogen is part of a halopyridine moiety for which the halogen has been further activated towards halogen bond formation either by protonation of the pyridine or its coordination to a metal center. These studies also illustrate that $M-Cl\cdots F-C$ interactions are not formed in the corresponding fluoropyridine-containing compounds. Finally we refer to a study in which hydrates are formed for the salts $[HpyX-3]_2[PtCl_6]$ ($X = I, Br$). While water molecule incorporation could in principle disrupt either the anticipated hydrogen bonds or halogen bonds it is only the latter that remain unaffected.

6. ACKNOWLEDGEMENTS

Support of this work from the EPSRC (GR/R68733/01) and the University of Sheffield is gratefully acknowledged. The Erasmus/Socrates program is thanked for support of the exchange visits of GME and LAM. Support from the Petroleum Research Fund, the ACA, and the Royal Society, which facilitated the participation of LB in the 2004 ACA Transactions Symposium, is greatly appreciated.

7. REFERENCES

- [1] L. Brammer, E.A. Bruton and P. Sherwood, *Cryst. Growth Des.* **1** (2001) 277.
- [2] F.H. Allen, *Acta Crystallogr.* **B58** (2002) 380.
- [3] A cone correction was applied. See J. Kroon and J.A. Kanters, *Nature* **248** (1974) 667.
- [4] L. Brammer, J.K. Swearingen, E.A. Bruton and P. Sherwood, *Proc. Nat. Acad. Sci., USA* **99** (2002) 4956.
- [5] J.C. Mareque Rivas and L. Brammer, *Inorg. Chem.* **37** (1998) 4756.
- [6] G.R. Lewis, and A.G. Orpen, *Chem. Commun.* (1998) 1873.
- [7] A. Angeloni and A.G. Orpen, *Chem. Commun.* (2001) 343.
- [8] B. Dolling, A.L. Gillon, A.G. Orpen, J. Starbuck and X.-M Wang, *Chem. Commun.* (2001) 567.
- [9] M.T. McBride, T.-J.M. Luo and G.T. Palmore, *Cryst. Growth Des.* **1** (2001) 39.
- [10] T.-J.M. Luo and G.T. Palmore, *Cryst. Growth Des.* **2** (2002) 337.
- [11] R. Banerjee, G.R. Desiraju, R. Mondal and J.A.K. Howard, *Chem. Eur. J.* **10** (2004) 3373.
- [12] N. Ramasubbu, R. Parthasarathy and P. Murray-Rust *J. Am. Chem. Soc.* **108** (1986) 4308.
- [13] J. P.M. Lommerse, A.J. Stone, R. Taylor and F.H. Allen *J. Am. Chem. Soc.* **118** (1996) 3108.
- [14] S.L. Price, A.J. Stone, J. Lucas, R.S. Rowland, A.E. Thornley, *J. Am. Chem. Soc.* **116** (1994) 4910.
- [15] (a) S.C. Nyburg, W. Wong-Ng, *Proc. R. Soc. London* **A367** (1979) 29. (b) S.C. Nyburg, C.H. Faerman, *Acta Crystallogr.* **A41** (1985) 274.
- [16] L. Brammer, G. Minguez Espallargas and H. Adams, *CrystEngComm* **5** (2003) 343.
- [17] R.D. Willett, F. Awwadi, R. Butcher, S. Haddad and B. Twamley, *Cryst. Growth Des.* **3** (2003) 301.
- [18] A.C. Legon, *Angew. Chem. Int. Ed.* **38** (1999) 2687.
- [19] E. Corradi, S.V. Meille, M.T. Messina, P. Metrangolo and G. Resnati, *Angew. Chem. Int. Ed.* **39** (2000) 1782.

- [20] F. Zordan, L. Brammer and P. Sherwood, *J. Am. Chem. Soc.* **127** (2005) 5979.
- [21] F. Zordan and L. Brammer, *Acta Crystallogr.* **B60** (2004) 512.

BORONIC ACIDS AS VERSATILE SUPRAMOLECULAR REAGENTS

Christer B. Aakeröy, John Desper, Brock Levin, and Debra J. Salmon
Dept. of Chemistry, Kansas State Univ., Manhattan, KS, 66506, USA
aakeroy@ksu.edu

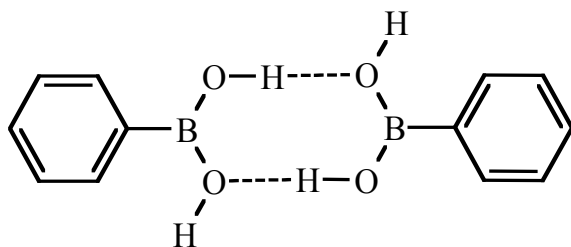
1. ABSTRACT

Crystal engineering and supramolecular synthesis is governed by the structural consequences of intermolecular forces, and by the way in which such interactions are utilized for controlling the assembly of molecules into predictable structural motifs. A vital part of crystal engineering is thus dedicated to identifying robust intermolecular synthons that can be used as reliable connectors between molecules. In this paper we describe how the hydrogen-bond capabilities of boronic acids R-B(OH)₂ can be translated into versatile co-crystallizing tools capable of forming heteromeric structure-directing hydrogen-bond interactions with a variety of complementary structural partners e.g. 2-aminopyrimidine and 4,4'-bipyridine.

2. INTRODUCTION

The synthesis of supramolecular assemblies composed of several different molecular fragments [1] held together by non-covalent forces is still a relatively young discipline and our understanding of how groups of molecules communicate, bind, organize, and function, is still incomplete [2]. Despite recent advances in supramolecular synthesis, the detailed control over the assembly of molecules into ordered solids remains an elusive goal, and we are rarely able to predict the structure of a simple crystalline material. Much more work is required to increase the choice of reliable building blocks of low-dimensional architectures and, more importantly, to allow us to rationalize and predict structural arrangements of molecules within new crystalline materials. An enhanced understanding of intermolecular forces may also enable us to better address crucial questions about polymorphism and crystal morphology.

Boronic acids are receiving considerable attention from the synthetic community due to the fact that they are invaluable intermediates in very versatile and useful aryl-aryl cross-coupling reactions [3]. However, the same chemical functionalities have, by and large [4, 5], remained unexplored as supramolecular connectors despite the fact that aryl-boronic acids can produce hydrogen-bonded dimers and ladders akin to motifs observed in carboxylic acids and carboxamides, Scheme 1 [6].



Scheme 1. Head-to-head hydrogen-bonded motif common among phenylboronic acids.

The boronic acid moiety may represent a potentially versatile supramolecular synthetic tool but there are still no systematic structural studies that have examined how this particular moiety competes or interacts with other hydrogen-bond functionalities e.g. carboxylic acids, carboxamides, oximes, 2-aminopyridines, etc.

In this study we employ co-crystallization techniques as a way of probing the supramolecular behavior of boronic acids, and we demonstrate that they are capable of engaging in a variety of predictable structure-directing intermolecular interactions. These results indicate that boronic acids may become an important addition to the tools employed in hydrogen-bond based crystal engineering and supramolecular synthesis. Here we present the crystal structures of 3-methylphenylboronic acid **1**, (4,4'-bipyridine)₃:(3-methylphenylboronic acid)₂ **2**, 2-amino-4-methylpyrimidine:(4-methylphenylboronic acid)₂ acid **3**, and 4,4'-bipyridine:4-carboxyphenyl boronic acid **4**, Table 1.

3. EXPERIMENTAL

3.1 Crystallography

X-ray data were collected on a Bruker SMART 1000 four-circle CCD diffractometer using a fine-focus molybdenum K α tube. Data were collected using SMART [7]. Initial cell constants were found by small, widely separated “matrix” runs. Preliminary Laué symmetry was determined from axial images. Generally, an entire hemisphere of reciprocal space was collected regardless of Laué symmetry. Scan speed and scan width were chosen based on scattering power and peak rocking curves. Unless otherwise noted, 0.3 ° scans were used.

Unit cell constants and orientation matrices were improved by least-squares refinement of reflections thresholded from the entire dataset. Integration was performed with SAINT [8] using this improved unit cell as a starting point. Precise unit cell constants were calculated in SAINT from the final merged dataset. Lorenz and polarization corrections were applied, but data were not corrected for absorption. Laué symmetry, space group, and unit cell contents were found with XPREP. Data were reduced with SHELXTL [9]. The structures were solved in all cases by direct methods without incident. In general, hydrogen atoms were assigned to idealized positions and were allowed to ride. Unless otherwise noted, the coordinates of hydrogen atoms engaged in hydrogen-bonding were allowed to refine. Thermal ellipsoids and labeling schemes are shown in **Figure 1** a-d and the crystallographic data are listed in Table 1.

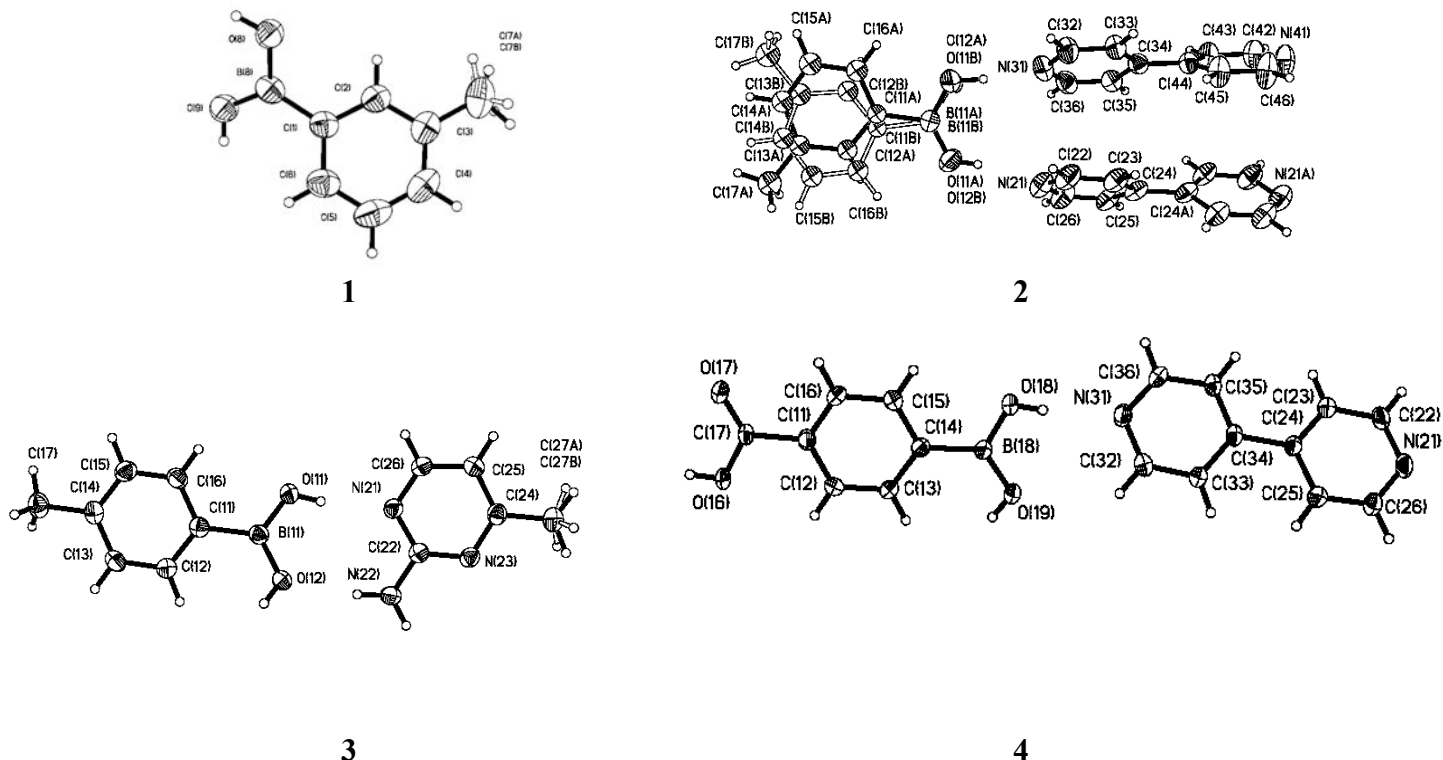


Figure 1. Thermal ellipsoids and labeling schemes for **1-4**.

Table 1

| Structure code | 1 | 2 | 3 | 4 |
|------------------------------|--|--|--|---|
| Systematic name | 3-methylbenzene-boronic acid | (3-methylbenzene-boronic acid) ₂ , (4,4'-bipyridine) ₃ | 2-amino-4-methyl-pyrimidine, 4-methylbenzene-boronic acid | 4-carboxybenzene-boronic acid, 4,4'-bipyridyl |
| Formula moiety | C ₇ H ₉ B O ₂ | (C ₇ H ₉ O ₂ B) ₂ (C ₁₀ H ₈ N ₂) ₃ | (C ₅ H ₇ N ₃) (C ₇ H ₉ B O ₂) | (C ₇ H ₇ B O ₄) (C ₁₀ H ₈ N ₂) |
| Empirical formula | C ₇ H ₉ B O ₂ | C ₄₄ H ₄₂ B ₂ N ₆ O ₄ | C ₁₂ H ₁₆ B N ₃ O ₂ | C ₁₇ H ₁₅ B N ₂ O ₄ |
| Molecular weight | 135.95 | 740.46 | 245.09 | 322.12 |
| Color, Habit | colorless prism | colorless prism | amber prism | colorless prism |
| Crystal system | Monoclinic | Monoclinic | Monoclinic | Triclinic |
| Space group, Z | P2(1)/c, 4 | C2/c, 4 | P2(1)/c, 4 | P1, 1 |
| a, Å | 15.063(4) | 20.2663(10) | 9.5084(10) | 3.9552(8) |
| b, Å | 5.6710(17) | 9.2707(5) | 11.9386(12) | 8.3612(16) |
| c, Å | 9.101(3) | 22.3043(11) | 11.2657(12) | 11.670(2) |
| a, ° | 90.00 | 90.00 | 90.00 | 101.613(3) |
| b, ° | 94.854(5) | 113.787(2) | 102.717(2) | 98.910(4) |
| g, ° | 90.00 | 90.00 | 90.00 | 98.038(4) |
| Volume, Å ³ | 774.6(4) | 3834.6(3) | 1247.5(2) | 367.59(13) |
| Density (g/cm ³) | 1.166 | 1.283 | 1.305 | 1.455 |
| Temperature (K) | 203(2) | 163(2) | 203(2) | 203(2) |
| X-ray wavelength | 0.71073 | 0.71073 | 0.71073 | 0.71073 |
| m, (mm ⁻¹) | 0.081 | 0.083 | 0.089 | 0.104 |
| Q _{min} (°) | 2.71 | 2.00 | 2.20 | 1.81 |
| Q _{max} (°) | 27.45 | 28.26 | 28.28 | 28.23 |
| Reflections | | | | |
| collected | 4389 | 13899 | 9199 | 2657 |
| independent | 1677 | 4428 | 2873 | 2225 |
| observed | 656 | 2332 | 2009 | 1860 |
| Threshold expression | I > 2s(I) | I > 2s(I) | I > 2s(I) | I > 2s(I) |
| R ₁ (observed) | 0.0387 | 0.0514 | 0.0474 | 0.0446 |
| wR ₂ (all) | 0.0997 | 0.1381 | 0.1407 | 0.1085 |

3.3 Synthesis

3-Methylphenylboronic acid was synthesized by adding the Grignard reagent of 3-bromotoluene to a THF solution of triisopropyl borate. The mixture was stirred at -78 °C for one hour, whereupon the reaction was quenched with sulfuric acid and the desired product was subsequently extracted with ether and recrystallized from hot water to produce colorless needles; yield: 84%; mp: 160-163 °C. 4-Methylphenylboronic acid was prepared in the same way; yield 83%; m.p. 244-246 °C. 4-carboxyphenyl boronic acid was synthesized by oxidation with potassium permanganate of 4-methylphenyl boronic acid; yield 59%; m.p. 232-233 °C.

The crystal structure determination of **1** shows that the two hydroxyl groups are arranged in a *syn* and *anti* manner, respectively. [10] The primary hydrogen-bond motif in this structure, Table 2, is a head-to-head dimeric interaction composed of two symmetry related O-H...O interactions (similar to a classic dimeric carboxylic acid motif) **Figure 2**.

Table 2.
Hydrogen-bond geometries for 1-4

| | D-H | H...A | D...A | \angle (DHA) | Generator for A |
|-----------------|-----------|-----------|------------|----------------|-------------------|
| 1 | | | | | |
| O8-H8...O9 | 0.922(19) | 1.804(19) | 2.7241(19) | 175.5(18) | -x, -y, -z |
| O9-H9...O8 | 0.873(19) | 1.848(19) | 2.7024(19) | 165.6(18) | X, -y-1/2, z-1/2 |
| 2 | | | | | |
| O11A-H11C...N21 | 0.83(3) | 1.99(2) | 2.80(2) | 170(3) | |
| O12B-H12D...N21 | 0.86(4) | 1.99(2) | 2.83(3) | 167(3) | |
| O11B-H11D...N31 | 0.92(4) | 1.793(19) | 2.70(3) | 169(2) | |
| O12A-H12C...N31 | 0.98(3) | 1.793(19) | 2.76(2) | 169.9(18) | |
| 3 | | | | | |
| O11-H11...N21 | 0.85(2) | 1.93(2) | 2.7719(16) | 169.8(18) | |
| N22-H22A...O12 | 0.894(19) | 2.131(19) | 2.9987(17) | 163.4(16) | |
| N22-H22B...O11 | 0.90(2) | 2.19(2) | 3.0003(18) | 151.0(16) | x, -y-1/2, z-1/2' |
| O12-H12...N23 | 0.80(2) | 2.03(2) | 2.8094(17) | 164.3(18) | -x, y+1/2, -z+1/2 |
| 4 | | | | | |
| O16-H16...N21 | 0.82 | 1.85 | 2.667(3) | 173.9 | |
| O18-H18...N31 | 0.82 | 2.00 | 2.813(3) | 173.0 | |
| O19-H19...O17 | 0.82 | 2.11 | 2.839(2) | 148.8 | |

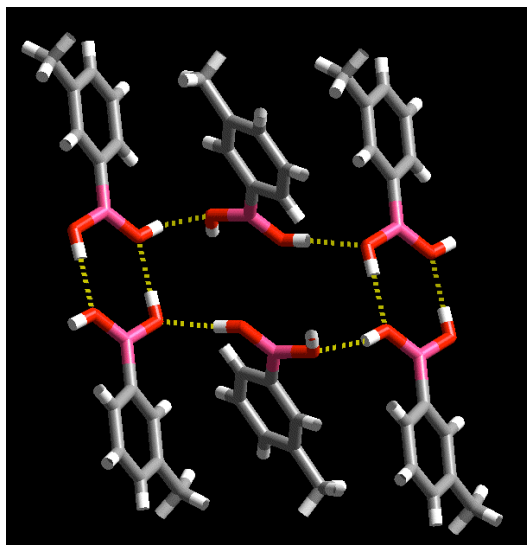


Figure 2. Head-to-head hydrogen-bonded dimers interconnected into an infinite ladder in the crystal structure of 1.

The centrosymmetric dimers are further connected into a ladder like structure with the same connectivity as the motif commonly displayed by primary amides [11]. However, whereas the latter are often more or less planar, the boronic acid ladder is composed of dimers that are arranged in alternating perpendicular fashion along the ladder.

The crystal structure of **2** [12] demonstrates that a pyridyl moiety is capable of breaking the boronic acid dimer and replacing it with near-linear O-H \cdots N hydrogen bonds (Table 2), which is similar to the well-known structure-directing COOH \cdots py [13] and R-OH \cdots py synthons, **Figure 3**[14].

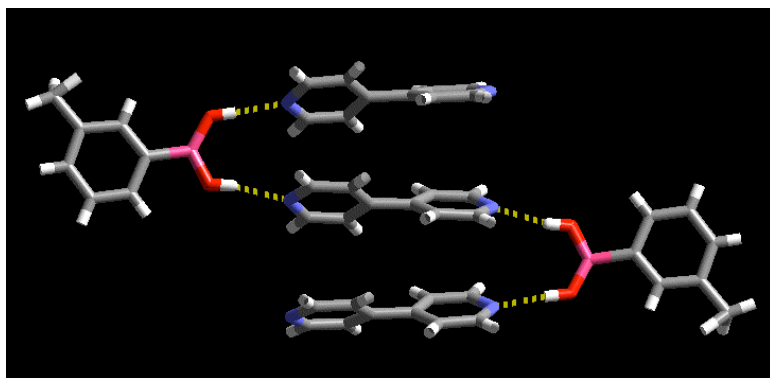


Figure 3. Discrete pentameric supermolecule in **2** assembled via four (two equivalent) O-H \cdots N hydrogen-bond interactions.

One part of the hydrogen-bonded motif in **2** is akin to the interactions that commonly take place between resorcinol-based components and bipyridyl-type compounds [15]. However, the separation between OH groups in boronic acid is not sufficient to allow for the formation of a discrete tetramer as observed in resorcinol:4,4'-bipy [16]. The end result is a discrete pentameric supermolecule that leaves two terminal nitrogen atoms, N(41) without any strong hydrogen-bond interactions. There are also no C-H \cdots N interactions involving this nitrogen atom (the shortest N(41) \cdots C distance is over 3.4 \AA).

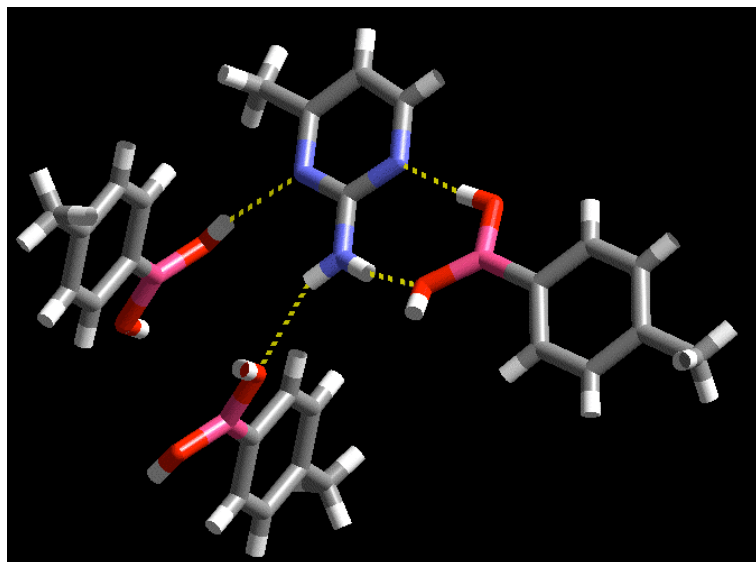


Figure 4. The complementarity of 2-aminopyrimidine:boronic acid drives the formation of the co-crystal in **3**. The additional proton on boronic acid provides a crosslink.

A paper by Etter *et al* [17] reporting the crystal structure of a carboxylic acid: 2-aminopyrimidine co-crystal provided a classic example of how heteromeric complementary hydrogen-bond interactions can be employed as the driving force for binary molecular solids. The crystal structure of **Figure 4** shows that the boronic acid moiety engages in an R₂(8) motif with 2-aminopyrimidine (as do carboxylic acids), Table 2. However, the additional hydrogen-bond donor on boronic acid creates a more complex 3-D motif compared with the discrete 0-D motif (between 2-aminopyrimidine and monocarboxylic acids) or 1-D motif (in the case of 2-aminopyrimidine and dicarboxylic acids).

Finally, given the fact that both carboxylic acids and boronic acids are capable of forming strong and directional O-H···N hydrogen bonds to a pyridyl moiety, the crystal structure of **4** [18], does not reveal any surprising primary intermolecular interactions, **Figure 5**. The primary interaction is likely to be the py···COOH hydrogen bond; a common supramolecular interaction that has been instrumental in the design of one- and two-dimensional supramolecular architectures, such as infinite chains, [19] honeycomb layers,[20] and sheets,[21]. Since the reaction was carried out in a 1:1 ratio, this leaves a good hydrogen-bond donating moiety, the B(OH)₂ group) and one good hydrogen-bond acceptor, the remaining pyridyl moiety. As demonstrated in previous studies [4, 5] the self-complementary boronic acid dimer can be broken in favor of a B(OH)₂···py interaction, which is exactly what happens in the crystal structure of **4**.

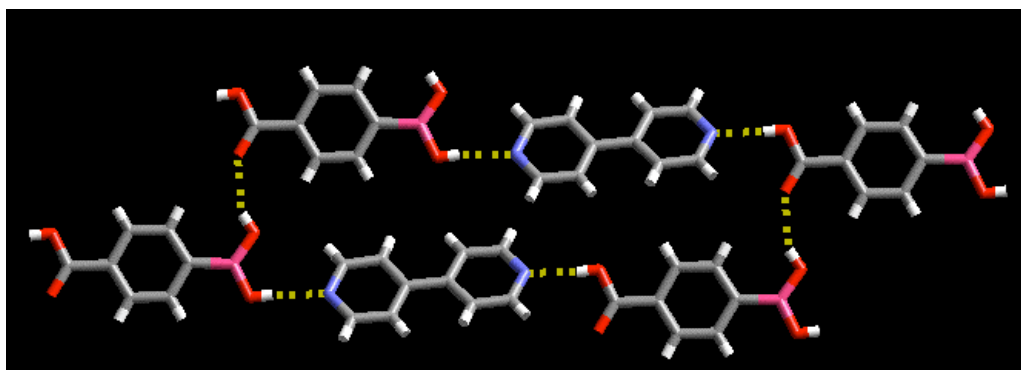


Figure 5. Horizontal infinite chains of bipy and 4-carboxyphenylboronic molecules in the crystal structure of **4** connected through O-H···N hydrogen bonds.

The combination of the acid···py, B(OH)₂···py, and B(OH)₂···acid hydrogen bonds leads to infinite chains of alternating bipy and 4-carboxyphenyl boronic acid held together via COOH···py and R-OH···py, which are cross-linked by O-H···O interactions (from boronic acid to carboxylic acid) resulting in a 2-D hydrogen-bonded sheet.. All primary hydrogen-bond donors and acceptors are satisfied and the main intermolecular interactions in **4** are readily rationalized based upon existing structural information.

This study has demonstrated that the boronic acid moiety may be incorporated into more complicated modular supramolecular synthetic strategies by virtue of its ability to form predictable hydrogen-bond interactions with a variety of well-known acceptor sites. It remains to be seen how reliable this moiety is, or how it can be made to fit in a hierarchical approach to the assembly of ternary and higher-order supermolecules and molecular solids. However, these results indicate that it can become a useful building block along the lines of carboxylic acids, carboxamides and oximes in the construction of robust and reliable extended architectures.

4. ACKNOWLEDGEMENTS

Financial support from NSF (CHE-0316479) and Kansas State University is gratefully acknowledged.

CCDC 249705 – 249708 contains the supplementary crystallographic data for this paper. These data can be obtained free of charge via www.ccdc.cam.ac.uk/data_request/cif, by emailing data_request@ccdc.cam.ac.uk, or by contacting The Cambridge Crystallographic Data Centre, 12, Union Road, Cambridge CB2 1EZ, UK; fax: +44 1223 336033.

5. REFERENCES

- [1] N. Miyaura and A. Suzuki, *Chem. Rev.* **95** (1995), 2457.
- [2] C.B. Aakeröy, J. Desper, and B. Levin, *CrystEngComm.*, **7**, (2005), 102.

- [3] S.J. Rettig and J. Trotter, *Can. J. Chem.* **55** (1977), 3071.
- [4] SMART v5.060, © 1997 - 1999, Bruker Analytical X-ray Systems, Madison, WI.
- [5] SAINT v6.02, © 1997 - 1999, Bruker Analytical X-ray Systems, Madison, WI.
- [6] SHELXTL v5.10, © 1997, , Bruker Analytical X-ray Systems, Madison, WI.
- [7] Two $-CH_3$ rotamers were included in the structure model, with common carbon temperature factors and coordinates, and total occupancy constrained to 1.0.
- [8] L. Leiserowitz and F. Nader, *Acta Crystallogr. Sect. B*, **33** (1977), 2719.
- [9] Colourless needles, m.p. 62–65 °C, obtained via slow evaporation from 1:1 ethanol/water.
- [10] (a) C.B. Aakeroy, A.M. Beatty and B.A. Helfrich, *J. Am. Chem. Soc.* **124** (2002), 14425. (b) P. Vishweshwar, A. Nangia and V.M. Lynch, *Cryst. Growth Des.* **3** (2003), 783. (c) R. D. Bailey Walsh, M.W. Bradner, S. Fleischman, L.A. Morales, B. Moulton, N. Rodriguez-Hornedo and M.J. Zaworotko, *Chem. Commun.* **186** (2003) 186. (d) T. Nguyen, F.W. Fowler and J.W. Lauher, *J. Am. Chem. Soc.* **123** (2001), 11057.
- [11] Two superimposed boronic acid molecules were observed, occupying nearly the same volume but differing in the orientation of the *m*- CH_3 group. Thermal parameters for the two $B(OH)_2$ moieties were highly correlated and were therefore combined pairwise with free variables. Geometry for the two boronic acid molecules was constrained with a SHELXTL “SAME” command.
- [12] L.R. MacGillivray, J.L. Reid and J.A. Ripmeester, *J. Am. Chem. Soc.*, **122** (2000), 7817.
- [13] The separation between hydroxylic protons in 1,3-resorcinol is 3.5 Å, which is ideally suited for bringing two aromatic systems together for a 2+2 photodimerization reaction.
- [14] M.C. Etter and D.A. Adsmond, *J. Chem. Soc., Chem. Commun.* (1990) 589.
- [15] The molecule lies on an approximate center of symmetry, with the boronic and carboxylic acid groups nearly superimposed. The structure refined poorly in the centrosymmetric space group P-1 and symmetry was decreased to P1 (Friedel coverage = 37%). Attempts to refine hydroxyl hydrogen atoms led to unreasonable bond distances; these hydrogen atoms were constrained to idealized positions with the SHELX “AFIX 83” constraint.
- [16] N. Shan, A.D. Bond, and W. Jones, *New J. Chem.* **2003**, 2, 365; N. Shan, E. Batchelor, and W. Jones, *Tetrahedron Lett.* **2002**, 43, 8721; R. Liu, S. Valiyaveettil, K.-F. Mok, J.J. Vittal, and A.K.M. Hoong, *CrystEngComm.* **2002**, 4, 574.
- [17] C.V.K. Sharma and M.J. Zaworotko, *Chem. Commun.* (1996), 2655; B.R. Bhogala and A. Nangia, *Cryst. Growth Des.* **3**, (2003), 547; B.-Q. Ma and P. Coppens, *Chem. Commun.* (2003), 2290.
- [18] K.K. Arora and V.R. Pedireddi, *J. Org. Chem.* **68**, (2003), 9177; P. Vishweshwar, A. Nangia, and V.M. Lynch, *J. Org. Chem.* **67**, (2002), 556.

HYDROGEN-BONDED HOST FRAMEWORKS WITH TUNABLE CAVITIES: STRUCTURAL CHARACTERIZATION AND INCLUSION-BASED SEPARATIONS OF MOLECULAR ISOMERS

Matthew J. Horner, Sara Grabowski, Kevin Sandstrom, K. Travis Holman, Mamoun Bader
and Michael D. Ward

*Dept. of Chemical Engineering and Materials Science, Univ. of Minnesota, Amundson Hall, 421
Washington Ave SE, Minneapolis, MN, 55455, USA
wardx004@umn.edu*

Woo-Sik Kim

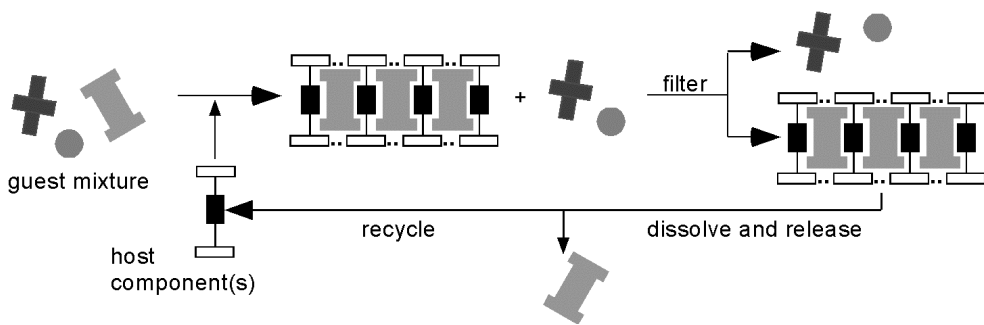
Dept. of Chemical Engineering, Kyung-Hee Univ. Kyungki-do 449-701, Korea

1. ABSTRACT

Single crystal X-ray diffraction reveals that inclusion compounds formed from **G₂MDS** and **G₂TMBDS** hosts (**MDS** = mesylenedisulfonate; **TMBDS** = 2,4,5,6-tetramethylbenzenedisulfonate) and various isomeric methylated benzene guests crystallize in polar space groups with guests occupying one-dimensional channels between sheets of hydrogen-bonded guanidinium ions and sulfonate moieties. The inclusion selectivity for isomeric mixtures of trimethylbenzenes and tetramethylbenzene guests by these host frameworks has been examined. The organic residues of the **MDS** and **TMBDS** pillars mimic the isomeric trimethylbenzenes and tetramethylbenzenes, respectively, suggesting an avenue to a separations protocol based on molecular recognition during inclusion and subsequent crystallization. Pairwise competition experiments, in which inclusion compounds are crystallized from solutions containing a mixture of two molecular isomers, map the inclusion selectivity of a particular host as a function of guest content in solution. The single crystal structures suggest that guest inclusion selectivity is governed by the ability of a host to achieve efficient packing with the guest molecules and its ability to allow efficient guest-guest packing in the one-dimensional channels. Consequently, the more compliant **G₂MDS** host exhibits higher selectivities for guest inclusion. Overall, the selectivity patterns appear to reflect size and shape compatibility between the host and guest, suggesting opportunities for separations of isomers based on straightforward crystallization processes.

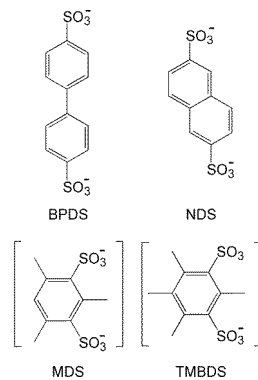
2. INTRODUCTION

Distillation, crystallization, and liquid-liquid extractions are commonly employed unit operations that isolate constituents of a mixture based on differences in volatility or solubility. If the components of a mixture have extremely similar properties, as is generally the case for molecular isomers, traditional separation methods can be unfeasible to the extent that less conventional approaches, such as selective sorption or inclusion within a host material, may be required. Whereas traditional porous materials, such as inorganic zeolites, have been studied extensively and have achieved considerable commercial success in this respect,[1] modern “designer” inclusion materials, such as molecule-based organic[1,2] and metal-organic[4] hosts, also hold considerable promise for selective inclusion. Unlike covalent host frameworks, which rely on selective sorption and diffusion through pre-existing pores, the “pores” in non-covalent frameworks are typically created during assembly of the crystalline inclusion compound and are generally only sustainable when occupied by guest molecules.[5] Nevertheless, if the host is selective, the preferentially included guest can be separated from a solution mixture by filtration of the crystallized inclusion compound. The guest can then be retrieved, for example by dissolution and extraction, under mild conditions and the host material can be recycled (Scheme 1).



Scheme 1.

Organic or molecular hosts are particularly appealing candidates for selective inclusion because their general solubility allows for both effective retrieval of included guests and recycling of the host material. Serious limitations still exist, however, with respect to the design of an appropriate organic host for a particular separations application. For example, many traditional organic hosts, such as (thio)urea,[6] tri-*o*-thymotide,[7] Dainin's compound,[8] perhydrotriphenylene,[9] and cyclotrimeratrylene,[10] cannot be chemically modified or tailored without the concomitant loss of the inclusion capabilities of the host. Although some molecular hosts, such as Werner complexes[11] and many diol hosts,[12,13] are amenable to chemical modification, such modifications rarely lead to *predictable* changes in the size or shape of the inclusion cavities. Therefore, even though numerous inclusion hosts are available and strategies for the *de novo* molecular-level design of hosts have been proposed,[3] a particular separation typically requires the design and testing of a variety of hosts, frequently with rather disparate compositions and architectures. In contrast, libraries of homologous inclusion hosts, in which the composition of the host is systematically adjusted but key architectural features are retained, may provide a route to effective and facile optimization of a particular separation.



We have recently reported a family of homologous inclusion hosts that fulfill the above criteria.[14] Guanidinium (**G**) salts of organosulfonate anions (**S**) readily form lamellar motifs through hydrogen bonding between the N-H moieties of the **G** cations and the sulfonate moieties of the **S** anions.[14,15] The H-bonded **GS** lamellae adopt either a “quasi-hexagonal” arrangement (**Figure 1**) that reflects the complementary symmetries of the **G** ions (D_{3h}) and the sulfonate moieties (C_{3v}), or a closely related, albeit less common, “shifted-ribbon” motif (not shown). In either arrangement, the **GS** lamellae can be pillared in the third dimension by the readily modified organic residues of organodisulfonate anions, thereby creating inclusion cavities between the sheets that are occupied by guest molecules during assembly of the **GS** host lattice. The lamellar character of the **GS** host framework persists for a diverse collection of pillars and guests, a feature that can be partially attributed to an inherent ability of the **GS** sheet to pucker about an axis of hydrogen bonds connecting adjacent rigid one-dimensional **GS** “ribbons,” thus allowing the host to optimize packing of the pillars and guests. Furthermore, these hosts can adopt several architectures that differ with respect to the manner in which the pillars connect adjacent sheets.[16]

Our laboratory recently capitalized on the unique characteristics of these pillared hosts to separate molecular isomers of xylenes and dimethylnaphthalenes,[17] demonstrating that remarkable selectivities could be achieved by choosing hosts with inclusion cavity sizes that straddled the steric boundary between two host architectures –in this case the “discrete bilayer” and the “simple brick” forms – for a particular set of guest isomers (**Figure 1**). This protocol relied on linear organodisulfonate pillars in which the sulfonate groups were strictly antiparallel, for example, 4,4'-biphenyldisulfonate (**BPDS**) and 2,6-naphthalenedisulfonate (**NDS**). Our laboratory, however, also has reported inclusion compounds based on “bent,” or “banana-shaped,” pillars, such as mesitylenedisulfonate (**MDS**) and 2,4,5,6-tetramethylbenzenedisulfonate (**TMBDS**). These inclusion compounds adopted layered orthorhombic and monoclinic brick architectures, with the **GS** sheets puckered as a consequence of the geometric constraints imposed by the pillar (rather than puckering driven by close-packing between pillars and guests for linear pillars).[18] Furthermore, the geometry of the bent pillar and the continuous architecture of the simple brick host enforce polar symmetry (*Imm2* for the orthorhombic compounds). The guests in these compounds were confined to one-dimensional channels perpendicular to the pleats of the **GS** sheet (**Figure 2**).

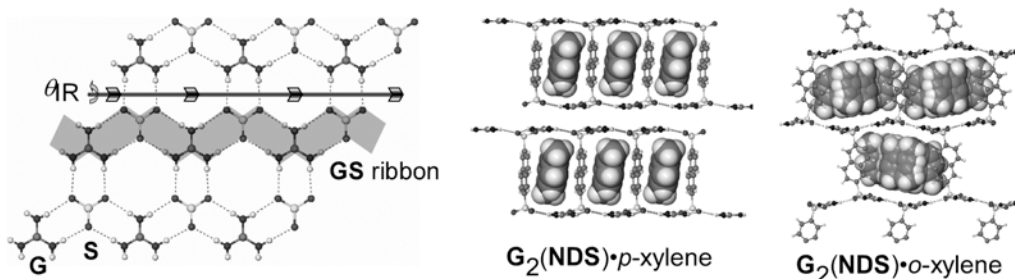


Figure 1. (left) Schematic representation of the **GS** sheet, illustrating the hydrogen-bonding “hinge” about which the sheet puckers to optimize host-guest packing when “straight” pillars are used. (right) The discrete bilayer and simple brick architectures observed for guanidinium-2,6-naphthalenedisulfonate with *p*-xylene and *o*-xylene guests, respectively.

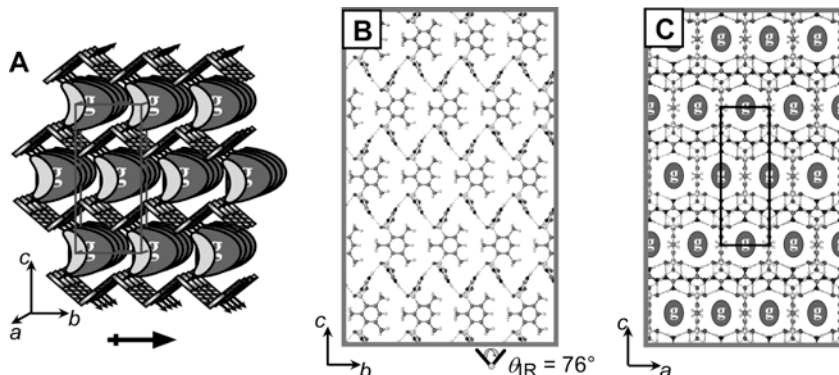


Figure 2. (A) Schematic representation of an inclusion compound prepared with a bent “banana-shaped” organodisulfonate and dipolar guest molecules. The host is inherently polar because the framework can only assemble with all the bent pillars oriented in the same direction. (B, C) Views of a typical inclusion compound, here illustrated by $G_2\text{MDS}\cdot(\text{nitrobenzene})$.

The organic residues of the **MDS** and **TMBDS** pillars mimic isomeric trimethylbenzenes (3MB) and tetramethylbenzenes (4MB), respectively, suggesting they may provide some degree of molecular recognition with these isomers, which is essential for the crystallization-based separations protocol. Furthermore, the size of the channels in these hosts is comparable to the dimensions of the 3MB and 4MB isomers, a characteristic that could yield selectivity due to subtle shape differences among the isomeric guests. We describe herein the crystal structures of several inclusion compounds based on these pillars and guests and the selectivity of guest inclusion by these hosts.

3. RESULTS AND DISCUSSION

3.1 Selectivity And Separations Protocol

Pairwise competition experiments, wherein inclusion compounds are grown from a series of solutions of known guest composition, can be used to determine the dependence of inclusion selectivity on the solution content of the two guests (A and B). The selective preference of a host (**H**) for one compound (A) from the mixture can be described by a *selectivity coefficient* ($K_{A:B}$), defined according to equation (1), where X_A and X_B represent the mole fractions of the two competing guests in the original solution and Y_A and Y_B represent the corresponding mole fractions of the same guests in the resulting inclusion compound. If the selectivity coefficient is constant over the entire range of X_A , the selectivity profile will be symmetrical about a line drawn from the lower right to the upper left corners (**Figure 3**, curves a-d). Symmetrical curves are common for host materials with pre-existing pores and host structures that are unchanged upon guest inclusion.[1a] The $K_{A:B}$ of molecular hosts, however, can be influenced by the relative concentrations of guests in the original solution mixture, affording less symmetrical curves such as that depicted in curve (e) of **Figure 3**.[8] Asymmetric curves also can reflect the formation of structurally dissimilar inclusion compounds for different guests.

$$(1) \quad K_{A:B} = (K_{B:A})^{-1} = Y_A/Y_B \cdot X_B/X_A \quad (X_A + X_B = 1)$$

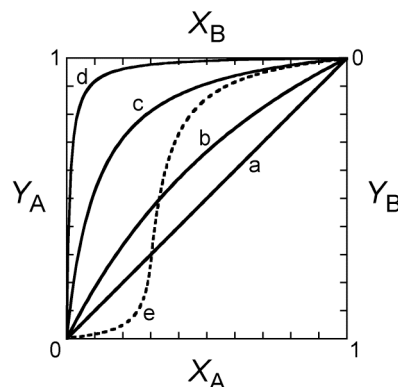


Figure 3. Pairwise competition experiments can be used to map the inclusion selectivity of one guest (A) relative to another (B). The mole fractions of guests in the inclusion compound (Y_A or Y_B) are plotted as a function of the mole fraction of guests in the original solution mixture (X_A or X_B). The selectivity coefficient, $K_{A:B}$ (or $K_{B:A}$) can be extracted from any point on the curve. Larger selectivity coefficients correspond to a greater enrichment of guest A in the inclusion compound. (a) $K_{A:B} = 1$ (no selectivity), (b) $K_{A:B} = (K_{B:A})^{-1} = 2$, (c) $K_{A:B} = (K_{B:A})^{-1} = 10$, (d) $K_{A:B} = (K_{B:A})^{-1} = 100$. (e) $K_{A:B}$ is concentration dependent. Under conditions of low X_A ($0 < X_A < 0.3$) guest B is preferentially included ($K_{A:B} < 1$). At larger X_A ($0.3 > X_A > 1$) the selectivity is inverted ($K_{A:B} > 1$) and guest A is included preferentially.

The inclusion selectivity of molecular isomers by the **GS** hosts with bent pillars was examined by pairwise competition experiments, wherein crystals of inclusion compounds were retrieved from methanolic solutions containing a particular **GS** host and a combined excess of guest isomers. The mole fractions of the two guests in solution were varied and their compositions in the crystallized inclusion compounds were determined by gas chromatography and plotted in a manner identical to **Figure 3**, with X_{guest} and Y_{guest} representing the mole fraction of one of the guests in the original solution and the inclusion compound, respectively.

3.2 Single Crystal Structures Of Inclusion Compounds

G₂MDS and **G**₂TMBDS readily form crystalline inclusion compounds with various trimethylbenzene (3MB) and tetramethylbenzene (4MB) isomers. Single crystal structures for **G**₂MDS·(1,2,4-3MB), **G**₂MDS·(1,3,5-3MB), **G**₂TMBDS·(1,2,3-3MB), **G**₂TMBDS·(1,3,5-3MB), and **G**₂TMBDS·(1,2,3,5-4MB) (Table 1) reveal the anticipated polar host architecture in which the **GS** sheet is highly puckered and the banana-shaped pillars are oriented along the polar *b* axis of the crystals. The guest molecules are confined within 1D corrugated channels, oriented along the *b* axis (**Figure 4**). The guests are offset in the *b* direction with respect to the bent pillars such that they occupy inclusion cavities between “pinch-points” created by the pleats of **GS** sheets. For convenient comparison of these structures, which crystallize in orthorhombic or

monoclinic structures, the crystallographic lattice constants are rearranged at the bottom of Table 1 so that the polar axis is along b for all these compounds. The monoclinic structures deviate from the ideal $Imm2$ space group symmetry due to a slight twist [19] of the disulfonates, which ranges from 11° for $\text{G}_2\text{TMBDS}\cdot(1,2,3\text{-}3\text{MB})$ to 17° for $\text{G}_2\text{TMBDS}\cdot(1,3,5\text{-}3\text{MB})$. This in turn induces a tilt of the guest molecules along the a direction, ranging from 13° to 18° with respect to the normal to the GS sheet. The guests in the $\text{G}_2\text{MDS}\cdot(1,2,4\text{-}3\text{MB})$ and $\text{G}_2\text{TMBDS}\cdot(1,2,3\text{-}3\text{MB})$ structures are disordered over multiple positions and orientations. For $\text{G}_2\text{TMBDS}\cdot(1,2,3\text{-}3\text{MB})$ the guest molecules are disordered over a mirror plane located at the center of the channels parallel to the GS sheets. The guests in $\text{G}_2\text{MDS}\cdot(1,2,4\text{-}3\text{MB})$ are disordered over four positions because they sit on mirror planes that intersect in the center of the guest channels.

Table 1
Crystallographic Data and Selected Structural Features for the Guanidinium Organodisulfonate Inclusion Compounds

| compound | G₂MDS·(1,2,4-3MB) | G₂MDS·(1,3,5-3MB) | G₂TMBDS·(1,2,3-3MB) | G₂TMBDS·(1,3,5-3MB)[18] | G₂TMBDS·(1,2,3,5-4MB) |
|--|--|--|--|--|--|
| formula | $\text{C}_{20}\text{H}_{34}\text{N}_6\text{O}_6\text{S}_2$ | $\text{C}_{20}\text{H}_{34}\text{N}_6\text{O}_6\text{S}_2$ | $\text{C}_{21}\text{H}_{36}\text{N}_6\text{O}_6\text{S}_2$ | $\text{C}_{21}\text{H}_{36}\text{N}_6\text{O}_6\text{S}_2$ | $\text{C}_{22}\text{H}_{38}\text{N}_6\text{O}_6\text{S}_2$ |
| formula wt. | 518.66 | 518.66 | 532.68 | 532.68 | 546.70 |
| crystal system | orthorhombic | orthorhombic | monoclinic | monoclinic | monoclinic |
| space group | $Imm2$ | $Imm2$ | $C2$ | $C2$ | $C2$ |
| color | colorless | colorless | colorless | colorless | colorless |
| a (Å) | 19.246(3) | 20.578(7) | 20.061(3) | 20.018(5) | 19.929(4) |
| b (Å) | 7.512(1) | 7.386(2) | 9.255(1) | 9.211(2) | 9.297(2) |
| c (Å) | 9.219(2) | 8.168(3) | 7.555(1) | 7.558(2) | 7.581(2) |
| α ($^\circ$) | 90 | 90 | 90 | 90 | 90 |
| β ($^\circ$) | 90 | 90 | 108.723(2) | 107.459(4) | 107.757(4) |
| γ ($^\circ$) | 90 | 90 | 90 | 90 | 90 |
| V (Å ³) | 1332.9(4) | 1241.4(7) | 1328.6(3) | 1329.4(6) | 1337.6(5) |
| temp. (K) | 173(2) | 173(2) | 173(2) | 173(2) | 173(2) |
| Z | 2 | 2 | 2 | 2 | 2 |
| R_1 [$I > 2\sigma(I)$] | 0.0703 | 0.0450 | 0.0389 | 0.0344 | 0.0270 |
| wR_2 [$I > 2\sigma(I)$] | 0.2064 | 0.1138 | 0.1079 | 0.0865 | 0.0721 |
| G.O.F. | 1.267 | 1.100 | 1.017 | 1.012 | 1.052 |
| θ_{IR} ($^\circ$) | 96.2 | 80.5 | 97.4 | 96.6 | 98.0 |
| Torsion[19] ($^\circ$) | 0.0 | 0.0 | 11.6 | 17.0 | 16.4 |
| Guest Tilt ($^\circ$) | 0 | 0 | 13 | 18 | 17 |
| Packing Fraction[20] | 67.7 | 70.3 | 68.2 | 68.5 | 69.8 |
| Rearranged lattice constants (a , b , c) for direct comparison of orthorhombic and monoclinic structures | | | | | |
| a (Å) | 7.512(1) | 7.386(2) | 7.555(1) | 7.558(2) | 7.581(2) |
| b (Å) | 9.219(2) | 8.168(3) | 9.255(1) | 9.211(2) | 9.297(2) |
| c (Å) | 19.246(3) | 20.578(7) | 20.061(3) | 20.018(5) | 19.929(4) |
| α ($^\circ$) | 90 | 90 | 90 | 90 | 90 |
| β ($^\circ$) | 90 | 90 | 108.723(2) | 107.459(4) | 107.757(4) |
| γ ($^\circ$) | 90 | 90 | 90 | 90 | 90 |

The inter-ribbon puckering angles (θ_{IR}) ranged from 80.5° to 98° , smaller than the value of 120° expected from the geometry of the pillars. These values reflect a contraction along the b -direction that supercedes the geometric enforcement of the pillars, which results in pillar-to-pillar distances ranging from 8.17 \AA to 9.30 \AA along b . For example, the inter-ribbon puckering angle for **G₂MDS**·(1,3,5-3MB) is noticeably lower ($\theta_{IR} = 80.5^\circ$) than **G₂MDS**·(1,2,4-3MB), as reflected by the smaller b value for **G₂MDS**·(1,3,5-3MB). This can be attributed to greater steric crowding between the methyl groups of the 1,2,4-3MB guest molecules along the channel direction (the *para* methyl substituents of the 1,2,4-3MB guest are oriented along the channel direction). The ability of the **G₂MDS** host to accommodate this steric crowding illustrates the compliant nature of this host, a property associated with the ease of puckering of the **GS** sheet. Furthermore, these structures reveal that the channel dimensions are dictated more by the guest-guest contacts than steric crowding between the **MDS** pillars. The effect of steric crowding between pillars, however, is evident from a comparison of **G₂MDS**·(1,3,5-3MB) and **G₂TMBDS**·(1,3,5-3MB), which have channel lattice constants of 8.168 \AA and 9.211 \AA , respectively, even though the guests are identical. Clearly, the fourth methyl group on the **TMBDS** pillar, which is pointing along the channel direction, forces expansion along the channel and a larger puckering angle. This steric crowding naturally makes the **G₂TMBDS** host less compliant, to the extent that is unable to shrink to dimensions that would optimize packing with the 1,3,5-3MB guest molecules. Notably, the packing fraction for **G₂MDS**·(1,3,5-3MB) is larger than that of **G₂TMBDS**·(1,3,5-3MB). It is not unreasonable to suggest that the compliance of the host would be an important factor in determining inclusion selectivity for guest isomers.

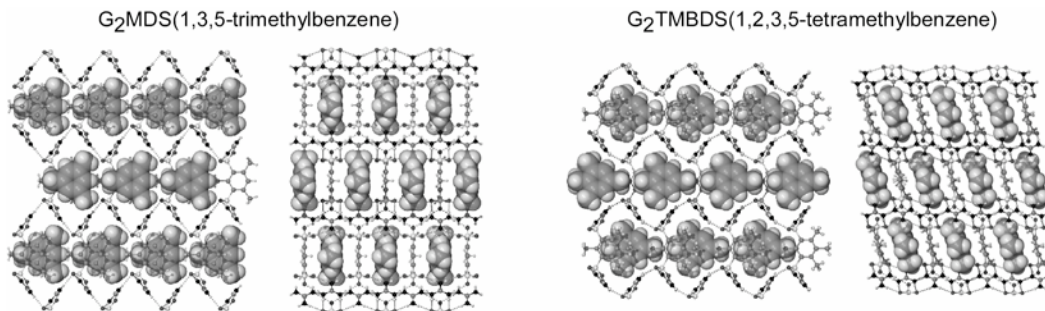


Figure 4. Representative structures of inclusion compounds obtained for the **G₂MDS** and **G₂TMBDS** hosts, here depicted with 1,3,5-trimethylbenzene (1,3,5-3MB) and 1,2,3,5-tetramethylbenzene (1,2,3,5-4MB) guests, respectively. The side views on the left reveal the puckering of the **GS** sheets enforced by the strict geometric constraints of the bent pillars. The views on the right depict the infinite channels running through the crystal, with the **G₂TMBDS** host exhibiting an unusual tilt of the pillars associated with a slight rotation of the sulfonates out of the plane of the **GS** ribbons.

3.3 Inclusion-Based Separations And Selectivity

Pairwise competition experiments were employed to determine the selectivity of the **G₂MDS** host towards different 3MB and 4MB isomers. The selectivity profiles, in which the mole fraction of a particular guest included in the host (Y) is plotted against the mole fraction of the same guest present in the initial crystallization medium (X), are depicted in **Figure 5**. Moderate selectivity is observed during separation of the 3MB isomers with the **G₂MDS** host, with the preference for inclusion decreasing in the order 1,3,5-3MB > 1,2,3-3MB > 1,2,4-3MB. The selectivity coefficients are $K_{1,3,5-3MB:1,2,4-3MB} = 9.2$, however, $K_{1,3,5-3MB:1,2,3-3MB} = 1.8$ and $K_{1,2,3-3MB:1,2,4-3MB} = 2.9$. [21] The selectivity for the 4MB isomers with the **G₂MDS** host decreases in the order 1,2,3,5-4MB >> 1,2,4,5-4MB > 1,2,3,4-4MB, with 1,2,3,5-4MB included almost exclusively in pairwise competition with 1,2,4,5-4MB ($K_{1,2,3,5-4MB:1,2,4,5-4MB} = 32$). This selectivity was observed when $0.3 < X_{1,2,3,5-4MB} < 1.0$, but fell steeply with decreasing $X_{1,2,3,5-4MB}$, becoming negligible at $X_{1,2,3,5-4MB} = 0.1$. Similar behavior was observed for 1,2,3,4-4MB/1,2,4,5-4MB competition, with a selectivity coefficient of $K_{1,2,3,4-4MB:1,2,4,5-4MB} = 5.6$, although the profile was more symmetrical. Negligible selectivity was observed for 1,2,3,5-4MB vs. 1,2,3,4-4MB ($K_{1,2,3,5-4MB:1,2,3,4-4MB} = 1.1$).

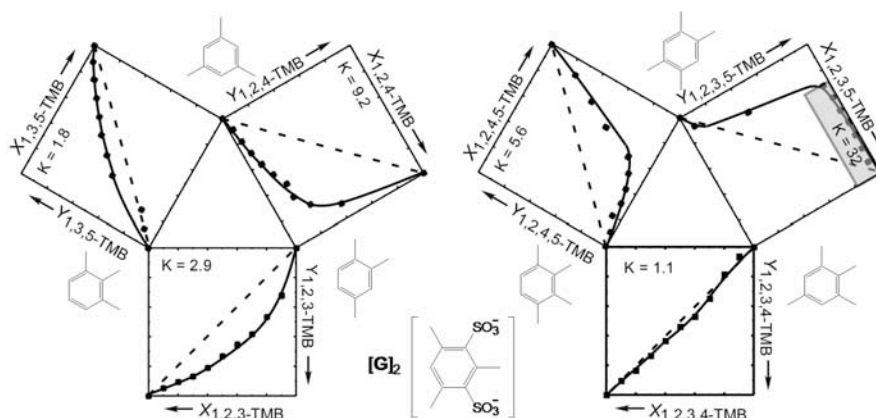


Figure 5. (left) Selectivity profiles for the inclusion of trimethylbenzene isomers by $\mathbf{G}_2\text{MDS}$. The results of pairwise competition experiments are depicted as points on the plots at the periphery of the central triangle. The smooth curves represent average selectivity coefficients derived from the point data for pairwise competition. (right) Selectivity profiles for the inclusion of tetramethylbenzene isomers by $\mathbf{G}_2\text{TMBDS}$. The smooth curves for 1,2,3,4-TMB/1,2,4,5-TMB and 1,2,3,4-TMB/1,2,4,5-TMB represents an average selectivity coefficients derived from the point data. The selectivity profile for 1,2,3,5-TMB/1,2,3,4-TMB competitions are highly concentration dependent, and the curves represent an arbitrary best fit of the data.

The selectivity profiles for inclusion of 3MB and 4MB isomers with $\mathbf{G}_2\text{TMBDS}$ are depicted in **Figure 6**. Modest selectivities were observed for the 3MB isomers with the $\mathbf{G}_2\text{TMBDS}$ host, decreasing in the order 1,2,4-3MB > 1,2,4-3MB > 1,2,3-3MB. The selectivity profiles are nearly symmetric, with $K_{1,3,5-3\text{MB}:1,2,3-3\text{MB}} = 3.4$, $K_{1,3,5-3\text{MB}:1,2,4-3\text{MB}} = 2.0$ and $K_{1,3,5-3\text{MB}:1,2,3-3\text{MB}} = 1.43$. The selectivities for the 4MB isomers are also modest, with $K_{1,2,3,5-4\text{MB}:1,2,3,4-4\text{MB}} = 4.1$, $K_{1,2,3,5-4\text{MB}:1,2,4,5-4\text{MB}} = 1.7$ and $K_{1,2,3,5-4\text{MB}:1,2,4,5-4\text{MB}} = 1.1$.

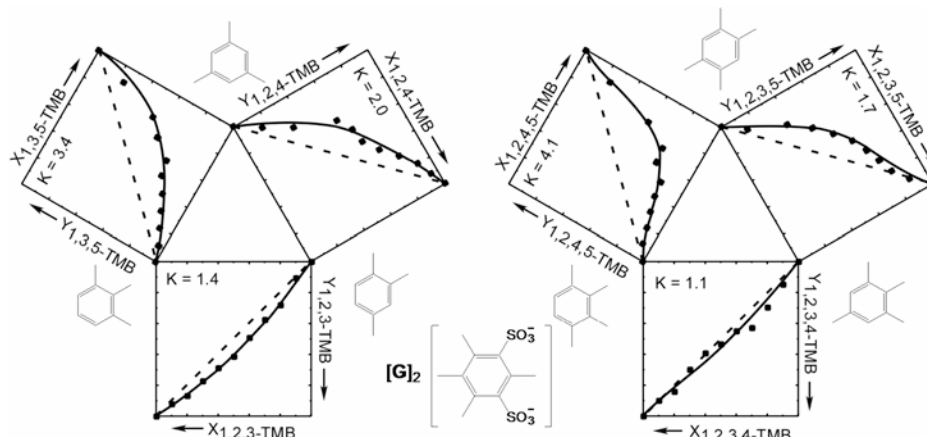


Figure 6. (left) Selectivity profiles for the inclusion of trimethylbenzene isomers by $\mathbf{G}_2\text{TMBDS}$. The results of pairwise competition experiments are depicted as points on the plots at the periphery of the central triangle. The smooth curves represent average selectivity coefficients derived from the point data for pairwise competition. (right) Selectivity profiles for the inclusion of tetramethylbenzene isomers by $\mathbf{G}_2\text{TMBDS}$.

4. CONCLUSION

The inclusion selectivity for trimethyl- and tetramethylbenzene isomers by the $\mathbf{G}_2\text{MDS}$ and $\mathbf{G}_2\text{TMBDS}$ hosts is moderate overall compared with the selectivities observed previously in our laboratory when architectural isomerism accompanied inclusion of different xylene and dimethylnaphthalene isomers by hosts with certain linear pillars. Instead, the selectivities observed here for the bent pillar host more closely resemble the behavior for the separation of xylenes with the $\mathbf{G}_2\text{BPDS}$ host, for which each xylene isomer was included in the bilayer architecture. Therefore, it is perhaps not surprising that bent-pillar hosts exhibit only marginal selectivities, simply because these hosts cannot adopt different architectures. Consequently,

effective isomer separation can only be achieved through some form of molecular recognition, most likely driven by differences in the compatibility of the shape of the host inclusion cavity and the included guest. Such an effect must be responsible for the rather high selectivity observed for **G₂MDS**·(1,2,3,5-4MB) and **G₂MDS**·(1,3,5-3MB). Notably, the selectivity coefficients generally are higher for the **G₂MDS** host. Inspection of the crystal structures of the **G₂MDS** and **G₂TMBDS** described above, as well as others reported previously, reveals that the former is more compliant and has the ability to achieve a smaller lattice constant along the channel direction. Consequently **G₂MDS** can achieve smaller inclusion cavity volumes that can better discriminate between guest isomers based on subtle shape differences. In contrast, the extra methyl group of the **TMBDS** pillar forces a larger separation between pillars and makes this host less compliant compared with **G₂MDS**. This in turn would create larger and more rigid inclusion cavities with reduced discriminating ability.

5. EXPERIMENTAL

5.1 Materials

Trimethylbenzenes and tetramethylbenzenes were used as received from either TCI America or Aldrich (Milwaukee, WI). Mesitylenedisulfonyl chloride and Tetramethylbenzenedisulfonyl chloride were purchased from TCI America. The disulfonic acids were prepared by hydrolysis of the corresponding disulfonyl chlorides by refluxing in dioxane/water overnight. The **G₂MDS** and **G₂TMBDS** hosts were prepared first as acetone clathrates by direct reaction of guanidinium tetrafluoroborate, prepared by neutralization of guanidinium carbonate with tetrafluoroboric acid, with the corresponding disulfonic acid in acetone. These compounds readily lose enclathrated acetone under ambient conditions to yield pure guanidinium organodisulfonate apohosts. Single crystals for X-ray diffraction were obtained from methanolic solutions containing the dissolved **GS** apohost and the corresponding guest where applicable. In addition to single crystal X-ray diffraction, the stoichiometry of guest inclusion was determined by ¹H NMR (Varian INOVA 200 MHz spectrometer) or thermal gravimetric analysis (Perkin Elmer TGA 7).

5.2 X-ray Crystallography

Single crystal structures of the inclusion compounds were determined at -100 °C using either a Siemens or Bruker CCD platform diffractometer with graphite monochromated Mo-K α radiation ($\lambda = 0.71073 \text{ \AA}$). The structures were solved by direct methods and refined with full-matrix least-squares/difference Fourier analysis using the SHELX-97-2 suite of software. [22] Where appropriate, all non-hydrogen atoms were refined with anisotropic displacement parameters and all hydrogen atoms were placed in calculated positions and refined with a riding model. Data were corrected for the effects of absorption using SADABS. Experimental details of the crystal structure determinations are compiled in Table 1. Single crystals of the inclusion compounds suitable for X-ray structure determination were prepared under ambient conditions by slow evaporation of methanolic solutions containing the appropriate host and guest components.

5.3 Inclusion Selectivity

A prepared isomeric mixture (with mole fractions ranging from 0.0 to 1.0) of two potential guests was added, in an approximate twenty-fold excess, to a methanolic solution of the guanidinium organodisulfonate host. Crystallization of the corresponding inclusion compounds commenced upon standing or after slow evaporation of some solvent. After approximately 25% of the total host material had precipitated from solution, the resulting crystals were harvested by filtration and washed briefly with cold methanol (to remove surface residue). The crystals were then dissolved in methanol and the solution was evaluated for isomer composition by gas chromatographic analysis. When the quality of the crystalline inclusion compounds permitted, the data obtained from batches of crystalline material were compared to data that could be obtained from what were seemingly individual single crystals. In all cases the results were essentially identical.

5.4 Gas Chromatography

Gas chromatographic analyses were performed with an HP 6890 series instrument using helium carrier gas and a flame ionization detector. The inlet and detector were held at constant temperatures of 200 °C and 250 °C, respectively, for all analyses. Complete resolution of trimethylbenzene and tetramethylbenzene

isomers was achieved with an All Tech Econocap capillary column (30m x 25mm diameter x 0.25 μ m stationary phase of EC-Wax) using a constant 1 ml/min flow rate and 150 °C.

6. ACKNOWLEDGEMENTS.

This work was supported by the Korea Research Foundation Grant, the National Science Foundation (DMR-0305278) and the University of Minnesota National Science Foundation Materials Research Science and Engineering Center (DMR-0212302). W-S. Kim wishes to thank the KRF visiting research program.

7. SUPPORTING INFORMATION

CCDC 233456-233459 contains the supplementary crystallographic data for this paper. These data can be obtained free of charge via www.ccdc.cam.ac.uk/data_request/cif, by emailing data_request@ccdc.cam.ac.uk, or by contacting the Cambridge Crystallographic Data Centre, 12 Union Road, Cambridge CB2 1EZ, UK; fax: +44 1223 336033.

8. REFERENCES

- [1] (a) Q.-Q. Guo, H. Chen and Y.-C. Long, *Microporous Mesoporous Mater.* **39** (2000), 149. (b) J. Padin and R. T. Yang, *Chem. Eng. Sci.* **55** (2000), 2607. (c) H.-R. Lee and C.-S. Tan, *Ind. Eng. Chem. Res.* **39** (2000), 1035.
- [2] (a) J. L. Atwood, J. E. D. Davies, D. D. MacNicol (Eds) *Inclusion Compounds, Vol. 2 (Structural Aspects of Inclusion Compounds Formed by Organic Host Lattices)* Academic Press: London, (1984). (b) E. Weber and H.-P. Jösel, *J. Inclusion Phenom.* **1**, (1983), 79. (c) E. Weber, *Top. Cur. Chem.* **140** (1987), 1. (d) R. Bishop, *Chem. Soc. Rev.* **25** (1996), 311. (e) Y. Aoyama, *Top. Curr. Chem.* **198** (1998), 131. (f) F. H. Herbstein, *Acta Chim. Hung.* **130** (1993), 377.
- [3] (a) E. Weber, *Top. Curr. Chem.* **149** (1988), 45. (b) E. Weber, in *Comprehensive Supramolecular Chemistry* (J. L. Atwood, J. E. D. Davies, D. D. MacNicol, F. Vögtle and K. S. Suslick, Eds.) **Vol. 6**, Elsevier: Oxford, (1996), 535. (c) O. Ermer and L. Lindenberg, *Helv. Chim. Acta* **74** (1991), 825. (d) R. K. R. Jetti, S. S. Kuduva, D. S. Reddy, F. Xue, T. C. W. Mak, A. Nangia and G. R. Desiraju, *Tetrahedron Lett.* **39** (1998), 913.
- [4] (a) M. J. Zaworotko, *Chem. Comm.* (2001), 1. (b) R. Robson, *Dalton* (2000), 3735. (c) P. J. Hagrman, D. Hagrman and J. Zubietta, *Angew. Chem. Int. Ed.* **38** (1999), 2639. (d) M. O'Keeffe, M. Eddaoudi, H. Li, T. Reineke and O. M. Yaghi, *J. Solid State Chem.* **152** (2000), 3. (e) S. R. Batten and R. Robson, *Angew. Chem. Int. Ed.* **37** (1998), 1461.
- [5] Some examples of molecule-based materials which maintain structural integrity upon guest removal have been recently reported: (a) M. Eddaoudi, D. B. Moler, H. Li, B. Chen, T. M. Reineke, M. O'Keeffe and O. M. Yaghi, *Acc. Chem. Res.* (2001), 34, 319. (b) P. Brunet, M. Simard and J. D. Wuest, *J. Am. Chem. Soc.* **119** (1997), 2737. (c) S.S.-Y. Chui, S.M.-F. Lo, J. P. H. Charmant, A. G. Orpen and I. D. Williams, *Science* **283** (1999), 1148. (d) S. Noro, S. Kitagawa, M. Kondo and K. Seki, *Angew. Chem. Int. Ed.* **39** (2000), 2082.
- [6] (a) K. D. M. Harris, *Chem. Soc. Rev.* **26** (1997), 279. (b) M. D. Hollingsworth and K. D. M. Harris, in *Comprehensive Supramolecular Chemistry Chemistry* (J. L. Atwood, J. E. D. Davies, D. D. MacNicol, F. Vögtle and K. S. Suslick, Eds.) **Vol. 6**, Elsevier: Oxford, (1996), 177.
- [7] (a) R. Gerdil, in *Comprehensive Supramolecular Chemistry Chemistry* (J. L. Atwood, J. E. D. Davies, D. D. MacNicol, F. Vögtle and K. S. Suslick, Eds.) **Vol. 6**, Elsevier: Oxford, (1996), 239. (b) R. Gerdil, *Top. Curr. Chem.* **140** (1987), 71.
- [8] D. D. MacNicol, in *Inclusion Compounds* (J. L. Atwood, J. E. D. Davies and D. D. MacNicol, Eds.) *Vol. 2*, Academic Press: London, (1984), 1.
- [9] (a) J. Hulliger, S. W. Roth, A. Quintel and H. Bebie, *J. Solid State Chem.* **152** (2000), 49. (b) M. Farina and S. G. P. Di Sozzani, in *Comprehensive Supramolecular Chemistry Chemistry* (J. L.

- Atwood, J. E. D. Davies, D. D. MacNicol, F. Vögtle and K. S. Suslick, Eds.) **Vol. 6**, Elsevier: Oxford, (1996) 371. (c) M. Farina, in *Inclusion Compounds* (J. L. Atwood, J. E. D. Davies and D. D. MacNicol, Eds.) **Vol. 2**, Academic Press: London, (1984), 69.
- [10] (a) A. Collet, in *Comprehensive Supramolecular Chemistry Chemistry* (J. L. Atwood, J. E. D. Davies, D. D. MacNicol, F. Vögtle and K. S. Suslick, Eds.) **Vol. 6**, Elsevier: Oxford, (1996), 281. (b) A. Collet, J.-P. Dutasta, B. Lozach and J. Cancéll, *Top. Curr. Chem.* **165** (1993), 103. (c) A. Collet, *Tetrahedron* **43** (1987), 5725. (d) A. Collet, in *Inclusion Compounds* (J. L. Atwood, J. E. D. Davies and D. D. MacNicol, Eds.) **Vol. 2**, Academic Press: London, (1984), 97.
- [11] (a) W. D. Schaeffer, W. S. Dorsey, D. A. Skinner and C. G. Christian, *J. Am. Chem. Soc.* **79** (1957), 5870. (b) F. V. Williams, *J. Am. Chem. Soc.* **79** (1957), 5876. (c) J. Lipkowski, in *Comprehensive Supramolecular Chemistry Chemistry* (J. L. Atwood, J. E. D. Davies, D. D. MacNicol, F. Vögtle and K. S. Suslick, Eds.) **Vol. 6**, Elsevier: Oxford, (1996), 691.
- [12] (a) F. Toda, in *Comprehensive Supramolecular Chemistry Chemistry* (J. L. Atwood, J. E. D. Davies, D. D. MacNicol, F. Vögtle and K. S. Suslick, Eds.) **Vol. 6**, Elsevier: Oxford, (1996), 465.
- [13] (a) M. R. Caira, A. Horne, L. R. Nassimbeni and F. Toda, *J. Mater. Chem.* **7** (1997), 2145. (b) M. R. Caira, A. Horne, L. R. Nassimbeni and F. Toda, *J. Mater. Chem.* **8** (1998), 1481. (c) M. R. Caira, L. R. Nassimbeni, D. Vujovic and F. Toda, *J. Phys. Org. Chem.* **13** (2000), 75. (d) M. R. Caira, L. R. Nassimbeni, F. Toda and D. Vujovic, *J. Am. Chem. Soc.* **122** (2000), 9367. (e) J. Deng, Y. Chi, F. Fu, X. Cui, K. Yu, J. Zhu and Y. Jiang, *Tetrahedron: Asymmetry* **11** (2000), 1729. (f) K. Deketov, E. Weber, J. Seidel, K. Köhnke, K. Makhkamov and B. Ibragimov, *Chem. Comm.* (1999), 91.
- [14] (a) J. A. Swift, A. M. Pivovar, A. M. Reynolds and M. D. Ward, *J. Am. Chem. Soc.* **120** (1998), 5887. (b) K. T. Holman, A. M. Pivovar, J. A. Swift and M. D. Ward, *Acc. Chem. Res.* **34** (2001), 107-118. (c) J. A. Swift, A. M. Reynolds and M. D. Ward, *Chem. Mater.* **10** (1998), 4159. (d) V. A. Russell, C. C. Evans, W. Li and M. D. Ward, *Science* **276** (1997), 575. (e) K. T. Holman and M. D. Ward, *Angew. Chem. Int. Ed.* **39** (2000), 1653. (f) C.C. Evans, L. Sukarto and M.D. Ward, *J. Am. Chem. Soc.* **121** (1999), 320. (g) J. A. Swift and M. D. Ward, *Chem. Mater.* **12** (2000), 150.
- [15] (a) V. A. Russell, M. C. Etter and M. D. Ward, *J. Am. Chem. Soc.* **116** (1994), 1941. (b) V. A. Russell, M. C. Etter and M. D. Ward, *Chem. Mat.* **6** (1994), 1206. (c) V. A. Russell and M. D. Ward, *J. Mater. Chem.* **7** (1997), 1123.
- [16] K. T. Holman, S. M. Martin, D. P. Parker and M. D. Ward, *J. Am. Chem. Soc.* **123** (2001), 4421.
- [17] A. M. Pivovar, K. T. Holman and M. D. Ward, *Chem. Mater.*, **13** (2001), 3018.
- [18] K. T. Holman, A. M. Pivovar and M. D. Ward, *Science* **294** (2001), 1907.
- [19] The torsion angle is measured as the angular rotation along the bond between the sulfur atom and adjacent carbon atom containing the methyl group.
- [20] Packing Fraction (PF) calculations were performed using MSI Cerius² v.4.2. PF values were obtained from the following relationship $PF = (V_{cell} - V_{available})/V_{cell}$: where V_{cell} = Unit cell volume and $V_{available}$ is obtained by determining the “available volume” (probe radius = 0.5 Å, grid spacing of “fine”).
- [21] A selectivity coefficient, K , can be assigned for each data point on the respective competition plots. The values reported are averages of the selectivity coefficients obtained from the points in the regions of X specified. It should be noted that, owing to the limited amount of data, extremely small variation in the experimental values of Y lead to large differences in the calculated selectivity coefficients, consequently, the errors associated with K can be as large as ±60%.
- [22] *SHELX-97*, Sheldrick, G. M., University of Göttingen, (1997).

MAKING, USING, TRANSFORMING CRYSTALS: AN ORGANOMETALLIC HYDROGEN BONDED MATERIAL THAT REACTS WITH VAPOURS AND CRYSTALS

Dario Braga, Lucia Maini, Marco Polito, Stefano Giaffreda

Dipartimento di Chimica G. Ciamician, Univ. of Bologna, Via Selmi 2, 40126 Bologna, Italy
dario.braga@unibo.it

Katia Rubini

Centro CNR per la Fisica delle Macromolecole, c/o Dipartimento di Chimica G. Ciamician, Via Selmi 2, 40126 Bologna, Italy

Fabrizia Grepioni[†]

Dipartimento di Chimica, Univ. of Sassari, Via Vienna 2, 07100 Sassari, Italy
grepioni@ssmain.uniss.it

1. ABSTRACT

The organometallic zwitterion $[\text{Co}^{\text{III}}(\eta^5\text{-C}_5\text{H}_4\text{COOH})(\eta^5\text{-C}_5\text{H}_4\text{COO})]$ **1** reacts as a crystalline solid with both vapors and solids in solvent-free processes. When exposed to hydrated vapors of volatile acids (HCl , CF_3COOH , HBF_4 , HCOOH) or bases (NH_3 , NMe_3 , NH_2Me) the corresponding salts or co-crystals are produced quantitatively. All these reactions are reversible, with the acid or base molecules being easily removed by thermal treatment under vacuum regenerating the starting material. The same compound reacts as a solid with crystalline alkali salts MX ($\text{M} = \text{K}^+$, Rb^+ , Cs^+ , NH_4^+ ; $\text{X} = \text{Cl}^-$, Br^- , I^- , PF_6^- , though not in all permutations of cations and anions). Manual co-grinding of the powdered materials generates supramolecular complexes of formula $[\text{Co}^{\text{III}}(\eta^5\text{-C}_5\text{H}_4\text{COOH})(\eta^5\text{-C}_5\text{H}_4\text{COO})]_2\cdot\text{M}^+\text{X}^-$. In some cases the mechanochemical complexation requires *kneading* of the two solids with a catalytic amount of water. The robustness of the organometallic solid is due to the $\text{O-H}\cdots\text{O}$ hydrogen bond network joining carboxylic and carboxylate groups in molecular chains. Both solid-gas and solid-solid processes occur with profound transformations of the hydrogen bond networks. The solid-state structures of the novel compounds $[\text{Co}^{\text{III}}(\eta^5\text{-C}_5\text{H}_4\text{COOH})(\eta^5\text{-C}_5\text{H}_4\text{COO})]\cdot[\text{Co}^{\text{III}}(\eta^5\text{-C}_5\text{H}_4\text{COOH})_2]^+\text{I}^-$ and $[\text{C}_6\text{H}_{12}\text{N}_2\text{H}_2]^{2+}[\text{Co}^{\text{III}}(\eta^5\text{-C}_5\text{H}_4\text{COO})_2]^{2-}\cdot1.5\text{ H}_2\text{O}$ are also reported. The former has been obtained directly from solution crystallization while the latter has been obtained by mechanochemical treatment of the organometallic zwitterion **1** with the solid base 1,4-diazabicyclo[2.2.2]octane [$\text{C}_6\text{H}_{12}\text{N}_2$].

2. INTRODUCTION

Crystal engineering is *making crystals by design* [1]. The paradigm is that of being able to assemble molecular or ionic components into a given target functional structure by controlling the periodical distribution of supramolecular interactions responsible for recognition, nucleation and growth of the crystalline material [2]. The deliberate construction of a molecular solid that can perform a desired function is conceptually related to the construction of a supermolecule [3]. In both cases, crystals and supermolecules, the collective properties depend on the aggregation via intermolecular bonds of two or more component units [4]. These interactions can be coordination bonds between ligands and metal centers and non-covalent bonds between neutral molecules or ions or – of course – any of their combinations.

A popular motivation for crystal engineering investigations and experiments is the design and preparation of nanoporous structures with voids and channels of controllable size that can be used for sensing, trapping, and storing small molecules [5]. Remarkable results have indeed been obtained [6]. An alternative to

[†] Present address: Dipartimento di Chimica, G. Ciamician, Univ. Bologna

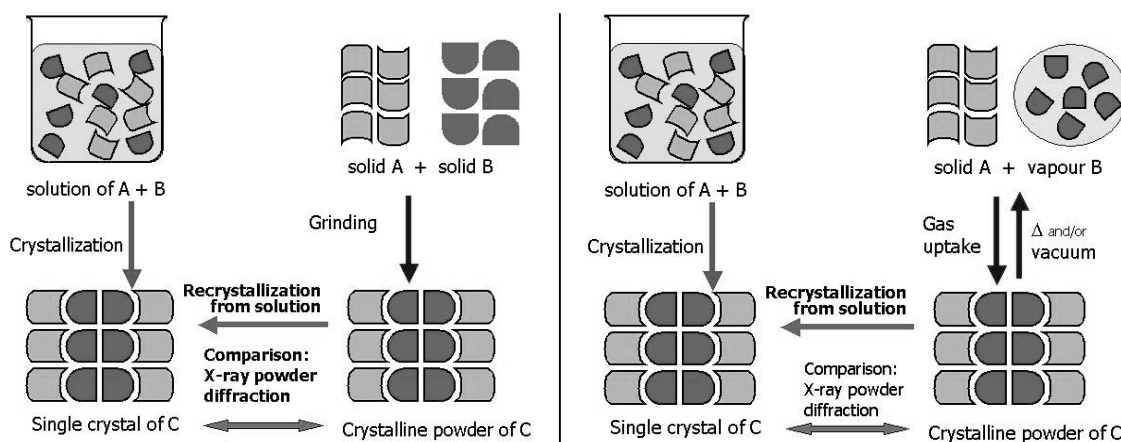
nанопористость (nanoporosity) is represented by *conventional* chemical reactivity. The controlled uptake and release of small molecules can be achieved by means of (possibly reversible) heterogeneous gas-solid reactions [7]. Solid-gas reactions of the type useful for gas uptake often imply profound transformations of the chemical and physical nature of the solid material and rarely are of practical use, unless fully reversible [8].

It is interesting to speculate on the analogy between the uptake of small molecules by a nanoporous material and the reaction between a molecular crystal and molecules to yield a co-crystal or a salt: both processes are *supramolecular reactions* whereby non-covalent interactions between guest and the host are broken and formed [9]. Solvent-free reactions between a molecular crystal and a gas or between two molecular crystals to yield molecular crystalline products are of interest in the quest for environmentally friendly processes (green chemistry) [10].

Here we report that the peculiar molecular and supramolecular features of the zwitterion sandwich complex $[\text{Co}^{\text{III}}(\eta^5\text{-C}_5\text{H}_4\text{COOH})(\eta^5\text{-C}_5\text{H}_4\text{COO})]$ [11], (**1**), permits both reversible gas-solid reactions with the hydrated vapors of a variety of acids (e.g. HCl, CF_3COOH , CCl_3COOH , CHF_2COOH , HBF_4 [12-14] but also weaker acids such as HCOOH [15]) and bases (e.g. NH_3 , NMe_3 , NH_2Me [12]) as well as solid-solid reactions with crystalline alkali salts MX ($\text{M} = \text{K}^+$ [16a], Rb^+ , Cs^+ , NH_4^+ ; $\text{X} = \text{Cl}^-$, Br^- , I^- , PF_6^- , though not in all permutations of cations and anions) generates by means of mild manual co-grinding of the powdered materials supramolecular complex of formula $[\text{Co}^{\text{III}}(\eta^5\text{-C}_5\text{H}_4\text{COOH})(\eta^5\text{-C}_5\text{H}_4\text{COO})]_2\cdot\text{M}^+\text{X}^-$ [16b]. Two new derivatives of **1** have also been obtained and are described herewith. Compound $[\text{Co}^{\text{III}}(\eta^5\text{-C}_5\text{H}_4\text{COOH})(\eta^5\text{-C}_5\text{H}_4\text{COO})]\cdot[\text{Co}^{\text{III}}(\eta^5\text{-C}_5\text{H}_4\text{COOH})_2]^+\text{I}^-$ has been obtained directly from solution crystallization while $[\text{C}_6\text{H}_{12}\text{N}_2\text{H}_2]^{2+}[\text{Co}^{\text{III}}(\eta^5\text{-C}_5\text{H}_4\text{COO})_2]^{2-}\cdot1.5\text{H}_2\text{O}$ has been obtained by mechanochemical treatment of the organometallic zwitterion **1** with the solid base 1,4-diazabicyclo[2.2.2]octane [$\text{C}_6\text{H}_{12}\text{N}_2$].

It is worth pointing out, before proceeding that both gas-solid and solid-solid reactions involving **1** yield powdered materials, which renders the determination of the solid-state structure rather complicated because of the lack of single-crystals. We have circumvented this problem by taking advantage of the *seeding* technique [17]. The use of pre-formed micro crystals of the desired phase can be exploited to instruct to generate the desired product [17].

Seeding procedures are commonly employed in pharmaceutical industries to make sure that the desired crystal form is always obtained from a preparative process [18]. The use of a *seeding* procedure often allows preparation of single crystals of suitable size, which, in turn, can be used to confirm *a posteriori* that the same phase obtained from solution crystallization and that yielded by solid-solid mixing processes has been obtained by comparing calculated and observed powder diffraction patterns [19]. The process described above, and used throughout this study, is pictured in **Scheme 1**.



Scheme 1. Schematic representation of the procedure adopted to characterize products of mechanochemical treatments. The solid yielded by grinding reactants in a mortar is compared *via* X-ray powder diffraction with the solids obtained by crystallization *via seeding* of a solution of the ground powder of the adduct.

The zwitterion $[\text{Co}^{\text{III}}(\eta^5\text{-C}_5\text{H}_4\text{COOH})(\eta^5\text{-C}_5\text{H}_4\text{COO})]$ **1** can be quantitatively prepared from the corresponding dicarboxylic cationic acid $[\text{Co}^{\text{III}}(\eta^5\text{-C}_5\text{H}_4\text{COOH})_2]^+$. The amphoteric behavior of the zwitterion depends on the presence of one -COOH group, which can react with bases, and one -COO⁽⁻⁾ group, which can react with acids (see **Figure 1**). Incidentally, the organometallic zwitterion **1** is easy to handle and it is thermally stable up to a temperature of 506 K.

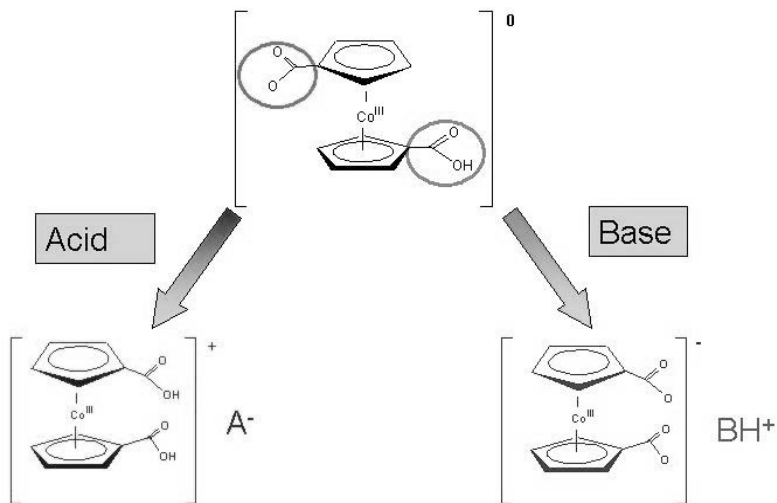


Figure 1. Compound $[\text{Co}^{\text{III}}(\eta^5\text{-C}_5\text{H}_4\text{COOH})(\eta^5\text{-C}_5\text{H}_4\text{COO})]$ **1** reacts with bases to yield the fully deprotonated form $[\text{Co}^{\text{III}}(\eta^5\text{-C}_5\text{H}_4\text{COO})_2]^-$ and with acids to yield the fully protonated form $[\text{Co}^{\text{III}}(\eta^5\text{-C}_5\text{H}_4\text{COOH})_2]^+$.

3. SOLID STATE REACTIVITY: GAS-SOLID REACTIONS AND SOLVATION PROCESSES

As mentioned above $[\text{Co}^{\text{III}}(\eta^5\text{-C}_5\text{H}_4\text{COOH})(\eta^5\text{-C}_5\text{H}_4\text{COO})]$ undergoes fully reversible heterogeneous reactions with the hydrated vapors of a variety of acids (e.g. HCl, CF_3COOH , CCl_3COOH , CHF_2COOH , HBF_4 , and HCOOH) and bases (e.g. NH_3 , NMe_3 , NH_2Me), with formation of the corresponding salts.

For instance, complete conversion of the neutral crystalline zwitterion into the crystalline chloride salt is attained in 5 min of exposure to vapors of aqueous HCl 36%. Formation of the salt in the heterogeneous reaction is easily assessed by comparison of the observed X-ray powder diffraction pattern with that calculated on the basis of the single-crystal structure determined previously.

Crystalline $[\text{Co}^{\text{III}}(\eta^5\text{-C}_5\text{H}_4\text{COOH})_2]\text{Cl}\cdot\text{H}_2\text{O}$ (see **Figure 2**) can be converted back to neutral $[\text{Co}^{\text{III}}(\eta^5\text{-C}_5\text{H}_4\text{COOH})(\eta^5\text{-C}_5\text{H}_4\text{COO})]$ by heating the sample for 1h at 440 K in an oil-bath under low pressure (10^{-2} mbar). Thermogravimetric analysis (TGA) demonstrates that the solid product releases one water molecule and one HCl molecule per molecular unit at 394 and 498 K, respectively. The powder diffractogram of the final product corresponds precisely to that of the anhydrous $[\text{Co}^{\text{III}}(\eta^5\text{-C}_5\text{H}_4\text{COOH})(\eta^5\text{-C}_5\text{H}_4\text{COO})]$ (see **Figure 2**). The formation of $[\text{Co}^{\text{III}}(\eta^5\text{-C}_5\text{H}_4\text{COOH})_2]\text{Cl}\cdot\text{H}_2\text{O}$ from **1** requires that the O-H \cdots O bonds involving the protonated -COOH group and the deprotonated -COO⁽⁻⁾ of neighboring zwitterion molecules are replaced, upon absorption of HCl, by $(^+)\text{O}-\text{H}\cdots\text{Cl}^{(-)}$ interactions between the -COOH groups on the fully protonated organometallic cation $[\text{Co}^{\text{III}}(\eta^5\text{-C}_5\text{H}_4\text{COOH})_2]^+$ and the $\text{Cl}^{(-)}$ anions.

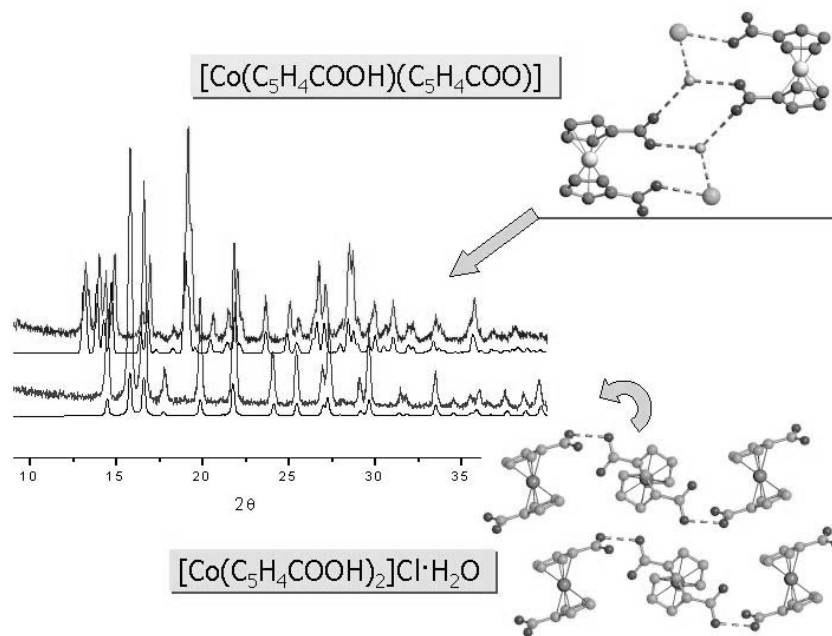


Figure 2. The solid state structures of $[\text{Co}^{\text{III}}(\eta^5\text{-C}_5\text{H}_4\text{COOH})_2]\text{Cl}\cdot\text{H}_2\text{O}$ and $[\text{Co}^{\text{III}}(\eta^5\text{-C}_5\text{H}_4\text{COOH})(\eta^5\text{-C}_5\text{H}_4\text{COO})]$, and a comparison of calculated and measured powder diffractograms.

The behavior of the zwitterion towards NH_3 is similar to that towards HCl but obviously opposite in terms of proton exchange. Single crystals of the ammonium salt for X-ray structure determination can be obtained if the reaction of the zwitterion with ammonia is carried out in aqueous solution. 1–10 mg of the neutral system quantitatively transforms into the hydrated ammonium salt $[\text{Co}^{\text{III}}(\eta^5\text{-C}_5\text{H}_4\text{COO})_2][\text{NH}_4]\cdot 3\text{H}_2\text{O}$ (see **Figure 3**) upon 5 min exposure to vapors of aqueous ammonia 30%. The structure is shown in Figure 3a. The salt is characterized by the presence of charge-assisted $(^+\text{N-H}\cdots\text{O}^-)$ interactions between the ammonium cation and the deprotonated $-\text{COO}^-$ groups on the organometallic anion.

As in the case of the chloride salt, formation of $[\text{Co}^{\text{III}}(\eta^5\text{-C}_5\text{H}_4\text{COO})_2][\text{NH}_4]\cdot 3\text{H}_2\text{O}$ in the heterogeneous reaction is assessed by comparing observed and calculated X-ray powder patterns. Absorption of ammonia is also fully reversible: upon thermal treatment (1 h at 373 K, ambient pressure) the salt converts quantitatively into the neutral zwitterion.

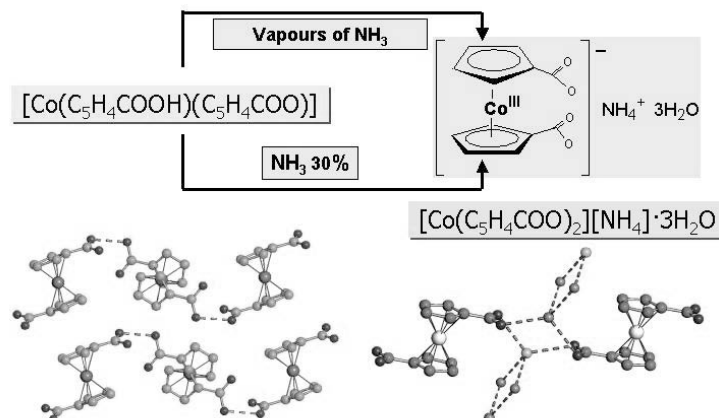


Figure 3. The structures of $[\text{Co}^{\text{III}}(\eta^5\text{-C}_5\text{H}_4\text{COOH})(\eta^5\text{-C}_5\text{H}_4\text{COO})]$ and of $[\text{Co}^{\text{III}}(\eta^5\text{-C}_5\text{H}_4\text{COO})_2][\text{NH}_4]\cdot 3\text{H}_2\text{O}$ as obtained from solution and solid-gas reactions.

The two crystalline powders $[\text{Co}^{\text{III}}(\eta^5\text{-C}_5\text{H}_4\text{COOH})_2]\text{Cl}\cdot\text{H}_2\text{O}$ and $[\text{Co}^{\text{III}}(\eta^5\text{-C}_5\text{H}_4\text{COO})_2][\text{NH}_4]\cdot 3\text{H}_2\text{O}$ can be cycled through several absorption and release processes without decomposition or detectable formation of amorphous material. Infrared spectroscopy can also be utilized to quickly detect formation of the organometallic cation or anion upon reaction with volatile acids or bases.

3.1. Reactions With Other Acid Vapors

Exposure of solid **1** to vapors of CF_3COOH and HBF_4 quantitatively produces the corresponding salts of the cation $[\text{Co}^{\text{III}}(\eta^5\text{-C}_5\text{H}_4\text{COOH})_2]^+$, viz. $[\text{Co}^{\text{III}}(\eta^5\text{-C}_5\text{H}_4\text{COOH})_2][\text{CF}_3\text{COO}]$ (see **Figure 4**) and $[\text{Co}^{\text{III}}(\eta^5\text{-C}_5\text{H}_4\text{COOH})_2][\text{BF}_4]$ (see **Figure 5**). As in the previous cases, all heterogeneous reactions are fully reversible and the acids can be removed by thermal treatment, which quantitatively regenerates the starting material.

In terms of crystal structure organization, formation of $[\text{Co}^{\text{III}}(\eta^5\text{-C}_5\text{H}_4\text{COOH})_2][\text{CF}_3\text{COO}]$ (see **Figure 4**) and $[\text{Co}^{\text{III}}(\eta^5\text{-C}_5\text{H}_4\text{COOH})_2][\text{BF}_4]$ (see **Figure 5**), beside leading from a formally neutral system to molecular salts, implies profound molecular rearrangements and breaking and forming of non-covalent interactions. From the analogy between gas-solid and solution reactions, one may thus suppose that the gas-solid reactions occur *via* a process of dissolution and recrystallization as the vapors are adsorbed by the crystalline powder. The reverse process, *i.e.* reconstruction of the zwitterion crystals, is more difficult to explain as it implies proton removal from the cationic acid.

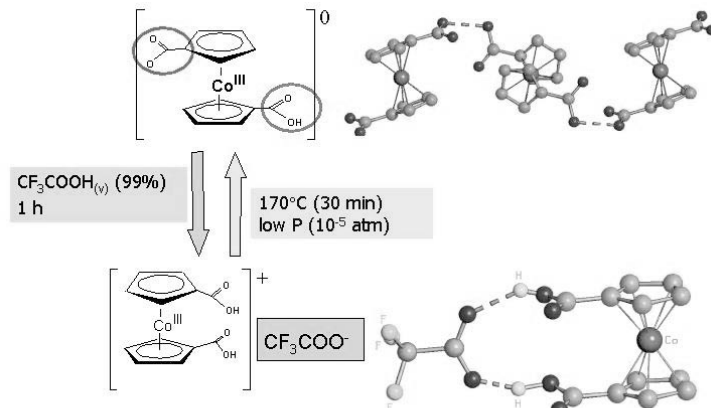


Figure 4. The reaction between **1** and CF_3COOH to yield $[(\eta^5\text{-C}_5\text{H}_4\text{COOH})_2\text{Co}^{\text{III}}][\text{CF}_3\text{COO}]$ as obtained from solution and solid-gas reactions.

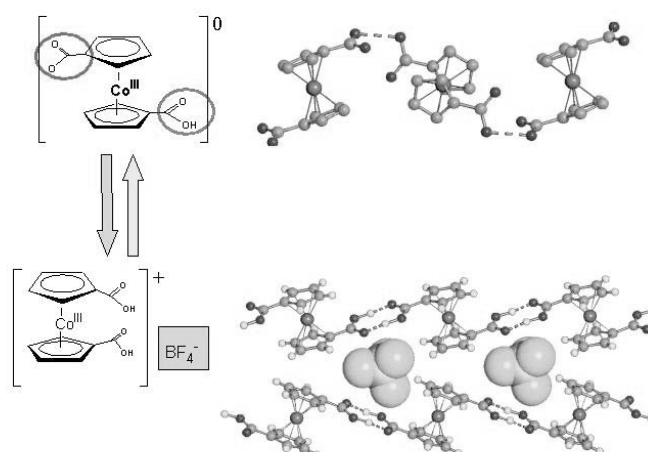


Figure 5. The reaction between **1** and HBF_4 structure to yield $[(\eta^5\text{-C}_5\text{H}_4\text{COOH})_2\text{Co}^{\text{III}}][\text{BF}_4]$ as obtained from solution and solid-gas reactions.

Analogously to the reaction with CF_3COOH , exposure of the solid zwitterion to vapors of CHF_2COOH quantitatively produces the corresponding salt of the cation $[\text{Co}^{\text{III}}(\eta^5\text{-C}_5\text{H}_4\text{COOH})_2][\text{CHF}_2\text{COO}]$. As in the cases discussed above the solid-gas reaction implies a profound rearrangement of the hydrogen bonding patterns (see **Figure 6**). In fact, the chain of zwitterions linked by $\text{O}-\text{H}\cdots\text{O}$ hydrogen bonds between the carboxylate and the carboxylic acid groups needs to be broken and each molecule is required to change conformation to yield the observed ionic pairs between organometallic and organic moieties.

The reaction with hydrated vapors of CH_2ClCOOH produces the hydrated salt $[\text{Co}^{\text{III}}(\eta^5\text{-C}_5\text{H}_4\text{COOH})_2][\text{CH}_2\text{ClCOO}] \cdot \text{H}_2\text{O}$. Crystalline **1** was also made to react in solution with CHF_2COOH and CH_2ClCOOH ; single crystals of $[\text{Co}^{\text{III}}(\eta^5\text{-C}_5\text{H}_4\text{COOH})_2][\text{CHF}_2\text{COO}]$ and anhydrous $[\text{Co}^{\text{III}}(\eta^5\text{-C}_5\text{H}_4\text{COOH})_2][\text{CH}_2\text{ClCOO}]$ for X-ray diffraction were obtained from solution crystallization, allowing comparison between computed and measured powder diffraction patterns.

All compounds share the same feature, regardless of how they are obtained: formation of ion pairs (or adducts) between the two acids. What varies is the conformation of the cyclopentadienyl rings and the inter-acid hydrogen bonds as compared in **Figure 7**. In the case of $[\text{Co}^{\text{III}}(\eta^5\text{-C}_5\text{H}_4\text{COOH})_2][\text{CH}_2\text{ClCOO}]$ there is evidence of formation of pseudo-polymorphic forms depending on the reaction condition (whether heterophase or solution). As in the cases discussed above, the heterogeneous reactions are fully reversible; the acids can be quantitatively removed by mild thermal treatment, which regenerates the starting material.

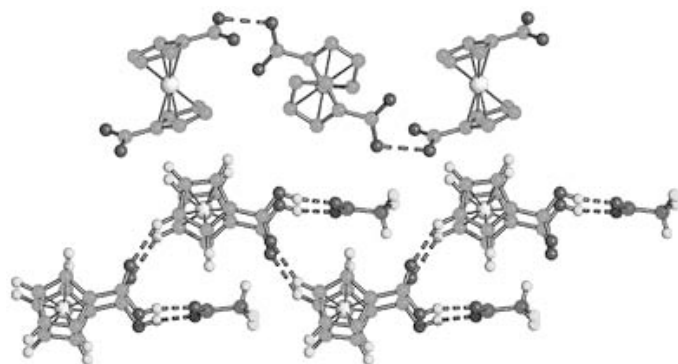


Figure 6. The “transition” from the zwitterionic chain present in crystalline $[(\eta^5\text{-C}_5\text{H}_4\text{COOH})(\eta^5\text{-C}_5\text{H}_4\text{COO})\text{Co}^{\text{III}}]$ **1** (top) and the packing in $[\text{Co}^{\text{III}}(\eta^5\text{-C}_5\text{H}_4\text{COOH})_2][\text{CHF}_2\text{COO}]$ (bottom).

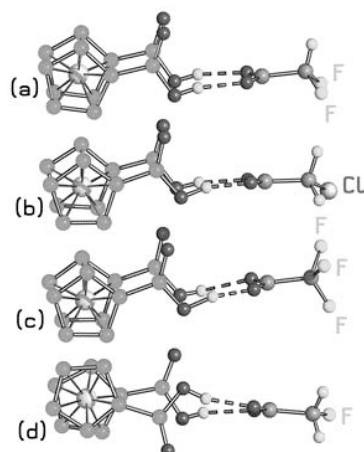


Figure 7. Ion pairs in the solid-state structure of $[\text{Co}^{\text{III}}(\eta^5\text{-C}_5\text{H}_4\text{COOH})_2][\text{CHF}_2\text{COO}]$ and $[\text{Co}^{\text{III}}(\eta^5\text{-C}_5\text{H}_4\text{COOH})_2][\text{CH}_2\text{ClCOO}]$, as obtained from single-crystal X-ray diffraction. The (a) $[\text{CHF}_2\text{COO}]^-$ and (b) $[\text{CH}_2\text{ClCOO}]^-$ anions “pinch” the two protonated COOH groups on the organometallic moiety. A similar arrangement is present in crystals of $[\text{Co}^{\text{III}}(\eta^5\text{-C}_5\text{H}_4\text{COOH})_2][\text{CF}_3\text{COO}]$ (c) and in crystalline $[\text{Co}^{\text{III}}(\eta^5\text{-C}_5\text{H}_4\text{COOH})_2][\text{CH}_2\text{FCOO}]$ (d).

Compound **1** also reversibly absorbs formic acid from humid vapors forming selectively a 1:1 co-crystal, $[\text{Co}^{\text{III}}(\eta^5\text{-C}_5\text{H}_4\text{COOH})(\eta^5\text{-C}_5\text{H}_4\text{COO})][\text{HCOOH}]$, from which **1** can be fully recovered by mild thermal treatment. Complete conversion of crystalline **1** (50 mg) into $[\text{Co}^{\text{III}}(\eta^5\text{-C}_5\text{H}_4\text{COOH})(\eta^5\text{-C}_5\text{H}_4\text{COO})][\text{HCOOH}]$ is attained in 4h of exposure to hydrated vapors of HCOOH.

It is worth noting that, contrary to the other compounds described above, no proton transfer from the adsorbed acid to the organometallic moiety is observed. Hence, the reaction between **1**(solid) and HCOOH(vapor) would be more appropriately described as a special kind of solvation rather than as a heterogeneous acid-base reaction.

As shown in **Figure 8**, crystalline $[\text{Co}^{\text{III}}(\eta^5\text{-C}_5\text{H}_4\text{COOH})(\eta^5\text{-C}_5\text{H}_4\text{COO})][\text{HCOOH}]$ is composed of pairs of zwitterion molecules linked by O-H \cdots O bonds between the protonated -COOH and the deprotonated -COO $^-$ groups [O \cdots O separation 2.526(4) Å]. On the other hand, the C-O distances within the HCOOH moiety [C-O5 1.305(5), C-O6 1.199(5) Å] indicate that the formic acid molecule retains its acidic hydrogen. This is also confirmed by ^{13}C CPMAS NMR spectroscopy.

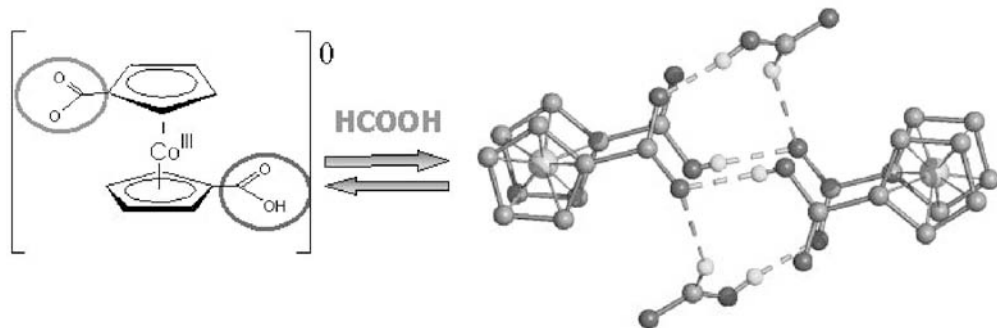


Figure 8. The reaction between **1** and HCOOH to yield $[\text{Co}^{\text{III}}(\eta^5\text{-C}_5\text{H}_4\text{COOH})(\eta^5\text{-C}_5\text{H}_4\text{COO})][\text{HCOOH}]$ as obtained by gas-phase or solution chemistry.

The product, as the others, can be converted back to **1** by leaving the sample at room temperature in the air for few days or by mild heating in a thermogravimetric experiment (stoichiometric loss of formic acid at 417 K). The powder diffractogram of the degassed product corresponds precisely to that of **1**, which can be cycled through several absorption and release processes without decomposition or detectable formation of amorphous material.

In a previous paper [20] we reported the synthesis of the iodide salt $[\text{Co}^{\text{III}}(\eta^5\text{-C}_5\text{H}_4\text{COOH})_2]^+\text{I}^-$ obtained from 1-1'-dimethylcobaltincinium and using the acid HI as a 54% aqueous solution. In the context of this work we were interested in the preparation of the same salt *via* vapor uptake of HI from the zwitterion **1**. Unfortunately, no reaction was observed even after long exposure of the organometallic reagent to the hydrated acid vapors. The reaction was also conducted in solution, by reacting **1** directly with HI in a 1:1 molar ratio. The resulting compound, which we were able to characterize by single crystal X-ray diffraction, turned out to possess a different stoichiometry from the one already reported earlier since the cation $[\text{Co}^{\text{III}}(\eta^5\text{-C}_5\text{H}_4\text{COOH})_2]^+$ co-crystallizes with one equivalent of the zwitterion $[\text{Co}^{\text{III}}(\eta^5\text{-C}_5\text{H}_4\text{COOH})(\eta^5\text{-C}_5\text{H}_4\text{COO})]$ **1** with formation of a salt of formula $1 \cdot [\text{Co}^{\text{III}}(\eta^5\text{-C}_5\text{H}_4\text{COOH})_2]^+\text{I}^-$. In view of the structural relationship with the compounds described thus far, it is worth pointing out some essential structural features of this novel compound. (See **Figure 9**)

The two organometallic moieties form a sort of hydrogen bonded dimeric unit linked by intermolecular hydrogen bonds. The hydrogen bonded system is, however, disordered because the two moieties are related by an inversion center. This crystallographic symmetry is very likely due to the fact that in the crystal the two sites of the sandwich compounds are occupied randomly by the neutral zwitterionic form and by the cations dicarboxylic acid with a total of three protons for six potential hydrogen bonds. One of the possible

combinations of hydrogen bonds compatible with this structure and with the site symmetry is shown. No H atoms have been located (see Experimental section).

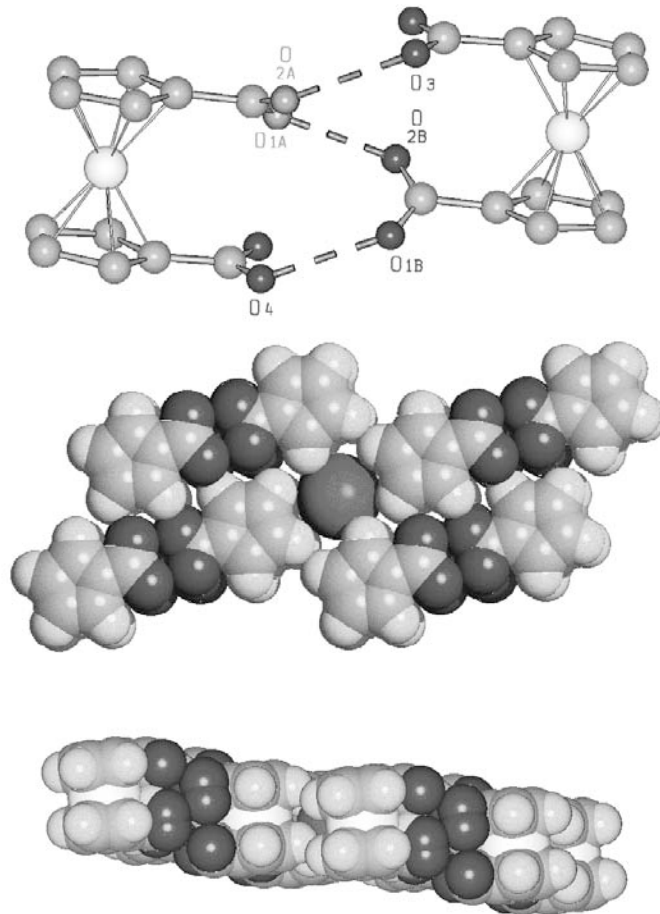


Figure 9. (Top) One of the possible structures of the “super”-cation $\mathbf{1}\cdot[\text{Co}^{\text{III}}(\eta^5\text{-C}_5\text{H}_4\text{COOH})_2]^+$ in the iodide salt. The disorder of O1 and O2 is due to the necessity of optimizing the O(H) \cdots O interactions within the $\mathbf{1}\cdot[\text{Co}^{\text{III}}(\eta^5\text{-C}_5\text{H}_4\text{COOH})_2]^+$ unit. (Middle, bottom) space-filling views of the way the iodide ion is encapsulated between the super-cations.

4. SOLID-SOLID REACTIONS

In the context of our investigation of solid-state processes, [21] we have prepared hybrid organometallic-inorganic salts by reacting anhydrous **1**(solid) with a number of alkali salts MX (M = K $^+$, Rb $^+$, Cs $^+$, NH $_4^+$; X = Cl $^-$, Br $^-$, I $^-$, PF $_6^-$ though not in all permutations of cations and anions, see below). As in the cases discussed above, exact information about the solid state structures of the reaction products were obtained by single-crystal X-ray diffraction experiments carried out on crystals obtained from the reaction powders. Information on the hydrogen bonding nature and on the relationship between structures in solution and those obtained in the solid-state by mechanical grinding were obtained by a combination of solution and solid state NMR.

In view of the analogies in preparation and the likelihood of the structures obtained by solid-state complexation, the supramolecular complex $[\text{Co}^{\text{III}}(\eta^5\text{-C}_5\text{H}_4\text{COOH})(\eta^5\text{-C}_5\text{H}_4\text{COO})_2]^+\cdot\text{Cs}^+\text{T}^-$, $\mathbf{1}_2\cdot\text{Cs}^+\text{T}^-$ can be used as an example.

Compound $\mathbf{1}_2\cdot\text{Cs}^+\text{T}^-$ is isostructural with the members of the family of hexafluorophosphate salts $[\text{Co}^{\text{III}}(\eta^5\text{-C}_5\text{H}_4\text{COOH})(\eta^5\text{-C}_5\text{H}_4\text{COO})_2]^+\text{M}^+[\text{PF}_6]^-$, $\mathbf{1}_2\cdot\text{M}^+[\text{PF}_6]^-$ (M = K $^+$, Rb $^+$, Cs $^+$, [NH $_4^+$]) previously

obtained from the cationic acid $[\text{Co}^{\text{III}}(\eta^5\text{-C}_5\text{H}_4\text{COOH})_2][\text{Co}^{\text{III}}(\eta^5\text{-C}_5\text{H}_4\text{COOH})(\eta^5\text{-C}_5\text{H}_4\text{COO})]^+[\text{PF}_6]^-$ by treatment with MOH or ammonia. Compound $\mathbf{1}_2\text{-Cs}^+\text{I}^-$ is thus characterized by the presence of a supramolecular cage formed by four zwitterionic molecules encapsulating the Cs^+ cations. The cage is sustained by O-H \cdots O hydrogen bonds between carboxylic -COOH and carboxylate -COO $^-$ groups, and by C-H \cdots O bonds between -CH $_{\text{Cp}}$ and -CO groups, while the I $^-$ anions form layers in between the cationic complexes, as shown in **Figure 10**. The structure determination was instrumental to the identification and characterization of the product obtained by solid-state grinding. **Figure 10b** shows a comparison between the XRPD patterns of polycrystalline $\mathbf{1}_2\text{-Cs}^+\text{I}^-$, obtained by grinding the reagents together, and that calculated on the basis of the single crystal structure described above.

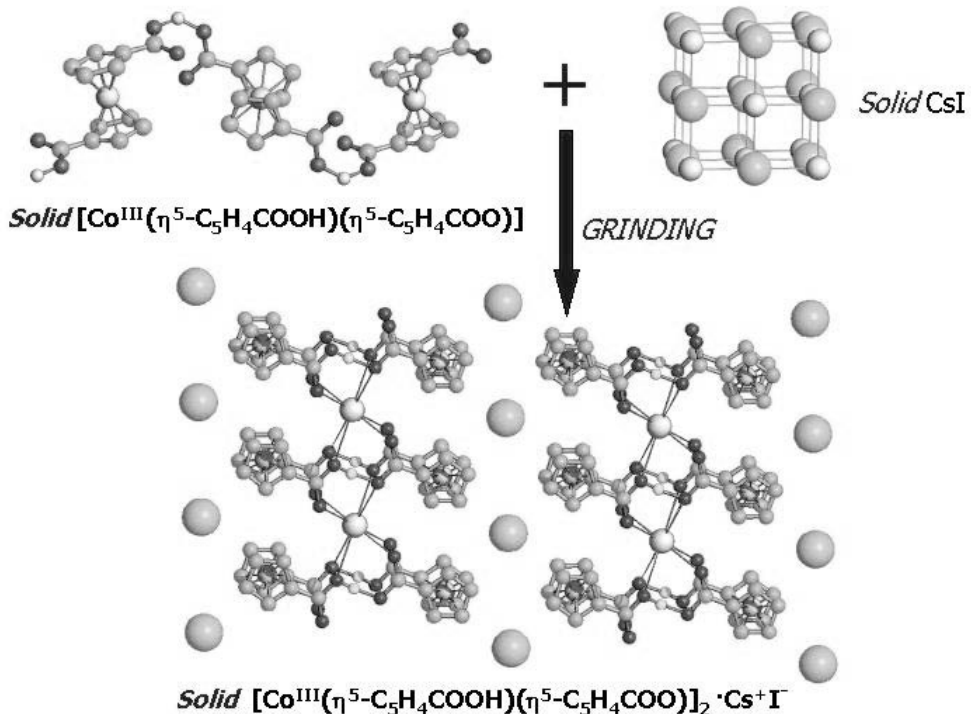


Figure 10. (a) The structure of the Cs adduct $\mathbf{1}_2\text{-Cs}^+\text{I}^-$; (b) shows a comparison between the XRPD patterns of polycrystalline $\mathbf{1}_2\text{-Cs}^+\text{I}^-$, obtained by grinding the reagents together, and that calculated on the basis of the single crystal structure.

The organometallic zwitterion **1** has also been utilized recently in the mechanochemical reaction with the solid base 1,4-diazabicyclo[2.2.2]octane [$\text{C}_6\text{H}_{12}\text{N}_2$]. The 1:2 reaction generates quantitatively the hydrated 1:2 adduct $[\text{C}_6\text{H}_{12}\text{N}_2\text{H}_2]^{2+}[\text{Co}^{\text{III}}(\eta^5\text{-C}_5\text{H}_4\text{COO})_2]^{2-} \cdot 1.5\text{H}_2\text{O}$. The solid-solid reaction does not occur *via* formation of eutectic phases. Structural characterization (see below) allows us to see that the formation of the hybrid organic-organometallic compound imply proton transfer from the acid to the base, breaking and forming of the hydrogen bonding network in **1** and is accompanied by a profound structural rearrangement.

The mechanochemical preparation was carried out by manual grinding in an agata mortar of equimolar quantities of the two solid reactants (see Experimental section). After grinding, the polycrystalline material was used as such for powder diffraction experiments. In separate experiments (i) the zwitterion and base were dissolved in methanol in 2:1 and the solvent was allowed to evaporate at room temperature and (ii) small portions of the ground samples were dissolved in the minimum amount of solvent, in order to act as *seeds* and allow growth of single crystals suitable for X-ray diffraction experiments. By comparison with the diffractograms measured on the raw reactants, it was possible to ascertain whether the starting materials had been completely converted into products. The structure of the compound obtained mechanochemically is the same as the one obtained from solution crystallization.

Grinding of the zwitterion with the base in stoichiometric amounts other than 1:2 (i.e. 1:1, and 2:1) does not appear to lead to formation of different compounds, rather a mixture of the 1:2 products and of unreacted base or acid (as ascertained by X-ray powder diffraction) was invariably observed.

Figure 11 (top) shows that the adduct is characterized by the presence of a $[C_6H_{12}N_2H_2]^{2+}$ dication acting as a bridge between two $[Co^{III}(\eta^5-C_5H_4COO)_2]^-$ anions in *transoid* conformation, with formation of *charge-assisted* (\cdots) $O\cdots H-N^{(+)}$ hydrogen bonding interactions. **Figure 11** (bottom) shows how one of the water molecules (oxygen O5) is used to link together the $[C_6H_{12}N_2H_2]^{2+}[Co^{III}(\eta^5-C_5H_4COO)_2]_2^{2-}$ adducts.

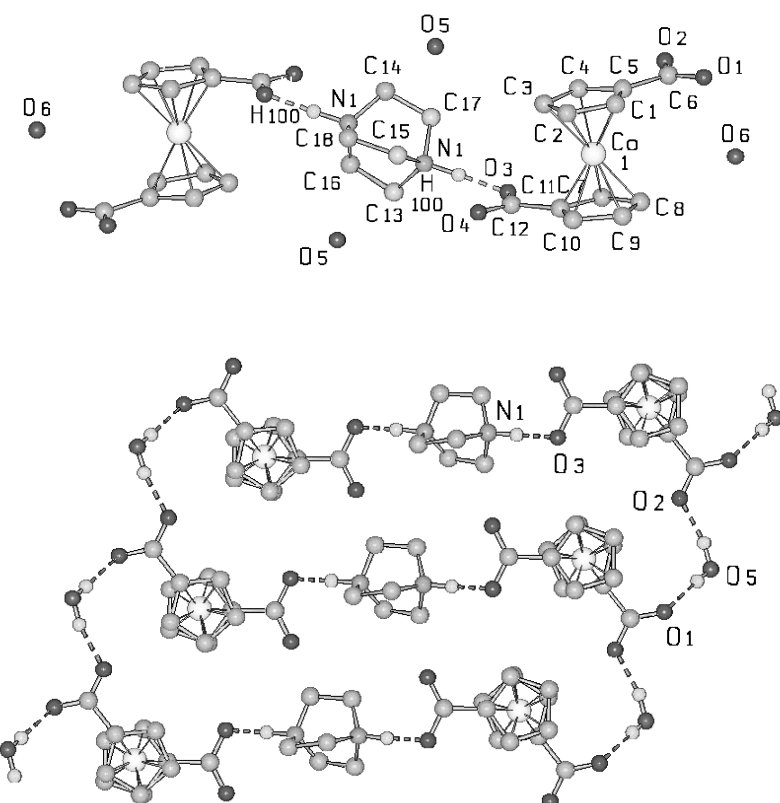


Figure 11. (Top) the adduct $[C_6H_{12}N_2H_2]^{2+}[Co^{III}(\eta^5-C_5H_4COO)_2]_2^{2-}$ is characterized by the presence of a $[C_6H_{12}N_2H_2]^{2+}$ dication acting as a bridge between two $[Co^{III}(\eta^5-C_5H_4COO)_2]^-$ anions in *transoid* conformation; (bottom) water molecules link together the $[C_6H_{12}N_2H_2]^{2+}[Co^{III}(\eta^5-C_5H_4COO)_2]_2^{2-}$ adducts. Relevant hydrogen bond parameters are N(1) \cdots O(3) 2.580(6), O(5) \cdots O(2) 2.733(7), O(5) \cdots O(1) 2.766(7) Å.

5. EXPERIMENTAL SECTION

All the starting materials were purchased from Aldrich and used without further purification. Reagent grade solvents and bidistilled water were used.

Mechanochemical and solution syntheses of $[C_6H_{12}N_2H_2]^{2+}[Co^{III}(\eta^5-C_5H_4COO)_2]_2^{2-}\cdot 1.5H_2O$. 20.2 mg (0.073 mmol) of **1** and 8.2 mg (0.073 mmol) of 1,4-diazabicyclo[2.2.2]octane were manually ground in an agate mortar for 5 min; single crystals of $[C_6H_{12}N_2H_2]^{2+}[Co^{III}(\eta^5-C_5H_4COO)_2]_2^{2-}\cdot 1.5H_2O$ suitable for single crystal X-ray diffraction were obtained by slow evaporation of a solution obtained dissolving 23.2 mg (0.084 mmol) of **1** and 9.4 mg (0.084 mmol) of 1,4-diazabicyclo[2.2.2]octane in 3 mL of methanol 99.8% seeded with 5 mg of the ground sample.

Crystal structure determination. X-ray diffraction data for $\mathbf{1}\cdot[\text{Co}^{\text{III}}(\eta^5\text{-C}_5\text{H}_4\text{COOH})_2]^+\text{I}^-$ and $[\text{C}_6\text{H}_{12}\text{N}_2\text{H}_2]^{2+}[\text{Co}^{\text{III}}(\eta^5\text{-C}_5\text{H}_4\text{COO})_2]_2^{2-}\cdot1.5\text{H}_2\text{O}$ were collected at room temperature on a Nonius CAD-4 diffractometer. Crystal data and details of measurements are summarized in Table 1. Common to both compounds: MoK α radiation, $\lambda = 0.71073 \text{ \AA}$, monochromator graphite, ψ -scan absorption correction. The SHELXL97 [23a] package was used for structure solution and refinement based on F^2 . All non-H atoms were refined anisotropically. The I $^-$ anion in $\mathbf{1}\cdot[\text{Co}^{\text{III}}(\eta^5\text{-C}_5\text{H}_4\text{COOH})_2]^+\text{I}^-$ is located on an inversion center, while the neutral and cationic moieties are related by a second inversion center; despite the good data quality, it was not possible to locate the three hydrogen atoms belonging to the -COOH groups. The anion in $[\text{C}_6\text{H}_{12}\text{N}_2\text{H}_2]^{2+}[\text{Co}^{\text{III}}(\eta^5\text{-C}_5\text{H}_4\text{COO})_2]_2^{2-}\cdot1.5\text{H}_2\text{O}$ is disordered over two positions, with 50:50 occupancy ratio; one of the two water molecules [O(6)] is also disordered around an inversion center, and was assigned an occupancy factor of 0.5. H_(CH) atoms were added in calculated positions. In $[\text{C}_6\text{H}_{12}\text{N}_2\text{H}_2]^{2+}[\text{Co}^{\text{III}}(\eta^5\text{-C}_5\text{H}_4\text{COO})_2]_2^{2-}\cdot1.5\text{H}_2\text{O}$ the H_(NH) atom and the hydrogen atoms belonging to the water molecule that is not disordered were located from a difference Fourier map and not refined. The program SCHAKAL99 [23b] was used for all the graphical representations. The program PLATON [23c] was used to calculate the hydrogen bonding interactions. In all cases, correspondence between the structures determined by single crystal X-ray diffraction and that of the bulk materials precipitated from solution was confirmed by comparing the experimental powder diffractograms obtained from the bulk material with those calculated on the basis of the single crystal structures.

Table 1
Crystal Data and Details of Measurements for
 $\mathbf{1}\cdot[\text{Co}^{\text{III}}(\eta^5\text{-C}_5\text{H}_4\text{COOH})_2]^+\text{I}^-$ *and* $[\text{C}_6\text{H}_{12}\text{N}_2\text{H}_2]^{2+}[\text{Co}^{\text{III}}(\eta^5\text{-C}_5\text{H}_4\text{COO})_2]_2^{2-}\cdot1.5\text{H}_2\text{O}$

| | $\mathbf{1}\cdot[\text{Co}^{\text{III}}(\eta^5\text{-C}_5\text{H}_4\text{COOH})_2]^+\text{I}^-$ | $[\text{C}_6\text{H}_{12}\text{N}_2\text{H}_2]^{2+}[\text{Co}^{\text{III}}(\eta^5\text{-C}_5\text{H}_4\text{COO})_2]_2^{2-}\cdot1.5\text{H}_2\text{O}$ |
|--|---|--|
| formula | $\text{C}_{24}\text{H}_{19}\text{Co}_2\text{IO}_8$ | $\text{C}_{30}\text{H}_{36}\text{Co}_2\text{N}_2\text{O}_{11}$ |
| M_w | 680.15 | 718.46 |
| system | Triclinic | Triclinic |
| space group | P-1 | P-1 |
| $a [\text{\AA}]$ | 6.898(3) | 6.081(3) |
| $b [\text{\AA}]$ | 7.704(2) | 10.605(4) |
| $c [\text{\AA}]$ | 11.161(2) | 12.776(6) |
| $\alpha [^\circ]$ | 87.87(1) | 113.77(4) |
| $\beta [^\circ]$ | 81.71(1) | 90.07(4) |
| $\gamma [^\circ]$ | 72.17(1) | 103.83(4) |
| $V [\text{\AA}^3]$ | 558.7(2) | 727.7(6) |
| Z | 1 | 1 |
| $F(000)$ | 334 | 744 |
| $\mu(\text{MoK}\alpha) [\text{mm}^{-1}]$ | 2.917 | 2.414 |
| measured reflns | 2064 | 2662 |
| unique reflns | 1955 | 2539 |
| parameters | 161 | 218 |
| GOF on F^2 | 1.134 | 0.979 |
| $R1$ (on F [$I > 2\sigma(I)$]) | 0.0285 | 0.0432 |
| $wR2$ (on F^2 , all data) | 0.0763 | 0.1255 |

6. CONCLUSIONS

The paradigm of crystal engineering is the “bottom-up” construction of crystalline assembly from components and the exploitation of the resulting crystalline materials for physical and chemical applications. The “bottom-up” paradigm, derived from supramolecular chemistry [22], implies the ability to assemble molecular or ionic components into the desired architecture by engineering a target network of supramolecular interactions.

Since the focus of crystal engineering is *making* crystals, methods of choice to exploit crystal engineering strategies invariably (and inevitably) end up with the problem of obtaining crystals. The desired material needs to be *by definition* in the crystalline form and is usually obtained by a crystallization method, whether from solution, melt or from more forcing hydrothermal syntheses. We have argued that reactions between solids and between solids and vapors can represent alternative ways to prepare crystals. Since reactions involving solid reactants or occurring between solid and gases do not generally require recovery, storage and disposal of solvents, they are of interest in the field of the so-called “green chemistry” where environmentally friendly processes are actively sought [10]. Furthermore solvent-less reactions often lead to very pure products and reduce the formation of solvate species.

In this paper we have discussed how crystal engineering strategies can be exploited to design and construct molecular crystals to take part in solvent-free solid-gas or solid-solid reactions with molecules or molecular aggregates. When the solid state process proceeds *via* breaking and forming of non-covalent interactions (such as hydrogen bonds), the crystalline product is the result of the supramolecular association of two or more units and can be regarded as a *supramolecular reaction* between solid supermolecules.

We have focused on the behavior of the zwitterionic organometallic molecule $[Co^{III}(\eta^5-C_5H_4COOH)(\eta^5-C_5H_4COO)]$, **1**, which has proved to be very versatile thanks to its amphoteric acid-base behavior and its coordinating capacity. The solid-gas and solid-solid processes discussed above rely on the possibility of ‘switching’ between O-H---O hydrogen bonds between molecules of **1** and charge-assisted ($^{(+)}O-H-X^{(-)}$) or $O^{(-)}-[H-NR_3]^{(+)}$ hydrogen bonds with cations and anions. In the case of the solid-gas reaction with formic acid, HCOOH, a third possibility has been ascertained: adduct formation without proton transfer. It is worth pointing out that these gas-solid reactions do not differ conceptually from gas-solid solvation. The main difference is in the energetic ranking of the interactions (whether covalent or non-covalent) that are broken or formed through the processes.

It is generally believed that molecular crystals held together only (or mainly) by hydrogen bonding interactions cannot compete with covalent or ionic inorganic solids in terms of cohesion and stability. In this paper we have shown that an organometallic molecule, such as **1**, easy to prepare and relatively inexpensive, can withstand both reversible gas-solid reactions with vapors of acidic and basic substances and mechanically activated reactions with inorganic salts and molecular crystals.

There are still several open issues, which we plan to address in the near future. For instance, we need to explore the effect of particle size and surface on the *kinetics* of the reactions as well as the relationship between composition of the vapor phase and exposure time in gas-solid reactions of **1** and the effect of the grinding time and of humidity on the product formation in the solid-solid reactions of **1**.

7. ACKNOWLEDGMENTS

We thank MIUR (COFIN and FIRB) the Universities of Bologna and Sassari for financial support.

8. REFERENCES

- [1] a) G. R. Desiraju, *Crystal Engineering: The Design of Organic Solids*, (Elsevier: Amsterdam, 1989); b) D. Braga, F. Grepioni, and G. R. Desiraju, Chem. Rev. **98** (1998) , 1375; c) D. Braga, F. Grepioni, and A. G. Orpen, eds., *Crystal Engineering: from Molecules and Crystals to Materials*,

- (Kluwer Academic Publishers, Dordrecht, 1999); d) A. J. Blake, N. R. Champness, P. Hubberstey, W. S. Li, M. A. Withersby, M. Schroder *Coord. Chem. Rev.* **183** (1999), 117; e) L. Brammer, D. Zhao, F. T. Ladipo and J. Braddock-Wilking, *Acta Crystallogr., Sect. B*, **51** (1995), 632; f) C. B. Aakeröy, *Acta Crystallogr., Sect. B*, **53** (1997), 569; g) M. W. Hosseini, *Coord. Chem. Rev.*, **240** (2003), 157; h) *Proceedings of the Dalton Discussion on Inorganic Crystal Engineering*, *J. Chem. Soc. Dalton Trans.*, (2000), 3705. the whole issue; i) B. Moulton and M. J. Zaworotko, *Chem. Rev.*, **101** (2001), 1629; j) D. Braga, G. R. Desiraju, J. Miller, A. G. Orpen and S. Price, *CrystEngComm*, **4** (2002), 500; l) M. D. Hollingsworth, *Science* **295** (2002), 2410; m) D. Braga, *Chem. Commun.*, (2003), 2751.
- [2] a) A.M. Beatty, *CrystEngComm* (2001); b) M.W. Hosseini and A. De Cian, *Chem. Commun.*, (1998), 727; c) C.B. Aakeröy and K.R. Seddon, *Chem. Soc. Rev.*, (1993), 397; d) T. Maris ; J.D. Wuest *J. Org. Chem.*, **69** (2004), 1776.
- [3] *The Crystal as a Supramolecular Entity. Perspectives in Supramolecular Chemistry*. G. R. Desiraju, Ed.; Wiley: Chichester, 1996.
- [4] a) G. R. Desiraju, *Angew. Chem. Int. Ed.*, **34** (1995), 2311; b) G. Gilli and P. Gilli, *J. Mol. Struc.*, **552** (2000), 1; c) D. Braga, L. Maini, F. Grepioni, F. Mota, C. Rovira, and J. J. Novoa, *Chem. Eur. J.*, **6** (2000), 4536; d) D. Braga, E. D'Oria, F. Grepioni, F. Mota, and J.J. Novoa, *Chem. Eur. J.*, **8** (2002), 1173; e) T. Steiner, *Angew. Chem. Int. Ed.*, **41** (2002), 48; f) G. R. Desiraju, *Acc. Chem. Res.*, **35** (2002), 565.
- [5] a) S. R. Batten and R. Robson, *Angew. Chem. Int. Ed.*, **37** (1998), 1461; b) S. R. Batten, B. F. Hoskins and R. Robson, *Chem. Eur. J.*, **6** (2000), 156; c) N. L. Rosi, M. Eddaoudi, J. Kim, M. O'Keeffe and O. M. Yaghi, *Angew. Chem. Int. Ed.*, **41** (2001), 284; d) O. M. Yaghi, H. L. Li, C. Davis, D. Richardson and T. L. Groy, *Acc. Chem. Res.*, **31** (1998), 474; e) H. Li, M. Eddaoudi, M. O'Keeffe and O. M. Yaghi, *Nature*, **402** (1999), 276; f) M. Eddaoudi, J. Kim, N. Rosi, D. Vodak, J. Wachter, M. O'Keefe and O. M. Yaghi, *Science*, **295** (2002), 469; g) S. A. Bourne, J. Lu, B. Moulton and M. J. Zaworotko, *Chem. Commun.*, (2001), 861; h) B. Rather and M. J. Zaworotko, *Chem. Commun.*, (2003), 830; i) B. Moulton, H. Abourahma, M. W. Bradner, J. Lu, G. J. McManus and M. J. Zaworotko, *Chem. Commun.*, (2003), 1342; l) M. Fujita, *Chem. Soc. Rev.*, **27** (1998), 417; m) B. Olenyuk, A. Fechtenkötter and P. J. Stang, *J. Chem. Soc., Dalton Trans.*, (1998), 1707; n) N. L. Rosi, M. Eddaoudi, J. Kim, M. O'Keeffe and O. M. Yaghi, *Cryst. Eng. Comm.*, **4** (2002), 401; o) N.L. Rosi, J. Eckert, M. Eddaoudi, D.T. Vodak, J. Kim, M. O'Keeffe and O. M. Yaghi, *Science*, **300** (2003), 1127; p) M. D. Ward, *Science*, **300** (2003), 1124; q) L. Pan, M. B. Sander, X. Huang, J. Li, M. Smith, E. Bittner, B. Backrush and J. K. Johnson, *J. Am. Chem. Soc.*, **126** (2004), 1309; r) G. Frey, M. Larches, C. Sere, F. Mélange, T. Roseau and A. Percheron-Guégan, *Chem. Commun.*, (2003), 2976.
- [6] a) F. A. Cotton, C. Lin and C. A. Murillo, *J. Chem. Soc., Dalton Trans.*, (2001), 499; b) F. A. Cotton, C. Lin, and C. A. Murillo, *Chem. Commun.*, (2001), 11; c) M. E. Braun, C. D. Steffek, J. Kim, P. G. Rasmussen and O. M. Yaghi, *Chem. Commun.*, (2001), 2532; d) W. Mori and S. Takamizawa, *J. Solid State Chem.*, **152** (2000), 120; e) L. Carlucci, G. Ciani, D. M. Proserpio and S. Rizzato, *CrystEngComm.*, **4** (2002), 121; f) L. Carlucci, G. Ciani and D. M. Proserpio, *CrystEngComm.*, **5** (2003), 269; g) L. Carlucci, G. Ciani and D. M. Proserpio, *Coord. Chem. Rev.*, **246** (2003), 247.
- [7] See, for example: a) M. Albrecht, M. Lutz, A. L. Speck and G. van Koten, *Nature*, **406** (2000), 970; b) M. Albrecht, R. A. Gossage, M. Lutz, A. L. Speck and G. van Koten, *Chem. Eur. J.*, **6** (2000), 1431.
- [8] D. Braga and F. Grepioni, *Angew. Chem. Int. Ed. Engl.*, **43** (2004), 4002.
- [9] D. Braga, L. Maini, M. Polito, L. Mirolo and F. Grepioni, *Chem. Eur. J.*, **9** (2003), 4362.
- [10] P. T. Anastas and J. C. Warner, *Green Chemistry: Theory and Practice*, (Oxford University Press, New York, 1998).
- [11] D. Braga, L. Maini, M. Polito and F. Grepioni, *Organometallics*, **18** (1999), 2577.
- [12] D. Braga, G. Cojazzi, D. Emiliani, L. Maini and F. Grepioni, *Chem Commun.*, **21** (2001), 2272.
- [13] D. Braga, G. Cojazzi, D. Emiliani, L. Maini and F. Grepioni, *Organometallics*, **21** (2002), 1315.

- [14] D. Braga, L. Maini, M. Mazzotti, K. Rubini and F. Grepioni, *CrystEngComm.*, **5** (2003), 154 .
- [15] D. Braga, Lucia Maini, M. Mazzotti, K. Rubini, A. Masic, R. Gobetto and F. Grepioni, *Chem. Commun.*, (2002), 2296.
- [16] a) D. Braga, G. Cojazzi, D. Emiliani, L. Maini, and F. Grepioni, *Chem. Commun.*, (2001), 2272; b) D. Braga, G. Cojazzi, D. Emiliani, L. Maini, and F. Grepioni, *Organometallics*, **21** (2002), 1315.
- [17] a) D. Braga, F. Grepioni, *Chem. Soc. Rev.*, **4** (2000), 229; b) D. Braga and F. Grepioni in *Crystal Design, Structure and Function. Perspectives in Supramolecular Chemistry*, (Vol. 7, Ed. G. R. Desiraju), (J. Wiley, Chichester, UK, 2003).
- [18] a) T. L. Threlfall, *Analyst*, **120** (1995), 2435; b) N. Kubota, N. Doki, M. Yokota and D. Jagadish, *J. Chem. Eng. Japan.*, **35** (2002), 1063.
- [19] D. Braga, L. Maini, G. de Sanctis, K. Rubini, F. Grepioni, M. R. Chierotti and R. Gobetto, *Chem. Eur. J.*, **9** (2003), 5538.
- [20] D. Braga, D. Emiliani, G. Cojazzi, L. Maini, M. Polito, F. Grepioni *J. Mol. Struc.*, **647**, (2003), 113.
- [21] a) D. Bradley, *Chemistry in Britain*, (2002), 42; b) K. Tanaka, F. Toda, *Chem. Rev.*, **100** (2000), 1025; c) K. Tanaka, *Solvent-free Organic Synthesis*, (Wiley-VCH, 2003); d) G. W. V. Cave, C. L. Raston and L. Scott, *Chem. Commun.*, (2001), 2159; e) G. Rothenberg, A. P. Downie, C. L. Raston and J. L. Scott, *J. Am. Chem. Soc.*, **123** (2001), 8701; f) G. Kaupp, *CrystEngComm.*, **5** (2003), 117; g) V. V. Boldyrev and K. Tkacova, *J. Mat. Synth. Proc.*, **8** (2000), 121; h) L. R. MacGillivray, *CrystEngComm.*, **4** (2002), 37; i) F. Toda, *CrystEngComm.*, **4** (2002), 215.
- [22] a) J. M. Lehn, *Supramolecular Chemistry: Concepts and Perspectives*, (VCH, Weinheim, 1995); b) J. W. Steed and J. L. Atwood, *Supramolecular Chemistry*, (Wiley & Sons, 2000).
- [23] a) G. M. Sheldrick, *SHELXL97, Program for Crystal Structure Determination*, (University of Göttingen: Göttingen, Germany, 1997); b) E. Keller, *SCHAKAL99, Graphical Representation of Molecular Models*, (University of Freiburg, Germany, 1999); c) A. L. Spek, *Acta Crystallogr.(Sect. A)*, **46** (1990), C31.